Instituut voor
Kern- en Stralingsfysica
Departement natuurkunde en sterrenkunde
Faculteit Wetenschappen

KATHOLIEKE UNIVERSITEIT
LEUVEN

A gas catcher for the selective production of radioactive beams through laser ionization

Promotoren:
Prof. Dr. M. Huyse
Prof. Dr. P. Van Duppen

Proefschrift ingediend tot
het behalen van de graad van
doctor in de wetenschappen
door

Marius Facina

Leuven 2004

To my lovely wife, Diana, and our wonderful daughter, Ecaterina.

Acknowledgements

I want to express my sincere gratitude to my promoters Prof. Mark Huyse and Prof. Piet Van Duppen for their encouragement during this research and for their support in my scientific work. Their constructive criticism as supervisors, based on a wide experience of scientific and academic career, has deepened my understanding in the field of my research. Thank you!

I am also very much obliged to Dr. Yuri Kudryavtsev who facilitated my first steps in the field of laser ionization. His experience in running and developing the laser ion source of LISOL was essential for this work. Thank you!

Not at least I wish to thank to Johnny Gentens and Paul Van den Bergh for running the LISOL mass separator.

Many thanks to the cyclotron group at CRC Louvain-La-Neuve for excellent beams.

Many thanks to the administrative staff of IKS: Josee, Katia and Sally.
Many thanks to the IT-team: Joris and Luc.
Many thanks to the people of the mechanical workshop as well.

I also want to thank all my present and past colleagues: Astrid, Bart, Daniel, Dieter, Dmitri, Farouk, Irina, Ivan, Jan, Jan (Van Roosbroeck), Jarno, Jean-Charles, Johnny, Karen, Kirill, Marisa, Oleg, Paul, Pascale, Riccardo, Rob, Sarah, Shelly. Their support and the great time spent together have been essential in making these four years at IKS a productive and wonderful time.

Lastly, thanks to the jury members for their careful reading of this text and helpful comments.

Contents

Introduction

Widespread scientific interest exists in using accelerated Radioactive Ion Beams (RIBs) for nuclear physics, astrophysics, solid-state physics, and applied studies. Two general approaches can be used to produce RIBs: the In-Flight (IF) separation method and the Isotope-Separator-On-Line (ISOL) method. The RIBs can be further used in secondary reactions aiming at production of more exotic nuclei far from stability. The IF method requires one accelerator and electro-magnetic filters to select radioactive fragments produced in medium-energy reactions of heavy-ion beams incident on thin targets. IF facilities exist and are in use in several laboratories: GSI (Germany), GANIL (France), Dubna (Russia), RIKEN (Japan), MSU (USA). The ISOL method requires two accelerators and is used to produce low-emittance beams at lower energies than in the IF method. A primary beam induces spallation, fusion evaporation, fission or fragmentation reaction on a thick target, which is usually kept at high temperatures to facilitate the diffusion of reaction products. The extracted isotopes are conducted into an ion source. After the extraction of the desired charge-state from the ion source, and mass separation, the radioactive species can be used for experiments at low energy (a few tens to a few hundreds of keV) or may be re-accelerated by a second accelerator up to few tens of MeV/amu. ISOL facilities exist and are in use in laboratories worldwide spread: Louvain-la-Neuve (Belgium), Jyväskylä (Finland), REX-ISOLDE CERN (Switzerland), SPIRAL-GANIL (France), Oak-Ridge (USA), ISAC TRIUMF (Canada).

The advantage of the IF method is that it is fast, while the delay time of the ISOL method depends on the chemical properties of the element. The ISOL technique delivers good quality beams in contrast to the IF method, thus the two methods are complementary and they overlap in a narrow energy range around 25 MeV/amu. The next generation of the RIBs facilities will combine the principles of the above mentioned IF and ISOL techniques aiming at production of the most exotic short-lived isotopes. Taking advantage of the two systems, the long delay of the ISOL technique could be avoided by stopping the reaction products in a noble-gas filled chamber, guide the ions using electrical fields and extract them through an RF cooler.

The most important parameters of an ion source for production of RIBs are the efficiency and the selectivity. As the on-line conditions are different from one facility to another, different options have been successfully applied in order to achieve higher efficiencies and selectivities. At the Leuven Isotope Separator On-Line (LISOL) resonant laser ionization of the reaction products stopped and stored in a buffer noble-gas (helium or argon) cell has been used for years. Thin-foil targets are usually placed at the entrance in the buffer gas cell and bombarded by a primary beam delivered by the CYCLONE 110 MeV cyclotron. The whole spectrum of reaction products recoiling out of the target is entering the gas. The

produced isotopes are slowed down and, depending on their initial kinetic energy, they stop in gas, in a major fraction. The primary beam is traversing the gas cell and it is stopped in a beam dump placed outside the gas cell. In the background of the electron-ion pairs produced by the slowing down of the primary beam in gas, the reaction products neutralize and follow the gas flow lines towards the exit hole of the gas cell. Apart from diffusion losses in gas, a large fraction of isotopes produced in the reaction arrive in atomic form at the exit hole of the gas cell, where an element of interest is resonantly re-ionized via a two-step process.

In order to enlarge the possibilities of a gas cell for the production of intense RIBs it is of crucial importance to characterize the different stages a radioactive ion undergoes from its production to the decay station. The usual delays in the gas cell at LISOL are from few tens of milliseconds up to several hundreds of milliseconds, depending on the geometrical configuration. The history of the radioactive ion starts with the recoil after the nuclear reaction into the gas cell, followed by the slowing process down to thermal energies. From then on a major role is played by the different interactions of the radioactive nucleus, in its atomic or ionic form, with the buffer gas atoms, with impurities, with electrons and with electric fields. Prior to the optimization of the gas cell parameters, the energy of the primary beam has to be tuned on the maximum cross section for the production of the nuclei of interest, in connection with the optimization of the target thickness for a maximum yield and transmission. The properties of the RIB extracted from the gas cell are mainly determined by the properties of the gas jet flowing out through the exit hole. Differential pumping has to deliver the right jet properties for a proper injection of the ion beam into an RF guide coupled to an acceleration section, and further on to an electromagnetic separator.

The characterization and optimization of such a setup for production of exotic RIBs is complex and long. In off-line tests, a particular element is evaporated from a filament in the gas cell and it is resonantly ionized, extracted, accelerated, mass separated and measured. An alternative is to implant in the gas cell a controlled amount of stable ions from an accelerator. After stopping in the buffer gas a fraction of the implanted ions is thermalized in +1 state. However, the large majority have neutralized and resonant laser ionization is used to re-ionize those atoms which have survived loss processes. Quantitative and qualitative information about the processes ongoing in the gas cell are studied in this manner. This includes the interaction of the ions of interest with the impurity molecules, with the buffer gas atoms and ions, with the electrons and with electrical fields as well as the ionization and recombination processes. In on-line experiments, radioactive isotopes from a target are catched in the gas cell, laser ionized, extracted, accelerated, mass separated and implanted onto a movable tape in front of a gamma ray detector system which records the decay spectra. The off-line and on-line conditions are essentially different given the high electron-ion pair density created by the presence of a primary beam passing through the gas. Beyond the technical challenges, the performance of the laser ion source is case dependent and it is influenced by the primary beam type, the buffer gas used for stopping and guiding the reaction product, the element which is laser ionized and the interaction of the atoms and ions of interest with the impurities present in the buffer gas.

The thesis is structured as follows. In Chapter 1 we introduce the experimental procedure used at LISOL for production of Radioactive Ion Beams. A brief motivation from the point of view of the physics which can be performed is given. The experimental setup is presented in details in Chapter 2. The front-end of the installation, the gas cell, laser system, post accelerator and the beam control and diagnostic system are described in dedicated sub-chapters. The processes occurring

in the gas cell are discussed in Chapter 3. We start with the slowing down and stopping mechanism of ions in a buffer gas. Then the behavior of ions and atoms in a buffer gas is described, followed by an extensive introduction into the physics of ionized gases. Chapter 4 highlights the effect of DC electrical fields on the electrons and ions in a gas. The theoretical approaches used for ionization detectors are discussed in connection with the charge collection process in the gas cell. Chapter 5 concerns the experimental results obtained at LISOL and their interpretation. First, the experimental results obtained with a stable ^{58}Ni beam converted from high energy to low energy are presented. The laser ion source efficiency, selectivity and the evacuation properties of the ion source as well as the experimental results obtained using DC electrical fields in the gas cell are extensively discussed. The effect of RF electrical fields in the gas cell is briefly introduced in the Appendix A. The experimental results obtained using RF electrical fields in the gas cell of the LISOL laser ion source are presented and discussed in this appendix. The experimental results obtained with the heavy ion fusion guide are presented in a dedicated sub-chapter of Chapter 5. The laser ion source efficiency and selectivity for the production of neutron deficient Ru/Rh isotopes in heavy ion induced fusion reactions are presented and discussed. Appendix B concerns the results obtained in proton induced fission of ^{238}U reactions. The laser ion source efficiency and selectivity for the production of neutron-rich Ni and Rh isotopes are presented and discussed in this appendix. The recapitulation of the major issues and the outlook are given at the end of the thesis, in Chapter 6.

Chapter 1

Radioactive ion beams

The relatively new experimental technique of Radioactive Ion Beams offers unique opportunities to explore the rich nuclear "landscape". Especially studies of nuclear structure and reaction mechanisms have benefitted greatly from the availability of radioactive nuclear beams, as wholly new possibilities to investigate the influence of extreme neutron-proton ratios (also known as isospin) become available. Nuclei far from beta stability are thought to play a decisive role in those astrophysical processes that build up heavier elements from lighter nuclei, e.g. in supernovae, and thus knowledge about such "exotic" nuclei can help us understand our own origin. Nuclei far from stability are also interesting since we do not know whether those physical models we have constructed in order to explain more stable systems are still valid at the limits of stability of nuclear matter. Radioactive ion beams are also used within so diverse fields as atomic physics, material research/solid state physics, nuclear chemistry and medicine. The radioactive ion beams -based research is in a strong phase of expansion, and a number of new facilities are being designed and/or constructed all over the world. The field is both very exciting and on the frontline of nuclear science.

1.1 Motivations for studies with radioactive ion beams

The atomic nucleus represents one of the fundamental building blocks of matter in the universe. The basic problem of nuclear structure physics is a quantal many-body one whose unique aspect stems from the number of constituents and the nature of the force. A nucleus consists of a large, but finite number of nucleons, interacting via a strong, short range, force. The most critical ingredients in determining the predicted properties of a nucleus from a given effective interaction, is the overall number of nucleons and the ratio N/Z of neutrons to protons. It is the extremes in these quantities, which define the limits of existence for nuclear matter that are opened up for study by the advent of radioactive beam accelerators.

Although the Chart of the Nuclides includes about 3000 different nuclides, current models predict that at least 4000 more could be discovered. Figure 1.1 shows a plot of the known atomic nuclei as a function of their proton and neutron number. The black squares mark stable nuclei, while the color squares indicate nuclei which

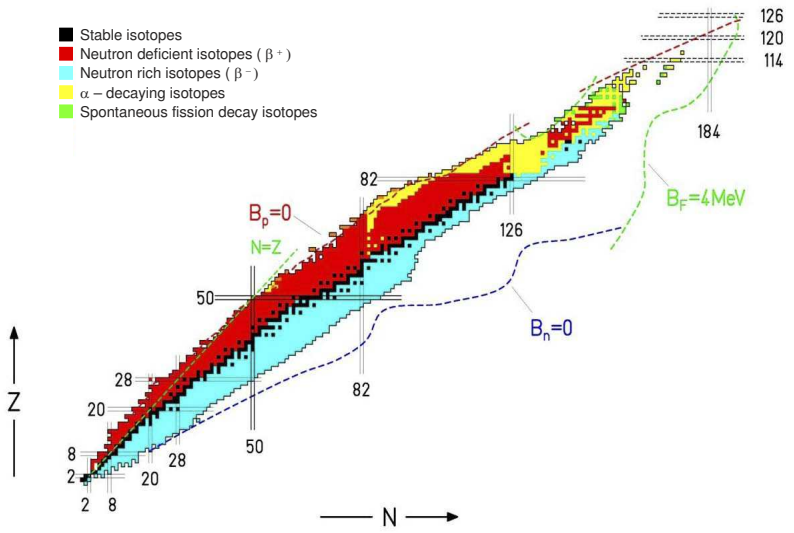

FIG. 1.1: The nuclear chart. The black squares represent the stable nuclei and the nuclei having half-lives comparable to or longer than the Earth's age (4.5 billion years). By adding either protons or neutrons one moves away from the "valley of stability" formed by the stable isotopes: blue squares - neutron-rich isotopes, red squares - proton-rich isotopes. All charted unstable isotopes have been produced and studied in laboratories. The un-charted isotopes between the proton and neutron drip lines form the so-called "terra incognita".

are unstable and eventually transform into the stable ones by radioactive decays. The color characterizes the dominant nuclear instability (blue: β^- unstable; red: β^+ unstable; yellow: α unstable, green: spontaneous fission). The black vertical and horizontal lines show the magic numbers, reflecting regions where nuclei are expected to be more tightly bound and have longer half-lives.

The borders of this landscape, in the chart of nuclides (see Fig.1.1), are defined by the proton (B_p=0) and neutron drip lines (B_n=0), outside which the nuclear binding forces are no longer strong enough to hold the nuclei together, leading to prompt decays by emission of protons and neutrons. The proton drip line is already relatively well delineated experimentally up to Z=83. In contrast, the neutron drip line is considerably further from the valley of stability and harder to approach. Except for the lightest nuclei where it has been reached experimentally, the neutron drip line has to be estimated on the basis of nuclear models, hence it is very uncertain due to the large involved extrapolation. Apart from the proton and neutron drip lines, the location of the third frontier of nuclear matter requires knowledge of the maximum charge and mass that a nucleus and atom can reach. The number of elements which can be created in nuclear reactions is limited by the increasing probability of fission, α- and proton emission with increasing nuclear charge.

As the radioactive nuclides cannot be found in nature, they must first be pro-

duced in some nuclear reactions, for example in heavy-ion induced fragmentation or in neutron induced fission. Neutron-rich exotic nuclei far from the valley of stability are not accessible with stable beams and stable targets, thus they can only be produced with radioactive beams and/or radioactive targets. Therefore the continuous development of radioactive beam facilities will provide the opportunity to study inaccessible regions of the nuclear chart and, in particular, to study nuclear matter at the extremes of particle stability. Physics associated with the radioactive ion beams has a leading role in nuclear science and it addresses basic questions on the nuclear structure, nuclear astrophysics and fundamental interaction physics.

1.2 Techniques for production of radioactive ion beams

As argued in the previous section the studies in the field of nuclear structure and interaction physics have mostly been focused on exotic isotopes which can be divided into three major categories:

- proton rich nuclides (or neutron deficient),
- neutron rich nuclides,
- superheavy nuclides.

The most efficient mechanisms for populating proton- and neutron-rich nuclei are different due to the different proton to neutron ratio. Proton rich nuclei are best produced using heavy ion induced fusion reactions with projectiles and targets having nearly equal masses. Also the spallation reactions are a good way to produce them. The most efficient mechanism to produce neutron-rich isotopes is fission or spallation of neutron-rich heavy nuclei [Gar92]. The use of very neutron-rich products as beams is particularly interesting to provide access to even more neutron-rich nuclides.

1.2.1 How to make radioactive beams?

There are two general methods used to produce radioactive beams. One is the fast beam or In-flight (IF) fragment separator method, and the second is the Isotope Separator On-Line (ISOL) or re-accelerated beam approach [Sav02, VDu03, Huy04].

The ISOL technique uses the radioactive ions produced by the beam of a primary accelerator or by neutrons from a nuclear reactor. It was born in 1951 when O. Kofoed-Hansen and K. O. Nielsen produced neutron-rich noble gas isotopes by bombarding an uranium target with fast neutrons coming from the break-up of a 11 MeV d beam [Kof51]. The target/catcher system arrangement stops the recoils from the nuclear reaction, and further on the activity is transmitted to an ion source through diffusion or jet transport. Chemical selectivity during the transfer process to the ion source can be obtained by a proper choice of the target material, of its operating temperature and of the "connection" to the source. Fig.1.2.a shows a schematic view of an ISOL-based facility. The resulting beams are ion-optically (emittance, energy resolution, timing structure) of excellent quality but the thermalization process and the eventual re-ionization in the ion source can be slow and it can induce losses of short-living nuclei.

The concept of In-Flight fragment separator was pioneered with relativistic heavy ion beams at Oak Ridge, USA [Coh58, Arm67]. This technique relies on the

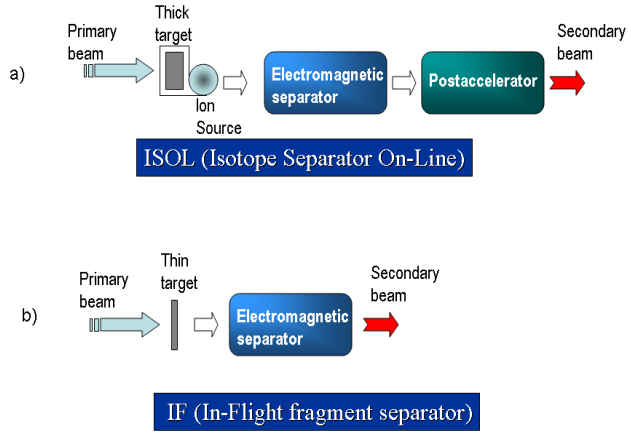

FIG. 1.2: The schematic view of the a) ISOL method, and b) In-flight (IF) method for production of radioactive ion beams.

forward focusing present in peripheral nuclear reactions, such as projectile fragmentation and fission of 30-1500 MeV/amu heavy ions [Mun92, Gei92]. In the In-Flight separation technique, a thin target is used and the primary beam is not stopped in the target. The mixture of unreacted primary and secondary ions are first filtered to select a single magnetic rigidity, $B \cdot \rho = m \cdot v/q$ [Wol87], by a dispersive beam line in conjunction with an aperture. Fig.1.2.b shows a basic layout of an in-flight separation facility. The In-Flight method is applicable to very short-living nuclei (μs) as only the flight time from the production target to the measuring station induces decay losses. With the In-Flight method the radioactive ions are energetic and can eventually be slowed down and stored.

In general terms one can identify the following complementary aspects of the ISOL and In-flight techniques:

- The In-flight method is fast, so short-lived radioactive ion beams can be made, and it does not suffer from the overall delay constraints of the ISOL technique induced by the dependence on the chemical properties of the element.
- Because of the thinner targets and smaller primary beam intensities, the radioactive ion beam intensities obtained with the In-flight technique can be several orders of magnitude lower than those from the ISOL method.
- The ISOL technique provides high-quality radioactive ion beams with very good transversal and longitudinal emittance, in contrast to the In-flight method.
- ISOL facilities add post-acceleration so one extra accelerator is needed, while on the other hand, the In-flight facilities add deceleration and cooling in order to achieve higher beam quality and intensity, at the expense of decay losses due to long delays.

1.2.2 Present and future radioactive isotope facilities: An overview

Today, a century after the discovery of the radioactivity phenomenon, radioactive beams have become an extraordinary tool for modern nuclear physics. The field of nuclear physics with exotic beams is both rich and diverse. The continuous development of beams and instrumentation has been crucial for nuclear-structure studies. It is important to stress that there are many critical scientific questions that can be addressed with these beams. Therefore concentrated effort is put world-wide into design, development and operation of radioactive ion beam facilities. Table 1.1 gives a partial list of the present running radioactive ion beam projects and their energy range for the produced radioactive ion beams.

Table 1.1: A list of radioactive beam facilities [EMIS02]. The given beam energies might well not be updated. "FS" stands for Fragment Separator.

Facility Name	Location	Energy	Type
	Louvain-la-Neuve, Belgium	0.2-1 MeV/u	
ATLAS-ANL	Argonne, USA	4-18 MeV/u	
BEARS-LBL	Berkeley, USA	1-30 MeV/u	ISOL
FRS-GSI	Darmstadt, Germany	$\leq$ 1 GeV/u	IF (FS)
HRIBF	Oak Ridge, USA	$\sim$ 4-5 MeV/u	ISOL
IGISOL	Jyväskylä, Finland	40 keV	ISOL
ISAC-TRIUMF	Vancouver, Canada	150 keV/u-1.5 MeV/u	ISOL
ISOL-GSI	Darmstadt, Germany	50 keV	ISOL
ISOLDE-CERN	Geneva, Switzerland	$\leq$ 3.1 MeV/u	ISOL
RIKEN	Saitama, Japan	light nuclei $\leq$ 500 MeV/u	
		Uranium ions $\leq$ 150 MeV/u	IF (FS)
SPIRAL-GANIL	Caen, France	2-25 MeV/u	IF (FS)
U400/U200 JINR	Dubna, Russia	$\leq$ 25 MeV/u	IF (FS)

A novel approach combining the positive aspects of both ISOL and In-flight techniques, such as high intensity and high quality beams, characteristic to ISOL method, and short delays, characteristic to In-flight method, respectively, could significantly lead to an increase of the yields of extremely exotic isotopes and make them available for study. In this new concept, isotopes produced by fragmentation or fission reactions delivered from a fragment separator are stopped and cooled in a high-purity buffer gas cell and extracted by electro-magnetic fields as thermal singly-charged ions [Sav03]. This technique promises large increase in efficiency for very short-lived isotopes. A second generation of radioactive ion beam facility

based on this approach is proposed for the future Rare Isotope Accelerator (RIA) [Sav02] in USA.

Substantial R&D work has to be accomplished as well in Europe, where the community is preparing for the next generation EURopean Isotope Separator On Line (EURISOL) facility. The EURISOL scheme is based on a 1 GeV 4 MW, continuous-wave proton linac. Using the full power of the proton beam, very high fluxes of neutrons will be produced in a spallation target which in turn will induce fission of uranium. Part of the proton beam can also be directed onto a heavy target producing large quantities of (mostly) proton-rich isotopes. The secondary beams will be post accelerated to a wide range of energies: from few tens of keV up to 10 MeV/u, and for masses $\leq$ 100 to about 100 MeV/u (for more details on the proposed facility see ref. [Eur03, NuP04]).

From an experimental point of view, a "figure of merit" can be defined for radioactive beam research as consisting of three main parts:

- **Intensity**: related to the secondary beam intensity.
- **Selectivity**: related to the purity of the secondary beam as well as to the resolving power of the experimental instrumentation.
- **Sensitivity**: related to the efficiency of the detection systems and their ability to provide complete experimental information.

The main aim for developing the second generation facilities and instruments is to increase the experimental figure of merit by several orders of magnitude. The study of the atomic nucleus has already witnessed several major developments over the last decade. New insight into dynamics of atomic nuclei has been gained, but unresolved problems remain and new ones emerge. The study of exotic nuclei in particular will shed light on new aspects of nucleonic matter and promises much more comprehensive understanding of strongly-interacting many-body systems in general. The research evolves more and more towards international large-scale facilities but, many experiments and important parts of R&D-work are carried out by university-based groups. Therefore the Nuclear Physics European Collaboration Committee (NuPECC) recognizes and encourages the efforts of these groups, as their support, including the local infrastructures, is essential for the success of the future large-scale projects.

1.3 Production of radioactive ion beams at LISOL

A short history of LISOL setup and its applications

The first on-line experiment performed at Leuven Isotope Separator On-Line (LISOL) has been performed in May 1975. At that time, five types of ion sources were used to produce long-lived Cd, In and Sn isotopes (A=103$\div$107) in heavy-ion induced fusion reactions. These were: a one filament (Cd) and three filament Nielsen sources (Ag and In), two types of Febiad sources (Sn and In) and a small volume source for elements with low ionization potential. Yields of $\sim 10^5$ atom/s from the ion source of these radioactive isotopes have been reported [Ver81], using up to 5 eμA $^{14}N^{4+}$ / $^{16}O^{4+}$ beam intensities delivered by the CYCLONE cyclotron at Louvain-la-Neuve. One limitation at that time was the long delay of radioactive ions in the ion sources from 7 s up to 40 s, depending on the element and configuration.

During the year 1986, the newly upgraded CYCLONE offered a wider beam type choice ranging from proton to krypton ion beams. The ion source of LISOL has

been modified according to the IGISOL principle [Arj81], i.e. the target chamber has been coupled to the mass separator through a He gas jet. The basic idea is that reaction products are thermalized in the ionic state +1 in helium buffer gas after recoiling out of the target. Further on they are extracted from the ion source with the gas jet flowing out through a Ø0.7 mm exit hole and injected into the accelerating section. The ^{98}Rh isotope ($T_{1/2}$=3.5 min) has been produced in the heavy-ion induced fusion reaction ^{16}O (210 MeV) (^{93}Nb, xn yp) with yields of $\sim$ 420 nuclei/μC, representing 0.03% of the primary production of ^{98}Rh coming out of the target [Den87]. The delay of ions in the gas chamber, $\sim$6 ms, has been measured by using trace ^{86}Kr gas mixed in low concentration with the helium gas.

1991-1992 is the period when a new idea emerges, and a laser ion source based on resonance photo-ionization is proposed [Qam92]. The basic principle of the laser ion source is to stop in a gas chamber the reaction products from a target. Two-step one-color photo-ionization of nickel atoms originating from a hot filament has been used in feasibility studies. The laser system consisted of a low-repetition rate (10Hz) Q-switched Nd-YAG [1] laser and a dye laser delivering UV light tunable over the 310-330 nm wavelength region.

In 1994 the construction of the laser ion source has been completed and the project "Development of a universal selective and efficient on-line laser ion source"[2] started. The principle of the new laser ion source combines the fast and universal thermalization of nuclear reaction products in a buffer gas, the high selectivity and efficiency of resonance photo-ionization and the ion-storage capability of noble gases. The new high pulse-repetition rate (200 Hz) laser system was brought into operation. It includes two time-synchronized excimer XeCl lasers (Lambda Physik LPX240i) that pump two dye lasers (Lambda Physik Scanmate-2). The frequency doubling option allows to perform a two-step laser photo-ionization of elements with ionization potential up to 10 eV.

Since the start of its operation, exciting results have been obtained with the laser ion source of LISOL. Elementally purified beams of ^{54,55}Ni and ^{54}Co produced in light-ion induced fusion evaporation, and ^{113}Rh, produced in proton-induced fission of ^{238}U, were obtained [Kud96]. Yields of 3.6 $\cdot 10^4$ atom/μC of ^{55}Ni isotope ($T_{1/2}$=204 ms) are reported in 1996, with a laser ion source selectivity of 280. The selectivity of the laser ion source for production of Ni isotopes is defined as the ratio of the yield of Ni with the lasers on, tuned to resonantly ionize Ni, to the yield of Ni without laser ionization.

One remarkable technical achievement was the first successful implementation of a new SextuPole Ion Guide (SPIG) in 1997 [VBe97]. This device ensured the transition from the high-pressure gas cell to the separator vacuum, playing in the same time the role of a cooler and improving the optical beam quality. Due to the unique combination at LISOL of resonant laser ionization with ion guidance, it was possible to measure and determine the half-lives of $^{68-74}$Ni neutron-rich isotopes produced in proton-induced fission of ^{238}U reaction [Fra98, Fra99, Fra01]. The level scheme has been extend for ^{69}Cu and newly established for ^{71,73}Cu isotopes [Fra01].

In 2001 the front-end of the LISOL setup has been upgraded, allowing a better beam control and diagnostics, and an improved differential pumping between the high pressure gas cell and the vacuum part of the installation. A maximal pressure of 1.5 bar of the buffer gas can be used.

One of the scientific directions has been the study of very neutron-deficient

[1] Quanta-Ray DCR-11 pulsed laser was used to pump a Quanta-Ray PPL-3 dye laser.
[2] or "DT-laser"

isotopes $^{90-91}$Ru and $^{91-93}$Rh produced in a ^{58}Ni (^{36,40}Ar, xn yp $z\alpha$) fusion-evaporation reaction. Simultaneously new γ and β detection systems have been developed and implemented. Measurements of high-spin isomeric beta-decay, as in the case of ^{92}Rh, as well as ground-state decay, including rare ground-state decays of ^{91,93}Rh to excited states in daughter nucleus have been successfully performed for the first time [Gor00, Dea04]. The β-delayed proton activity of ^{90}Rh and ^{89}Ru isotopes was also investigated and upper limits for this decay mode in these two nuclei have been deduced [Dea04].

The development program of the laser ion source included three main aims:

- Off-line studies of ion behavior in a gas cell.
- Study and optimization of short-lived radioactive beam production, for beta-decay studies.
- Feasibility study of the gas-catcher concept to thermalize fragmentation beams and prepare them for experiments or post-acceleration.

Common problems for all types of ion sources have been investigated, including ionization by the beam impact, neutralization of laser-produced ions by the accelerator beam, decomposition of molecules by beam impact, efficiency and selectivity of the laser ion source [Kud01]. In this respect, a 185 MeV ^{58}Ni $^{10+}$ beam has been implanted into the gas cell and converted to 40 keV ^{58}Ni $^{1+}$ beam using laser ionization. Systematic measurements of the laser ion source efficiency and selectivity have been performed in a wide dynamic range of beam intensities for conversion of a stable high-energy beam into low energy beam, and for production of neutron-deficient Rh/Ru isotopes in heavy-ion induced fusion reaction [Fac04]. The DT-laser program has been completed in 2003 and a proposal to study the β-decay of the neutron rich $^{70-71}$Co and $^{72-76}$Ni nuclei has been accepted and the beam time is allotted for the year 2004. In parallel, a new β-γ detection setup based on Si strip detectors-segmented Ge crystals and new acquisition system are under development.

1.3.1 Laser ion source principles

The operational principle of the laser ion source is based on selective resonant ionization of nuclear reaction products stopped in a high-pressure noble gas (for more details about resonant laser ionization see the section 1.4). In a setup combining a laser ion source and a mass separator, the selection of an isotope of interest emerging from the target is achieved in a two-step process: through resonant ionization of a specific element by laser light, followed by the A/q separation from the other isotopes by the mass separator.

A schematic layout of a laser ion source is shown in Fig. 1.3.

The cyclotron beam hits a target located in the chamber filled with noble gas (usually helium or argon) . The nuclear reaction products recoiling out of the target are thermalized as neutrals or as 1+ charged ions and move together with the noble gas in the direction of the exit hole.

In the approximation of a homogeneous flow, the evacuation time of all reaction products from the ion source should be equal to τ_{ev}=V/C, where V is the volume of the cell between the cyclotron beam path and the exit hole and C is the conductance of the exit hole. The conductance of the exit hole depends on the gas type and it can be calculated (in units of cm^3/s) using C=450·$(\text{Ø}_{ex})^2$ for the helium case, and C=155·$(\text{Ø}_{ex})^2$ for the case of argon gas, respectively. Here Ø_{ex} is the diameter (in mm) of the exit hole, usually 0.5 mm. Thus, if the volume of the gas cell from

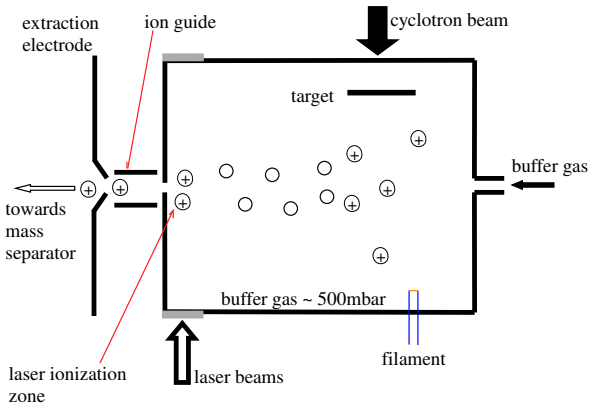

Fig. 1.3: Schematic layout of a laser ion source

the beam path position to the exit hole is V=9 cm^3, the evacuation of ions from a helium filled cell equals τ_{ev}^{He}=80 ms, while for an argon filled cell it is τ_{ev}^{Ar}=230 ms.

One of the governing processes, which controls the concentration of ions in the gas cell, is the recombination process (see section 3.6). After a few milliseconds, most of the ions are neutralized due to recombination with electrons created by the primary cyclotron beam. While the atoms move towards the exit hole they pass the laser ionization zone where only the atoms of interest are ionized by the laser beams.

The laser-produced ions together with the neutral atoms are then transported by the gas flow through the exit hole and injected into a SextuPole Ion Guide (SPIG) [VBe97]. A voltage V_{dc} =250V is applied between the gas cell and the SPIG rods to dissociate molecular ions, which might be formed inside the cell after laser ionization. The gas can expand through the gaps between the rods, while the ions are radially confined within the structure and they travel with the gas jet velocity towards the extraction electrode. This eliminates the need to accelerate the ions in a high pressure zone and consequently the spread of ions with respect to the energy and space is much smaller.

Subsequently, the ions are accelerated with a 40-50 kV high-voltage and mass separated in a 55° dipole magnet with a radius of 1.5 m. After mass separation the ions are implanted onto a movable tape which transports them at the position of a $\beta - \gamma$ detection system.

In off-line experiments, atoms of different elements (Ni, Co, Cu, Rh, Ti) can be produced inside the gas cell by resistive heating of a corresponding filament. The position of the laser beams is optimized using the stable isotope beams and by visual control. The laser frequencies are tuned and kept in resonance using a reference cell where an atomic beam of the studied element is created.

The laser ionization technique in a buffer gas cell has been successfully applied for the production of both neutron-rich isotopes in light-projectile induced fission reactions, and neutron-deficient isotopes in the case of light- and heavy-ion induced

fusion reactions. The electrons created by the beams that pass through the buffer gas cell neutralize not only the reaction products, but also the laser produced ions. This represents one of the limitations of the laser ion source. Therefore beam pulsing sequences have been studied and used in order to increase the survival probability of the laser ionized species. It has been found that the laser ionization is effective between two consequent cyclotron beam pulses, when the electron density available for recombination is a few orders of magnitude lower than during the beam-on period. Particular configurations and geometries of the gas cell have been used depending on the demands super-imposed by the production of a particular isotope or by the reaction itself. The choice of the target thickness, gas type and gas pressure combination is very important as the reaction cross section, transmission of the target and stopping power of the gas represent limiting factors for the final yield of isotopes of interest.

The main parameters of a laser ion source are the efficiency and the selectivity. The laser ion source efficiency for the production of a particular isotope is defined as the ratio of the number of radioactive ions extracted from the gas cell, and the number of ions recoiling out of the target into the volume of the gas cell. The selectivity is defined as the ratio of the number of ions measured at the detector position when the lasers are on, and the number of those ions measured with the lasers switched off. Therefore the selectivity is inversely proportional to the number ions that stay in the 1+ charge state after thermalization. This is strongly influenced by the condition of the gas used, thus a getter-based purifier has been installed in the gas handling system of LISOL laser ion source, allowing reduction of the impurity level in the buffer gas down to sub-ppb.

Not at least, the delay of radioactive ions in the buffer gas cell before being extracted might result in losses of short-lived exotic species that decay away. This can be overcome by applying electrical RF/DC fields to drag the ions towards the exit hole and keep them on trajectories away from the cell walls. However the application of electrical fields in the gas cell introduces another limitation, intensity related, as result of the space charge creation [Huy02].

The advance of the radioactive ion beam technique is an essential ingredient for the exploration of the "terra incognita" from the nuclear isotopes landscape. We are now on the "border" between two generations of radioactive ion beam facilities, therefore the studies performed at LISOL aim at optimization and performance enhancement of a laser ion source for production of exotic nuclei. The challenge is to characterize qualitatively and quantitatively the processes that influence the overall performance of the ion source, and based on that, to establish the principle and the configuration which best suit the needs for the study of more and more exotic nuclei.

1.4 Resonance laser ionization

The operational principle of the laser ion source is based on the resonance laser ionization process.

1.4.1 Ionization of atoms

In general terms, ionization means the removal of an electron from an atom or ion. In an ion source, different ionization mechanisms can be used: surface ionization, electron impact ionization or resonance laser ionization. The amount of energy

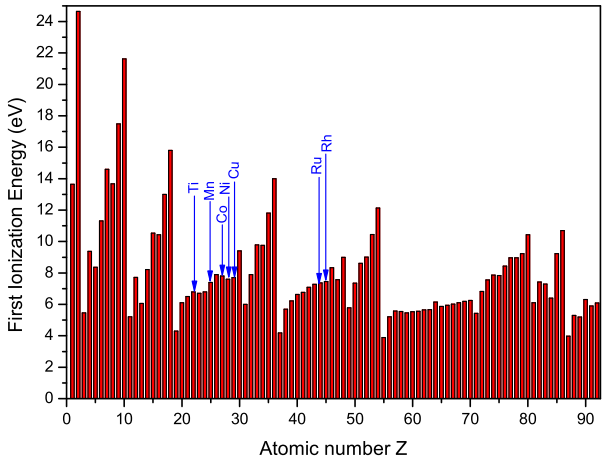

Fig. 1.4: First ionization energies for elements with Z=1÷92 as function of nuclear charge Z.

needed to remove an electron from the outermost shell of an atom, represents the first ionization energy. Fig.1.4 shows the first ionization energy (in eV) for elements with the atomic number from 1 to 92, as function of the atomic number Z (compilation from the website of the National Institute of Standards and Technology, USA[1]). The arrows indicate the elements which were so far produced with the LISOL laser ion source. The first ionization energy shows periodicity. That means that it varies in a repetitive way as you move through the Periodic Table. These variations in first ionization energy can all be explained in terms of the structures of the atoms involved.

1.4.2 Laser ionization of atoms

Using tunable dye lasers it is possible to match the photon energy of the laser light to the electronic transitions of a desired atomic species. An ionization scheme usually involves one or more resonant photon absorption steps in which the valence electron is firstly excited to a higher lying state, but still bound, and subsequently to a state above the ionization limit. It is the unique electronic structure of different atomic species that gives this process its selectivity. As it will be shown in the section 1.4.4, due to the broadening of the atomic lines, the selection of different isotopes of an element can not be performed at the LISOL laser ion source.

Qualitatively, the basic photoionization schemes may be classified as illustrated in Fig.1.5. The excited states that are far from the ionization limit (Fig.1.5.a) can be effectively ionized only by laser radiation. The following two possibilities exist

[1] http://physics.nist.gov/PhysRefData/IonEnergy/tblNew.html

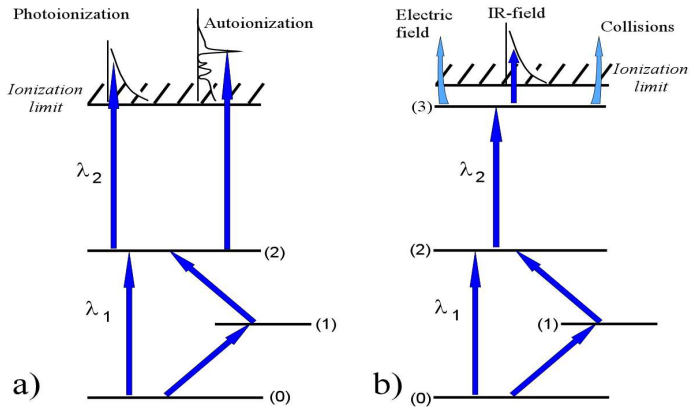

FIG. 1.5: Various ionization schemes of atoms from (a) low-lying excited states and (b) highly excited states

in this case: direct non-resonant photoionization to the continuum and resonant photoionization to an autoionizing state. The highly excited (Rydberg) states lying close to the ionization limit are comparatively easy to ionize with a high efficiency by one of the following means (Fig.1.5.b): an electric field pulse, an Infra Red (IR) radiation pulse, and collisions with other particles or with walls [Let87].

All the possible resonance ionization schemes can be classified by several characteristic features:

(1) the number of the independent radiation frequencies (colors) used;

(2) the number of excitation stages, including both resonance and nonresonance transitions;

(3) the type of the multiphoton resonance and nonresonance transitions used;

(4) the total number of the absorbed photons.

The choice of ionization scheme is governed by the ionization potential of the given atom and the arrangement of its energy levels. Of no small importance is, of course, the available selection of lasers to carry out the photoionization of the atom. Lists with the transition wavelengths for the ionization schemes of various atoms, according to their position in the Periodic Table, can be found in ref.[Hur79, Let87] for both two-step and three-step resonance ionization schemes. At LISOL, two dye lasers pumped by two time synchronized XeCl (308 nm) excimer lasers (for more details see section 2.4), are used to ionize elements in a two-step resonance process involving autoionizing states. Fig.1.6.a shows an idealized two step ionization scheme. By absorbing a first photon of energy hc/λ_1, the atom of interest is excited to the level (2). Before decaying to a lower energy level, the excited atom is subsequently ionized by absorbing a second photon with energy hc/λ_2.

When atoms are in the intermediate excited state, one of the following processes are possible:

(i) they can decay back to the ground-state, (0), with the natural radiative decay rate (Γ_{21}), from where re-excitation is possible;

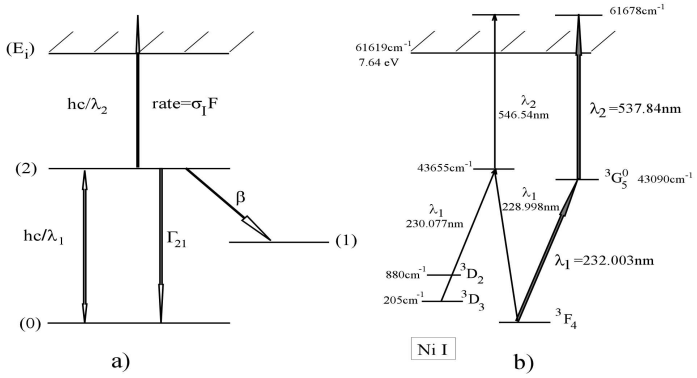

FIG. 1.6: a). Schematic atomic level scheme showing the principles of resonant photoionization (for various symbols see explanation in text). The rate of ionization equals $\sigma_I F$, with σ_I the ionization cross section and F the flux of photons. b). Partial atomic level diagram of nickel. The thick arrows indicate the path that was used to ionize nickel at LISOL laser ion source.

TABLE 1.2: The laser wavelenghts used for the two-step ionization of Ti, Mn, Co, Ni, Cu, Ru and Rh atoms.

Z	Element	First step (λ_1) (nm)	Second step (λ_2) (nm)
22	Ti	395.821	339.35
25	Mn	279.482	379.30
27	Co	230.903	481.90
28	Ni	232.003	537.84
29	Cu	244.164	441.60
44	Ru	228.538	553.09
45	Rh	232.258	572.55

(ii) they can leave the excited state into the continuum due to photoionization;

(iii) they may escape ionization through spontaneous emission to a metastable state, with the rate β.

The partial atomic level scheme of nickel is shown in Fig.1.6.b. An efficient ionization path starting from the $^3F_4$ ground-state via a 232.003 nm transition (λ_1) to the $^3G_5$ intermediate level at 43090 cm^{-1} followed by a 537.84 nm transition (λ_2) to an autoionizing state has been used at LISOL laser ion source[3] [Kud96, VDu97]. Other ionization paths are also available involving other atomic levels. The laser pulse length is 15 ns. The spectral bandwidth of the dye laser radiation equals 0.15 cm^{-1}. In order to get light in the region of 230 nm, the radiation from the first

[3] 1 cm^{-1} is equivalent to $\approx$ 30 GHz.

step laser is frequency doubled in a second harmonic generator. After doubling, the bandwidth is equal to 0.25 cm^{-1}.

The efficient schemes for the two-step laser ionization of Ti, Mn, Co, Ni, Cu, Ru and Rh through autoionizing states have been found using the laser system described in the section 2.4. Table 1.2 shows the wavelengths for the two-step laser ionization of these elements which were produced on-line at the LISOL laser ion source [Kud01].

1.4.3 Saturation conditions

In order to obtain ∼100% ionization efficiency, the atoms of interest that are irradiated with the lasers must be ionized with a probability near unity; the resonance ionization process must be saturated. This can be achieved if both the excitation and ionization steps are subsequently saturated. The intermediate excited state (2) (see Fig.1.6.a) is characterized by the half-life ($T_{1/2}$), usually in the range 10÷100 ns. If the decay from this state is not mainly to the ground state (0), but to an intermediate state (1), to have an efficient ionization the lasers pulse duration (τ_p) for completing the ionization must be much shorter than the decay half-life of the intermediate state ($T_{1/2}$), i.e.: $\tau_p \ll T_{1/2}$.

This implies conditions on the power of the lasers [Let87]. Both ground-state (0) and excited state (2) must be in quasi-steady state equilibrium, thus the rates of absorption and the stimulated emission have to be much larger than the depopulation rate (β [s^{-1}]):

$$\sigma_I F \gg \beta \Leftrightarrow F \gg \beta/\sigma_I \tag{1.1}$$

with σ_I [cm^2] the cross section for ionization from the excited state and F [$cm^{-2}s^{-1}$] the flux of photons. The expression (1.1) is called the "flux condition".

If the flux of photons F is large enough to keep the states (0) and (2) in equilibrium, the number of atoms, $N_0(t)$ and $N_2(t)$, occupying each of the states as function of time are related as:

$$N_0(t) = \frac{g_0}{g_2} N_2(t) \tag{1.2}$$

where g_0 and g_2 are the statistical weights of the states (0) and (2), respectively. The number of excited atoms (in state (2)) available for laser ionization represents a fraction $g_2/(g_2 + g_0)$ from the total number N_0 of atoms in both ground- and excited states. A second condition requires that the rate of photoionization has to be larger than the sum of irreversible destructive rates of the intermediate excited state, which means that there should be a large number of photons per unit of area (cm^2) during one laser pulse (τ_p) to ionize those atoms which are in the excited state (2). This reads:

$$\frac{g_2}{g_2 + g_0} \sigma_I F \tau_p \gg 1 \Leftrightarrow \Phi = F\tau_p \gg \frac{g_0 + g_2}{g_2 \sigma_I} \tag{1.3}$$

where Φ [cm^{-2}] is the fluence of photons. Condition (1.3) is called the "fluence condition", and it is responsible for the saturation of the ionization step.

When both conditions (1.1) and (1.3) are fulfilled, complete saturation is reached: essentially all the atoms irradiated by the laser light are also ionized. However, along with these conditions, depending on the element to be ionized, additional requirements may be imposed. It is not the aim of this sub-chapter to review the

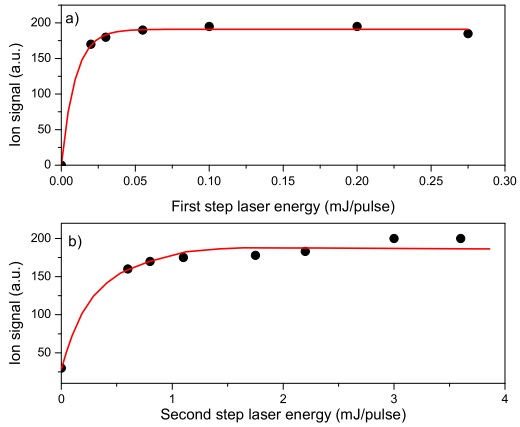

Fig. 1.7: The number of laser produced and mass separated ^{58}Ni ions is shown as function of the laser energy per pulse for the first step (a) and the second step (b). Note the saturation of the ion signals [Kud96].

complete field of resonance ionization and the reader is referred to the literature [Let87, Qam94, Kud96, VDu97].

A typical example of complete saturation of the two laser steps is shown in Fig.1.7 for the case of ^{58}Ni atoms resonantly ionized by laser light, extracted from the LISOL ion source and mass separated. It is clear from Fig.1.7 that the first step is completely saturated and that also for the second step not much can be gained if more laser power would be available. The slow rising of the ion signal with increasing second step laser energy (Fig.1.7.b) is not due to the absence of the saturation but due to increasing of the volume in which the saturation of the second step takes place. This effect is not observed in the first step as the size of the first laser spot area is bigger than that of the second step. The saturation curves indicate that all atoms in the irradiated volume are indeed ionized.

1.4.4 Line-width broadening and line shift

The spontaneous emission of a photon can be described by an oscillating electron whose amplitude is damped. The natural line-width is the minimum width of a transition and is given by the uncertainty principle from Heisenberg:

$$\Delta E \cdot \tau \cong \hbar \tag{1.4}$$

with the energy difference $\Delta E = \hbar \cdot \Delta\omega$, follows that the "life-time" (τ) of an excited state is related to the frequency difference between the excited state and a lower lying state ($\Delta\omega$), by:

$$\Delta\omega = \gamma = \frac{1}{\tau} \tag{1.5}$$

with γ being the full width at half maximum (FWHM).

It is essential to note that in a laser ion source, the conditions for resonant laser ionization are not ideal. Several effects do contribute to atomic line broadening which result in an overall shortening of the life-time of the states involved in the ionization process [Let87]. The most important contributions to the atomic line broadening are:

- Pressure broadening,
- Power broadening,
- Doppler broadening.

Pressure broadening is related to the interaction of atoms with the surroundings, i.e. collisions with gas atoms, which can be considered as a thermal bath. This can additionally shorten the lifetime of the excited state. In other words, the interaction with the surroundings causes "interruption" of the particle's wave-function phase in each of the steady states, which is not necessarily accompanied by the decay of the particle to the lowest energy state. Thus, atoms are "captured" into metastable states and they can not be resonantly ionized (see level (1) in the atomic scheme in Fig.1.6.a).

Power broadening of spectral lines is due to the excitation by a strong light field. The broadening of the excitation spectrum is the result of a simple physical effect, i.e., field splitting of atomic levels.

Doppler broadening arises from the distribution of absorption (emission) frequencies of atoms. The distribution of frequencies occurs because the atoms have a distribution of velocities relative to the laser beam. Therefore the transition frequencies are shifted by $\pm \vec{k}\,\vec{v}$, where $\vec{k}\,\vec{v}$ is the projection of the atomic thermal velocity on the propagation direction of the laser waves (v has a Maxwellian distribution).

As an example, the three above mentioned contributions to the line-width broadening of the first step transition of nickel (Fig. 1.6.b), of 232 nm, are evaluated in Table 1.3 [Kud96].

It is of interest to compare the isotope shift with the laser bandwidth and the different mechanisms of absorption broadening. For atoms in the middle of the periodic table ($50 < M < 120$) the isotope shift relative to the transition frequency ω_0 is of the order of 10^{-7}. For transitions in the wavelength region of 230 nm this corresponds to $\Delta\omega_{i.s} \sim 0.004$ cm^{-1}. Even for isotopes 20 neutrons away from the stable one the isotope shift is not more than 0.1 cm^{-1}. As can be seen from Table 1.3, the isotope shift is less than the pressure and power broadening. Thus, the bad news is that the use of laser ionization in a high pressure gas cell makes impossible the measurement of the isotope shifts. However, the good news is that the lasers

TABLE 1.3: Line broadening for the first step transition (λ_1= 232 nm) of nickel atom.

Pressure broadening, $\Delta\omega_{Pr}$	~ 0.5 cm^{-1}	P = 500 mbar
Power broadening, $\Delta\omega_{Pow}$	~ 0.1 cm^{-1}	$E_l \cong 10^5$ W/cm^2
		$\tau_p = 15$ ns
Doppler width, $\Delta\omega_D$	0.07 cm^{-1}	T=300K, M=58

can be tuned to ionize a particular isotope using the stable isotope of that element. This was confirmed experimentally [Kud96] by scanning the first step lase frequency for different stable nickel isotopes (M = 58, 60, 61, 64). Consequently, during the online experiments it is sufficient to tune the laser frequencies in resonance with any stable isotope in the reference cell.

Chapter 2

Experimental setup

The LISOL facility is hosted at Centre de Recherches du Cyclotron in Louvain la Neuve, Belgium. The laser ion source has been installed at the front-end of the mass separator LISOL, which is coupled on-line to the CYCLONE cyclotron. A schematic layout of the experimental setup is shown in Fig.2.1. The direction of the primary beam from the cyclotron is perpendicular to the extraction axis of the gas cell. The high-vacuum beam pipe of the cyclotron is connected to the front-end, and separated by an entrance window molybdenum foil (4-5 μm). The laser lab is situated on top of the "Igloo Z" housing the front-end. From up there, the laser beams are directed into the gas cell by deflecting them with optical prisms. The ions leaving the gas cell are guided into the radio-frequency guide and subsequently accelerated with a 40-50 kV high-voltage. The beam is focused for injection into the separator magnet in an Einzel lens situated just at the magnet entrance. The magnet can deliver ions in three beam lines: BTL-left, BTL-right and BTL-central.

2.1 The cyclotron

In on-line experiments with the LISOL laser ion source (see also Chapter 5 and Appendix B) the following ion beams delivered by a cyclotron accelerator were used: 185 MeV $^{58}Ni^{+10}$ (max. 200 enA), 250-270 MeV $^{36(40)}Ar^{+10(+11)}$ (max. 4 eμA) and 30 MeV H^+ (max. 4 μA), respectively. Except for the proton beam, for which an internal cyclotron ion source was used, the ions are produced in an Electron Cyclotron Resonance (ECR) ion source and, after a first magnetic separation, they are injected in a cyclotron accelerator, CYCLONE 110, which brings them to the required energy [Gae03]. The ion source is a single stage ECR source working at 6.4 GHz and originally designed to produce single charged ions with a high efficiency: ionization efficiencies of the order of 15% for N^{1+} and 40% for Ne^{1+} have been measured off-line [Dec91].

CYCLONE110 (CYClotron de LOuvain-la-NEuve) was built in the early seventies by Thompson CSF in collaboration with ACEC. It is used for nuclear physics, isotope production and medical and technological applications. CYCLONE is a multi-particle, variable energy, isochronous cyclotron capable of accelerating protons up to 80 MeV, deuterons up to 55 MeV, alpha particles up to 110 MeV and

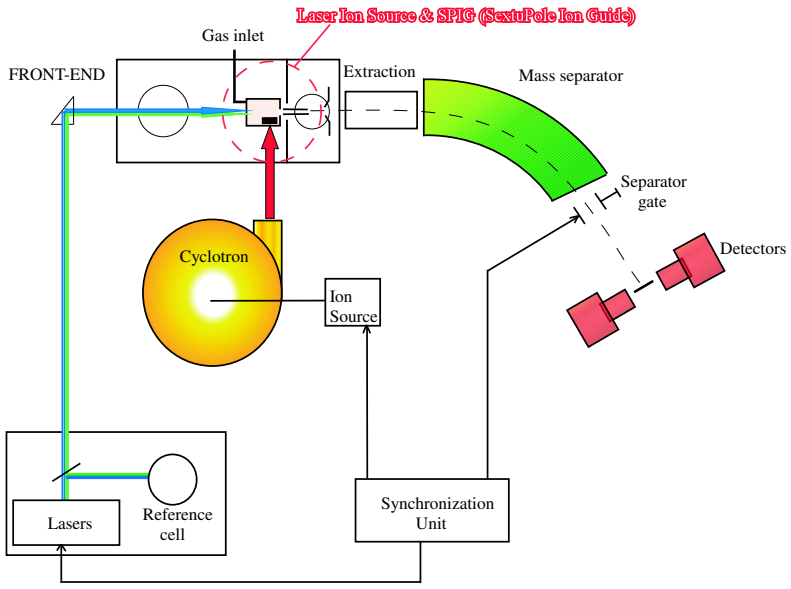

FIG. 2.1: Schematic view of the LISOL setup.

heavier ions up to an energy of 110 q^2/A MeV (where q is the charge and A the mass of the ion). The energy range for heavy ions extends from 0.6 to 27.5 MeV/amu depending, among other things, on the ion's charge state.

2.2 The front-end

In the fall of 2001 a new front end of the on-line mass separator has been build, specially designed to operate with the Laser Ion Source (LIS) (see 2.3). Fig.2.2 shows the side and the top view of the ion source chamber and the extraction chamber. The buffer gas from the ion source is removed by a Roots blower of 8000 m^3/h in series with a 2000 m^3/h Roots and a 250 m^3/h rotation pump [Kud03]. A 2000 l/s diffusion pump evacuates the extraction chamber. Differential pumping allows to use a pressure up to 1.5 bar of helium or argon gas in the ion source when an exit hole of diameter 0.5 mm is used. The ions are transported from the high-pressure zone of the exit hole to the high vacuum zone at the extraction electrode with a SextuPole Ion Guide (SPIG) structure (see the section 2.3.3). The LIS is mounted on a precision stage by which its position can be adjusted precisely: the distance between the LIS and the SPIG ion guide can be changed and the LIS can be aligned relative to SPIG. The alignment of the laser ion source is performed on two principal axis: the cyclotron beam direction and the extraction axis from the

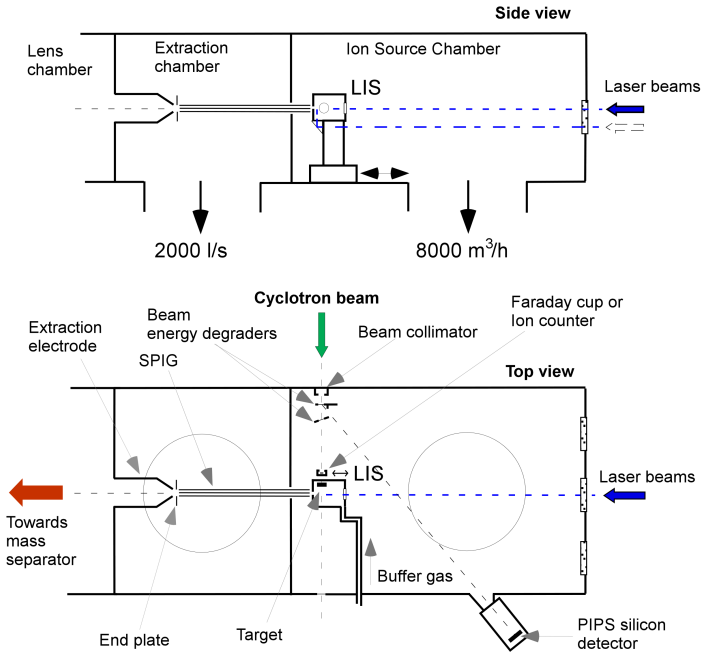

Fig. 2.2: General layout of the new front end of the LISOL mass separator.

gas cell, respectively. A laser beam is used for the alignment of the LIS, SPIG and extraction electrode.

Two main parameters of the cyclotron beam have to be controlled: energy and intensity. The energy of the primary beam can be changed by using fixed degraders, e.g. metallic foils mounted in 7 different positions on a rotatable wheel, and a tiltable degrader. Both, fixed degraders wheel and the tiltable degrader holder are computer controlled and their motion is performed with motors. The energy of the beam can be measured using the Rutherford scattering at 30° of the projectiles onto a PIPS silicon detector. Prior to the beam energy measurement, the PIPS silicon detector is energy calibrated using a triple α source (Am, Pu, Cf). Special care is taken to ensure light-tight conditions for the silicon detector, since the laser beams reflect all over in the ion source chamber.

The intensity of the primary beam is varied by changing the cyclotron and/or the ECR source settings. The beam current is measured just in front of the laser ion source using a Faraday cup or a scintillator plastic detector (see the section 2.6).

2.3 The laser ion source

A gas cell filled with noble gas (helium or argon) can be used to stop nuclear reaction products from heavy-ion induced fusion and fragmentation reactions after

in-flight separation. At LISOL the gas cell represents an essential component of the laser ion source.

2.3.1 The gas cell

The different spatial distribution of nuclear reaction products in fission and fusion reactions requires a different arrangement of the target and the stopping volume. Several configurations have been used on-line to perform experiments with stable or with radioactive isotope beams. Stable beams can be produced either by implanting a primary cyclotron beam into the gas cell and further-on extract laser re-ionized ions from it, or by resistive heating of a filament which is mounted inside the gas cell and laser resonantly ionizing that element. In total we have build and used four gas cells:

- the "large gas cell" used for off-line and stable ^{58}Ni beam studies (with a 5 cm diameter, 5 cm length and cylindrical geometry);
- the "heavy-ion fusion guide", used for the production of neutron-deficient isotopes in heavy-ion induced fusion reactions (this is in fact a version of the "large gas cell" containing an insert which holds the target);
- the "fission ion guide" used for the production of neutron-rich isotopes in fission of ^{238}U induced by 30 MeV protons (this is another version of the "large gas cell", containing an aluminum cylinder surrounding two targets of uranium);
- the "10 mm channel ion guide", which is a small volume gas cell with a 20 mm long channel of 10 mm diameter preceding the exit hole. It has inserted inside two parallel metallic plates allowing the use of electrical fields.

The flanges of the gas cell are indium sealed and the entrance and the exit windows are molybdenum foils with thickness of 4-5μm. Four heating elements are embedded in the body of the gas cell allowing to heat it up to 100°C and bake out eventual impurities.

The schematic side view of the "large gas cell" is shown in Fig.2.3 together with its connection to the extraction section, i.e. through the sextupole ion guide. The evacuation time of the gas cell through the gas flow is defined by the type of the gas and by the exit hole diameter. The diameter of the exit hole of our gas cells is always 0.5 mm. Indeed, evacuation times of 500 ms from the cyclotron beam axis were measured for this particular geometry. The buffer gas enters the cell homogenously through a ring slit of 0.3 mm in thickness and of 3.5 cm in diameter. Laser ionization can either be applied longitudinally, e.g. along the extraction axis of the gas cell, or transversally to the extraction axis of the gas cell, close to the exit hole. The body of the gas cell is stainless-steel made and it has special drilled channels to permit water cooling through a continuous flow. In the heavy ion fusion reactions, the spatial distribution of reaction products is forward peaked. A top view of the gas cell used in the heavy ion induced fusion reactions is presented in Fig.2.4. The target is fixed at 45° with respect to the beam direction, on an insert which is then mounted inside the large gas cell. The inner diameter of the insert, at the beam position, is 2.2 cm and the channel part has a diameter of 6 mm. This gas cell is particularly fast evacuated, for instance from the cyclotron beam position evacuation times as short as 80 ms have been measured for Ar buffer gas. Between the entrance window of the gas cell and the target there is buffer gas which contributes to energy loss of the primary beam. Therefore the tuning of the

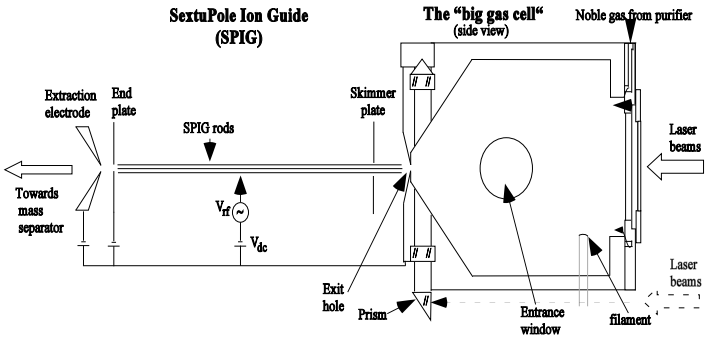

Fig. 2.3: A side view of the laser ion source together with the sextupole radio-frequency ion guide. In this configuration, the "large gas cell" is used. The laser beams can enter the source longitudinally (full-line arrow) or transversally (dashed-line arrow).

pressure in this gas cell for an optimum stopping of the reaction products, does also change the primary beam energy. A change of the primary beam energy can change the production as the cross-section is energy dependent and as the recoil velocity of the reaction products scales with the beam energy.

The isotropic emission of fragments in fission reactions causes specific requirements for the gas cell geometry. Therefore a special arrangement of the target has been used. Fig.2.5 shows the side and top views of the fission gas cell. Two targets of ^{238}U, 10 mg/cm^2 thick each, are mounted at 20° with respect to the beam direction, on the entrance and the exit flanges, respectively. They are surrounded by an aluminum cylinder with the diameter of 16 mm. The thickness of the aluminum foil is 3 μm and its function is to shield the path of the ionizing primary beam from the stopping volume of the gas cell. This is imposed by the fact that the proton

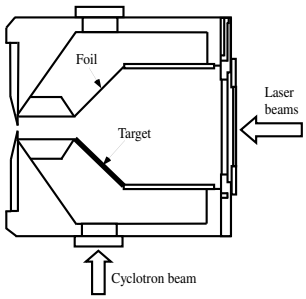

Fig. 2.4: Top view of the heavy ion fusion guide used in heavy ion induced fusion evaporation reactions.

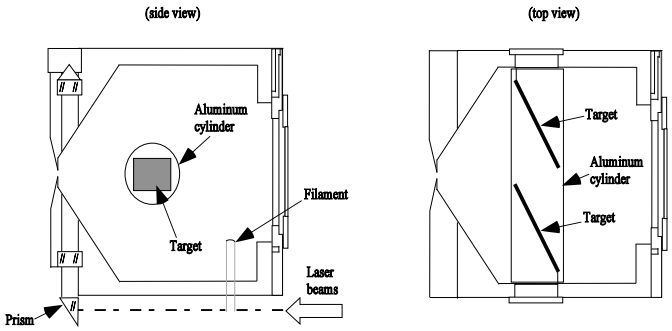

FIG. 2.5: Side and top view of the fission ion guide used in proton induced fission of ^{238}U reactions.

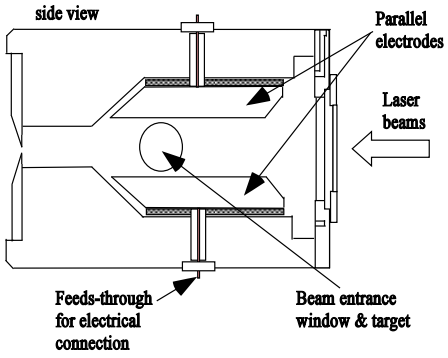

FIG. 2.6: Side view of the 10 mm channel gas cell used for the study of the electrical field influence in a buffer gas cell for catching and transporting ions.

beam is producing a large amount of electron-ion pairs in the buffer gas during its passage through the cell, which limits the survival of laser produced ions. The activity produced in the fission reaction during the on-line experiments is also large and it does contribute also to ionization of the buffer gas. After on-line experiments with the fission ion guide we have been able to extract ion beam from the gas cell using the resistive heating of a filament and without applying laser ionization. This is an indication of the high radioactivity present in the cell, which ionizes the buffer gas and the atoms produced by the filament. Due to the presence of the shielding cylinder, the laser beams can not be applied longitudinally in this configuration. The laser beams are transversally directed into the gas cell and the ionization of the elements of interest takes place close to the exit hole.

A special cell has been designed and built to allow the use of electrical fields in the buffer gas (see Fig.2.6). Two massive electrodes are mounted in a parallel geometry. Their spacing is 1.8 cm and they are insulated from the body of the

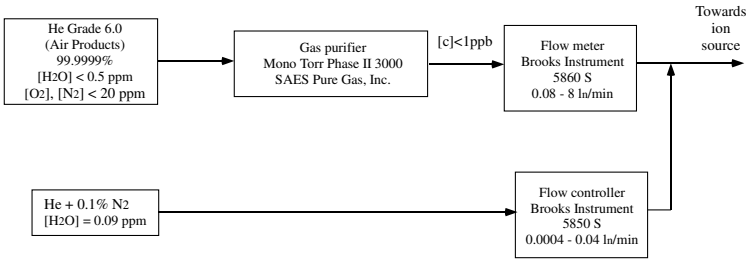

Fig. 2.7: Layout of the gas-handling system.

cell by ceramic elements. This geometry has been designed to ensure that the gas flows homogeneously between the electrodes. The feed-throughs for electrical connections are indium sealed. The channel part has a diameter of 10 mm and it is 2 cm long. The evacuation time of this cell from beam position, through gas flow, is 240 ms. This cell has also been tested in heavy-ion induced fusion reactions. The beam path length in the cell is 3.7 cm, compared to the 2.2 cm in the heavy ion fusion guide (see Fig.2.4). The target has been mounted next to the entrance molybdenum window, on the entrance flange of the cell. Because of the increased stopping range in this geometry, the ion guide can be operated at lower gas pressures, thus a better differential pumping between the laser ion source chamber and the extraction chamber is achieved. The presence of the gas between the entrance window and the target has also been avoided in this case.

2.3.2 The gas handling system

The gas handling system was especially designed to supply and to control the gas flow in the gas cell. It offers also the possibility to add a known amount of another gas to the main gas line. Electro-polished stainless steel tubes and metal sealed valves have been used in order to reduce the memory effect. The memory effect consists in persistence of impurity species inside the gas line for a long time. This effect is sensitive to the roughness as well as to the material of the tubes. The system can be heated up to 200°C and is pumped by oil-free pumps.

The scheme of the gas handling system is shown in Fig.2.7 [Kud01]. High purity helium or argon gas (grade 6.0, 99.9999%) is supplied by Air Products and an analysis of the impurities in the gas bottle is supplied by the manufacturer. Typically these impurities are H_2O (< 0.5 ppm), O_2 (< 20 ppb), N_2 (< 20 ppb). The gas is additionally purified in a getter-based purifier (Mono Torr Phase II 3000, SAES Pure Gas, Inc.) to the sub-ppb level. It is not possible to measure the impurity level inside the gas cell at this concentration. Only by adding a known amount of an impurity gas and observing the change in the mass spectra and in the ion time profile signals it is possible to make firm conclusions. The gas flow rate in the main line (and consequently in the pressure gas cell) is controlled by a needle valve and is measured by a digital mass flow-meter (Brooks Instrument, 5860 S). The maximum flow-rate is equal to 8 l_n/min (l_n = normalized liter for 0°C and 1 atm). At a helium pressure inside the gas cell of 500 mbar the measured gas flow is equal to 3.7 l_n/min, which is close to 3.4 l_n/min as calculated from

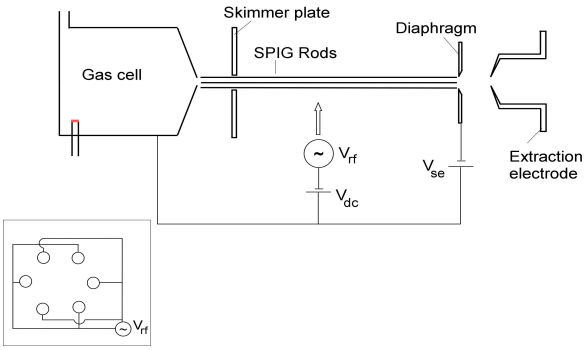

FIG. 2.8: Layout of the SPIG. The insert shows a cross-section of the six rods perpendicular to the beam axis with the manner that the RF voltage is applied.

the conductance of the exit hole. A small amount of impurity gas (O_2, N_2) can be admixed to the main gas line through a digital mass flow controller (Brooks Instrument, 5850 S). The flow-rate can be varied between 0.0004 and 0.04 l_n/min. A premixture of impurity gas in the noble gas in the ratio of 1:1000 was used. At a flow rate in the main line of 3.7 l_n/min, the level of impurities can then be changed from 0.1 to 10 ppm. It was checked that there is no memory effect of the system for oxygen and nitrogen at this level of impurities.

The most abundant impurity in the noble gas is however water vapor. The moisture concentration in the admixing gas (He + O_2/N_2) was specified by the manufacturer and equals to 1.2 ppm for O_2 and 0.09 ppm for N_2. This means that by adding 1 ppm of oxygen to the main line we get 1.2 ppb of H_2O in the gas cell at the noble gas pressure of 500 mbar. The corresponding value when adding nitrogen is equal to 0.09 ppb.

2.3.3 The SextuPole Ion Guide

The SextuPole Ion Guide (SPIG) has been constructed to couple the ion-guide based ion source to the on-line isotope separator [Xu93, VBe97]. A schematic drawing of the SPIG is shown in Fig.2.8. It consists of six rods cylindrically mounted. They are on a hexagonal structure between the exit hole of the cell and the extraction electrode, the structure being orientated parallel to the beam path. An oscillating voltage (V_{rf}) is applied between the rods, with every rod in antiphase with the neighboring rods. If the amplitude and the frequency of the RF signal is well chosen, ions can be radially confined within the structure. The gas can expand through the gaps between the rods, while the ions, confined within the structure, are transported to the extraction electrode with the velocity of the gas jet. This eliminates the need to accelerate the ions in a high pressure zone as is done with a conventional skimmer setup. In such a system the acceleration due to the electrical field can be reset by collisions resulting in a considerable energy spread of the final beam. This is not the case with the SPIG and even more, if the kinetic energy of the ions is higher than the energy of the gas atoms, the ions can be cooled by collisions with the gas atoms inside the SPIG. A skimmer plate further downstream

(see Fig.2.8) separates the medium pressure region around the gas cell (typically 10^{-2} mbar) from the high vacuum of the separator (typically 10^{-6} mbar). When the ions arrive at the end of the SPIG they can be extracted in good vacuum conditions and injected in the mass-separator. Implementation of SPIG at LISOL resulted in an improvement of the Mass Resolving Power (MRP) (see section 2.5 for definition) by a factor 5 which clearly illustrates the improved quality of the beam. An upper limit of 1 eV has been measured for the kinetic energy spread of the extracted ions along the SPIG axis of symmetry [VBe97].

The six rods of SPIG are constructed of inox and they have a diameter of 1.5 mm (Fig.2.8). The length of the rods is 126 mm and the diameter of the inner circle is 3 mm. The distance between the rods and the exit hole is 0.5 mm, but this can be further increased during the experiments by moving away the gas cell with a motor controlled device. The oscillator that supplies the RF signal (V_{rf}) has a fixed frequency of 4.7 MHz and a variable amplitude from 0 to 150 V. A DC voltage can be added to the RF signal (V_{dc}= 0 to +/- 300 V, relative to the potential of the cell). A diaphragm with the diameter of 2 mm is mounted at the end of the rods. The potential of the diaphragm (V_{se}), relative to the cell can be varied from 0 V to +/- 300V.

When V_{dc}, the offset voltage on the SPIG rods, is negative, and V_{se}, the voltage on the diaphragm is higher than V_{dc}, the ions can no longer leave the SPIG, and are thus trapped between the entrance and the exit of the SPIG. When V_{se} is lowered to a potential below or equal to V_{dc}, the SPIG is opened and the ions can be extracted by the extraction electrode. It has been measured [VBe97] that the stored ions are released within 150 μs when He is used as buffer gas. Therefore the SPIG offers the possibility to bunch the extracted beam. The storage efficiency depends on the storage time and the number of ions. It has been determined that up to 10^7 ions could be stored efficiently for storage times in the order of 100 ms.

2.4 The laser optical system

Two step resonant laser ionization has been used at LISOL to produce ion beams. The method has been explained in detail in the section 1.4. The scheme of the laser optical system is shown in Fig.2.9. Two excimer lasers with the wavelength $\lambda = 308$ nm (Lambda Physik LPX240i), pump two dye lasers (Lambda Physik Scanmate 2). Both excimer lasers are synchronized to a precision of a few ns. In our experiments we used Coumarin 47 dye for the first step laser and Coumarin 153 or Coumarin 102 for the second step laser. The pulse width of the dye laser is equal to 15 ns. The spectral bandwidth of the dye laser radiation is equal to 0.15 cm^{-1}. In order to obtain light in the region of 230 nm, the radiation from the first step laser is frequency doubled in the second harmonic generator (SHG). After doubling, the bandwidth is equal to 0.25 cm^{-1}. The laser beams are focused by telescopes and directed by a set of prisms into the ion source located at a distance of 15 m from the laser optical system. The laser beams can enter the ion source either longitudinally or transversally. To control the overlapping of the two laser beams inside the ion source, in the case of longitudinal entrance, a prism located in the laser beam path has been installed after the gas cell, deflecting the laser light onto a screen which is monitored by a camera. The overlapping is achieved by adjusting the position of the two beams passing through the exit hole of the gas cell.

To tune the laser wavelength in resonance with the atomic transitions and to keep them tuned during the experiment, a fraction of the laser beams is deflected

into a reference cell. It consists of a vacuum chamber in which an atomic beam is produced by evaporating the investigated element from a resistively-heated crucible. The laser beams ionize the atoms and the obtained ions are accelerated towards a time of flight mass spectrometer. The mass-separated ions are detected by a secondary electron multiplier.

The laser beams can enter the source in two ways, longitudinally or transversally (see Fig.2.3). In the first case the laser beams enter the cell through a quartz window and ionize the atoms along the axis of the cell. In the second case the laser beams are directed by the multipass optical system, consisting of two 90° quartz prisms, to enter the source transversaly to the extraction axis of the cell. In this way the laser beams intersect the atomic flow several times.

2.5 The mass separator

The ions extracted from the ion source are accelerated at energies up to 50 keV. The accelerated ions are then separated according to their mass to charge ratio in a 55° dipole magnet with a radius of 1.5 m. The mass resolving power (R) of a magnet is defined as the ratio $M/\Delta M$, where M is the separated mass and ΔM is is the width of the mass peak at FWHM in the focal plane. Prior to the implementation of SPIG a skimmer electrode was used instead [Kud96] and the resulting resolving power of the mass separator was $R = 300$ as result. The SPIG boosted up the resolving power to 1450 [VBe97], which is the present performance of the LISOL separator. This is due to the improved beam quality (emittance and energy spread) delivered by the SPIG. At the focal plane of the mass separator magnet the separated beam spatial distribution can be measured with a beam monitor, e.g. a vertical wire (Ø 0.2 mm) that is moved through the beam (see section 2.8).

2.6 Beam control and diagnostics

In any ion accelerator facility it is essential to control and diagnose the beam during its different stages in the machine. At LISOL both primary and the sec-

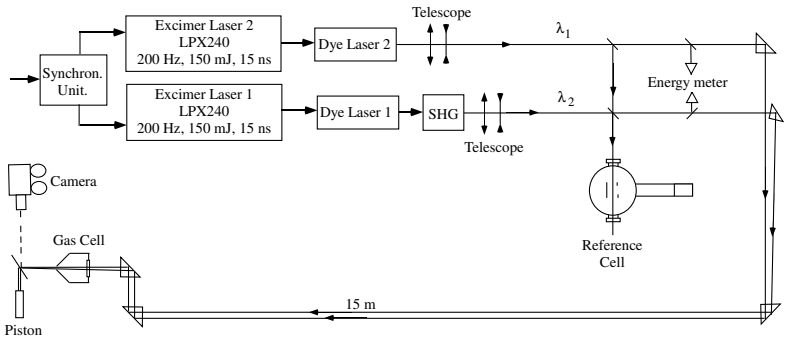

FIG. 2.9: Scheme of the lasr optical system.

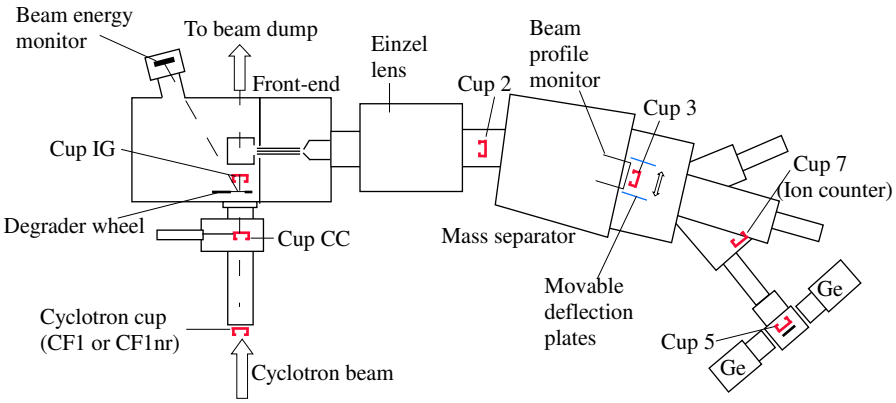

Fig. 2.10: Overview of the beam control and diagnostics system (see text for details).

ondary beams are carefully controlled and diagnosed. The primary cyclotron beam is checked from the cyclotron exit to the entrance of the laser ion source. The secondary beam, e.g. the beam extracted from the gas cell, is checked before the mass separator as well as after mass separation. The diagnostic system consists of Faraday cups[1] and/or ion counters. The Faraday cups range from a simple plate to cooled and secondary-electron-suppressed devices, depending on the application. A schematic overview of the present beam diagnostics is shown in Fig.2.10.

2.6.1 Control and diagnostics of the primary cyclotron beam

The primary beam current delivered by the cyclotron is firstly measured in a Faraday cup, called CF1 (range 10 enA to several eμA)[2] or CF1nr (range from 10 enA down to few epA). The CF1nr cup is an uncooled Faraday cup which is secondary-electron-suppressed and measures the current in an absolute way. The beam current entering the front-end box is measured in "Cup CC" ("Cyclotron Connection"). This cup is not cooled and it is used to tune the beam focus towards the laser ion source. The new control system of LISOL allows to insert Cup CC in the beam path, on a regular base for intensity monitoring. This cup is mounted on a pneumatic piston controlled by a computer. The visualization of the beam spot at the position of this cup is also possible with an aluminum-oxide screen which is mounted on a second piston that can be inserted in beam when the Cup CC is in the off-beam position (a camera transmits to a computer, images from this screen).

[1] The labelled names of these devices are those given by our engineer staff.

[2] 1 electrical Ampere (eA) = Intensity (particle/second) x charge state x electron charge ($1.6 \cdot 10^{-19}$ C). The abbreviation "pps" (particle per second) for the intensity will also be used.

After passing the entrance window of the front-end box, the heavy ions do change their charge state. If the initial beam consists of 185 MeV $^{58}Ni^{+10}$ ions, after passing the entrance window of the front-end (4-5 μm molybdenum foil), they become higher charged, with an average charge state of +17, according to the LISE code [LIS02, LISpr]. This current of ions is measured in "Cup IG" (from Ion Guide) and its value is used in later calculations for the evaluation of the beam current entering the gas cell. Part of the beam strikes a collimator which is mounted before the front-end entrance window. The current on the collimator can be measured, and its usual value is within 10% of the current measured in Cup CC. A fraction of 30-40% of the particle beam current measured at the cyclotron cup (CF1/CF1nr) reaches the gas cell, except for proton beams, for which the transport efficiency from the cyclotron to the gas cell is in general better than 80%. The degraders add more scattering to the beam, so that when the thickest degrader (4 μm Ta foil) was used, for a ^{58}Ni beam, only 3.5% of the particle beam current delivered by the cyclotron, has actually been implanted in the gas cell. The actual transmission efficiency of the particle beam current (as used in this thesis) is understood as the ratio of the particle beam current measured in Cup IG with or without degraders, to the particle beam current measured in the cyclotron cup (CF1/CF1nr).

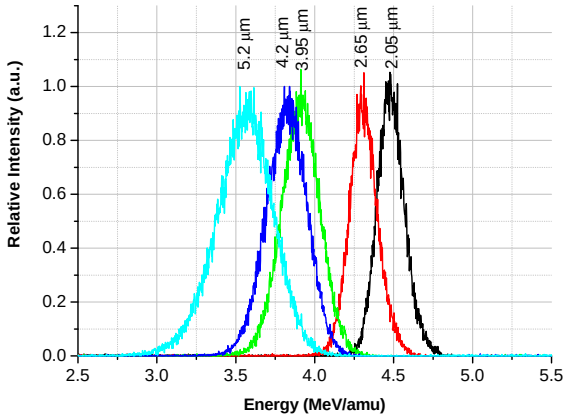

FIG. 2.11: The energy measurement of a ^{40}Ar beam Rutherford scattered at 30° in a PIPS Si detector. The five measurements correspond to five thicknesses of the Ta degraders, between 2.05 μm and 5.02 μm. The beam energy in front of the degrader foil was 220 MeV (5.5 MeV/amu). A havar foil with 1.5 μm thickness was placed in front of the PIPS detector.

Using degrader foils in the beam path does change the beam energy and the charge state of the ions. This is accounted for in the further analysis of the experimental data. The beam energy can be measured when degraders are used, by measuring the 30° Rutherford scattered beam into a Si PIPS detector. The detec-

tor has been energy calibrated using a triple α source[3]. The energy measurement of a ^{40}Ar beam after passing a degrader foil is shown in Fig.2.11. Five different thicknesses of the degrader have been used to measure the Rutherford scattered projectiles at 30°. The thickness of the degrader foils has been precisely measured using a transmission method of 5.48 MeV α particles from a ^{241}Am source. A comparison of the measured beam energies from Fig.2.11 with the calculated energies using the SRIM code [SRIpr] is made in Table 2.1. One can observe a systematic deviation of the mean values of the measured energy from the calculated ones. This can be due to the fact that an additional havar[4] foil (1.7 mum thickness as quoted by the manufacturer), for which no dedicated thickness measurement was performed, has been used in front of the PIPS detector in order to ensure light-tight conditions. The beam energy spread increases with the increase of the degrader thickness. This is due to the fact that the energy straggling of the projectiles passing the degrader foil is increasing with the foil thickness (see section 3.1.2 in Chapter 3).

In the experiments with stable ^{58}Ni beam we wanted particularly to operate the laser ion source with beam currents in the sub particle-pico-Ampère domain. These beam intensities could not be measured with the Cup IG. Therefore a plastic scintillator detector has been developed (1 cm width, 2 cm long and 1 mm thick). The scintillator has been connected to two phototubes through a half meter long light guide. Special care has been taken to ensure the light tightness of this system. Using this device, beam currents as low as 500 pps could be measured. Experimental values of the count rate of the scintillator versus the beam current measured with a Faraday cup are shown in Fig.2.12 (symbol) together with the calculated count rate as for an ideal counter (line). The very low beam intensities have been obtained proceeding in the following manner: as the Cup IG is able to measure beam intensities as low as 2 epA, beam currents in the range of several to tens of epA have been installed, and a metallic pepper pot (or grid) with very well known

[3]The composition of such an α source is ^{244}Cm/ ^{241}Am/ ^{239}Pu with the specific activities 1.182/ 1.690/ 2.407 kBq respectively.

[4]Havar is a high-strength non-magnetic alloy with the stoichiometric composition: Co42.5/Cr20/Ni13/Fe/W/Mo/Mn.

Table 2.1: The calculated [SRIpr] and measured energies of a ^{40}Ar beam scattered at 30° by Ta degrader foils with different thicknesses between 2.05 μm and 5.02 μm. The beam energy in front of the degrader foil was 220 MeV (5.5 MeV/amu). A havar foil with 1.5 μm thickness was placed in front of the PIPS detector.

Degrader thickness (μm)	Calculated energy (MeV)	Calculated energy (MeV/amu)	Measured energy (MeV)	Measured energy (MeV/amu)
2.05	182.0	4.55	179.2 ± 6.8	4.48±0.17
2.65	176.0	4.40	172.3 ± 7.1	4.31±0.18
3.95	161.5	4.04	156.4 ± 7.3	3.91±0.18
4.20	157.0	3.93	152.9 ± 8.5	3.82±0.21
5.20	147.0	3.68	142.5 ± 13.8	3.56±0.35

attenuation factor[5] of 100 has been inserted in-beam. Therefore the real beam current values impinging on the scintillator plastic are precisely known. For the highest beam current which could be measured with this device, the experimental count rate is with ∼18% lower than what expected for an ideal counter (i.e. 100% efficiency and zero dead-time).

2.6.2 Control and diagnostics of the secondary beam

The ion beam extracted from the gas cell is transported by the SPIG towards the extraction electrode (conical shaped stainless-steel structure with a hole Ø5mm). 1 kV of the accelerating voltage is applied on this electrode, the rest to 40 kV being applied in the Einzel electrostatic lens. In the lens, the beam is being both horizontally and vertically focused. The total beam current can be measured after focusing, and before the mass separation, in "Cup 2". The lowest beam current[6] that this cup is able to measure is around 1 pA.

The beam is further-on mass separated (see section 2.5 for details) and its spatial distribution can be measured in the horizontal plane with a beam profile monitor mounted in the "collector chamber" of the separator (see section 2.8 for details). The beam profile monitor is mounted on a movable stand together with a Faraday cup which can measure the mass separated beam current, called "Cup 3". When a primary beam is implanted in the gas cell, and if the lasers are off

[5]This attenuation factor has been measured with laser light as well as with particle beams, resulting in the same number.

[6]Herewith the beam consists of single charged ions, so that the electrical and particle currents are the same.

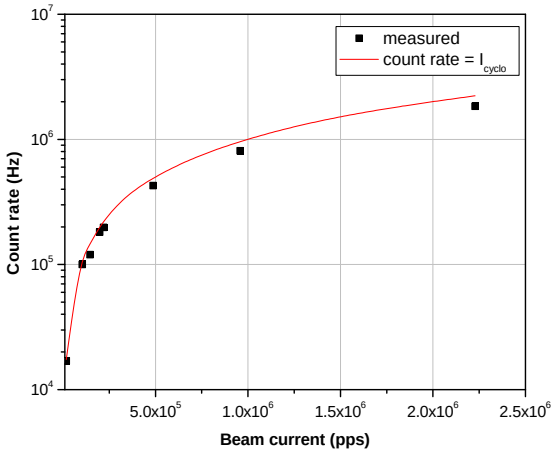

FIG. 2.12: The scintillator count rate as function of the beam current. The energy of the ^{58}Ni projectiles was 83 MeV.

and the dissociation voltage is on, the extracted beam consists mostly of buffer gas ions. Therefore, measuring the beam current in Cup 2, and subsequently in Cup 3, one can extract the transmission efficiency of the mass separator. The value of the separator transmission efficiency is close to unity.

As yet unknown is the transmission efficiency of the SPIG. This has been measured [Kud01] using radioactive cobalt ^{57}Co isotopes deposited on a filament inside the gas cell. The deposited activity on the filament was measured before resistive heating and after, by monitoring the characteristic 122 keV γ-ray of ^{57}Co in front of a Ge detector. It amounted to 1μCi. The cobalt atoms evaporated from the filament were subsequently laser ionized, extracted from the gas cell and mass separated. It has been found that one third of the evaporated radioactivity from the filament was deposited on the SPIG rods and on the skimmer plate (see Fig.2.8). Note that this value is due to the ions that are not efficiently captured by the RF-structure as well as to neutral atoms that were evacuated through the exit hole and stick on the SPIG rods and on the skimmer plate.

Hence a good estimate of the total transmission efficiency of the beam from the exit hole to the Cup 3 is around 60%. The mass separated beam can be deflected in one of the three beam lines were decay experiments are performed. Depending on the experiment, additional diagnostics can be implemented in these beam lines. As shown in Fig.2.10 one can measure the mass separated current in Cup 7 and Cup 5. The transmission efficiency for the beam from Cup 3 to any of these cups lies between 80 and 95%.

Cup 7 is in particular a highly sensitive device consisting of a Secondary Electron Multiplier (SEM). By changing the voltage to the SEM, the dynamic range of the SEM can be varied. Beam intensities as low as sub-femto-Ampere can be measured with it. This is necessary as sometimes the extracted ion beam current from the laser ion source, at certain masses, can be very weak. Cup 7 was mainly used in studies involving stable nuclei produced off- and on-line with the laser ion source. The SEM can be operated in two regimes: as a current meter and as an ion counter. In this latter case, the amplified signal from SEM is fed into a fast preamplifier and further into a counter. Given the maximum intrinsic (saturation) count rate of the digital counter (2 MHz), a metallic grid (pepper-pot) with an attenuation factor of 100 was used in front of SEM when necessary, in order to not exceed the dynamic range of the counter. Special care was taken to calibrate the digital counter using the SEM as both current meter and counter. When studies involving radioactive isotopes are performed, mainly Cup 5 is used in order to tune the beam optics settings for the optimum implantation on the tape at the detection station. In front of this cup is mounted a collimator in order to prevent implantation of long-lived isotopes on the implantation chamber wall or next to the tape.

The mass separated ions end up their journey at the decay station position, where β- and γ- spectroscopy studies are performed.

2.6.3 Detection of radioactive ions

After mass separation, the ions are implanted onto a tape situated in front of the detection setup consisting of two large-volume coaxial (90% and 70%)[7] germanium detectors for γ-detection and thin plastic ΔE-detectors for β-detection. The scintillators are made of polyvinyltoluene NE102A plastic with a thickness of 1 mm

[7]These nominal efficiencies are defined as the count rate for the 1332.5 keV ray of ^{60}Co at a distance of 250 mm, relative to the rate obtained by a standard 76 x 76 mm NaI(Tl) scintillator detector.

and a surface of 12×50 mm^2. The detection setup is described in more details in the ref. [Wei99, Fra99] and a schematic top view of it is shown in Fig.2.13. The

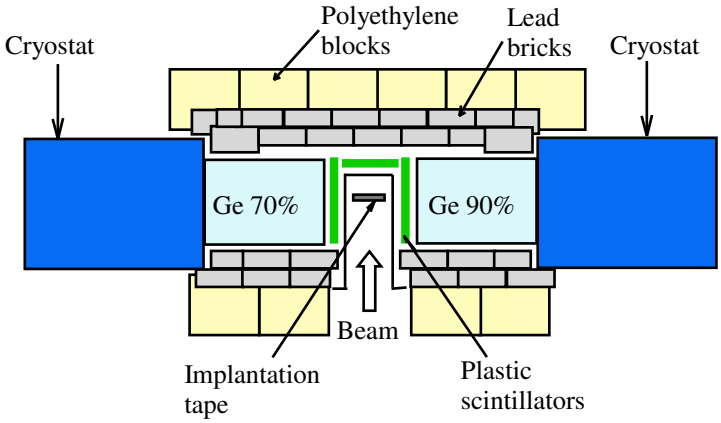

FIG. 2.13: A schematic view of the β-γ detection setup and its shielding. See text for details.

activity is implanted in a cycle mode with beam-on and beam-off periods adapted to the isotope's half-life. The tape is moved away from the detection station after every cycle in order to reduce the build-up of daughter radioactivity. Two types of data are collected in parallel [Dea04]:

- singles multispectra data;
- coincidence data in the event-by-event mode.

For the latter mode any of the $\gamma - \gamma$ or $\beta - \gamma$ coincidence conditions was used as a trigger to record the event. Every good event obtained a time stamp from a time-to-digital converter that marked the difference between the start of the implantation cycle and the detection of the event.

The germanium detectors have been energy calibrated with a gamma source of ^{152}Eu. The gamma detection efficiency for each detector was determined using an intensity calibrated ^{60}Co gamma source. The photopeak efficiency for the specific gamma line of 1331 keV was measured to be around 2% for each germanium detector, when the gamma source is placed at the implantation tape position.

The β-detection efficiency is mainly limited by the intrinsic detection efficiency on the one hand, and the absorption in the implantation chamber walls and the light-averting wrapping layers around the sensitive plastic on the other hand. The β-detection efficiencies have been determined by comparing singles gamma spectra with β-gated spectra. The measured value ranges from 35% to 50% for β-particle energies above 4 MeV [Fra99].

The detection setup is shielded from external γ radiation by lead bricks of 5 cm thick. To prevent fission neutrons from penetrating the detectors, the construction is surrounded by 20 cm of polyethylene blocks. Active background suppression is achieved by applying coincidence conditions on the data acquisition as well as implementing a pulsed time structure, (see section 2.7).

Presently (1^{st} half of year 2004) this detection system is being replaced by new segmented 3-folded germanium crystals (Miniball type) for γ-detection and Si-strip detectors for β-detection. First on-line results are expected for the June 2004. A new acquisition system using Digital Gamma Finder (DGF) modules is also being settled (i.e. pulse analysis modules - XIA components).

2.7 The timing

The timing (microcycle) of the whole setup is shown in Fig.2.14.a. A clock system

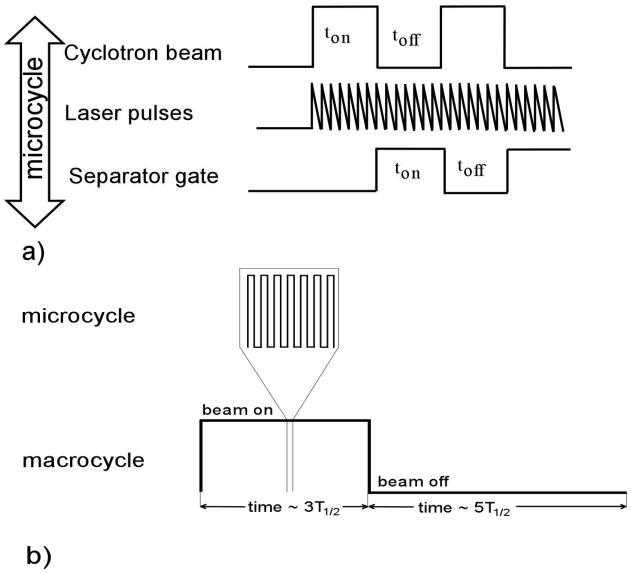

Fig. 2.14: Timing of the cyclotron beam, the lasers, the mass separator and the detection system during a) the microcycle and b) the macrocycle (the cyclotron beam microcycle structure is zoomed).

pulses the cyclotron beam and produces trigger signals with variable delay relative to the cyclotron pulse for the lasers, the mass separator and the detection system. The laser beams can probe the appearance of radioactive atoms close to the exit hole of the ion source as a function of delay time relative to the cyclotron pulse. In this case, the multipass system (see section 2.4) is removed and the beams pass the source only once. By changing the timing of the separator gate or the laser pulse delay it is possible to investigate, for example, the influence of the cyclotron beam on the ionization of stable nickel atoms. A reduction of the background evoked by fast neutrons can be performed by antigating the detection system with the cyclotron beam. Using helium as buffer gas, the typical value for the beam "ON" and "OFF" period of the cyclotron beam is 40 ms. The maximum efficiency of the laser ion source is achieved at the highest laser repetition rate, e.g. 200 Hz. At these

rates, the lasers are no longer synchronized with the cyclotron beam. During the radioactive life-time measurements an additional macro separator beam ON-OFF structure is imposed on the mass separator beam (see Fig.2.14.b).

2.8 The control system of the laser ion source and the mass separator

A control system of the laser ion source, extraction and mass separator has been developed and implemented in order to meet the requirements imposed by a specific application[8]. A schematic view of the control system[9] is shown in Fig.2.15. The parameters of the equipment are controlled from *Client PCs* connected through an ethernet network to a *Control System Server*. A *Programable Logic Controller* unit (PLC) receives the command from the server and transmits it further to the hardware component (input slot). The updated parameters from the hardware component are sent back to the PLC (output slot), server and displayed on the control panel of the client PC. The readout of the datapackage from the PLC is performed every 100 ms and it is displayed on the client PC panel windows. The client and server PC programs are written in Visual Basic language[10]. Other hardware components are connected directly to the server (not through the PLC unit), such as a multichannel SEM counter (for time profiles of the mass separated beam), cyclotron beam intensity counter (scintillator plastic), the motor controller for the optical prisms position in the lasers hut, a simple data acquisition system to readout a detector (e.g. silicon PIPS) (not shown on Fig.2.15). Communication to these modules is done via UDP/IP protocol over the ethernet network. A *Timing PC* directly connected to the equipment controls the SPIG RF and SPIG DC gate[11], separator beam gate[11], ion collector power supply gate[11], trigger of the beam current measurement, cyclotron beam gate[11] and data acquisition (*DACQ*) system synchronization. A separated file server (not shown on Fig.2.15) is used to store all the program-, configuration- and data-files, which are automatically backed-up. The application windows acting as user interface panels are:

- vacuum status control and display;
- ion source control (needle valve, filament settings (current, voltage), position (relative to SPIG rods));
- laser wavelength scanner;
- power circuit switches;
- beam current monitor and alarm;
- separator beam optics;
- panels to control and readout other equipment (SEM counter, cyclotron beam counter, motor controllers for optical prisms);

[8] This section is written through the courtesy of Paul Van den Bergh, the author of the control system.

[9] In this section the "control system" refers to the control of the laser ion source, extraction and mass separator parameters.

[10] Microsoft® - http://msdn.microsoft.com/vstudio/

[11] The term "gate" refers to the *open*- or *closed*-status of the component. When the SPIG gate is open it means that all the voltages (V_{rf}, V_{dc} and V_{se}) are set to transport the ions through the ion guide structure.

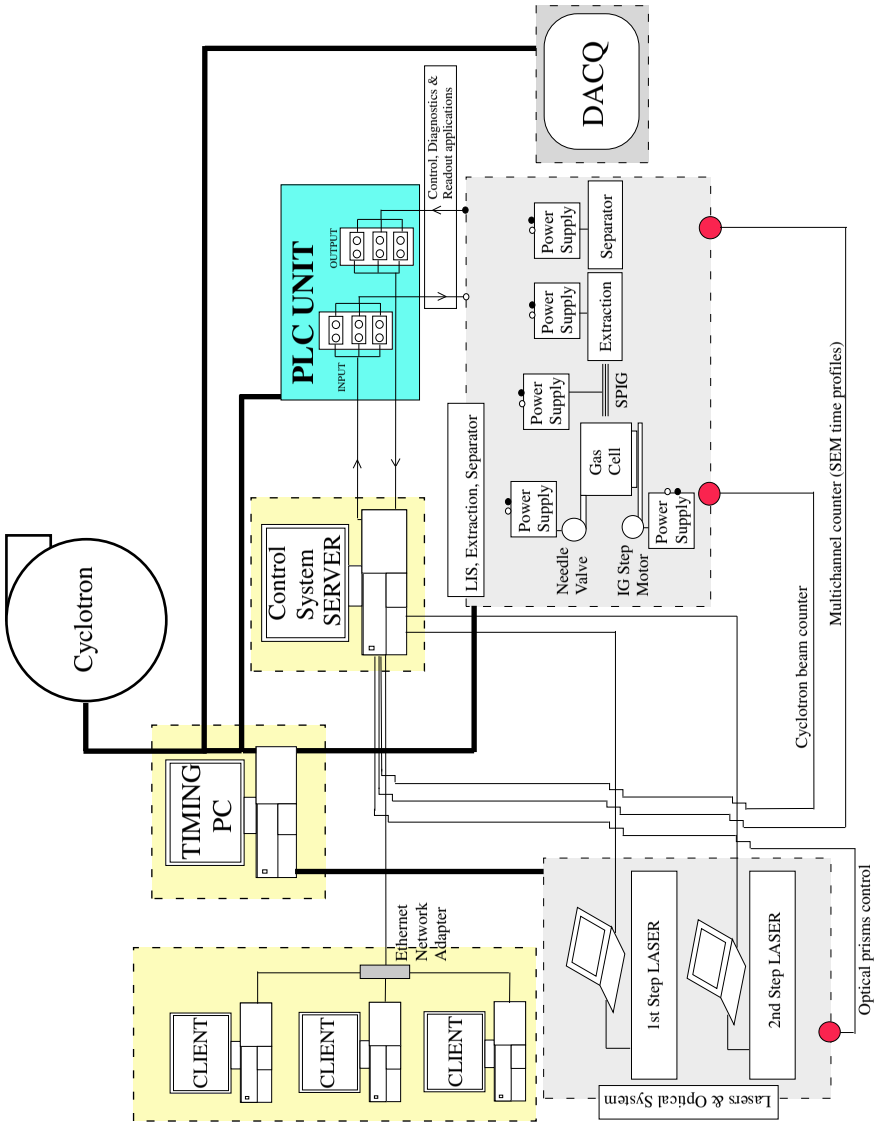

Fig. 2.15: A schematic view of the control system of the laser ion source, extraction and mass separator (see text for details).

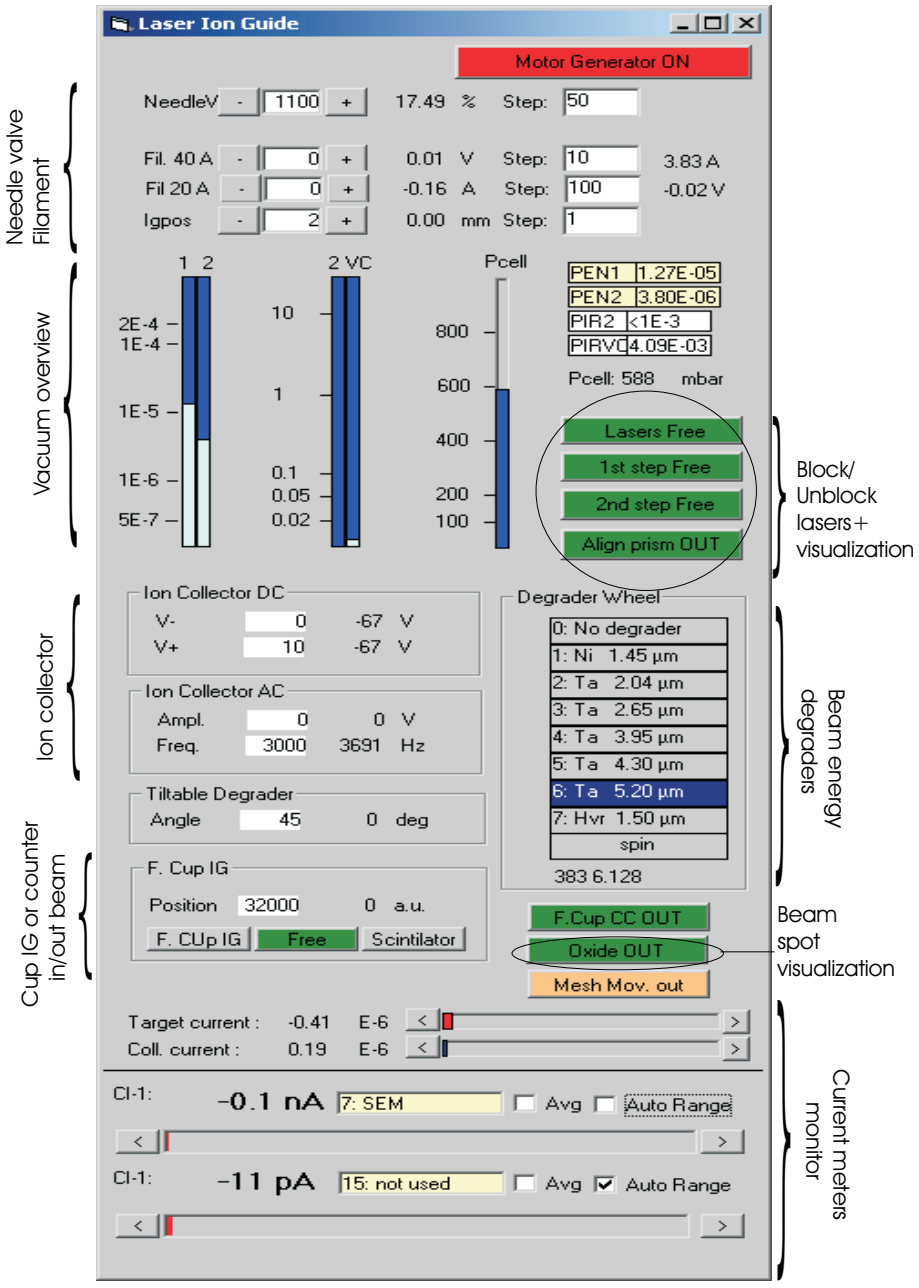

FIG. 2.16: The control window of the laser ion source parameters. In order, from top to bottom: Needle valve control; filament settings control: two filaments connected to a 20 A and 40 A power supplies, respectively; gas cell (ion guide position); vacuum gauges; blocking or un-blocking of the 1^{st}, 2^{nd} step or both laser beams; DC/AC voltage on ion collector control; Cup IG cyclotron current; list of degrader foils available - selection to insert one of them in the beam path; aluminum oxide screen in/out for cyclotron beam spot visualization; mechanical grid in/out for beam attenuation; Cup IG/collimator current readout (when connected); two current meters connected to different diagnostics equipment. Except the current-meters and vacuum/pressure gauges which provide absolute value measurements, the hardware settings are shown in calibrated setpoints and/or absolute values. The two current meters can be connected to the installed Faraday cups (see section 2.6).

- panels to scan beam optics parameters (SPIG RF amplitude, wirescanner for the mass separated beam);
- parameter scan (mass scan).

Fig.2.16 shows the control window of the laser ion source parameters, as viewed on the client PC. This concerns the control/monitor of the parameters of the cyclotron beam entering the gas cell (position, intensity, energy), the control/monitor of the parameters of the equipment of the gas cell (needle valve, filaments, biasing of the electrodes in the cell), gas cell position, vacuum overview in the front-end box, lasers blocking/unblocking and viewing control.

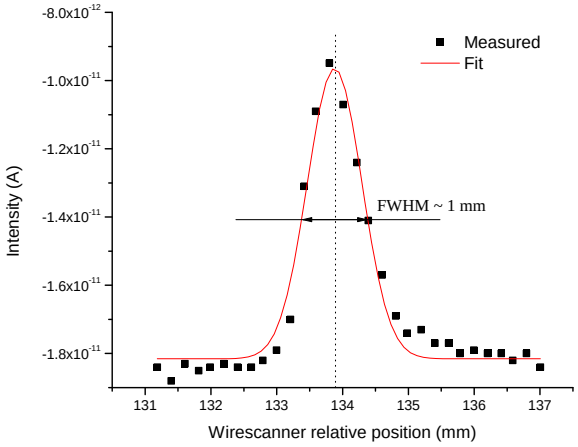

Fig. 2.17: Transversal profile of a ^{40}Ar beam measured with the wirescanner monitor in the focal plane of the separator.

Apart from intensity monitoring of the mass separated beam, as discussed in the section 2.6.2, a beam profile monitor installed at the exit of the magnet separator provides information on the beam spatial distribution at the focal plane of the separator. This is a standard equipment used for beam diagnostics in particle accelerators and it consists of a Ø0.2 mm wire that crosses the beam. The current in the wire, which results from the secondary electron emission, is recorded together with its position. An example of such a measurement is shown in Fig.2.17 where the profile of a ^{40}Ar beam extracted from the fission gas cell (see Fig.2.5) is shown. The beam FWHM[12] is 1 mm, which corresponds to an energy spread of about 1 eV [VBe97]. The voltages applied to the Einzel focusing lens and vertical deflection, before mass separator, are adjusted in order to achieve this spatial distribution of the mass separated beam. The mass composition of the extracted beam from the gas cell is checked by scanning the magnetic field of the separator and measuring the beam current in the focal plane of the separator. This can be performed with

[12]FWHM stands for Full Width at Half Maximum.

or without dissociation of molecules (see section 2.3.3). An example of a mass scan obtained off-line can be seen in Fig.5.2.a (Ni atoms evaporated from a filament in helium gas and resonantly laser ionized). The mass scans obtained on-line (e.g. when a cyclotron beam enters the gas cell) are more complicated, as can be seen in Fig.3.15 (laser ionized Co from a filament, in the gas cell filled with argon gas and a 30 MeV proton beam passing through the cell). Time-behavior analysis of the signal at specific masses, when the impurity concentrations are known, is required in order to make unambiguous assignment of the peaks in the mass spectrum [Kud01].

The time-behavior of the signal of mass separated beam is checked in Cup 7 (see Fig.2.10) by connecting the SEM to a fast oscilloscope (Philips MODEL). Many examples of such time profiles can be found in section 5.1.

Chapter 3

Processes in the gas cell

Production of radioactive beams at the LISOL laser ion source is based on the stopping and neutralization of reaction products from a target in a noble gas cell and resonant laser ionization of a particular radioactive species which is further extracted from the ion source and mass separated. This chapter concerns the study of the most important processes occurring in the gas cell during the slowing down and/or stopping of projectile ions. In order to characterize the gas cell as a target-ion catcher system it is essential to study the slowing down and stopping of the reaction products in the buffer gas.

The slowing down of energetic heavy-ions in matter is presented and discussed in the first section of this chapter. Subsequently, the charge state of the ion during the slowing down process, the multiple ionization of rare gas targets by heavy-ion beam impact and the energy spectra of the ejected electrons by heavy ion impact are presented and discussed in dedicated sections. The charge creation and recombination processes during the slowing down of reaction products and of the primary beam, the diffusion of electrons and ions as well as the presence of impurities in the buffer gas can strongly influence the release properties of the ion source. These processes are presented and discussed in the subsequent sections of this chapter. A summary of the main issues is given at the end of the chapter.

3.1 Slowing down and stopping of ions in matter

When energetic ions collide with a multi-electron atomic target, the target atom (projectile ion) may lose one or more electrons by ionization to the continuum or by transfer to the projectile (target). In heavy ion-atom collisions where both the projectile and the target are multi-electron systems, the ionization processes are generally very complicated involving different ionization mechanisms such as direct ionization to the continuum of the projectile and the target, electron transfer between the projectile and the target during the collision, and autoionization from excited state after the collision. It is not the intention of this paragraph to enter deep in the study of the slowing down of heavy ions in matter, and for more details the reader is referred to the extensive work of Ziegler et al. [Zie80, Zie85a, Zie85b,

Zie99, SRIpr].

The slowing down of projectile beams is used at LISOL in order to tune the energy of the primary projectiles for the maximum cross section for production of a particular isotope in nuclear reaction in the target. Secondly, the reaction products which have enough kinetic energy to leave the target, are slowed down and eventually stopped in the gas within the gas cell volume. Thirdly, the primary beam projectiles lose energy in the gas cell.

3.1.1 Stopping power and range of ions in matter

Three major mechanisms have to be considered when describing the slowing down process of a heavy ion:

- the nuclear stopping, i.e. the energy lost due to elastic Coulomb interaction between the "screened" nuclear charges of the projectile ion and the target atom;
- the electronic stopping, i.e. the inelastic interaction of the projectile ion with bound or free electrons of the target;
- the charge exchange between the moving ion and the target atom, i.e. during the close proximity between the projectile ion and the target atom electrons are transferred from one to another.

The term "screened" is here regarded as a partial screening of the Coulomb field of the target nucleus caused by the orbital electrons carried by the projectile. The total specific linear energy loss is thus taken to be the sum of three separable components: nuclear, electronic and charge-exchange:

$$\frac{dE}{dx} = (\frac{dE}{dx})_n + (\frac{dE}{dx})_{el} + (\frac{dE}{dx})_{ch-ex} \tag{3.1}$$

Fig.3.1 shows the variation of the first two components in the right-hand side of eq.(3.1) as a function of the projectile energy, for the case of H, ^{4}He, ^{40}Ar, ^{58}Ni and ^{103}Rh ions in argon gas at 500 mbar pressure. Both components increase with the ion's energy, reach a maximum and then decrease. In the low-energy domain the nuclear stopping dominates, while at high energies the projectile energy is dissipated in form of electronic, rather than nuclear motion. For sufficiently high energies of the projectile, the last term in eq.(3.1) can be neglected and mainly the electronic and nuclear stopping powers[1] are considered.

It is the famous Bethe-Bloch formula [Zie99] which can be used to estimate the stopping power of a projectile with atomic number Z_1 into a target formed by atoms with atomic number Z_2:

$$\frac{dE}{dx} = \frac{4\pi e^4 Z_2}{m_e v^2} Z_1^2 [ln\frac{2m_e v^2}{< I >} - ln(1-\beta^2) - \beta^2 - \frac{C}{Z_2} - \frac{\delta}{2}] \tag{3.2}$$

where m_e is the mass of electron, e is the electronic charge, v is the velocity of the projectile, $< I >$ is the averaged excitation potential per electron [And77, Leo87], $\beta = v/c$ (c = speed of light). The last two terms, shell correction, C/Z_2, and density effect correction, $\delta/2$, in eq.(3.2), are important at low- and high-energies, respectively [Leo87].

[1]The stopping power is the terminology to denominate the linear energy loss of the projectile particle in the target.

Table 3.1: The energy loss (dE/dx) and ranges of different projectiles with given energy in helium and argon gases at 500 mbar.

Projectile	dE/dx (keV/cm)		Range(cm)		Straggling(cm)	
	He	Ar	He	Ar	He	Ar
H (30 MeV)	1.65	11.7	$1.04{\cdot}10^4$	$14.56{\cdot}10^2$	$4.21{\cdot}10^2$	64.1
He (45 MeV)	15.1	105	$16.59{\cdot}10^2$	$2.59{\cdot}10^2$	68.00	10.66
Ar (130 MeV)	2163	12020	53.00	10.56	1.59	0.36
Ni (30 MeV)	4785	21950	16.87	3.04	0.48	0.24
Rh (650 MeV)	5810	36320	98.85	18.77	2.71	0.55

An energetic projectile passing a medium with the thickness d, slows down and loses an energy which is given by:

$$\Delta E = \int_0^d (\frac{dE}{dx})dx \tag{3.3}$$

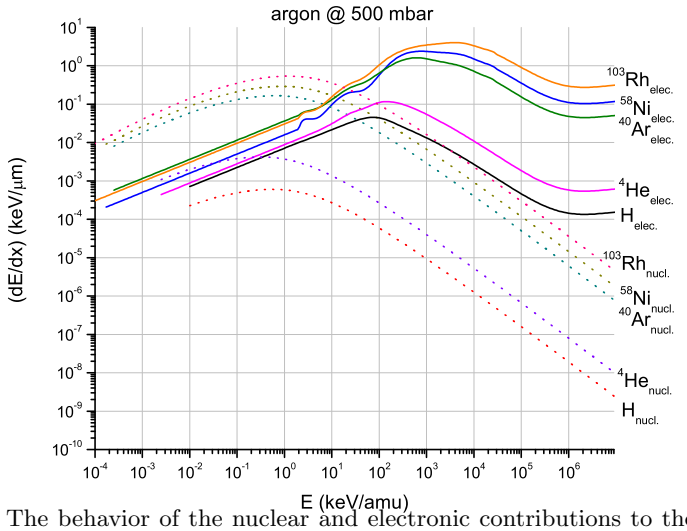

Fig. 3.1: The behavior of the nuclear and electronic contributions to the specific energy loss dE/dx of H, ^{4}He, ^{40}Ar, ^{58}Ni and ^{103}Rh ions in argon gas (500 mbar) as function of the kinetic energy (calculated with SRIM [SRIpr]).

A projectile with energy E_0 is stopped in the medium after a distance which is called the "range" (R):

$$R(E_0) = \int_0^{E_0} \frac{1}{dE/dx} dE \tag{3.4}$$

Different computer codes like SRIM[2] [SRIpr] and ATIMA [ATIpr] are freely available to be used in calculations of stopping powers and ranges of ions in elemental or compound targets. Using the SRIM code, the stopping power and range of different ions in gas targets (helium and argon) at 500 mbar pressure, have been calculated. The results are summarized in Table.3.1.

3.1.2 The energy and range straggling

The energy loss of an energetic projectile passing through matter is statistically distributed around its mean value given by eq.(3.2). The distribution, often referred to as energy straggling, is approximately Gaussian. The range of a charged particle (eq.(3.4)) in matter is subjected to fluctuations caused by the probability distribution of energy loss. These fluctuations are called range straggling.

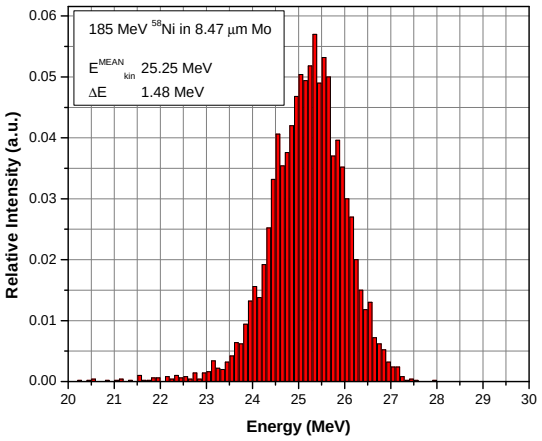

FIG. 3.2: The energy distribution of a 185 MeV ^{58}Ni after passing through two molybdenum foils (4.1 μm and 4.37 μm thickness). The calculation was performed with the SRIM code [SRIpr]. The mean energy of the Ni ions and the energy straggling (ΔE) are given in the insert.

An example of a ^{58}Ni beam energy distribution after passing through two molybdenum foils is shown in Fig.3.2. The initial beam is considered pencil-like, the energy of the ^{58}Ni ions is 185 MeV and the total thickness of the two foils is 8.47 μm. This is a configuration used in on-line experiments at LISOL to degrade the energy of a ^{58}Ni beam prior to its implantation into the gas cell. The stopping power of

[2]This code is also known as "TRIM".

the 185 MeV ^{58}Ni ions in Mo is 18.7 MeV/μm. After passing the molybdenum foils the mean energy of the projectiles is 25.25 MeV and the energy spread, defined as the standard deviation of the mean value, is 1.48 MeV. This corresponds to a momentum spread $\Delta p/p = 0.24$ of the beam after passing the foils.

The ^{58}Ni beam with the energy distribution from Fig.3.2 is subsequently stopped in the gas cell filled with argon gas at 500 mbar pressure[3]. The range distribution of the ^{58}Ni ions stopped in the gas cell is shown in Fig.3.3. The mean range of

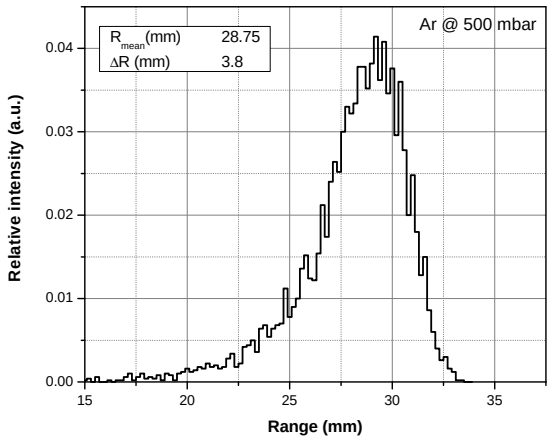

Fig. 3.3: The range distribution of the ^{58}Ni ion beam with the energy distribution from Fig.3.2 (25.25±1.48 MeV) stopped in a gas cell filled with argon gas at 500 mbar pressure. The calculation was performed with the SRIM code [SRIpr]. The mean range of the Ni ions and the range straggling (ΔR) are given in the insert.

^{58}Ni ions in 500 mbar argon is 28.75 mm and the range straggling, defined as the standard deviation of the mean value, is 3.8 mm.

Using helium as buffer gas is more difficult, as the cell size and the gas pressure are limiting factors. A 37 mm thick layer of helium at 500 mbar pressure is capable to stop ^{58}Ni ions with the maximum energy of 2 MeV. Therefore, the beam energy has to be degraded from 185 MeV down to 2 MeV by using degrader foils. A 185 MeV ^{58}Ni can be energy degraded down to $\sim$ 2 MeV using 3 successive foils[4]: 4.1 μm Mo (vacuum box window), 3.6 μm Ta (degrader foil) and 4.1 μm Mo (gas cell window). The energy distribution of the projectile beam after such an energy degrading system is shown in Fig.3.4. The mean energy of the ^{58}Ni ions is 1.92 MeV and the energy straggling, defined as the standard deviation of the mean value, equals 0.9 MeV. This corresponds to a momentum spread $\Delta p/p$ of $\sim$ 0.68. An important remark has to be made on the transmission of the above mentioned degrading system, as it may also contribute to loss of ions due to scattering in

[3]The gas cell has a volume with a width of 37 mm along the beam direction.

[4]This configuration was used at LISOL laser ion source to implant the Ni beam into the gas cell filled with helium gas.

the metallic foils. The result presented in Fig.3.4 has been obtained by simulating 10.000 ^{58}Ni ions in the initial 185 MeV beam. Only $\sim$ 6000 ions have actually been transmitted through the 12.1 μm thick Mo/Ta/Mo ensemble, i.e. 60% transmission efficiency. These ions are subsequently slowed down/stopped in the gas cell filled with helium gas at 500 mbar pressure. The range distribution of the ^{58}Ni ions stopped in the gas cell is shown in Fig.3.5, and one can see that the nickel ions are almost uniformly distributed in the gas cell.

The result of the simulation [SRIpr] shown that only 30% of the nickel ions entering the cell have actually been stopped in the gas, the rest of them being implanted onto the cell walls. Evidently this is not convenient, therefore one has either to increase the volume of the gas cell or to reduce the energy spread of the ion beam being implanted in the gas cell.

Beams with large momentum spread and dispersed spatial distribution are commonly obtained after an electro-magnetic spectrometer coupled to a production target (In-flight facilities). Preparation of such beams for precision and/or spectroscopy studies requires the efficient slow down of the ions prior their measurement. Wedge degraders [Wei00] (monoenergetic degrader) can be used after mass separation in order to compensate the momentum spread of spatially dispersed secondary beam by larger or smaller energy losses, i.e. all the ions exiting this degrader have the same momentum. In this way the use of a gas cell for stopping the (secondary) ion beam after mass separation becomes possible without major losses due to the range straggling.

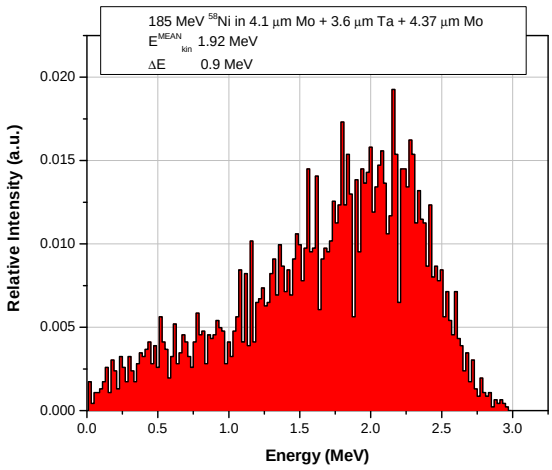

FIG. 3.4: The energy distribution of a ^{58}Ni beam (initial energy of 185 MeV) after passing through three metallic foils: Mo-4.1 μm, Ta-3.6 μm and Mo-4.37 μm thickness. The calculation was performed with the SRIM code [SRIpr]. The mean energy of the Ni ions and the energy straggling (ΔE) are given in the insert.

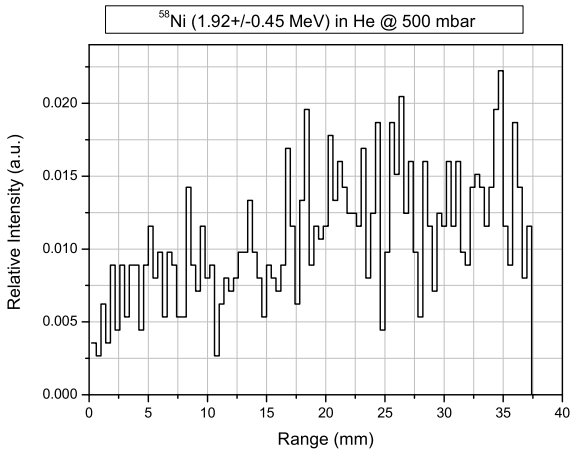

Fig. 3.5: The range distribution of the ^{58}Ni ion beam with the energy distribution from Fig.3.4 (1.92±0.9 MeV) stopped in a gas cell filled with helium gas at 500 mbar pressure. The calculation was performed with the SRIM code [SRIpr].

3.2 The charge state of the ion during the slowing down process

As a swift ion penetrates a target medium it undergoes a large series of ion-electron collisions. The statistical probabilities for electron-capture and electron-loss generally differ and depend on the charge state, the excitation state and the velocity of the ion. This, coupled with the discrete changes of the charge state ±1, implies that, as the ion traverses the medium, its charge q changes in a stepwise manner towards a charge-state equilibrium [Shi86]. Regardless of the thickness of the traversed medium or the incident ion energy, the equilibrium charge-state distribution of heavy ions, with atomic number Z_1, is characteristic of the velocity $v_1 = \beta c$ of the emergent projectile [Whi04]:

$$q_{eq} = Z_1[1 - exp(-\frac{0.97\beta c}{v_{TF}})] \tag{3.5}$$

where $\beta = \sqrt{1 - (\frac{Mc^2}{E+Mc^2})^2}$, with E and M the energy and the mass of the projectile ion, respectively, and c the speed of light. v_{TF} is the Thomas-Fermi velocity and it equals $Z_1^{2/3}v_0$, where v_0 is the Bohr velocity. The Bohr velocity is the typical velocity of outer shell electrons ($v_0 \cong 2.2\times10^8$ cm/s). The charge-state distribution of ^{58}Ni ions as function of the kinetic energy is shown in Fig.3.6. The Bohr criterion states that all the electrons of the ion which have orbital velocities below the ion velocity will be stripped off [Zie85a]. This means that at very low velocity the atom is unstripped, but as its velocity increases beyond the Bohr velocity, v_0, electrons

begin to be stripped off. For example, He, Ar, Ni and U projectiles with energy of ∼25 keV/amu have a velocity equal to the Bohr velocity, $v_1 = v_0$.

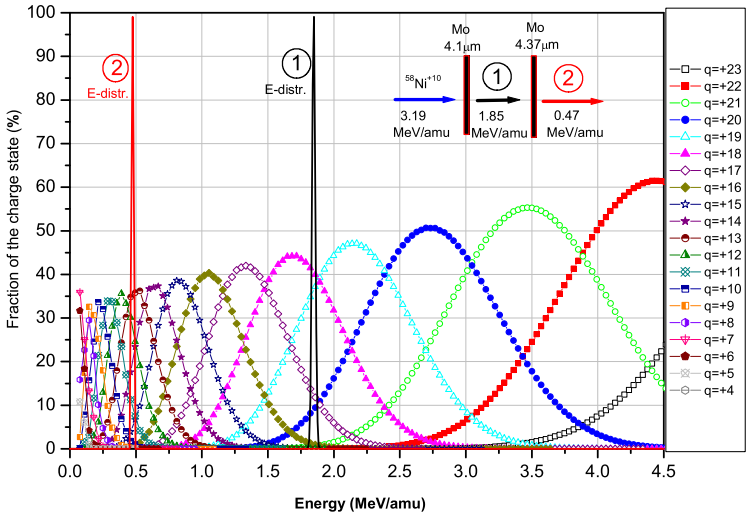

FIG. 3.6: The charge state distribution of ^{58}Ni ions as function of the kinetic energy of the ion (source: LISE program [LISpr]). The charge state distributions of ^{58}Ni ions starting with 185 MeV (3.19 MeV/amu) and passing through a Mo - 4.1μm foil and two Mo - 4.1μm + 4.37μm foils, respectively, are shown on the graph.

During the passage through the target medium the projectile ion losses energy. Therefore, in thick targets the ion's charge will evolve towards neutralization. When the velocity of the ion is lower than the Bohr velocity, the Bethe-Bloch formula (eq.(3.2)) does not hold and charge-exchange processes are dominant. It is worth to note that in the approach used in the Bethe-Bloch theory of slowing down of ions in matter, the projectile ions are assumed to be bare ions. Therefore, eq.(3.2) needs to be corrected for the actual charge state of the ion. The charge state of the ion during the passage through the target is described using the concept of the effective charge [Zie85b]. The explicit form of the Bohr criterion links the effective charge of a heavy ion to the charge of a proton:

$$\frac{Z_1^*}{Z_H} = 1 - exp[\frac{v_1}{v_0 Z_1^{2/3}}] \tag{3.6}$$

where Z_1^* is the effective charge of the partially ionized heavy projectile and Z_H is the charge of the proton. The stopping power of a heavy ion (S_1) can be expressed in terms of the stopping power of a proton (S_H) using the relation:

$$S_1 = S_H(\frac{Z_1^*}{Z_H})^2. \tag{3.7}$$

Eq.(3.7) is used to scale stopping powers of heavy ion projectiles to the proton ones. As a structureless projectile, the proton is an ideal tool for the study of the slowing down process. Therefore, protons have been extensively used in experimental studies of the slowing down process in all target materials [And77], resulting in a well understood theoretical model for this mechanism. When the projectile impinging on the target is not anymore structureless, i.e. heavy ion, the description of the slowing down process becomes more complicated and it has to account for many other parameters and effects [Kra94, Zie99]. Despite the impressive amount of experimental and theoretical work, the study of heavy ion slowing down in matter is far from being completely understood.

3.3 Multiple ionization of rare gas targets by heavy ion impact

Swift ions moving at a distance of few *atomic units*[5] or less from a target atom, may eject a number of the target electrons without simultaneously imparting much energy to the target recoil. This is due to the large ratio of target nuclear mass to that of the electron. The creation of multiply charged target ions in a gas cell is of interest as it may either be followed by Auger-electron ejection and subsequent light emission by re-arrangement of the electrons on the atomic orbitals, or direct radiative de-excitation of the ion by electron capture. The emitted photons can induce further ionization of the buffer gas in the region where laser ions are produced, thus unwanted recombination of the resonantly ionized species is enhanced.

Fig.3.7 shows the partial and total ionization cross sections of Ar at electron and proton impact, respectively as function of the energy of the projectile.

There is little experimental information on direct multiple ionization of rare gas targets by heavy ion impact, and the systematics is not as rich as for electron and proton impact. The multiple ionization of an atom in heavy ion collisions results from the many-body interaction between the projectile and the target electrons, which still remains unresolved theoretically [Cai96].

Ma et al. [Ma98] have shown that in collisions of 5.3 MeV/amu S^{9+} ions with Ar, the single ionization of the target atom is the predominant process, where the relative fraction of singly ionized Ar recoils is as much as 83%. Cai et al. [Cai96] have shown that the fraction of multiple ionization of argon in collision with O^{q+} ions depends on the initial charge state of the projectile ion ($q+$). They found that in collisions of 187.5 keV/amu O^{1-4+} with argon atoms, ∼70% of Ar recoils where single ionized, while the rest of ∼30% where 2 - 6+ recoil ions. These multiply charged ions are the result of a multi-step mechanism in direct ionization of target atoms in collision with heavy projectiles, but not the result of Auger transitions after single ionization. This hypothesis is also supported by work performed with 0.7 - 1.3 MeV Cl^{q+} [Coc79], 2.1 - 4.3 MeV/amu Si^{q+} [Sin99] and 1.05 MeV/amu Ar^{q+} [Ton89] ions colliding with argon targets.

[5]The atomic unit of length is defined as the Bohr radius or the radius of the lowest energy electron orbit of an atom.

3.4 Energy spectra of ejected electron by heavy ion impact

As suggested by Rodriguez [Rod97], in a complete description of the collision process of heavy ions with atomic targets, the final state in single ionization of atoms is characterized by the nine momentum components of the three particles: projectile ion, target ion and ejected electron. Only five components are independent owing to momentum and energy conservation during the collision. The final collisional state is completely described by a quintuply differential cross section given in terms of projectile scattering angle (Ω_p), electron energy (ϵ_e) and ejection angle (Ω_e):

$$\frac{d^5\sigma}{d\Omega_p d\epsilon_e d\Omega_e} = \frac{\mu^2}{4\pi^2} p_e |T_{if}|^2 \tag{3.8}$$

where T_{if} is the transition matrix and μ is the reduced mass.

Due to experimental requirements, the convenient quantities to be measured in ionization experiments are the doubly differential cross section (DDCS) $\frac{d^2\sigma}{d\Omega_e d\epsilon_e}$ [Rud76, Rud79, Sch88, Kel89] for ejection of electrons within an energy domain and in a specific angular range or single differential cross sections (SDC) for ejection of electrons within an energy domain $\frac{d\sigma}{d\epsilon_e}$ or over an angular range $\frac{d\sigma}{d\Omega_e}$ [Sch88, Kel89,

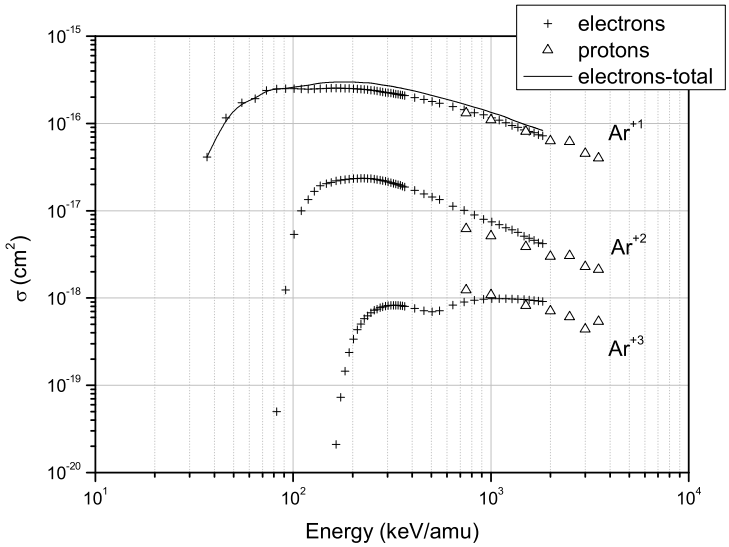

FIG. 3.7: The single, double, triple and total (line) ionization cross sections of Ar by electrons (+) [Kri88] and protons (△) [Cav03], as function of the kinetic energy of the projectile.

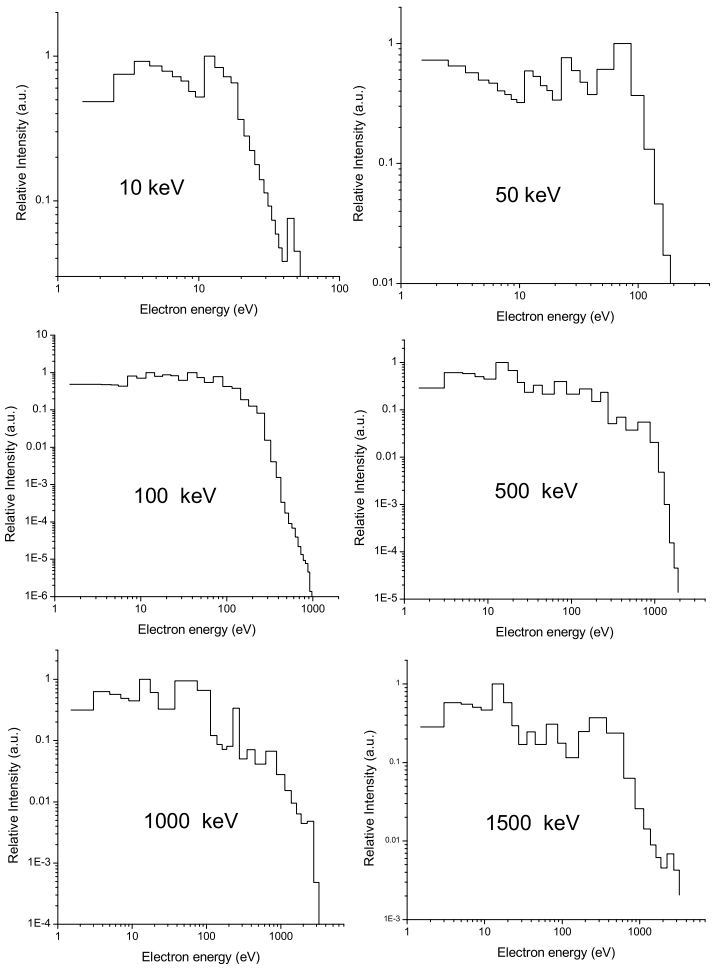

Fig. 3.8: Energy spectra of ejected electrons in collision of 10 - 1500 keV protons with Ar target [Rud79].

Mos94]. As in the case of ionization cross sections, the data for the electron ejection cross sections at heavy ion impact on atomic targets are scarce. Again, electrons and protons have been widely used to extract these cross sections.

Fig.3.8 presents the energy spectra of ejected electrons by proton impact in argon, at projectile kinetic energies in the range 10-1500 keV [Rud79]. One can deduce the fraction of ejected electrons owing energy of 110 eV and above, i.e. the energy corresponding to the maximum cross section for ionization of argon by

electrons (see Fig.3.7). These fractions are as follows: 0 for 10 keV proton, 6% for 50 keV proton, 23% for 100 keV proton, 58% for 500 keV proton, 61% for 1 MeV proton, and 82% for 1.5 MeV proton.

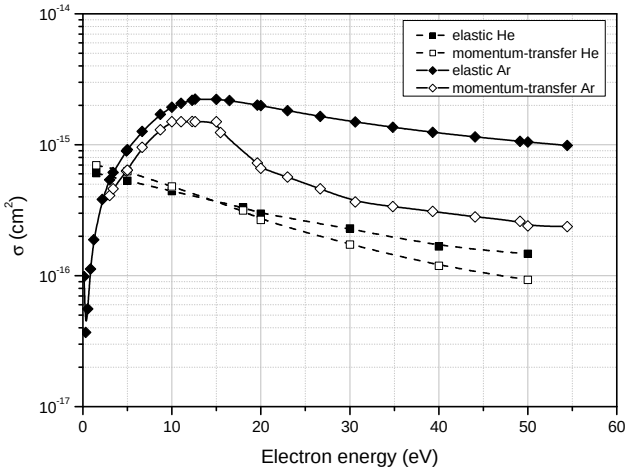

FIG. 3.9: Elastic and momentum transfer cross sections for electron collisions with Ar and He, respectively, as function of the electron energy. ♦ - elastic and ◊ - momentum transfer He [Bru92]; ■ - elastic and □ - momentum transfer Ar [Das85].

The electrons ejected by the projectile impact are subjected to collision with target atoms. Inelastic collisions proceeding with momentum transfer lead to thermalization of electrons. Electrons with energy higher than 100 eV have a large ionization cross section in both helium [Mit73] and argon [Kri88]. Below 100 eV energy, elastic and momentum transfer collisions with the target atoms predominate. Fig.3.9 shows the cross sections for elastic and momentum transfer collisions of electrons in helium and argon, respectively as function of electron energy. In momentum transfer collisions, an electron transfers in average a fraction $\frac{2m_e}{M}$ of its energy to the target atom, where m_e and M are the electron and target atom masses, respectively. In argon, however, the rate of electron energy transfer to gas atoms is highly energy dependent at low energies. The momentum transfer cross section for argon, exhibits a Ramsauer minimum at approximately 0.3 eV. When electrons in pure argon are at the energy of this minimum, the momentum transfer cross section σ_{MT}^{Ar} is smallest, i.e. $\sim 10^{-17}$ cm^2, and electron energy loss by collisions with argon atoms becomes very slow. In helium, the electron momentum transfer cross section has a smooth dependence with the electron energy, and since $\frac{2m_e}{M_{He}} = 10 \cdot \frac{2m_e}{M_{Ar}}$, helium gas is much more effective than argon in thermalizing the electrons. A measure of the thermalization effectiveness is the time of thermalization which can be extracted from the momentum transfer cross sections. Fig.3.10 shows the electron energy dependence of the thermalization time in 500 mbar helium and argon, respectively. One can see in Fig.3.10 that the thermalization of electrons in

helium is in average one order of magnitude faster than in argon gas. The thermalization time is strongly dependent on the nature of the gaseous system and the obtained values from the momentum transfer cross section (shown in Fig.3.9) are in good agreement with those values reported in literature [Coo93, War75], i.e. $\sim$50 ns in helium, and $\sim$1 μs in argon. It is important to note that thermalization must be essentially complete before substantial ion-electron recombination can occur, except for dissociative recombination (see section 3.6) which proceeds through collisions of electrons with large (molecular) ions.

3.5 Ionization due to the beam impact

During the slowing down process, an ion releases its energy to target atoms in the form of direct ionization or excitation. The energy loss mechanism is not completely described only by accounting for the ejected electrons in primary collisions. The ejected primary electrons (δ-electrons) induce secondary processes in the target, thus in order to account for these effects, the concept of mean energy for the creation of an electron-ion pair has been introduced [Leo87]. This mean energy, referred as W, is not identical to the ionization potential (introduced in section 1.4 of Chapter 1). The mean energy for the creation of an electron-ion pair in argon is 26 eV, while in helium it amounts to 46 eV [Sau91]. The production rate of ion-electron pairs depends on the projectile particles, their energy and the buffer gas. Table 3.2 shows the energy loss dE/dx [SRIpr] and the ion/electron production rate Q (cm^{-3} s^{-1}) in the accelerator beam path at gas pressure of 500 mbar for the ion beam density of 1 pμA/cm^2.

The beam intensity is given, in this thesis, in the units pμA or pps, where 1

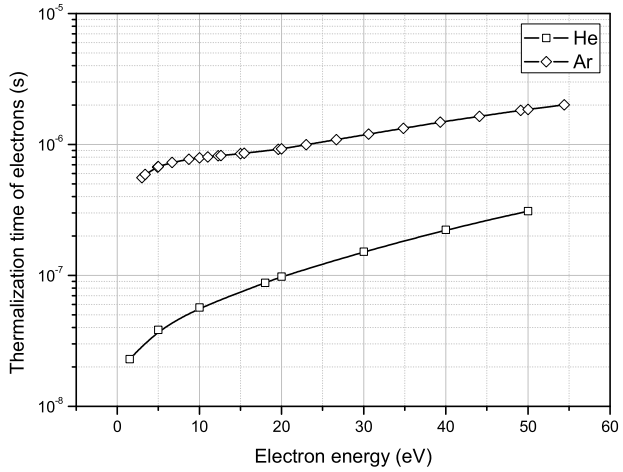

Fig. 3.10: The electron thermalization time in 500 mbar helium (□) and argon (◊), respectively, as function of the electron energy.

particle micro Ampere (pμA) corresponds with a beam of 6.25 10^{12} particles per second (pps). The production rate is calculated by

$$Q = 6.25 \cdot 10^{12} \cdot \frac{I}{A} \cdot \frac{(dE/dx)}{W} \qquad \text{ion-electron pairs/cm}^3\ \text{s}, \tag{3.9}$$

where I is the beam current in pμA, A is the beam spot area (cm^2), (dE/dx) is the linear energy loss of the ion (in eV/cm), W is the mean ionization energy needed for the production of one electron-ion pair. The type and the energy of the beam shown in the table were used in different experiments described in ref.[Huy02]. Even a 30 MeV proton beam of 1.3 μA with a diameter of 6 mm creates 10^{16} pairs/cm^{3}s in argon at 500 mbar.

The on-line studies performed at LISOL can, next to the study of the effect of a primary beam, be divided in three types:

(a) related to the heavy-ion induced fusion reactions;

(b) related to proton-induced fission reactions;

(c) related to the stopping of a beam of stable isotopes inside the gas cell.

In the first case (a) the particles of interest (the radioactive nuclei) are essentially stopped in the gas cell in the primary beam interaction zone. In the second case (b)

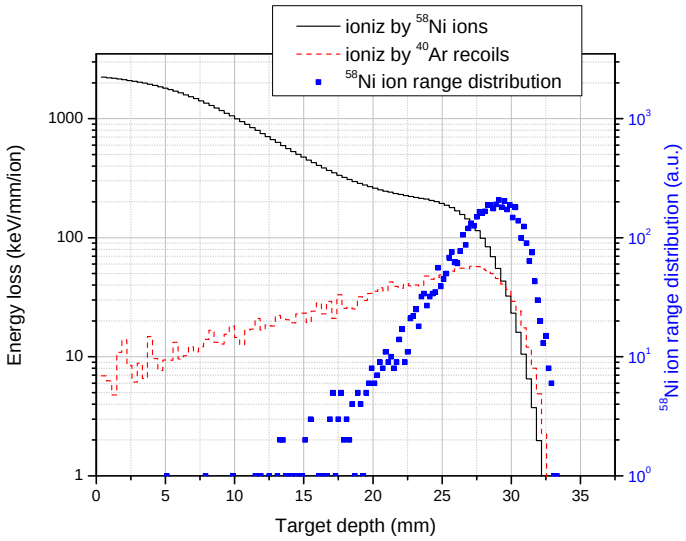

FIG. 3.11: The linear energy loss, dissipated in form of ionization, in the path of a 26 MeV ^{58}Ni ion beam stopped in 500 mbar Ar [SRIpr]. The range distribution of the stopped ^{58}Ni ions is shown (■). Note the double labelling of the vertical axis.

Table 3.2: The energy loss (dE/dx) and production rate Q of ion-electron pairs in 500 mbar helium and argon for different projectile beams of 1 pμA/cm^2. W = 46 eV (He), 26.4 eV(Ar).

Projectile beam	dE/dx (keV/cm)		Q(pairs/cm^{3}s)	
	He	Ar	He	Ar
H^+ (30 MeV)	1.65	11.7	$2.24{\cdot}10^{14}$	$2.77{\cdot}10^{15}$
He^+ (45 MeV)	15.1	105	$2.05{\cdot}10^{15}$	$2.48{\cdot}10^{16}$
Ar^+ (130 MeV)	2163	12020	$2.94{\cdot}10^{17}$	$2.84{\cdot}10^{18}$
Ni^+ (30 MeV)	4785	21950	$6.50{\cdot}10^{17}$	$5.20{\cdot}10^{18}$
Rh^+ (650 MeV)	5810	36320	$7.89{\cdot}10^{17}$	$8.60{\cdot}10^{18}$

of proton-induced fission reactions the energy imparted to the reaction products, which are isotropically emitted, is sufficiently high, thus the ions of interest travel longer distance in the gas cell. A major fraction of them is even implanted onto the cell walls (see the discussion in section B.3). Nevertheless, part of the ions to be

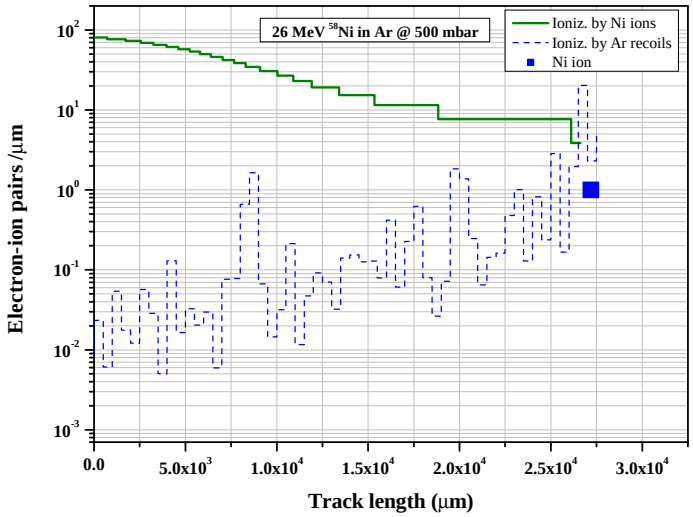

Fig. 3.12: The electron-ion pair density per μm created along the path of a 26 MeV ^{58}Ni ion in 500 mbar argon [SRIpr].

studied are stopped in the gas cell away from the primary beam interaction zone[6]. In the third case (c) the situation is different. A stable ^{58}Ni beam, accelerated to the required energy, penetrates and eventually stops in the gas cell. Due to the characteristic energy-loss pattern, the created number of ion-electron pairs is not uniform over the whole track a nickel ion follows when slowing down. Fig.3.11 shows the result of a SRIM calculation [SRIpr] for the electronic energy loss of 26 MeV ^{58}Ni ions in 500 mbar Ar.

Fig.3.12 shows the distribution of electron-ion pairs along the track of one ^{58}Ni ion stopped in 27 mm of 500 mbar argon. The number of created ion-electron pairs per unit of length is in the beginning of the gas cell 10 times higher than in the region where the Ni ions are stopped. As it will be seen latter this is important, as the lower density of electrons in the zone where the ^{58}Ni are stopped, can enhance the survival of these ions against neutralization.

Apart from the ionization produced by the beam impact, electron-ion pairs can be created in the buffer gas by the electrons ejected from the entrance window foil (Mo $\sim$ 4 μm) when the cyclotron beam is impinging on it. Experimental data on electron ejection from thin-foils when bombarded with heavy ion beams is scarce. Zäpfel et al. have studied the electron ejection from carbon, aluminum and gold foils irradiated with heavy-ion projectiles [Zap02]. Their observation was that in the backward direction the ejected electrons can have velocities v_e up to $2 \cdot v_p$, where v_p is the velocity of the projectile. In the forward direction electrons with $v_e \leq v_p$ were measured. Rothard et al. have measured the yields of electrons from carbon foils penetrated by swift ions (energy range, 20 keV/amu - 74 MeV/amu; projectiles, H-U) over four orders of electronic energy loss (0.01-25 keV/nm) [Rot98]. They have found maximum yields around 250 electrons per projectile. Assuming that a ^{58}Ni ion impinging on a 4 μm Mo foils produces this number of electrons ejected in the forward direction from the foil, and accounting for the fact that the nickel ion enters the foil with an energy around 90 MeV, thus the maximum energy imparted to an electron can be 0.84 keV (according to ref.[Zap02]), the total ionization produced in argon gas due to the electrons ejected from the entrance window is at maximum 9000 electron-ion pairs per incoming projectile ion. After passing the Mo window, the ^{58}Ni ion has an energy of $\sim$26 MeV which corresponds to a total number of 10^6 electron-ion pairs of created in the argon gas (where it also stops), which is two orders of magnitude larger than the number of pairs created by the ejected electrons from the Mo foil. Thus, one can conclude that the ionization in the buffer gas due to the electrons ejected from the entrance foil is negligible. However, measurements of the yields of electrons from Mo foils bombarded with heavy-ion projectiles are required in order to confirm the above simple extrapolation.

3.6 Evolution of the ion-electron pair density in the gas cell

The most important processes that will control the evolution of ion-electron density are charge creation, recombination and diffusion to the walls. Denoting by X the species of interest and by A the buffer gas species, the ionization and recombination processes, occurring in the gas cell of the laser ion source, can be of the type [Mas74, Pet02]:

[6] In the studies of type (a) and (b) the ions of interest are so-called "trace ions" compared to the primary beam ions.

(i) ionization through ion beam projectiles
A + ion beam $\rightarrow A^+ + e^-$ + products;

(ii) ionization through electrons
$A(X) + e^- \rightarrow A(X)^+ + 2e^-$;

(iii) photo-ionization
$h\nu|_{lasers} + X \rightarrow X^+ + e^-$ (resonant),
$h\nu|_{UV,X,\gamma} + A \rightarrow A^+ + e^-$ (nonresonant);

(iv) dissociative recombination
$A_2^+ + e^- \rightarrow A^* + A$,
$XM^+ + e^- \rightarrow X + M$,
where XM^+ is a molecular ion formed with an impurity molecule M (to be discussed in the section 3.10);

(v) three-body recombination with an electron as a third particle
$A_2^+ + e^- + e^- \rightarrow A^* + A + e^-$,
$X^+ + e^- + e^- \rightarrow X^* + e^-$;

(vi) three-body recombination with an atom as third particle
$A_2^+ + e^- + A \rightarrow A^* + 2A$ (see section 3.7 for details),
$X^+ + e^- + A \rightarrow X + A^*$.

3.7 Electron-ion recombination

Due to the relatively high gas pressure and the low ionization degree of the gas[7] ($< 10^{-6}$) in the gas cell used at LISOL, the above mentioned recombination processes of type (iv) and (vi) are predominant. The process of type (v) requires very high electron density ($\sim 10^{13}$ cm^{-3}) in order to give significant contribution to the total recombination rate [Mas74]. A question arises when referring to the first

Table 3.3: Experimental values for the two-body (α_2) and three-body (α_3) recombination rate constants of helium and argon at different temperatures of the gas. The quoted values are reproduced without changes from the original publications (given in brackets).

GAS	He (ref.[Son92])		Ar (ref.[Coo93])	
T (K)	$10^7 \cdot \alpha_2$ (cm^{3}s^{-1})	$10^{27} \cdot \alpha_3$ (cm^{6}s^{-1})	$10^6 \cdot \alpha_2$ (cm^{3}s^{-1})	$10^{27} \cdot \alpha_3$ (cm^{6}s^{-1})
200	0.48±0.03	5.2±0.40	-	-
235	0.68±0.06	3.33±0.30	-	-
275	0.79±0.06	1.34±0.27	-	-
295	1.12±0.05	2.20±0.25	1.07±0.19	5±7
335	-	-	1.52±0.13	-(5±7)
375	-	-	1.55±0.12	-(1±10)

[7]The ionization degree is defined as the ratio of the ionic density number to the atomic density number.

recombination process of type (iv): what is the origin of the dimer A_2^+ ion? The monomer A^+ ions initially created by the projectile rapidly dimerize in the pseudo-first-order three body reaction $A^+ + 2A \rightarrow A_2^+ + A$. The rate constant of this reaction is $k = 1.08 \cdot 10^{-31}$ cm^{6}s^{-1} in helium [Son92], and $k = 2.5 \cdot 10^{-31}$ cm^{6}s^{-1} in argon [Coo93]. The half-life for dimerization is therefore given by $t_{1/2} = \frac{ln2}{k[A]^2}$, where $[A]$ is the atomic density number of the gas (in cm^{-3}). With the above reaction constant rates, the half-life for dimerization in 500 mbar helium is 35 ns, and 15 ns in 500 mbar argon, respectively.

The three-body recombination process of type (vi) is characterized by the α_3 recombination coefficient (in cm^{6}s^{-1}) and the dissociative recombination process, i.e. two-body process, of type (iv) by the α_2 recombination coefficient (in cm^{3}s^{-1}). Thus the total recombination coefficient is then given by

$$\alpha = \alpha_3[A] + \alpha_2. \tag{3.10}$$

where $[A]$ is the atomic density number of the gas (in cm^{-3}). The recombination coefficients α_2 and α_3 for helium and argon have been measured accurately [Son92, Coo93] at different pressures and temperatures of the gas. Their values are quoted in Table 3.3.

The total recombination in helium gas α, at 295 K, has a pressure dependence (in the range 50 - 1200 mbar) that can be expressed as

$$\alpha_{He}^{295K} = (1.12 \pm 0.05) \cdot 10^{-7} + (2.20 \pm 0.25) \cdot 10^{-27}[\text{He}] \qquad \text{cm}^3\text{s}^{-1}, \tag{3.11}$$

which shows that in 500 mbar of helium, at room temperature, the three-body recombination contributes 20% of the total recombination rate. The temperature dependence of α_3 may be written as $\alpha_3 = c \cdot T^{-3}$ [Son92]. In contrast to helium, in argon, no pressure dependence of the total recombination coefficient has been found, in the pressure domain 200-1400 mbar [Coo93]. This indicates that the three-body recombination in argon does not contribute significantly to the total recombination, therefore, the two-body electron-ion recombination in pure Ar must be largely dominant. As one can see in Table 3.3, in argon above 295 K, little variation of the two-body recombination coefficient α_2 with temperature is observed.

If there is a constant production of ion-electron pairs Q [in cm^3 s^{-1}], given by eq.(3.9), such as occurring when the cyclotron beam passes through the gas cell, then the charge density $n = n_{ion} = n_{electron}$ evolves in time as given by the expression [McD64]:

$$\frac{dn}{dt} = Q - \alpha n^2, \tag{3.12}$$

which has a solution

$$n(t) = \sqrt{\frac{Q}{\alpha}} \cdot \frac{e^{2t/\tau} - 1}{e^{2t/\tau} + 1} \tag{3.13}$$

with a time constant τ,

$$\tau = \frac{1}{\sqrt{Q \cdot \alpha}}, \tag{3.14}$$

and the equilibrium density $n_{ion} = n_{electron} = n$ is then given by

$$n = \sqrt{\frac{Q}{\alpha}}. \tag{3.15}$$

At the moment when the beam is switched off the recombination process immediately starts and the density of ions and electrons ($n_{ion} = n_{electron} = n$) is governed by the following expression:

$$\frac{dn}{dt} = -\alpha n^2 \tag{3.16}$$

which leads to a time evolution of the density

$$n(t) = \frac{n_0}{1 + \alpha n_0 t} \tag{3.17}$$

where n_0 is the initial density of electrons. Fig.3.13 shows the time dependence of

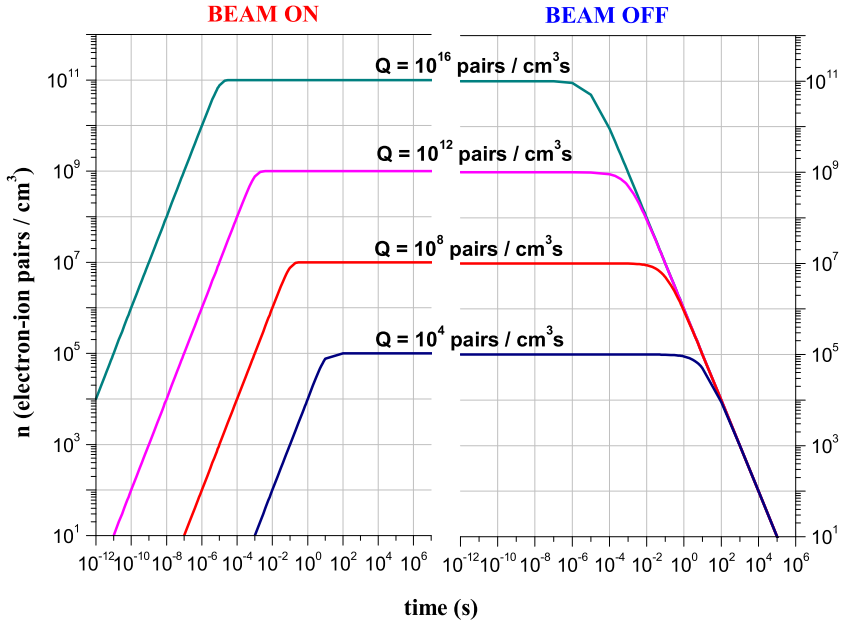

Fig. 3.13: Formation and decay of the ion-electron density as a function of time for different ion production rates Q. A recombination constant $\alpha = 10^{-6}$ cm^{3}s^{-1}, specific for Ar ions in their own gas, was used. Note that the time axis is divided in two. The beam on and beam off periods start at t=0.

the ion-electron concentration, created by the primary cyclotron beam, at different production rates Q and for $\alpha = 10^{-6}$ cm^3 s^{-1} (the recombination coefficient of argon ions in argon gas). The concentration evolves from a linear increase to an equilibrium density with a time constant given by eq.(3.14). As can be seen

from Fig.3.13, when the beam is switched off, the ion-electron density evolves to the same value, independent of the initial concentration. The recombination time constant, τ (using eq.(3.14)), and the equilibrium density, n (using eq.(3.15)), for given ionization ionization rates $Q = 10^5 \div 10^{17}$ electron-ion pairs/cm^{3}s in helium and argon gas, respectively, at 500 mbar pressure are given in Table 3.4.

TABLE 3.4: The recombination time constant, τ (using eq.(3.14)), and the equilibrium density, n (using eq.(3.15)), for given ionization rates $Q = 10^5 \div 10^{17}$ electron-ion pairs/cm^{3}s in helium and argon gas, respectively, at 500 mbar pressure. The recombination coefficients α_{He}^{295K} and α_{Ar}^{295K} from Table 3.3 have been used.

Q (pairs/cm^{3}s)	τ (s)		n(cm^{-3})	
	He	Ar	He	Ar
10^5	8.4	3.1	$8.40{\cdot}10^5$	$3.06{\cdot}10^5$
10^6	2.7	$9.7{\cdot}10^{-1}$	$2.66{\cdot}10^6$	$9.67{\cdot}10^5$
10^7	$8.4{\cdot}10^{-1}$	$3.1{\cdot}10^{-1}$	$8.40{\cdot}10^6$	$3.06{\cdot}10^6$
10^8	$2.7{\cdot}10^{-1}$	$9.7{\cdot}10^{-2}$	$2.66{\cdot}10^7$	$9.67{\cdot}10^6$
10^9	$8.4{\cdot}10^{-2}$	$3.1{\cdot}10^{-2}$	$8.40{\cdot}10^7$	$3.06{\cdot}10^7$
10^{10}	$2.7{\cdot}10^{-2}$	$9.7{\cdot}10^{-3}$	$2.66{\cdot}10^8$	$9.67{\cdot}10^7$
10^{11}	$8.4{\cdot}10^{-3}$	$3.1{\cdot}10^{-3}$	$8.40{\cdot}10^8$	$3.06{\cdot}10^8$
10^{12}	$2.7{\cdot}10^{-3}$	$9.7{\cdot}10^{-4}$	$2.66{\cdot}10^9$	$9.67{\cdot}10^8$
10^{13}	$8.4{\cdot}10^{-4}$	$3.1{\cdot}10^{-4}$	$8.40{\cdot}10^9$	$3.06{\cdot}10^9$
10^{14}	$2.7{\cdot}10^{-4}$	$9.7{\cdot}10^{-5}$	$2.66{\cdot}10^{10}$	$9.67{\cdot}10^9$
10^{15}	$8.4{\cdot}10^{-5}$	$3.1{\cdot}10^{-5}$	$8.40{\cdot}10^{10}$	$3.06{\cdot}10^{10}$
10^{16}	$2.7{\cdot}10^{-5}$	$9.7{\cdot}10^{-6}$	$2.66{\cdot}10^{11}$	$9.67{\cdot}10^{10}$
10^{17}	$8.4{\cdot}10^{-6}$	$3.1{\cdot}10^{-6}$	$8.40{\cdot}10^{11}$	$3.06{\cdot}10^{11}$

The consequences for the use of the gas cell for radioactive ion beams depends on the scheme utilized. In the IGISOL approach [Den97, Ays01], the extraction time of the radioactive ions out of the gas cell through the gas flow should be much less than the recombination time constant (see Table 3.4) in order to avoid neutralization. Opposite, in the case of the laser ion source, laser ionization should be applied in a zone where ion-electron pair density is low enough and the laser produced ions have a high survival chance. Thus in the latter case, the evacuation time should be longer than the recombination time constant to obtain neutralization, but the evacuation time of the laser produced ions should be shorter than the respective recombination time. When a pulsed beam structure is used, laser ionization is thus most effective between beam pulses (see section 2.7) because the laser produced ions do also recombine in the background of the ion-electron pairs present in the gas cell. A laser pulse repetition rate sufficiently high ensures that the recombination of the laser produced ions is compensated by resonant re-ionization by subsequent laser pulses.

Depending on the concentration of electron-ion pairs the recombination processes can be further divided into initial (columnar) and volume recombination [Kan98, Huy02] (see also sections 4.3 and 4.4). The initial recombination represents the recombination of ions with electrons within the track of the projectile,

and it is the dominant process at low projectile beam currents, when the overlapping of different projectile tracks is unlikely. This process will be described in more detail in the next chapter. As the projectile beam current density increases beyond 10^4 particle/cm^{2}s, the projectile tracks (typical diameter of 100 μm) start to overlap. Projectiles with energies around the Bragg peak[8] eject electrons mostly in forward direction [Rud79]. The electron trajectories are fastly randomized by collisions with target atoms, thus ions and electrons within different tracks can recombine, i.e. volume recombination is predominant.

Not yet discussed is the temperature of electrons (T_e) which represents another factor that influences the recombination rates. This will be discussed later in a section dedicated to plasma related effects (see section 4.7).

3.8 Neutralization vs. thermalization in ionic form

Beyond the recombination processes, mainly determined by the high density of electron-ion pairs created during the slowing down of ions in the gas cell, due to their high ionization energy (see section 1.4.1) the noble gases have the property to efficiently store ionic species for a much longer time than other gaseous mediums. This is the basic principle that ion catcher setups make use of. The slowing down of a charged particle in a gas can be described by three regimes (see eq.(3.2)). At high energies, the slowing down is mainly through excitation and ionization of the host gas atoms (Bethe-Bloch regime). As the particle slows down further, its velocity becomes comparable to those of the atomic electrons in the moderator. The particle then enters a regime of cyclic charge exchange, spending part of its time as a neutral species [Sen88]. This domain of cyclic charge exchange continues until the particle energy reaches a charge exchange threshold (electron capture or loss) [Bra72]. The charge exchange reaction between an ion A^q (with a charge q, usually positive) and an atom B can be expressed as:

$$A^q + B \rightarrow A^{q-1} + B^+. \tag{3.18}$$

During cyclic charge exchange, charge changing collisions are not the only type of slowing down mechanism available. The excitation-ionization process, which is the major mechanism in the Bethe-Bloch regime contributes significantly to the energy loss. Elastic collisions are also important particularly near the charge exchange thresholds in that they dictate whether the particle emerges from the cyclic charge exchange regime as a neutral or charged species. Below the electron capture and loss thresholds, the slowing down process proceeds mainly via elastic collisions down to thermal energy. The slowing down in the charge exchange regime is, therefore, a complex process which involves various mechanisms of at least two species, neutral and charged.

Because the ionization energy of the rare gases is higher than the ionization energies of most of the elements, trace ions from a nuclear reaction can be efficiently

[8]The Bragg peak represents the region of maximum energy deposition of a heavy particle as it travels into matter. When travelling through a medium, heavy particles have increased rates of energy loss due to their greater charge and lower velocities. Specific ionization increases as a particle slows down, leading to a marked increase in energy loss, and hence ionization density, towards the end of the trajectory.

stored in a noble gas cell. This is illustrated in Fig.3.14 where the ratio of the first

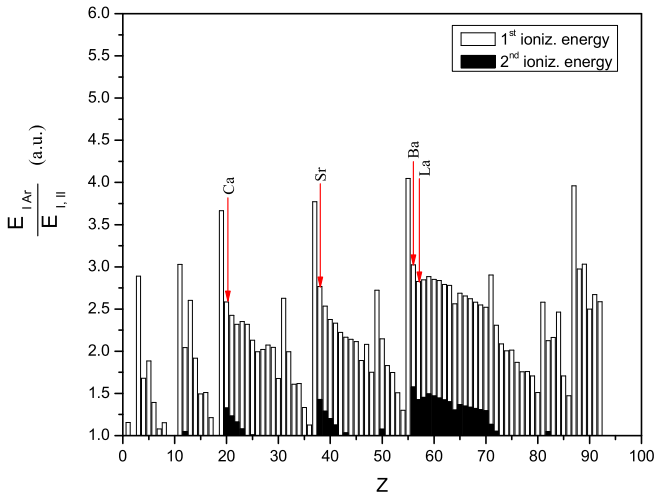

FIG. 3.14: The ratio of the first ionization energy of argon (15.759 eV) to the first (light bars) and the second ionization (dark bars) energy, respectively, of elements with $Z = 1 \div 92$.

ionization energy of argon (15.759 eV) to the first (light bars) and the second ionization (dark bars) energy of elements with $Z = 1 \div 92$, respectively, is plotted as function of Z [NIST]. The arrows indicate some elements which can be stored in argon gas as $+1$ as well as $+2$ ions. For example, in experiments performed at LISOL involving production of neutron-rich nuclei in 30 MeV proton-induced fission reactions Ba^{+2} and La^{+2} ions have been extracted from the gas cell filled with argon gas at 500 mbar pressure (see section B.3 of Appendix B). Nevertheless, low-energy ions in a gas will experience charge exchange reactions with the gas atoms, thus they either reduce their charge or neutralize. As result of the electron capture the buffer gas atoms can emerge the reaction in ionic form. In a complete description of the charge exchange process of type given by expression (3.18), the final state of the ionic (atomic) species is determined by the electronic configuration of the $A^q + B$ system [Bra72]. Therefore, the interpretation based on Fig.3.14 is only qualitative. Advanced theoretical models consider the charge exchange reaction as proceeding through the transfer of an electrons from an atom to a positive ion in a Coulomb potential well formed by the overlap of the Coulomb wells of the atomic nuclei of the two reactants [Ost95]. The experimental information on charge exchange reactions in noble gases is scarce or lacking. As in the case of the studies of ion slowing down in matter protons have been extensively used to investigate charge exchange processes [Bra72]. Nevertheless, due to the complexity of the charge exchange process, the scaling of the experimental charge exchange cross sections of protons for heavier ions is not straight forward. Some experimental results on charge exchange reactions involving highly- or single-charged ions in He and Ar can

be found in [Bra72, Hel77, Heg82, Mar87, Bli92].

3.9 Diffusion of electrons and ions in gas

Only a brief description of diffusion phenomena is given here and for more details the reader is referred to literature [McD64, Nas71, Mit73]. A summary of the important quantities is provided. In this section, charged species other than electrons are denominated as ions and the presented considerations do not deal with negative ions.

In the absence of an electric field, electrons and ions initially produced in the gas by the projectile beam, quickly thermalize and their velocity distribution at thermal equilibrium becomes Maxwellian. If the density of ionization is low, each species of charged particle may be considered as a separate gas, and charged particles of each type diffuse through the neutral gas without interacting appreciably with one another or with other charged species. Diffusion of electrons and ions in a gas is caused by local gradients of concentration. Fick's law of diffusion, which is the basic equation of diffusion theory, states that the particle current density $\mathbf{J}$, the diffusion coefficient $\mathcal{D}$, and the gradient of the diffusing particles ∇N, are related by

$$\mathbf{J} = -\mathcal{D}\nabla N. \tag{3.19}$$

As $\mathbf{J} = N \cdot \overline{v}$, with $\overline{v}$ the average velocity of a particular charged species, the amount of diffusing particles is proportional to the average velocity of its population. The importance of this observation lies in the fact that the thermal velocity of electrons ($\overline{v_e}$) is about two orders of magnitude larger than that of ions ($\overline{v_i}$), at NPT[9] of surrounding gas.

From an experimental point of view, it is impossible to measure the effect of diffusion in the absence of any electrical field. In the presence of an electric field, the velocity of charged particles scales with the electric field (E) with the proportionality factor μ, called mobility:

$$\overrightarrow{v} = \mu \cdot \overrightarrow{E}. \tag{3.20}$$

The total current is now given by the sum of drift current and the diffusion current:

$$\overrightarrow{\mathbf{J}} = N \cdot \overrightarrow{v} - \mathcal{D}\overrightarrow{\nabla} N. \tag{3.21}$$

Provided that there is no temperature difference between charged species and neutrals ($T_e = T_i = T$), it is found that for ions the ratio $\frac{\mathcal{D}_i}{\mu_i}$ depends solely on the temperature of the ion and is given by the Einstein relation:

$$\frac{\mathcal{D}_i}{\mu_i} = \frac{kT}{e}. \tag{3.22}$$

Extending this relation to the case of the electrons under the assumption it holds also for electrons[10], one finds the same equality:

$$\frac{\mathcal{D}_e}{\mu_e} = \frac{kT}{e}. \tag{3.23}$$

[9] NPT = Normal Pressure and Temperature

[10] The mobility concept is not always applicable to electrons.

TABLE 3.5: The classical mean free path λ, average velocity $\overline{v}$, diffusion coefficient $\mathcal{D}$, collision frequency with neutrals ν and mobility μ of electrons and ions of like gas under normal conditions [Nas71, Huy02].

Charged species	Gas	λ (cm)	$\overline{v}$ (cm/s)	$\mathcal{D}$ (cm^2s^{-1})	ν (s^{-1})	μ ($cm^2V^{-1}s^{-1}$)
e^-	He	$1.05{\cdot}10^{-4}$	$1.05{\cdot}10^{7}$	$1.45{\cdot}10^{3}$	$1.0{\cdot}10^{11}$	$5.7{\cdot}10^{4}$
He^+	He	$2.80{\cdot}10^{-5}$	$1.40{\cdot}10^{5}$	0.26	$5.0{\cdot}10^{9}$	10.20
e^-	Ar	$3.77{\cdot}10^{-3}$	$1.05{\cdot}10^{7}$	$1.33{\cdot}10^{2}$	$3.0{\cdot}10^{9}$	$5.22{\cdot}10^{3}$
Ar^+	Ar	$1.00{\cdot}10^{-5}$	$4.40{\cdot}10^{4}$	0.04	$4.4{\cdot}10^{9}$	1.70

Table 3.5 gives the values of the principal transport parameters of charged species in helium and argon gas, respectively, at NPT[9]. Note that an electrical field has no strong effect on the mean energy of the ions and electrons in a high pressure gas cell. If one considers a chamber with 1 atm of helium, given the mean free path of electrons and ions (see Table 3.5), the average energy gain between two collisions in a 10 V/cm electrical field is only $1.05{\cdot}10^{-3}$ eV for electrons and $2.8{\cdot}10^{-4}$ eV for ions and thus well below thermal energies (0.025 eV). However, the application of electric fields alters the diffusion, so that it is necessary to introduce two diffusion coefficients $\mathcal{D}_L$ and $\mathcal{D}_T$, one for the longitudinal and one for transverse direction with respect to the electric field [Sau91].

As the electrons tend to diffuse faster to the container walls, a positive charge is left behind, and an electric field is set up of such polarity as to retard the loss of electrons and accelerate the loss of ions. Both species of charged particles will finally diffuse with the same velocity, and since there is now no difference in the flow of particles of opposite sign the diffusion is called *ambipolar* (characterized by the ambipolar diffusion coefficient $\mathcal{D}_a \simeq 2 \cdot \mathcal{D}_i$). However, this picture is legitimate for ionization densities below or about 10^7-10^8 cm^{-3}, as beyond this concentration the interaction among charged particles during diffusion becomes important, i.e. space charge effects (discussed in the next chapter). Ionization densities of about 10^7-10^8 cm^{-3} are obtained, for example, when a 26 MeV ^{58}Ni beam with the intensity of 10^4-10^5 pps enters the gas cell filled with 500 mbar argon.

As a measure of diffusion one can calculate the root-mean-square (rms) displacement of an ion during a given time t

$$x_D = \sqrt{2\mathcal{D}t}. \tag{3.24}$$

The evacuation time of a helium filled gas cell is about 50 ms, while for the argon case it is in the range of 300-500 ms. Thus, in both buffer gas types the rms-displacement of an ion during its journey to the exit hole, is at maximum 2 mm. Even in the case of ambipolar diffusion, the rms-displacement is about 3 mm, and compared with the dimensions of the gas cell, one can state that not the diffusion itself is a problem, but the initial distribution of ions in the gas cell. Not of less importance is the size of the ion cloud as the mutual repulsion of the ions may lead to an expansion of spatial distribution of ions. This will be discussed in the next chapter.

3.10 Reaction of ions with impurity molecules

In on-line conditions, the majority of produced ions by the primary beam impact are neutralized during their journey to the exit hole of the cell. However a fraction of them is surviving the thermalization process, and thus they can be mass separated and measured. The reaction products recoiling out from the target experience the same effect, and when most of them arrive in atomic form in the vicinity of the exit hole, they are resonantly laser ionized.

During their transport in the gas cell, the ions are colliding with buffer gas atoms and impurity molecules and can interact with electrons, all these leading eventually to neutralization and thus losses of the ion signal or to formation of molecular ions.

The most abundant impurity molecules in helium and argon gas cylinders as quoted by the manufacturer [AirPr] are given in Table 3.6. The gas is additionally purified before flowing into the gas cell, thus the actual level of impurities in the gas cell is reduced approximately two orders of magnitude compared to the values given in Table 3.6.

Table 3.6: The concentration level of impurities in helium and argon gas as certified by the manufacturer [AirPr].

Gas	Maximum impurities Components	(vppm)*
He 6.0	O_2	0.1
	N_2	0.1
	$CO + CO_2$	0.1
	CH_4	0.1
	H_2O	0.5
Ar 6.0	O_2	0.1
	N_2	0.3
	$CO + CO_2$	0.05
	CH_4	0.05
	H_2O	0.5

* volumetric parts per million

Apart from recombination processes, another possible loss processes of ions in the gas may be:

(I) Molecular ion formation
$X^+ + M \rightarrow XM^+$,

(II) Charge-exchange reaction with atoms or molecules
$X^+ + M \rightarrow X + M^+$,

(III) Charge transfer in dissociation of a molecule
$X^+ + B_iD_j \rightarrow X + B^+ + B_{i-1}D_j$

In the process of type (I) an ion X^+ interacts with a molecule M and in the final state they share an electron by forming the molecular ion XM^+. It is worth to note that molecular ions extracted from the gas cell can be dissociated by the DC voltage applied between the cell and SPIG rods (see section 2.3.3), thus the ions of interest can be re-gained. In the reaction of type (II) the ion X^+ transfers its charge, during

TABLE 3.7: Reaction rate constants and time constants of some ions with impurity molecules at 300K. The time constants are based on an impurity concentration of 1ppb in the main gas (He or Ar) at 1 bar pressure. When the column of the product ions is blank, the total reaction rate constant is given.

Crt.	Reaction	Product Ions	$\mathbf{k}$ (cm^3s^{-1})	τ (s)	Reference
1.	$He^+ + N_2$	N_2^+	5.0×10^{-10}	0.074	[Son92]
2.	$He^+ + O_2$		8.0×10^{-10}	0.046	[Rak78]
3.	$He^+ + CO_2$		10.0×10^{-10}	0.037	[Rak78]
4.	$He^+ + CH_4$		16.0×10^{-10}	0.023	[Rak78]
5.	$Ar^+ + O_2$	O_2^+	4.30×10^{-11}	0.867	[Coo93]
6.	$Ar^+ + H_2O$	H_2O^+	1.50×10^{-10}	0.247	[Lin73]
7.	$Ar^+ + N_2$	N_2^+	3.70×10^{-12}	10.08	[Coo93]
8.	$Ar^+ + CO_2$	CO_2^+	5.60×10^{-10}	0.066	[Rak78]
9.	$Ar^+ + H_2O$	ArH^+	1.31×10^{-9}	0.028	[Lin73]
10.	$Ti^+ + O_2$	TiO_2^+	4.6×10^{-10}	0.080	[Koy02]
11.	$Co^+ + O_2$	CoO_2^+	1.5×10^{-13}	247	[Koy02]
12.	$Ni^+ + O_2$	NiO_2^+	2.0×10^{-13}	185	[Koy02]
13.	$Nb^+ + O_2$	NbO^+	4.3×10^{-10}	0.086	[Koy02]
14.	$Mo^+ + O_2$	MoO^+	7.5×10^{-11}	0.493	[Koy02]
15.	$Ru^+ + O_2$	RuO_2^+	1.7×10^{-13}	218	[Koy02]
16.	$Rh^+ + O_2$	RhO_2^+	9.2×10^{-14}	402	[Koy02]

a collisional process, to a molecule(atom) (see previous section). Process of type (III) proceeds through dissociation of the poly-atomic molecule B_iD_j and transfer of the charge from the ion X^+ to one of the dissociation products. If one denote by $[X^+]$ the concentration of some ionic population and by $[M]$ the concentration of molecular (atomic) reactant, the number of ions ($cm^{-3}s^{-}1$) changing to molecular ions or neutrals by one of the reactions (I-III) can be described by

$$\frac{dX^+}{dt} = -\mathbf{k}[X^+][M] \tag{3.25}$$

where $\mathbf{k}$ is a reaction constant rate (in cm^3/s) characteristic for a specific process of type (I-II). A time constant for neutralization or formation of the molecular ion XM^+ can be defined as

$$\tau = \frac{1}{\mathbf{k}[M]}. \tag{3.26}$$

In Table 3.7 reaction rate constants and time constants of some ions with impurity molecules at 300K are given. In a complete description of the evolution of a particular species of molecular ion eventually formed in the gas cell, one has to consider both the formation and the destruction of it. Molecular ions at their turn can recombine via a two- or three-body reaction or they can further react with impurities forming higher order products.

Constant rates are given in Table 3.8 for some secondary and higher order

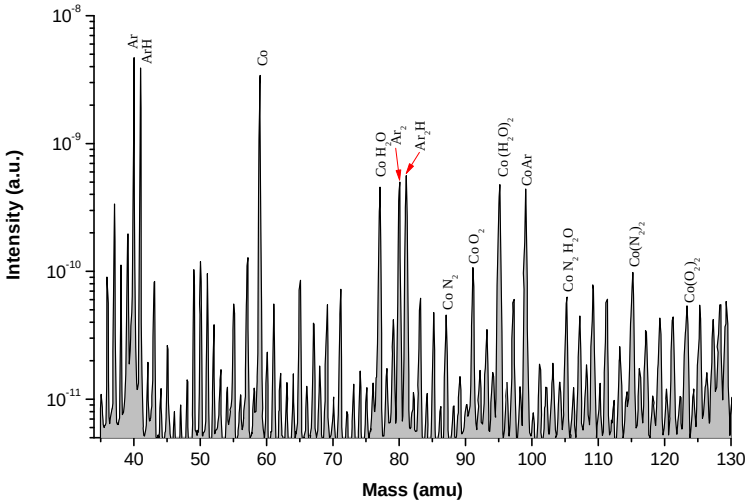

Fig. 3.15: Mass scan of the extracted beam from the ion source taken on-line with a Co filament in the gas cell, lasers on tuned to ionize Co (50 Hz pulse repetition rate) and a 30 MeV proton beam passing through the gas cell. Two 10 mg/cm^2 ^{238}U targets were mounted in the cell at 20° with respect to the cyclotron beam direction. The dissociation voltage between gas cell exit and SPIG rods was off. Note the log vertical scale.

reaction channels of molecular ions. With the reaction rates from Tables 3.7 and 3.8 the evolution of buffer gas ions becomes a complicated puzzle. In on-line conditions, dissociation of molecular ions by the primary beam impact is also possible, therefore reaction channels can be interrupted.

It is possible to compare recombination and ion-molecule interaction time scales with the evacuation time of the gas cell. If one takes an initial ionization rate of 10^{10} electron-ion pairs/cm^{3}s in Ar, the equilibrium charge density, as controlled by the dimerization and recombination processes, is $[Ar_2^+] \simeq 3 \times 10^8$ cm^{-3}. When the primary beam is switched off the recombination and ion-molecule reaction processes decrease the charge density. The half-life for recombination $t_{1/2}^R$ is only 4 ms. Taking an impurity level of 1 ppb and an ion-molecule reaction rate constant of 10^{-10} cm^3/s, the half-life for molecular ion formation becomes $\sim$ 500 ms which is comparable with the evacuation time of the gas cell by flow ($\sim$ 500 ms). Thus, the evacuation and molecular ion formation time scales are appreciably long compared to the recombination time scale. However, in on-line experiments strong molecular peaks are observed in the mass spectra when no dissociation voltage is applied. This suggests that either the impurity level is higher than 1 ppb, or the molecular ions are formed close to the exit hole of the gas cell or in the gas jet leaving the ion source. If one takes an impurity level of 1 ppm, with the above reaction rate constant, the half-life for molecular formation becomes 500 μs. An example of a

TABLE 3.8: Rate constants for some secondary and higher order reaction channels of molecular ions with impurity molecules or electrons at 300K.

Crt.	Reaction	Type	Product	**k** (cm^3s^{-1})	Reference
1.	$ArH^+ + H_2O$	Ion-molecule reaction	H_3O^+	4.5×10^{-9}	[Lin73]
2.	$NbO^+ + O_2$	O atom addition	NbO_2^+	4.1×10^{-10}	[Koy02]
3.	$NbO_2^+ + O_2$	O_2 addition	NbO_4^+	1.9×10^{-12}	[Koy02]
4.	$MoO^+ + O_2$	O atom addition	MoO_2^+	5.8×10^{-10}	[Koy02]
5.	$MoO_2^+ + O_2$	O_2 addition	MoO_4^+	4.1×10^{-12}	[Koy02]
6.	$RuO_2^+ + O_2$	O_2 addition	RuO_4^+	1.3×10^{-12}	[Koy02]
7.	$RhO_2^+ + O_2$	O_2 addition	RhO_4^+	3.2×10^{-13}	[Koy02]
8.	$H_2O^+ + H_2O$	Ion-molecule reaction	H_3O^+	1.3×10^{-9}	[Lin73]
9.	$H_3O^+ + e^-$	Charge exchange	H_2O	1.1×10^{-6}	[Lin73]
9.	$CO_2^+ + e^-$	Dissociative recombination	CO+O	5.65×10^{-7}	[Sei03]

mass scan of the extracted beam from the ion source taken on-line is shown in Fig.3.15. In that measurement a Co filament in the gas cell was heated and the lasers were tuned to ionize Co atoms. A 30 MeV cyclotron proton beam (260 pnA) passed through the gas cell filled with 500 mbar Ar. Two targets (10 mg/cm^2 ^{238}U) were mounted on the entrance- and exit-flange, respectively, at 20° with respect to the cyclotron beam direction (as in the fission ion guide - see Fig.2.5). Many peaks in the mass spectrum can be seen and their assignment is not necessarily unambiguous. A precise assignment would require further checks by adding known proportions of an impurity (e.g. O_2, N_2, H_2O) in the buffer gas as well as looking to the time-behavior of the signal at a specific mass. The Ar^+ and Ar_2^+ ion signals are the result of the ionization of buffer gas atoms by the proton beam and the dimerization process of argon ions with argon atoms (as explained in section 3.7), respectively.

3.11 Summary

A gas cell filled with noble gas can be used to stop nuclear reaction products from heavy-ion fusion-evaporation, fragmentation and fission reactions after in-flight separation. High-energetic beams with large divergence can thus be converted into low-energetic ones for precision experiments or subsequent post-acceleration. Due to its higher stopping power, argon gas can ensure an efficient stopping of nuclear reaction products in a relatively small volume cell. Due to its higher ionization energy helium is often preferred in the target-ion catcher systems as it can be more effective than argon in thermalization of reaction products in ionic state. However, the lower stopping power of helium imposes actual limitations of the size of a gas cell used for stopping nuclear reactions products.

In on-line experiments performed at the LISOL laser ion source the primary projectile beam impinging on the target passes through the gas cell. Apart from the ionization produced by the slowing down and eventually stopping of the nuclear reaction products, a high ion-electron density is created by the primary particle beam. This causes additional recombination losses of laser-produced ions. Furthermore ionization of the buffer gas also leads to chemical reactions of impurity molecules with beam created ions. The consequence of the use of a gas cell for production of radioactive beams with a laser ion source is that during the primary projectile beam passage through the buffer gas (beam-on period) a high-density of electron-ion pairs is created, and subsequent neutralization of most of the created pairs and ions of interest in a beam-off period can take place. Laser ionization of the species of interest can be applied in a zone where ion-electron pair density is low enough and the laser-produced ions have a high survival chance against recombination. The evacuation time of the gas cell should be longer than the recombination time constant to obtain neutralization, but the evacuation time of the laser-produced ions should be shorter than the respective recombination time. Additional losses of the ions of interest (laser produced or surviving ions) can occur through the formation of molecular ions with impurity molecules present in the buffer gas. Molecular ions rapidly undergo a dissociative process. The evacuation and molecular formation time scales are appreciably long compared to the recombination time scale. However, the impurity level in the buffer gas can dramatically affect the time scale for formation of molecular ions. Even though molecular ions extracted from the LISOL gas cell can be dissociated between the exit hole and the SPIG rods, the buffer gas purity in an ion gas-catcher system is an essential issue and an impurity level as low as possible is desirable.

Chapter 4

Electric fields in the gas cell

A fast way to transport ions in a gas cell is by using electrical fields inside the gas cell. An electrical field is applied along the extraction axis of the gas cell in order to drag the ions towards an exit hole. Radial RF electrical fields may be used in order to keep the ions confined in the gas volume and to minimize the losses to the walls. Using only DC electrical fields the setup is very similar to an ionization chamber for detection of ionizing radiation, called the *drift gas cell*. The only difference here with the well-studied cases of drift gas cell and an ionization chamber is the continuous flow of the gas.

This chapter provides a comprehensive study of the behavior of electrons and ions in a gas cell using DC electrical fields. An effective collection of the electrons produced by the primary beam in the gas cell, i.e. stopping of initial and volume recombination processes, can lead to an enhancement of the ion survival chance against recombination and an efficient release of the ions from the gas cell. A practical limit is encountered when the space charge induced voltage completely counteracts the applied voltage on the electrodes collecting the electrons. An important section of this chapter concerns the space charge effect in connection with the theoretical formalisms used to describe it and the direct application to the gas cells and electrode configurations used at the LISOL laser ion source. Conclusions are drawn on the maximum intensity of the incoming ion beam. Additional limitations introduced by the mutual Coulomb repulsion among ions and "plasma effects" are discussed.

4.1 Drift of electrons and ions

In the majority of practical cases most, but not all, of the positive ions are singly ionized, so that in an electric field they will be accelerated by an acceleration $\dot{v}$ where

$$\dot{v} = \frac{e \cdot E}{m} \tag{4.1}$$

e being the electron charge ($1.6{\cdot}10^{-19}$ C), E the electric field and m the mass of the ion. In a gas, the accelerated particle loses energy by collisions with gas atoms; v, known as *drift velocity*, is measured in the direction of the electric field. In the case of a mixture of electrons and ions, it may at once be pointed out that electron drift velocities will be several orders of magnitude higher than those of positive ions.

The mobility μ of a particle is defined as the ratio of its velocity in field direction to the magnitude of the field intensity, or the drift velocity per unit applied field. Thus for any particle

$$\mu = \frac{v}{E} \quad (\mathrm{cm}^2/\mathrm{V{\cdot}s}). \tag{4.2}$$

Since the mean free path λ is inversely proportional to the pressure p of the gas, μ will be inversely proportional to p [Nas71]:

$$\mu = \alpha \frac{e}{8\sqrt{\pi m}} \frac{(kT)^{1/2}}{r^2 p} \tag{4.3}$$

where T is the temperature of the gas, k is the Boltzmann's constant, r is the ionic or molecule radius and α represents a particular method of averaging and lies between 0.6 and 1. However, eq.(4.3) does not allow to determine the mobility of a certain ion within molecules of a different gas. Langevin has obtained the relation for the mobility of an ion in a "foreign" gas [Nas71]:

$$\mu = 0.815 \frac{e\overline{\lambda_i}}{M\overline{v}} \sqrt{\frac{m+M}{m}} \tag{4.4}$$

where m and M are the masses of the ion and the gas molecule, respectively, $\overline{\lambda_i}$ is the mean free path of the ion in the gas and $\overline{v}$ is the mean random velocity of the gas particles.

TABLE 4.1: Measured mobility of some ions in various gases at 1 atm pressure, in units of $\mathrm{cm}^2/\mathrm{V{\cdot}s$ [Nas71, Sau91].

\ Ion Gas\	H^+	He^+	Li^+	O^+	Na^+	Ar^+	K^+	Rb^+	Cs^+	Hg^+
H_2	13.0	-	13.3	-	13.6	-	13.5	13.4	13.4	-
He	-	10.2	25.3	-	23.2	-	22.4	21.0	19.0	19.6
Ne	-	-	14.35	-	9.0	-	8.0	7.18	6.58	5.95
N_2	-	-	4.21	-	3.0	-	2.7	2.39	2.25	-
O_2	-	-	-	2.2	-	-	-	-	-	-
Ar	-	-	4.99	-	3.22	1.7	2.78	2.39	2.24	1.84

Some experimental values of the mobility μ of different ions in various gases at 1 atm pressure are given in Table 4.1. The values tabulated are obtained at temperature of 0°C, thus to obtain the mobility at any given temperature and pressure one has to apply:

$$\mu_+ = \mu_0 \frac{T}{p \times 273} \tag{4.5}$$

provided that μ_0 are the mobilities given in Table 4.1, p is the pressure in atmo-

sphere and T is the temperature in K. As one can see from eq.(4.2) and eq.(4.5), the mobility has an E/p dependence, which is a consequence of the fact that the average energy of the ions is almost constant during its drift to the cathode electrode. Only at very high electric fields this dependence changes to $\sqrt{E/p}$. In order to account for the mobility dependence on the ratio of the field intensity over the pressure, the *reduced field strength* E/N has been introduced (with N the density number of the gas), with as unit - the Townsend (1 Townsend = 10^{-17} V cm^2).

The situation is quite different for electrons. The mobility of electrons is not constant as their energy increases, in between collisions with gas molecules, under the influence of electric field. Table 4.2 gives the measured electron drift velocities in helium, taken from reference [Eva74]. The mobility of electrons is several orders

Table 4.2: Measured electron drift velocities in helium, as presented in [Eva74].

E (V/cm)	E/N (Townsend) @ 0.5 atm	v_- (cm/s)
10	0.082	1.1 $\times 10^5$
50	0.41	3 $\times 10^5$
250	2.05	6 $\times 10^5$
500	4.1	1 $\times 10^6$
1000	8.2	1.8 $\times 10^6$

of magnitude higher than the mobility of positive ions. Of prime importance to keep this fast drift is to prevent negative ion formation as those ions move with the speed of positive ions and thus some 1000 times slower than the electrons. Such negative ions can be formed when impurities, such as O_2 for example, are present in the gas. However, attachment of electrons to Oxygen molecules is negligible over the drift region and occurs primarily in dead zones, i.e. field free zones, where the electrons reside for a greater time [Zwa03]. There, the electrons will attach with a time constant $\tau_{attach} = (67/\varrho)$ ms, where ϱ is the impurity level in ppm. For this reason O_2 and water impurities should be kept below the ppm level (see also section 2.3.2). This has been achieved at LISOL facility where the buffer gas is purified down to sub-ppb level [Kud96, Kud01].

4.2 Charge collection in the gas cell

In ionization chambers one is interested in collecting all the charges created by the ionizing radiation. In the application for slowing down and transporting radioactive ions one is in fact only interested in the radioactive ion. All other ion-electron pairs, created in the slowing down process, are rather a nuisance but it is difficult to discriminate the two kinds of ions and therefore one has also to take into account all created charges. A schematic view of an ionization chamber is shown in Fig.4.1 together with a typical $I - V$ characteristic, i.e. the plot of the collector current I measured on the electrodes as function of the applied difference voltage V between them [Leo87]. In order to have a good intensity and deposited energy determination, no recombination of the positive and negative charges should occur.

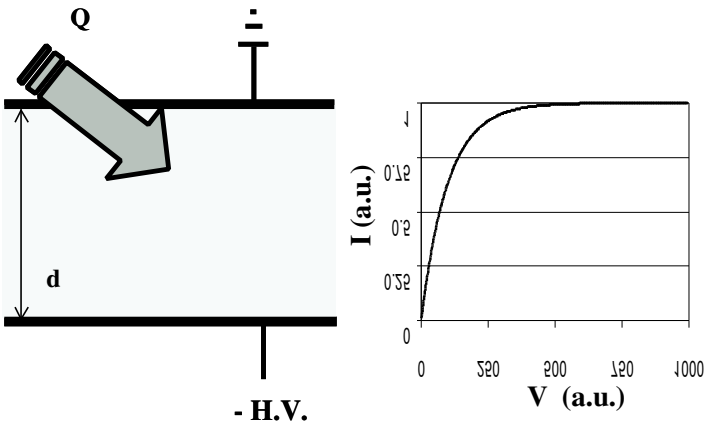

FIG. 4.1: A schematic view of a gas-filled ionization chamber. A beam with an ionizing rate Q enters the gas cell and the created ions and electrons will be collected on the respective electrodes. At low electrode voltage, the recombination rate will be high. But eventually at the so-called saturation voltage, the collected current will reach its maximum and all charges are collected.

The most important loss factor of ions in a gas cell which does not make use of electrical fields will be the neutralization due to recombination (see section 3.6). In an ionization chamber, two types of recombination are considered: columnar or initial recombination where the ion recombines with an electron from the same track, and volume or general recombination where the ion recombines with an electron from a different track.

4.3 Columnar (initial) recombination

It is possible to estimate the intensity of the electric field needed to separate the electrons from the ions[Mus78]. The average separation d_i between the positive ions having a density n_i, is roughly

$$d_i \approx (n_i)^{-1/3}. \tag{4.6}$$

This is also the average separation between electrons, provided that the densities of ions and electrons are equal. Thus, the Coulomb force F_C acting between an ion-electron pair is

$$F_C \approx \frac{1}{4\pi\epsilon} e^2 (n_i)^{2/3}. \tag{4.7}$$

with ϵ the di-electric constant of the gas ($\epsilon \cong \epsilon_0$, the di-electric constant for vacuum) and e is the electron charge.

The field needed to produce an equal and opposite force is then

$$\frac{V_t}{d} \approx \frac{1}{4\pi\epsilon_0} e (n_i)^{2/3}. \tag{4.8}$$

TABLE 4.3: Field strengths needed to produce a repulsive force counteracting the attractive Coulomb force between ions and electrons at a given density $n_+ = n_- = n_i$.

n_i (cm^{-3})	10^3	10^5	10^7	10^9	10^{11}	10^{13}
V_t/d (V/cm)	$1.44{\cdot}10^{-5}$	$3.11{\cdot}10^{-4}$	$6.69{\cdot}10^{-3}$	$1.44{\cdot}10^{-1}$	3.11	66.9

Table 4.3 gives an estimation of the field strengths needed. Even at high ion-electron densities, the field strengths required are moderate. However the above argument does give only a static description of the problem and time dependent considerations should be implemented.

At low ionizing radiation intensities moderate sweeping voltages are needed to reduce the volume recombination. For applied voltages higher than V_t from eq.(4.8) the columnar recombination is dominant, and the volume recombination (see next section) is negligible. The degree of (initial) columnar recombination in high pressure gases depends on the ion density along the tracks of the primary and secondary charged particles and hence can be related to the linear energy transfer. For highly ionizing particles the saturation voltage, from where on all charges are collected (see Fig.4.1) and the columnar recombination losses become negligible, will be element- and energy-dependent. This will lead to a characteristic $I-V$ plot and this principle is presently used in modern dosimetry detectors called *recombination detectors* [Zie96, Kan98]. In such a device an appropriate set of collecting voltages is sequentially applied to the chamber electrodes during the irradiation. Ions which escape columnar recombination are collected on the electrodes. The radiation dose is then determined from the collected charge applying a correction for the columnar recombination which is dependent on the linear energy transfer.

4.4 Volume recombination

The volume recombination represents the recombination process which allows neutralization of ions with electrons from different projectile tracks. An ionization track has typically a diameter of 100 μm [Sau91]. The ion cloud and the electron cloud from a single track move under the influence of an electric field in opposite directions. As the electron velocity direction is fastly randomized by collisions with neutrals, at high ionization rates one electron can encounter positive ions from different tracks and recombine. The average inter-ionic distance (eq.(4.6)) decreases with the increase of the ionizing radiation intensity. The reduced inter-ionic distance acts to enhance the volume recombination on account of an increased Coulomb interaction (eq.(4.7)). This indicates that the volume recombination should increase with the ion-number density in the manner as eq.(4.7). According to Sharpe [Sha64] and later also Colmenares [Col74] the recombination loss f in parallel plate ionization chambers (see Fig.4.1) can be estimated as

$$f = \frac{Q\alpha d^2}{6v_+v_-} \tag{4.9}$$

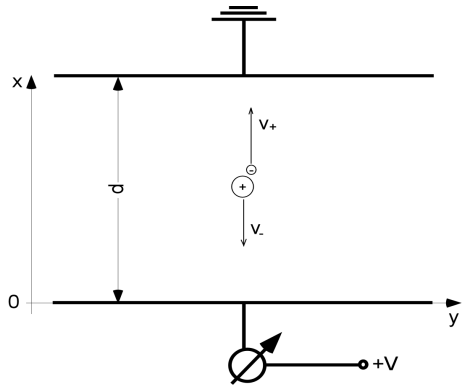

FIG. 4.2: A schematic view of a parallel plate ionization chamber. A beam of ionizing particles produces uniformly distributed electron-ion pairs, with the rate Q, and the created ions and electrons will be collected on the respective electrodes. The anode is positioned at $x = 0$ and the cathode at $x = d$, respectively. An Ampère-meter is inserted in the circuit.

with d the spacing of the electrodes (cm), α the recombination coefficient (cm^3s^{-1}) and Q the ionizing rate ($cm^{-3}s^{-1}$). As one can immediately see from eq.(4.9) the volume recombination is ionization rate dependent. Using the values for ion and electron mobility from Tables 4.1 and 4.2 and an ion-electron recombination coefficient $\alpha = 1.71 \cdot 10^{-7}$ cm^3s^{-1} characteristic for 1 atm of He (see Table 3.3 in Chapter 3), the losses can be calculated in function of the electrical field strength (see Table 4.4).

Inspecting Table 4.4 shows that for all configurations considered quite high ionization rates can be accepted by the ionization chamber provided large field strengths are used. However, this brings us to another limiting factor namely *space charge* effects resulting from the high density of positive ions.

4.5 Space charge effect

It has been argued before that the electrons are drifting several orders of magnitude faster than the positive ions in a gas subjected to an electric field. Therefore, when an electric field is applied in the gas chamber in order to collect the charges, an uncompensated slowly moving positive charge is left behind by the fast drifting electrons [Pal99].

Quantitatively, this positive charge, called *space charge*, is described by its density number n_+ (in ions/cm^3), which, as it will be shown later, has a time and position dependence. A schematic view of a parallel plate ionization chamber is shown in Fig.4.2. The electrode positioned at $x = 0$ is positively biased and the electrode at $x = d$ is kept grounded.

In the case of an uniformly distributed ionization rate Q in the gap of the electrodes, the basic set of equations describing the space charge density evolution

Table 4.4: Volume recombination losses in parallel plate ionization chamber filled with 1 atm helium (μ_0 = 10.2 cm^2/V·s) as a function of the ionization rate Q, the applied electrical field E and the distance d between the plates.

			Q (cm^{-3}s^{-1})					
			$d = 1cm$		$d = 10cm$		$d = 50cm$	
E (V/cm)	v_{ion} (cm/s)	v_{elec} (cm/s)	1% loss	10% loss	1% loss	10% loss	1% loss	10% loss
10	1.0 10^2	1.1 10^5	3.9 10^{12}	3.9 10^{13}	3.9 10^{10}	3.9 10^{11}	1.6 10^9	1.6 10^{10}
50	5.1 10^2	3.0 10^5	5.4 10^{13}	5.4 10^{14}	5.4 10^{11}	5.4 10^{12}	2.1 10^{10}	2.1 10^{11}
250	2.6 10^3	6.0 10^5	5.4 10^{14}	5.4 10^{15}	5.4 10^{12}	5.4 10^{13}	2.1 10^{11}	2.1 10^{12}
500	5.1 10^3	1.0 10^6	1.8 10^{15}	1.8 10^{16}	1.8 10^{13}	1.8 10^{14}	7.1 10^{11}	7.1 10^{12}
1000	1.0 10^4	1.8 10^6	6.4 10^{15}	6.4 10^{16}	6.4 10^{13}	6.4 10^{14}	2.6 10^{12}	2.6 10^{13}

and its effect, is:

$$\frac{\partial E}{\partial x} = \frac{\rho_+}{\epsilon}, \tag{4.10}$$

$$\frac{\partial \rho_+}{\partial t} + \frac{\partial(\rho_+ v_+)}{\partial x} = Qe \tag{4.11}$$

where $\rho_+ = e \cdot n_+$ is the charge density (in C/cm^3), e is the elementary charge and ϵ is the di-electric constant of the gas. Eq.(4.10) is the well-known Poisson equation and eq.(4.11) is the charge conservation law. All electrons are considered to be immediately collected at the anode.

Velissaris has derived the mathematical formalism for the time development of the space charge in a parallel plate detector [Vel02]. Considering intense beam spills (pulses of several micro-seconds) irradiating an ionization chamber, one can assume that during the beam-on period the positive ions are practically immobile, and their spatial distribution is dictated by the ionizing source distribution and not by the applied electric field. This is true at least for some time at the beginning of the external ionization, as predicted by the short pulse approximation [Vel01]. Combining eqs.(4.10) and (4.11) with $v_+ = \mu_+ E$ and recalling that ρ_+ is independent on x, the space charge density can be found by solving the equation

$$\frac{\partial \rho_+}{\partial t} = Qe - \frac{\mu_+}{\epsilon}\rho_+^2, \tag{4.12}$$

which after integration over a time interval $(0, t)$ issues

$$\rho_+(t) = \frac{1 - e^{-2\chi t}}{1 + e^{-2\chi t}} \sqrt{\frac{Qe\epsilon}{\mu}}, \tag{4.13}$$

where $\chi = \sqrt{Qe\mu/\epsilon}$. Eq.(4.12) satisfies the initial condition of zero space charge at $t = 0$ (when the ionization begins). The validity of this solution lasts as long as the *saturation free* condition is fulfilled, i.e. the space charge is space independent as it consists of slow moving ions. This is true at least for some time at the beginning of the external ionization. According to Velissaris [Vel01], the saturation free condition in a parallel plate geometry is

$$\frac{V_0}{d^2} \geq \frac{\rho}{2\epsilon}. \tag{4.14}$$

If one considers a parallel plate ionization chamber with the electrodes spacing $d = 2$ cm and a voltage difference $V_0 = 200$ V applied between them, the saturation free state lasts only 55 μs when the ionization rate is $Q = 10^{10}$ cm^{-3}s^{-1}. Therefore the dependence of the space charge density as given by eq.(4.12) is appropriate only for the case when the ionization occurs in very short pulses.

For the case of ionizing pulses in the domain of milliseconds, the time dependence of the space charge density vanishes after a time period, which in a plane parallel geometry, is proportional to the distance between the electrodes (d) and inverse proportional to the drift velocity of the positive ions (v_+), thus independent on the ionizing rate Q:

$$t_{sat} = \frac{\overline{\rho_+}}{Q} \simeq \frac{d}{v_+}. \tag{4.15}$$

Table 4.5 gives the values of the saturation time t_{sat} of the space charge density in three different plane parallel configurations at field strength values of 10, 50, 100 and 200 V/cm for ionization chambers filled with 500 mbar helium and argon,

Table 4.5: The saturation time of the space charge density in three different plane parallel configurations, both for the case of helium and argon filled ionization chambers. The drift velocity of ions is taken as for 500 mbar gas pressure.

	$t_{sat}(s)$					
E	d = 1 cm		d = 10 cm		d = 50 cm	
(V/cm)	He	Ar	He	Ar	He	Ar
10	$4.9\ 10^{-3}$	$3.0\ 10^{-2}$	$4.9\ 10^{-2}$	$2.9\ 10^{-1}$	$2.4\ 10^{-1}$	1.5
50	$9.0\ 10^{-4}$	$6.0\ 10^{-3}$	$9.8\ 10^{-3}$	$5.9\ 10^{-2}$	$4.9\ 10^{-2}$	$2.9\ 10^{-1}$
100	$4.9\ 10^{-4}$	$3.0\ 10^{-3}$	$4.9\ 10^{-3}$	$2.9\ 10^{-2}$	$2.4\ 10^{-2}$	$1.5\ 10^{-1}$
200	$2.5\ 10^{-4}$	$1.9\ 10^{-4}$	$2.4\ 10^{-3}$	$1.5\ 10^{-2}$	$1.2\ 10^{-3}$	$7.3\ 10^{-2}$

respectively. From Table 4.5 one can observe that in small systems the space charge saturation is reached within very short time periods. For the case of a gas cell, it is legitimate to compare t_{sat} with the evacuation time of the chamber. The evacuation time depends on the gas type and geometry [Kud96]. For the gas cell used at LISOL the evacuation time by gas flow amounts to $\sim$ 300 ms for an argon filled chamber, and $\sim$ 10 ms for a helium filled gas cell, respectively. These evacuation times are much longer than the time that space charge needs to reach its steady state provided the electrode spacing is less than a few centimeters. Therefore, it is realistic to neglect the time dependence of the space charge in such a system. For a gas cell with larger dimensions (used here as an ion collector) resolving the equations describing the space charge evolution (eqs.(4.10) and (4.11)) both time and position dependence must be taken into account, thus a dynamic description of the space charge is appropriate.

In what follows the time dependence of the space charge built-up will be neglected and one will assume steady state condition. The mathematical formalism for the description of the steady state of the space charge can be found in ref.[Boa52, Pal99] for a plane parallel geometry and in ref.[Boa63, Nov96, Pou99] for a cylindrical geometry. The effect of the space charge consists in the occurrence of an electric field opposite to the applied electric field, due to the accumulation of positive charges in the gap between the electrodes. When the electric field produced by the space charge at the anode electrode equals the applied field, the limiting situation is reached, i.e. space charge limit, in which the net field at the anode is zero, thus electrons are not anymore collected in its vicinity. Recombination processes take over in this zone and if the intensity of the ionizing source is increased, the region where the net field is zero acquires a finite width, called the field free region.

The net electric field in a parallel plate ionization chamber (as shown in Fig.4.2), is given by [Pal99]

$$E(x) = \sqrt{E_a^2 + \frac{Qe}{\epsilon\mu_+}x^2} \tag{4.16}$$

where E_a represents the net electric field at the anode electrode for a given uniform ionization rate Q. The net electric field at the anode E_a is determined by the boundary condition placed by the applied voltage V_0:

$$V_0 = \int_0^d E(x)dx. \tag{4.17}$$

The space charge density is found from eq.(4.10) with the expression from eq.(4.16) for the net electric field inside the gap of the electrodes

$$\rho_+(x) = \frac{Qex}{\sqrt{E_a^2 + Qx^2/(\epsilon\mu_+)}}. \tag{4.18}$$

Sharpe [Sha64] calculates the voltage induced by the slowly moving positive ions in an ionization chamber and thus screening the applied electrical field. The electrons are assumed to be collected immediately. For a parallel plate chamber the following equation is derived:

$$V_{ind} = \sqrt{\frac{eQ}{4\epsilon_0\mu_+}d^2}. \tag{4.19}$$

Using the value for the He ion mobility from Table 4.1, the ionizing rate Q can be calculated where the space charge induced voltage V_{ind} equals the bias voltage V_0 for three values of d and in function of the electrical field strength (see Table 4.6). By comparing Tables 4.4 and 4.6 is is clear that space charge limitations

TABLE 4.6: The ionizing rate Q is given[a] for which the field strength induced by the space charge effects equals the applied field strength. Three different distances between the parallel electrodes are given.

	$Q(V_0 = V_{ind})$ (ion-electron cm^{-3}s^{-1})		
E (V cm^{-1})	d = 1 cm	d = 10 cm	d = 50 cm
10	2.3 10^9	2.3 10^7	9.0 10^5
50	5.6 10^{10}	5.6 10^8	2.3 10^7
100	2.3 10^{11}	2.3 10^9	9.0 10^7
250	1.4 10^{12}	1.4 10^{10}	5.6 10^8
500	5.6 10^{12}	5.6 10^{10}	2.3 10^9
1000	2.3 10^{13}	2.3 10^{11}	9.0 10^9

[a] Eq.(4.19) for He as gas (μ_+ = 10.2 cm^2/V s) is used.

are occurring already at lower rates than those where volume recombination losses become important. The effect of space charge is that the net field that the ions do feel will decrease leading to a reduced velocity and thus a higher space charge. Furthermore the net field felt by the electrons will also decrease and the basic assumption that the electrons are collected immediately can be questioned as the electron velocity will be reduced. Two effects are the result: the simple eq.(4.19) is not anymore valid and secondly neutralization according to eq.(4.9) will become more important as the electron- and ion drift velocity will decrease. The values from Table 4.6 give thus only a rough estimate which field strengths should be used for a given ionization rate in order to minimize recombination effects.

Plane parallel ionization chambers have been developed for precise beam monitoring of synchrotron radiation [Ahm00, Sat97] and of high-energetic ($\sim$ GeV/nucleon) p, d and α beams [Sug96]. In the first case, X-ray photon (around 20 keV) rates up to 10^{12} photons/s were directed to the chamber (1 atm Ar) creating ionization

currents up to the 0.1 mA level. High beam intensities could also be measured in the second case: up to 10^{11} protons per spill (1 spill every 1.5 s). In Fig.4.3, some saturation field strengths are given as function of the the ionization rate Q for the three ionization chambers. The saturation field strength is the electrical field strength in which for a given incoming beam intensity the measured current saturates (see Fig.4.1). This does not mean that the ionization chamber has no recombination losses anymore and different methods can be used to determine the saturation current [Mus78]. However, for the discussion presented here, the saturation voltage is deduced from inspecting the I-V (current versus voltage) plots presented in different articles. In all cases, the gas was argon but similar values for other gases are also presented in [Sat97]. The distance between the two parallel plates varied from 0.8 to 1.25 cm, thus in the range of the 1 cm arrangement presented in Table 4.6. All measurements do show a square-root dependence of Q, the ionizing rate, as expected from eq.(4.19). In order to show this behavior, the calculation for different electrode distances of the induced voltage by space charge effects given by eq.(4.19) and using the mobility coefficient for Ar (see Table 4.1)

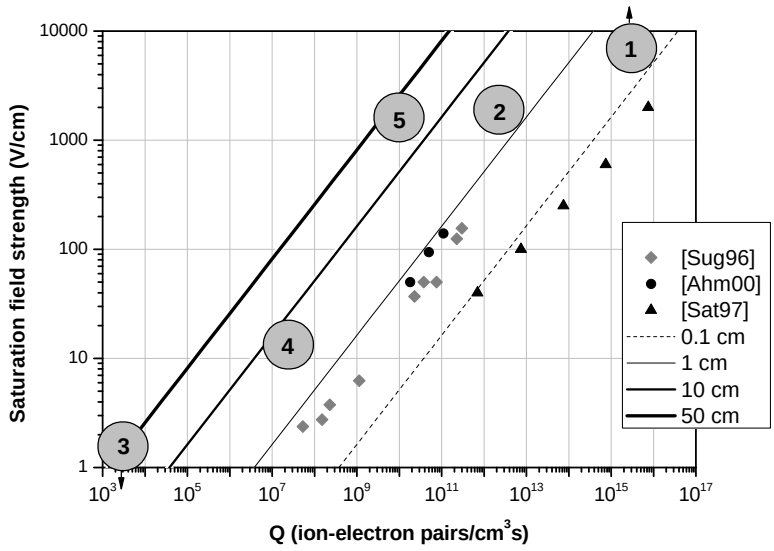

Fig. 4.3: The field strength needed to reach the plateau in the I-V plot is given as function of Q, the ionizing rate for three different ionization chambers filled with argon as buffer gas (diamonds, circles and triangles refer respectively to the work of Sugaya et al. [Sug96], Ahmed et al. [Ahm00] and Sato et al. [Sat97]). Also given is the calculated field strength for a number of electrode distances as function of Q using eq.(4.19) for Ar ($\mu_+ = 1.7$ cm^{2}V^{-1}s^{-1}). The five cases, given in Table 4.7 and discussed in ref. [Huy02] are also given; note that for case 4 and 5 helium is used as buffer gas and therefore the results from Table 4.6 are used.

TABLE 4.7: The number of ion-electron pairs created per cm^3 and per s in a gas cell by passage of different beams. The dimensions of the gas cell have been adapted to the reactions. The p-induced fission relates to the work at Leuven [Kud96] and Jyväskylä [Den97] where the primary beam is shielded from the gas cell with a thin foil. The ^{242}Am refers to the work of Mainz [Bac97], also here the primary beam is not entering the gas cell. The example of the 65 MeV Po beam is illustrative for radioactive beams produced in heavy-ion fusion reactions and separated in-flight from the primary beam. The so-called SHIPTRAP project [SHIP] is coupling a drift gas cell to the SHIP velocity separator. Case 5 describes the parameters for a gas cell coupled to a heavy-ion fragment separator in order to produce intense radioactive ion beams [Sav02].

Case	Incoming beam	Gas	Q (pairs $cm^{-3}s^{-1}$)
1	1 nA 200 MeV ^{40}Ar	0.5 atm Ar	2.6 10^{15}
2	5.6 10^8 fission-fragments per s (induced by 1 μA 30 MeV protons)	0.5 atm Ar	5.1 10^{12}
3	5.5 ^{242}Am per s (induced by 5 μA d)	0.04 atm Ar	2.6 10^3
4	10^3 × 65 MeV Po	0.5 atm He	1.3 10^7
5	10^8 × 650 MeV Rh	0.5 atm He	1.6 10^{10}

is also given in Fig.4.3. The measurements of Sugaya et al. for protons [Sug96] coincides with those from Ahmed et al. [Ahm00] for 17 keV X-rays and qualitatively agree with the 1 cm electrode gap calculation. The measurements of Sato et al. [Sat97] do deviate from the others. In contrast, the beam here is extremely focused to a spot size of 0.5 × 0.6 mm^2 in the middle of the gap between the electrodes (d = 1.25 cm), while in the other cases the beam is distributed uniformly over the gap, as also assumed in eq.(4.19). The last point measured by Sato et al. (at a field strength of 200 V/cm) did not give full saturation yet for the given ionizing rate. In fact, the maximum applicable voltage of the chamber before breakdown limits this experimental point.

In on-line experiments at LISOL two plane parallel configurations have been used to test the effect of electrical fields in the gas cell. Fig.4.4.a shows the configuration consisting of two thin (1 mm thickness) plates placed in the gas cell (on the horizontal and vertical axes the dimensions are given in centimeters) spaced by a gap of 2 cm. It is important to mention that in this configuration the electric field in the gas cell penetrates to the exit hole. The calculated electric field intensity at the exit hole as function of the applied voltage on the biased electrode is shown in Fig.4.4.b. As it will be seen in section 5.1.3, the presence of an electric field at the exit hole will affect the evacuation of ions from the gas cell. The gas enters the cell from the left side and it can flow above and below the electrodes. The electric field map has been calculated using the POISSON SUPERFISH computer code [POIpr]. The effect of the grounded walls of the chamber is small and the electric field between the electrodes is like in plane parallel geometry (see also Fig.5.13.b in section 5.1.3 for a schematic drawing of the biasing). However, it is important to observe that the polarity of the biasing voltage plays also a role as it defines the area of the anode electrode. For a positive bias voltage, the cathode consists of the

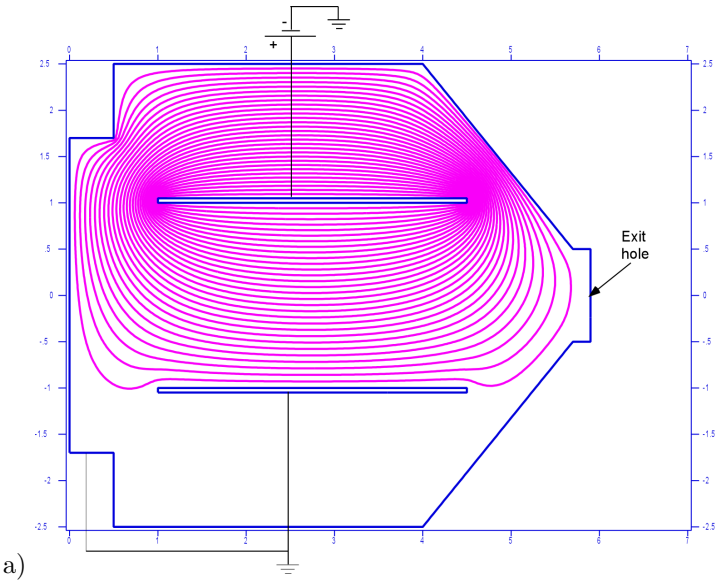

a)

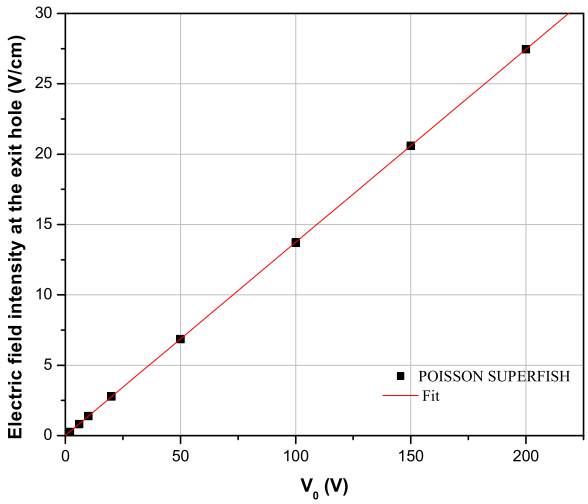

b)

Fig. 4.4: a) A side cross view of the gas cell used as ion collector (the dimensions are in centimeters). The two thin metallic plates (1 mm thick) are spaced by 2 cm. The bottom electrode is kept grounded as the body of the gas cell and the top electrode is either negatively or positively biased. The equipotential lines have been calculated for a biasing voltage of +100V [POIpr]; b) The calculated electric field intensity at the exit hole as function of the applied voltage on the biased electrode.

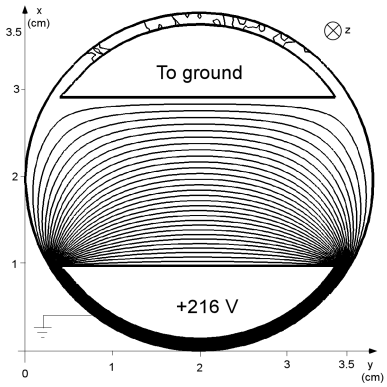

FIG. 4.5: A cross section view of the massive electrodes configuration in the gas cell used as ion collector. The top electrode is kept grounded as the body of the gas cell and the bottom electrode is negatively of positively biased. The equipotential lines are calculated for a biasing voltage of +216 V [POIpr].

grounded electrode and the body of the gas cell. Therefore the area of the anode is smaller for a positive bias voltage than for a negative one. This geometrical effect influences the collection of electrons as the effect of the space charge is larger at a smaller anode area than a bigger one.

A second configuration has been designed such that the gas was allowed to flow only between the two electrodes (see Fig.2.6 in Chapter 2 for a side view). A cross section view of this geometry is shown in Fig.4.5. The POISSON SUPERFISH computer code [POIpr] has been used to compute the electric field map for this geometrical configuration. The result of the calculation is shown in Fig.4.6, where the dimensions and the spatial coordinates are taken as in Fig.4.5. The calculated electric field across the electrodes gap along the extraction axis of the gas cell (y = 1.85 cm) is shown in Fig.4.7.a (full symbol) together with the electric field (line) as in a cylindrical geometry shown in Fig.4.7.b. Thus, contrary of what one can infer from the geometry as given in Fig.4.5 the electric field resembles more to the field in a cylindrical chamber (as shown in Fig.4.7.b) than in a plane parallel geometry. This is due to the fact the metallic walls of the gas cell are grounded as well. Therefore we will assume from now on that the electric field in the geometry given in Fig.4.5 is well described by the field in an "equivalent" cylindrical geometry with the parameters given in Fig.4.7.b.

In the presence of a uniformly distributed ionization source with the rate Q, the space charge density $\rho_+(r)$ and the net electric field $E(r)$, in a cylindrical collector chamber (Fig.4.7.b) are determined by the charge conservation and Poisson equations [Pou99] (in cylindrical coordinates). Solving these equations with the boundary condition

$$\rho_+(r_a) = 0, \tag{4.20}$$

provides the solution for the space charge density:

$$\rho_+(r) = \frac{Q(r^2 - r_a^2)}{2r\mu_+ E(r)}, \tag{4.21}$$

and the net electric field at any point between the electrodes ($r_a \leq r \leq r_b$):

$$E(r, Q, \mathcal{C}) = \sqrt{Q\frac{e}{4\epsilon_0}\frac{(r^2 - 2r_a^2)}{\mu_+} + \frac{\mathcal{C}}{r^2}}, \tag{4.22}$$

where $\mathcal{C}$ is a constant of integration whose value is found from the boundary and voltage conditions. The voltage condition reads:

$$\int_{r_a}^{r_b} E(r)dr = V_0, \tag{4.23}$$

if the space charge limit has not been reached, and

$$\int_{s}^{r_b} E(r)dr = V_0, \tag{4.24}$$

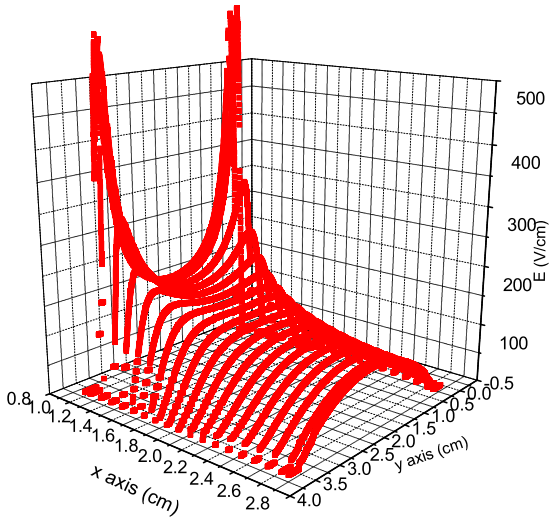

Fig. 4.6: The electric field map calculated with the POISSON SUPERFISH computer code [POIpr], for the geometry from Fig.4.5, with +216 V applied on the bottom electrode (x = 1 cm) and the top electrode (x = 2.8 cm) grounded.

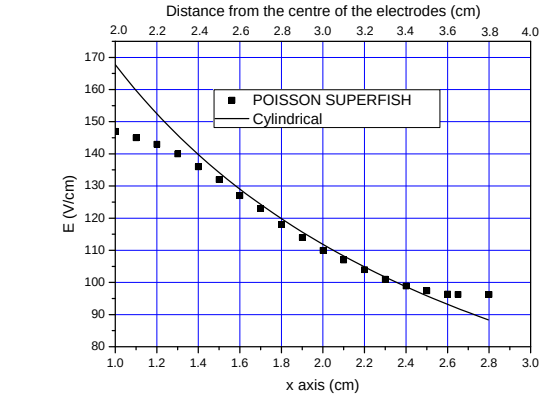

a)

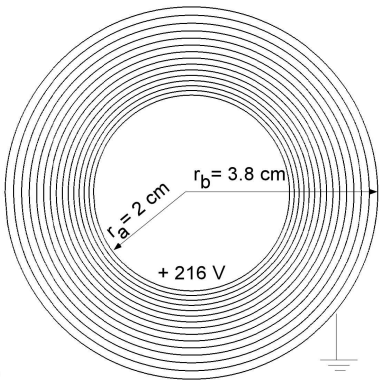

b)

FIG. 4.7: a) The electric field across the electrodes gap, along the extraction axis of the gas cell (■) calculated with the POISSON SUPERFISH computer code [POIpr], for the geometry from Fig.4.5, with +216 V applied on the bottom electrode (x = 1 cm) and the top electrode (x = 2.8 cm) grounded. The line represents the electric field in a cylindrical ionization chamber with the dimensions given in b), for the case when +216 V is applied on the inner electrode and the outer electrode is kept grounded. Note that for the field in a cylindrical geometry, the horizontal axis is the top axis.

if the space charge limit regime has been reached, resulting in formation of a field free region with the width $s - r_a$ (where s is measured from the common center of the electrodes). If eq.(4.24) holds, one has to replace r_a in eqs.(4.20), (4.21) and (4.22) by s, respectively.

The numerical solution of eq.(4.22) is shown in Fig.4.8.a (line + symbol) together with the external applied field (full line) as function of the position in the gap of the electrodes, at different uniform ionization rates Q. In this geometry, the spacing between the electrodes d equals the difference $(r_b - r_a)$ of the outer and inner electrode radius, respectively. The electric field produced by the the space charge built-up between the electrodes at different ionization rates and fixed applied voltage (216V) is shown in Fig.4.8.b. This field counteracts the external applied field at the anode resulting in a decrease of the net electric field at that electrode. When the ionization rate is as low as 10^9 pairs cm^{-3} s^{-1} the electric field produced by the space charge itself is very small (open diamonds on Fig.4.8.b) and the net field in the chamber is almost equal to the applied field (full line on Fig.4.8.a). Increasing the ionization rate results in a much higher counteracting field of the space charge at the anode, such that when $Q = 5.25\times10^{10}$ pairs cm^{-3} s^{-1} (open squares on Fig.4.8.b), the applied electric field at the anode is completely screened. Thus the collection of charges in its vicinity stops and the recombination of charges is taking over in this region. If the ionization rate is further increased, the field free zone develops and it acquires a finite width. The charges created in this zone are freely recombining and, as result, they do not give contribution to the collector current measured on the biased electrode. The calculated width of the field free zone, i.e. where the majority of the charges are lost through recombination, increases from 30% of d at $Q = 1.55\times10^{11}$ pairs cm^{-3} s^{-1} up to 96% of d at $Q = 1.55\times10^{16}$ pairs cm^{-3} s^{-1}.

In the absence of field free zones in the gap of the electrodes, all the charges produced by the primary ionizing particles are collected in the net electric field, which corresponds to the so-called saturation current of the ion collector, i.e. 100% collection efficiency. When space charge effects lead to formation of a field free zone at the anode, the measured ionization current I_c represents a fraction η of the saturation current (I_s), where η is defined as the collector efficiency. Assuming that in the field free region all the charges are lost due to recombination, the collection efficiency in a space charge limited collector chamber is given by the ratio of the active volume to the total volume. Thus, for a parallel plate chamber (Fig.4.2), the collection efficiency is given by:

$$\eta = \frac{s}{d}, \tag{4.25}$$

where the field free zone develops at the anode placed at $x = 0$. In a cylindrical chamber (Fig.4.7.b) the collection efficiency is given by:

$$\eta = \frac{r_b^2 - s^2}{r_b^2 - r_a^2} \tag{4.26}$$

with the anode being the inner electrode of radius r_a, and the cathode being the outer electrode of radius r_b.

The charge conservation law and the Poisson equation can be employed including the negatively charged species, i.e. electrons [Pou99]. The density of electrons anywhere in the gap of the electrodes is then given by

$$\rho_-(r) = \frac{Q(r_b^2 - r^2)}{2r\mu_- E(r)}, \tag{4.27}$$

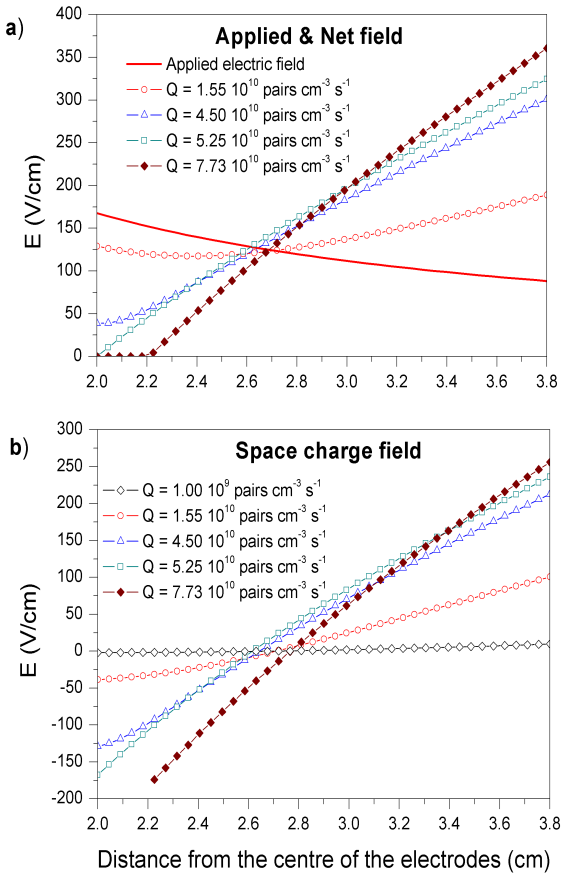

FIG. 4.8: The calculated electric field with and without space charge, a), and the electric field produced by the space charge, b), as function of the position in the gap of the electrodes, for a cylindrical collector chamber as shown in Fig.4.7.b, for different uniform ionization rates Q. The inner electrode is biased at +216V and the outer electrode is kept grounded.

with ($r_a \leq r \leq r_b$) and $E(r)$ the net electric field. Recalling that $\mu_- \gg \mu_+$, one can observe from eqs.(4.21) and (4.27) that the density of electrons (ρ_-) is several orders of magnitude less than that of positive ions (ρ_+) anywhere between the electrodes, therefore only the positive ions contribute to the perturbation of the applied external field. However, this does not exclude the recombination of positive ions with the electrons as they drift in opposite directions in a net electric field given by eq.(4.22), and the collector current measured on the biased electrode has to be corrected with a factor

$$\delta I_{recomb} = \int_V (\alpha \rho_+ \rho_- d\tau), \tag{4.28}$$

where the integration is made over the active volume of the collector chamber and α is the total recombination coefficient (see section 3.7). This correction is evaluated by replacing ρ_- and ρ_+ by their values from eqs.(4.27) and (4.21), respectively. For the case of an argon filled collector chamber, this correction amounts to 1.5% of the collector current as calculated theoretically at an ionization rate $Q = 1.55 \times 10^{16}$ pairs cm^{-3} s^{-1}.

Finally, collection of charges may be altered by the gas flow if there are regions where the flow velocity is higher than the drift velocity. We have computed a three-dimensional map of the flow velocities for the cell geometry shown in Fig.4.5 (side view in Fig.6 of Chapter 2) filled with argon gas at 500 mbar pressure, using the commercial flow code FLUID32 [FLUID]. The flow velocity along the extraction axis in the center of the gas cell is about 7 cm/s, which is equal to the drift velocity of an Ar^+ ion in its own gas at 500 mbar pressure, in an electric field of 2 V/cm. As one can see in Fig.4.8.a, the net electric field in the gap of the electrodes is much higher than this value, when 216V are applied between them, therefore the losses due to the gas flow are expected to be negligible.

4.6 Mutual repulsion of positive ions

When a heavy ion beam is stopped in the gas cell, a huge ion-electron pair density is created. DC and/or RF electric fields can be applied in the gas cell in order to collect the electrons and prevent the recombination of the ions of interest (see the Appendix A for more details about application of an RF field). Due to the lack of negative charges, after collecting all the electrons (provided no space charge effects affect the collection of electrons), the positive ions left behind experience Coulomb repulsion due to the neighboring ions[1].

If a number of positive ions is created inside the gas cell with the initial number density n_0, after removing the electrons, the charges from the whole body of the cloud will start move in the field created by the neighboring ions. The charge continuity equation is written[2]:

$$-\frac{\partial n}{\partial t} = n\frac{\partial v}{\partial r} + v\frac{\partial n}{\partial r}, \tag{4.29}$$

where it is considered that the initial charge density is created in a cylindrical volume with R_0, the initial radius, and l, the cylinder's length. We are studying the radial expansion of the charge cloud. The last term in the right-side of eq.(4.29)

[1] We deal with singly charge ions only.

[2] In this section the subscript "+" is omitted as all the quantities refer to positive ions.

can be dropped for the reason that the space charge repulsion will prevent the charge density n from varying rapidly with the position. From the Poisson law (eq.(4.10)) in cylindrical coordinates and using that $v = \mu E$, one finds that

$$\frac{dn}{n^2} = -\frac{e\mu}{\epsilon_0} dt, \tag{4.30}$$

which after integration provides the expression for the ion density inside the cloud at a moment t:

$$n(t) = \frac{n_0}{1 + \frac{e\mu}{\epsilon_0} n_0 t}. \tag{4.31}$$

The numerical result of eq.(4.31) is plotted as function of time in the Fig.4.9 for some initial ion number densities in the range 10^6 - 10^{16} cm^{-3}, created in argon gas at 500 mbar. From Fig.4.9 it is obvious that the effect of mutual repulsion is large and that the space charge density is not only controlled by the removal of electrons, as treated in the previous section, but also by the Coulomb repulsion among ions in the regions where there is no confining electric field applied. For example, in a cylindrical ionization chamber, the positive ion cloud left behind by the removal of electrons in the radial direction, is allowed to expand in the axial direction as there is no constraint in that direction. If the initial charge density is $5\times$ 10^8 ions/cm^3 (corresponding to an ionization rate $Q = 7.7 \times 10^{11}$ pairs/cm^{3}s created by a 26

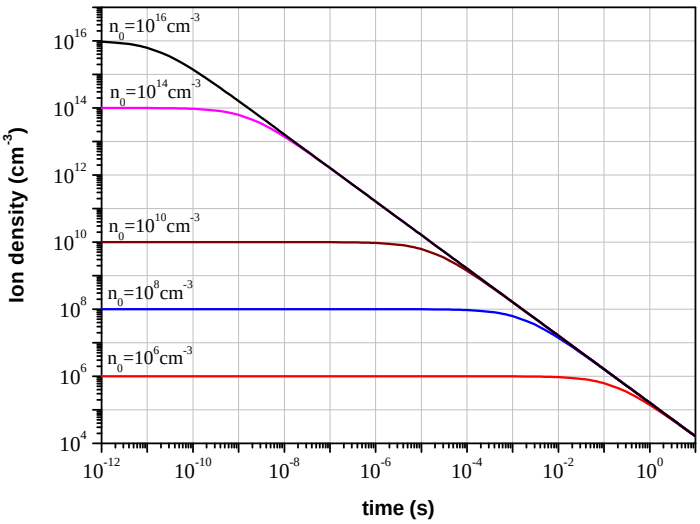

FIG. 4.9: The time evolution of charge number density in a positive ion cloud in argon gas at 500 mbar pressure. The ion mobility is taken as for Ar^+ ions in their own gas (Table 4.1) recalculated for the given pressure (eq.(4.5)).

MeV ^{58}Ni beam in Ar at 500 mbar), in only 3 ms the ion density drops by a factor of 10 as result of the escape of ions from the active volume of the collector due to the mutual repulsion within the space charge cloud.

Before leaving the subject of the mutual repulsion among particles of charge like in gas, it is appropriate to discuss another phenomena that produces similar effect even though it has a fundamentally different origin, i.e. the diffusion of ions in the gas environment. The diffusion of charged particles through a gas smooths out the inequalities in the concentration and causes particles to be lost to the walls of the chamber (see also section 3.9). Recalling eq.(3.24) from section 3.9 it is possible to ask that the effect of the mutual repulsion among ions and diffusion is the same[3] by imposing that the root-mean-square displacement of an ion due to diffusion alone (x_D) during the time t equals the distance the ion drifts outside the sheath of a spherical ion cloud having a radius r and an ionic density n_0, due to mutual repulsion:

$$x_D = \mu E t = \frac{\mu n_0 e r t}{3\epsilon_0} \tag{4.32}$$

where μ, e and E are the ion mobility, the charge of the electron and the electric field outside the sheath of the spherical ion cloud, respectively. Replacing x_D in eq.(4.32) with its expression from eq.(3.24) one obtains the time t_{DMR} for which the two effects of diffusion and mutual repulsion among ions assume equal importance:

$$t_{DMR} = \frac{18\mathcal{D}\epsilon_0^2}{(\mu n_0 r e)^2} \tag{4.33}$$

where $\mathcal{D}$ is the diffusion coefficient of the ions in gas (see section 3.9). Table 4.8 gives the values of the t_{DMR} calculated using eq.(4.33) for the case a spherical ion cloud with a volume of 1 cm^3 in 500 mbar of He and Ar, respectively. The diffusion coefficients from Table 3.5 were used. The diffusion of ions is the dominant effect

Table 4.8: The values of the t_{DMR} (in seconds) calculated using eq.(4.33) for the case a spherical ion cloud with a volume of 1 cm^3 in 500 mbar of He and Ar, respectively. The diffusion coefficients from Table 3.5 were used.

n_0 (cm^{-3})	10^6	10^8	10^{10}	10^{14}	10^{16}
He	8.96E-03	8.96E-07	8.96E-11	8.96E-19	8.96E-23
Ar	4.96E-02	4.96E-06	4.96E-10	4.96E-18	4.96E-22

for times $t < t_{DMR}$, whereas mutual repulsion predominates for $t > t_{DMR}$. From Table 4.8 it is easy to observe that for the case of helium as buffer gas the mutual repulsion fastly becomes dominant at moderate ionic densities ($\sim 10^6$ cm^{-3}). For the case of Ar used as buffer gas, the loss of ions within an ion cloud with a density of 10^6 cm^{-3} is diffusion dominated for as long as $\sim$50 ms. Therefore, the losses of ions due to mutual repulsion within an ion cloud with this density can be minimized if the evacuation time from the gas cell is shorter than $\sim$50 ms, i.e. the cloud is created in a zone close to the exit hole of the gas cell. An increased ionic density

[3]Treating the effect of the diffusion and of the mutual repulsion at the same time is a complicate matter [McD64].

within the cloud leads to a steep shorten of t_{DMR}, thus an enhance of the losses due to mutual repulsion.

4.7 Plasma effects

In ionization chambers one should in principle not consider plasma effects as the electrons are immediately collected and no neutral plasma can be created. However, once the space charge limit is reached the situation will be totally different and the field free region as discussed in ref. [Sug96] will eventually expand over the whole cell: a weakly ionized plasma will be formed ($n_i \sim n_e \gg n_g$ with n_i, n_e and n_g respectively the ion-, electron- and neutrals density). The recombination rate in such a plasma is high and the gas cell cannot longer be used to store and transport efficiently the incoming ions. The ion and electron density will similarly evolve to a saturation value given by eq.(15) of Chapter 3 with a time constant given by eq.(14) of the same chapter. It is difficult to estimate the electron temperature in the gas cell and it could well be that the plasma is not in thermal equilibrium, therefore it is not easy to characterize the plasmas observed in such systems.

Petrov et al. [Pet02][4] have calculated and analyzed the plasma parameters in Ar and He buffer gases (100 torr pressure) for projectile beam intensities from 10^9 to 10^{17} pps cm^{-2}. They have found that for both helium and argon gas targets the temperature of the bulk of electrons is $T_e = 300$K. In the case of argon buffer gas, for beam intensities exceeding 10^{12} pps cm^{-2} (Q $\simeq 10^{15}$ electron-ion pairs/cm^{3}s), the projectiles transfer a sufficient amount of energy to the electrons so that the temperature of the bulk electrons exceeds the gas temperature. The electron temperature gradually increases with the primary beam intensity and it approaches a maximum of 0.4 eV (4600K) when the beam intensity is 10^{17} pps cm^{-2} (see Table 4.9). The situation is different in He gas targets, for which the electron temperature remains at 300K even at very high beam intensities, because the elastic collisions with He are very efficient due to the large momentum transfer cross section and the small mass ratio.

A consequence of plasma formation is that collective effects emerge. An important observation is the occurrence of ambipolar diffusion (see section 3.9) where the ions and the electrons do move with the same velocity ($v_e \simeq v_i$). A necessary condition for a plasma description is that the Debye length of the plasma is of the same order or less than the dimensions of the cell. The Debye length λ_D (in mm) is given by the following expression [Che74]:

$$\lambda_D = 69\sqrt{\frac{T_e}{n_e}}, \tag{4.34}$$

with T_e the electron temperature in K and n_e the electron density in cm^{-3}. Assuming the electrons at room temperature and a density of 10^8 cm^{-3}, one can see from Table 4.9 that the Debye length is already in the 0.1-mm range. Increasing the electron density up to 10^{13} cm^{-3} brings the Debye length down in the μm range.

A second phenomenon is that the plasma shields itself for external fields through the formation of a plasma sheath. The Debye length is a measure for the penetration of external fields in the plasma. A necessary condition is that the number of charges

[4] In this work, the considered projectile beam has a spot area with 1 cm diameter and it consisted of 40 MeV He^{++} ions. The gas target is 1 cm thick, therefore one projectile ion creates ∼100 electron-ion pairs in helium gas and ∼1100 pairs in argon, respectively.

Table 4.9: The parameters of a heavy ion beam generated argon plasma: the electron/ion density, the electron temperature [Pet02], the Debye length, the number of charges in the Debye sphere and the product of the plasma frequency and the mean time between two collisions of an Ar ion. The projectile beam consists of 40 MeV He^{++} ions in a spot of 1 cm diameter, which creates in average 1100 pairs/projectile in a 100 torr Ar gas target 1 cm thick.

I_{beam} (pps)	$n_e \simeq n_i$ (cm^{-3})	T_e (K)	λ_D (mm)	N_D	$\omega \cdot \tau$
10^7	10^8	300	$1.1{\cdot}10^{-1}$	660	0.002
10^9	10^9	300	$3.5{\cdot}10^{-2}$	210	0.007
10^{11}	10^{10}	350	$1.2{\cdot}10^{-2}$	83	0.022
10^{13}	10^{11}	600	$4.9{\cdot}10^{-3}$	60	0.070
10^{15}	10^{12}	1700	$2.6{\cdot}10^{-3}$	90	0.223
10^{17}	10^{13}	4600	$1.4{\cdot}10^{-3}$	125	0.704

in the plasma sheath region N_D is much larger than 1. This number is given by [Che74]

$$N_D = 1380 \frac{T_e^{3/2}}{n_e^{1/2}}. \tag{4.35}$$

Typical values of N_D for a heavy ion beam generated argon plasma (given in Table 4.9) show that the second condition for a plasma to exist is fulfilled in the domain of 10^8 - 10^{13} cm^{-3} electron/ion densities. Another condition states that the number of ion collisions with neutral atoms should be small, i.e. the plasma is dominated by interactions between the charged species. This condition can be quantified as follows [Che74]:

$$\omega\tau \gg 1 \quad \text{with} \quad \omega \approx 9000\sqrt{n_i} \quad \text{and} \quad \tau = \frac{\lambda}{\overline{v}}, \tag{4.36}$$

where ω is the ion plasma frequency, τ is the average time between two ion-neutral collisions and λ, $\overline{v}$ are the mean-free path and the average speed of ions (see Table 3.5) in the buffer gas for a given pressure (100 torr of Ar for the values given in Table 4.9). Using the values for the product $\omega\tau$ given in Table 4.9 it is clear that the third condition is not fulfilled and one only can speak of a weakly ionized plasma.

The term "plasma effects" can be found in many publications on IGISOL setups [Den97]. The term is used to discuss the losses of ion-guide efficiency due to the intensity of the incoming primary beam and related to this, the rate of recombination. Although some conflicting results can be found in literature, Dendooven [Den97] concludes that in most measurements a drop in ion-guide efficiency is observed when the energy deposition in the ion-guide stopping chamber leads to creation of more than 10^{16} electron-ion pairs per second. However, in the same survey [Den97], evidence is presented where the drop in efficiency seems to be related to extraction problems near the exit of the gas cell. The strength of the IGISOL approach is based on an attempt to evacuate the ions out of the ion-guide system within time scales (usually sub-ms [Hui04]) shorter than the time scale for the recombination (see eq.(3.14) of Chapter 3). As the recombination time scale is beam

dependent, the effective volume of the gas cell (i.e. the volume of the gas cell which is evacuated before recombination processes reduce the density of ions to one half of its initial value) can then be reduced. The obtained efficiency will be the result of a multi-parameter balance involving the gas cell design, the beam properties, the purity of the gas and the extraction conditions. Therefore it is difficult to compare the results obtained at different laboratories or even within the same laboratory if the above-mentioned parameters are not controlled in a reproducible way. The results of the studies with ion guide set-ups cannot directly be used for the drift gas cell as here the concept is completely different with the use of electrical fields to collect all created electrons.

4.8 Summary

DC electrical fields can be applied in a gas cell for stopping, storing and transporting radioactive ions in order to drift the ions towards the exit hole of the gas chamber and/or remove the electrons created during the slowing down of the primary beam. In this way, the residence time of the ions in the gas chamber is shortened and the recombination losses of ions are reduced. A practical limit is reached when, at high ionization rates created by the primary beam, the positive space charge induces an electric field equal to the applied field, i.e. the so-called *space charge limit*. Using the correct configuration of the electric field in the gas cell it is possible to calculate the ionization rate (Q_{SCL}) for which the space charge limit is encountered, by applying the theoretical formalism developed to describe the charge collection in classical ionization chambers. Collection of charges in the gas cell at ionization rates beyond Q_{SCL} can be explained through the formation of field free zones with finite widths in the anode vicinity. The evolution of electron-ion pair density in the field free zones is recombination dominated. In the zones of the gas cell where the collection of charges takes place, the positive ions still drift about three orders of magnitude slower than the electrons. Accumulation of positive ions in a cloud can lead to an increase of the effect of mutual repulsion among ions and consequently, an increase of the loss of ions to the gas cell walls. The loss of ions due to mutual repulsion can be compensated through a fast evacuation of the ion cloud from the gas cell. However, at moderate ionic densities within the cloud (i.e. 10^{10} cm^{-3}) evacuation times as short as $\sim 10^{-5}$ s are required for a cell filled with 500 mbar of argon in order to avoid these losses. This is not feasible from a practical standpoint and one has to consider the electron collection in the gas cell in connection with the formation of ion clouds having densities not higher than 10^{6} cm^{-3}.

Chapter 5

Results and discussion

In the study of exotic nuclei far from stability at on-line isotope separators the target-catcher-ion source system should be universal, in order to produce beams of all elements of the table of Mendelejev; it should be fast, in order to minimize decay losses of the shortest living species and it should be element-selective, in order to separate the rare nuclei of a particular element from the more stable isobaric contaminants, which are typically orders of magnitude more produced in the used nuclear reactions. It is therefore essential to characterize qualitatively and quantitatively the different stages a radioactive ion undergoes in a gas cell (catcher) system, as used at LISOL, from its creation until its detection. In that respect, two major categories of studies have been performed at the LISOL isotope separator:

1. off-line studies;
2. on-line studies, with the sub-categories:
    a. Conversion of a high energy ^{58}Ni beam into a low energy mass-separated ^{58}Ni beam, involving stopping, thermalization and laser ionization in a noble gas cell;
    b. Production of neutron-deficient Ru and Rh isotopes in heavy ion induced fusion reactions.

In off-line studies, a radioactive isotope or a stable element is evaporated from a hot filament inside the gas cell. Laser light is used to resonantly ionize that species prior to the extraction from the gas cell. As most of the off-line studies were done before this thesis work, only a selection of results obtained off-line will be presented here and for more details the reader is referred to the paper of Kudryavtsev et al. [Kud01]. However, it is worth to mention the conclusions drawn in that paper:

- Although argon has a higher stopping power than helium, making it a better choice for slowing down energetic reaction products, it manifests a considerably faster bonding chemistry than helium, which could induce faster neutralization;
- The total efficiency of laser ionization in argon was found to be four times lower than in helium although less diffusion losses to the walls were observed;
- Although in most cases molecular ions do not form a major problem as they later can be broken up efficiently, they could become a loss factor in the presence of electrons;

- Ion-electron recombination reactions are strongly influencing the ion signal exiting the gas cell when the electron density exceeds 10^7 cm^{-3}.

On-line conditions are essentially different from off-line ones. First of all a much more dense electron-ion density is created by the passage of the primary particle beam through the gas cell or by the slowing down process of the produced ions. A second difference consists in the fact that the produced nuclei are changing during their slowing down from multi-charged atomic ions to doubly and singly charged ions or to neutral atoms. Finally, the gas cell is located in a highly radioactive area. A series of on-line experiments have been conducted to study these effects and they will be presented in the following sections. They include the study of:

- the influence of the cyclotron beam on the signal of laser produced ions from a filament;
- the study of stopping, thermalization, laser re-ionization and extraction from the gas cell of a stable ion beam;
- the influence of the primary projectile beam on the production of radioactive isotopes in heavy-ion induced fusion and proton induced fission reactions in a gas cell.

5.1 Experiments with stable ions

In on-line conditions, the electron-ion density created by a cyclotron beam passing the gas cell can be very high. The main processes controlling the charge density are the charge creation (with a rate given by eq.(3.9) in section 3.5), the electron-ion recombination (see section 3.7) and the electron/ion diffusion (see section 3.9).

5.1.1 The influence of the beam on laser produced ion signal from a filament

The effect of the locally increased ion/electron density created by an impinging beam can be studied with laser-produced stable nickel ions, evaporated in atomic form from a filament.

Neutralization of laser produced ions by the primary cyclotron beam

In this experiment a gas cell, filled with helium gas (0.5 atm), having an inner diameter of 20 mm and an exit hole of 0.5 mm diameter was used. The lasers were tuned to ionize nickel atoms evaporated from a filament and the influence of a cyclotron beam on the extracted signal from the gas cell has been probed. The 45 MeV $^3He^{2+}$ beam had a spot area of 6 mm diameter and it passed through the gas cell at 29 mm distance from the exit hole.

When no cyclotron beam is present and only one pulse of lasers is fired, the neutral nickel atoms in the laser path are ionized, extracted and mass separated, and a typical time profile is seen as in the curve from Fig.5.1.a (for more details see [Kud01]).

This nickel ion time profile does change when a $^3He^{+2}$ beam pulse (1 pnA intensity when measured in DC, 1 ms long) enters the gas cell. The lasers are fired only 0.1 ms before the cyclotron beam enters the cell. The resulting ion signal has

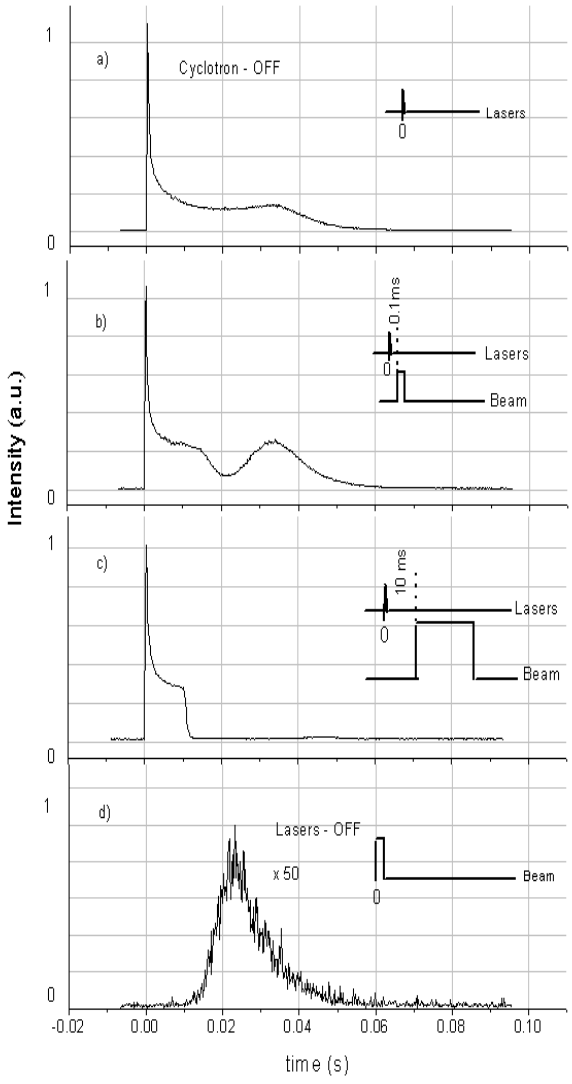

Fig. 5.1: a) The time profile of nickel ions ($^{58}Ni^{+1}$) extracted from the gas cell and mass separated, when one laser pulse is fired at t=0; The influence of the impact of the $^{3}He^{+2}$ cyclotron beam on the time profile of nickel ions extracted from the laser ion source in the subsequent pictures: b) a pulse of 1 ms, 1 pnA (measured in DC) 0.1 ms after the laser pulse, c) a pulse of 20 ms, 200 pnA (measured in DC) 10 ms after the laser pulse, d) Ionization of nickel atoms due to a beam impact. The beam settings are: a pulse of 1 ms, 1 pnA (measured in DC). The inserts show the lasers pulse and beam pulse timing scheme. Note that the vertical scale is multiplied by a factor of 50.

a minimum at the time of 22 ms, as one can see in Fig.5.1.b, which corresponds to the ion evacuation time from the region where the cyclotron beam path crosses the laser beam path in this gas cell. The ion/electron production rate in this case (500 mbar of helium) is equal to $7.3 \cdot 10^{12}$ pairs $s^{-1}cm^{-3}$. Taking a recombination coefficient of $\alpha = 1.42 \cdot 10^{-7}$ cm^3s^{-1} [Son92] (see also Table 3.3), an equilibrium density of $7.2 \cdot 10^9$ pairs cm^{-3} is reached after 1 ms, thus at the end of the cyclotron pulse.

During the beam pulse and shortly after, the ion-electron recombination in the beam interaction zone is important and consequently a number of laser-created Ni ions present in this zone will be neutralized, creating the dip in the time profile at 22 ms.

If the cyclotron intensity is higher the depth and the width of the dip is enlarged as can be seen in Fig.5.1.c, where now a cyclotron beam intensity of 200 pnA, when measured in DC mode, and a pulse length of 20 ms was used. The cyclotron pulse is fired 10 ms after the lasers pulse. An equilibrium ion/electron density of 10^{11} ion/electron pairs per cm^3 is reached in the cyclotron beam path in $7 \cdot 10^{-5}$ s (with $\alpha = 1.42 \cdot 10^{-7}$ cm^3s^{-1}). In contrast to the previous situation, full neutralization of laser-produced ions takes place in the first 2.5 ms after the cyclotron pulse and the ion signal does not reappear over the whole cell already at the end of the beam pulse. More than 99% of the laser-produced ions present before the beam impact are neutralized under the action of the accelerator beam and this over the whole laser beam path. This fast ion-electron recombination in the high ion/electron density created by the projectile beam is the base of the operational principle of the laser ion source. In experiments involving nuclear reactions one has to separate a particular species from the rest of reaction products. Allowing all the reaction products to neutralize in the moderator gas of the cell and subsequently ionizing resonantly one species of interest which is further extracted and mass separated offers the prospects for a selective ion source.

Nickel ions can also be created due to the cyclotron beam impact (see section 3.5). Fig.5.1.d shows the time profile of stable nickel ions at mass 58 ionized by the cyclotron beam (1 pnA intensity when measured in DC, 1 ms long fired at $t = 0$). The maximum of the signal is observed at 22 ms, which corresponds to the travel time to the exit hole. The width of the peak in Fig.5.1.d is larger than the width of the dip in Fig.5.1.b. This is related to the fact that laser ions are created in the laser beam path in the center of the gas cell while cyclotron-related nickel ions are created along the cyclotron beam axis, perpendicular to the cell axis. The flow pattern of the latter will include slower parts.

Decomposition of molecules by the beam

Atoms evaporated from the filament during their journey to the exit hole can form molecules with impurities that are present in the buffer gas. The main impurity in the helium (argon) gas is water, < 5 ppm (see section 2.3.2), which after passing the gas purifier levels down to sub-ppb level. Also Ni ions will be sensitive to such adduct reactions. If Ni atoms are evaporated from a filament and laser ionized in the large gas cell (see Fig.2.3) filled with He at 0.5 atm a typical mass spectrum of the extracted signal looks like in Fig.5.2.a. The mass spectrum is dominated by the Ni ions but one can observe molecular side-bands formed by the nickel ions and water molecules. Typical time profiles of the signal of nickel ions and nickel hydrate ions extracted from the gas cell are shown in Fig.5.2.b. Note that the plotted ion signals for the $Ni^+(H_2O)$, $Ni^+(H_2O)_2$ and $Ni^+(H_2O)_3$ ions are increased by a factor 50.

The time behavior indicates that the sequence of nickel hydration proceeds with the consecutive formation of $Ni^+(H_2O)$, $Ni^+(H_2O)_2$ and $Ni^+(H_2O)_3$ ions, respectively [Kud01].

The formation of molecular neutrals results in a reduced number of atoms in their atomic ground state, available for laser ionization. This process is hard to study in off-line conditions. In the on-line experiments, proof has been found that the cyclotron beam decomposes previously formed molecules and as consequence enhances the laser ionization efficiency. Fig.5.3 shows the time profiles of laser produced stable rhodium ions extracted from the fusion gas cell (see Fig.2.4). A rhodium filament delivers a constant supply of atoms; the buffer gas is argon at a pressure of 500 mbar. The lasers are only fired once and the time spectrum of the ions is taken. The profile indicated as "off" corresponds to the signal obtained in

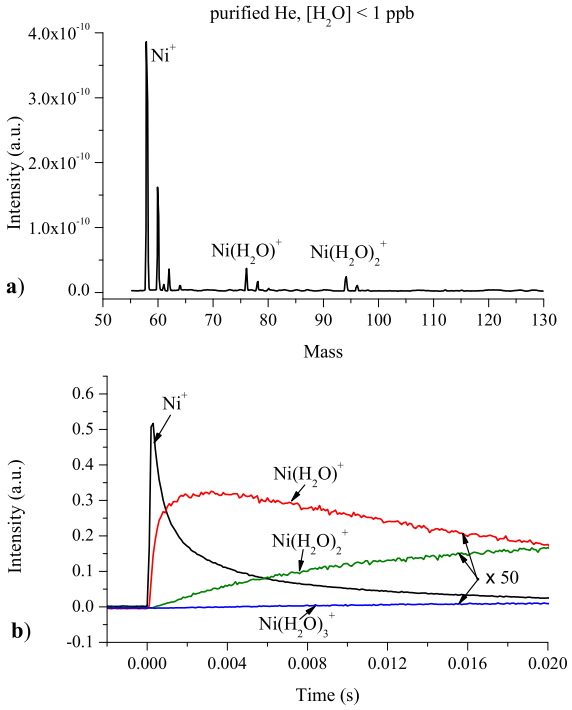

Fig. 5.2: a) The mass spectrum of ions extracted from the gas cell after laser ionization of nickel atoms in purified He gas. Nickel has five stable isotopes, M = 58, 60, 61, 62 and 64 with relative abundance of 68.27%, 26.10%, 1.13%, 3.59%, 0.91%, respectively; b) The time profiles of ions extracted from the gas cell after laser ionization of nickel atoms at mass 58-Ni, 76-$Ni^+(H_2O)$, 94-$Ni^+(H_2O)_2$, 112-$Ni^+(H_2O)_3$. The vertical scale for the $Ni^+(H_2O)$, $Ni^+(H_2O)_2$ and $Ni^+(H_2O)_3$ ions is increased by a factor 50.

the absence of the cyclotron beam. The evacuation time of the channel part of the cell equals to 13 ms. For times longer than this value, the ion signal drops which is

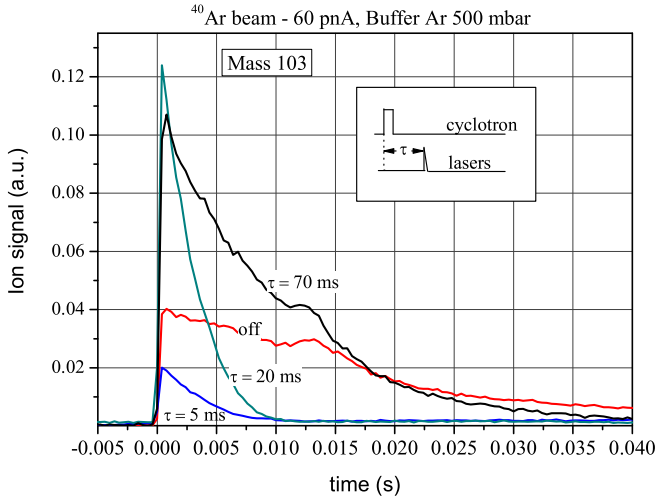

FIG. 5.3: The time profiles of ions (M=103) extracted from the ion source after laser ionization of stable rhodium atoms in argon buffer gas (500 mbar) with different delay relative to the cyclotron beam pulse (130 MeV ^{40}Ar, 60 pnA measured in DC, 50 ms). The insert shows the timing of cyclotron and laser pulses.

related to the reduced atom concentration due to the conical shape of the cell. If the laser is now fired 5 ms after the beginning of the cyclotron beam pulse (250 MeV ^{40}Ar, 60 pnA when measured in DC, pulse width 50 ms) the signal is considerably weaker due to ion-electron recombination as explained in the previous paragraph. When the delay increases to 20 ms, the ^{103}Rh signal increases significantly.

This can be explained by the decomposition of molecules containing rhodium atoms in the cyclotron beam path, so more atoms in the ground state are available for laser ionization. At this time delay the ion-electron recombination still takes place inside the channel part of the cell. When the delay time with which the lasers are fired is longer than the cyclotron pulse width the recombination is strongly reduced. As the lasers are fired with a delay of 70 ms (20 ms after the end of the cyclotron pulse), the high ion/electron density, responsible for neutralization, is already decayed away. Note the increase of the signal. It is interesting to mention that no such effect was observed during similar measurements in helium as buffer gas. The time structure of the cyclotron beam was identical. This is consistent with the fact that the chemistry in helium is much slower compared to the evacuation time of the cell by gas flow (see ref. [Kud01]). The evacuation time of the gas cell used in these experiments, when filled with helium gas, is around 50 ms. As already discussed in section 3.10, the half-life for molecular ion formation, with a rate constant of 10^{-10} cm^3/s, is 500 ms provided an impurity level of 1 ppb.

5.1.2 Conversion of a 185 MeV $^{58}Ni^{+10}$ beam into a 40 keV mass separated $^{58}Ni^{+}$ beam

Another major branch of studies involving stable ions was the conversion of a high energy ^{58}Ni (185 MeV) beam delivered by the CYCLONE cyclotron of Louvain-la-Neuve (see section 2.1) into a low energy one (40 keV) involving stopping and resonant re-ionization in a gas cell. The method of using stable beams implanted in an ion source was firstly used by Kirchner et al. [Kir92, Kir97] in order to measure the release times of ions from a catcher-ion-source-system. They have implanted an ion beam into a catcher-ion-source-system, and since the rate of implanted particles is known the release profile was unambiguously determined. The parameters of the ion beam implanted in the gas cell, such as intensity, time structure, charge state and energy can accurately be controlled, thus one can determine with precision crucial parameters of the ion source for an efficient release of the ions. Two ion guide configurations have been used, one with the large gas cell from Fig.2.3 (owing a volume of $\sim$34 cm^3 from the beam position to the exit hole) and second with the 10 mm channel gas cell from Fig.2.6 (having a volume of $\sim$16 cm^3 from the beam position to the exit hole). The advantage in these experiments is that one can

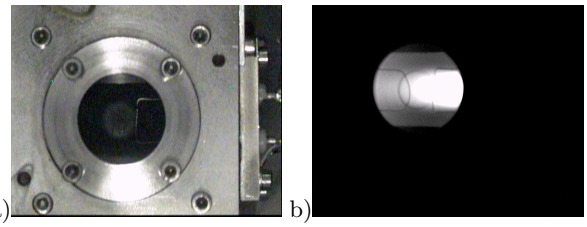

Fig. 5.4: The view through the laser entrance window a) without beam passing the gas cell, and b) when $2.2{\cdot}10^9$ pps of 26 MeV ^{58}Ni beam current is stopped in the cell filled with argon gas at 500 mbar pressure. The beam is coming from the right side. Note that the right picture is taken in dark in order to emphasize the emitted light by the fluorescence of Ar atoms excited by the beam impact.

carefully control the amount of primary ions implanted in the gas cell. In this respect dedicated beam diagnostics has been developed in order to cover a wide range of beam intensities from single-particle-counting up to the particle-micro-Ampere level.

Fig.5.4 shows the view through the quartz laser entrance window in the 10 mm channel gas cell (see Fig.2.6 in section 2.3.1) filled with 500 mbar argon gas, without beam (a) and with $2.2{\cdot}10^9$ pps of ^{58}Ni beam current (b) being implanted in the cell. The energy of the beam after passing the front-end box window (Mo-4.1 μm) and the cell entrance window (Mo-4.37 μm) equals to 26 MeV. Fig.5.5.a shows the gas cell and the position of cyclotron and laser beams. Fig.5.5.b shows the spatial distribution of the stopped ions, calculated with the SRIM code [SRIpr]. The position of the stopped nickel ions is very well localized and the longitudinal straggling due to the stopping is 2.5 mm. If the gas pressure is reduced below 300 mbar, the nickel ions will be implanted into the cell wall, see Fig.5.5.c.

The ions created by the stopping of the ^{58}Ni beam and eventually flowing out

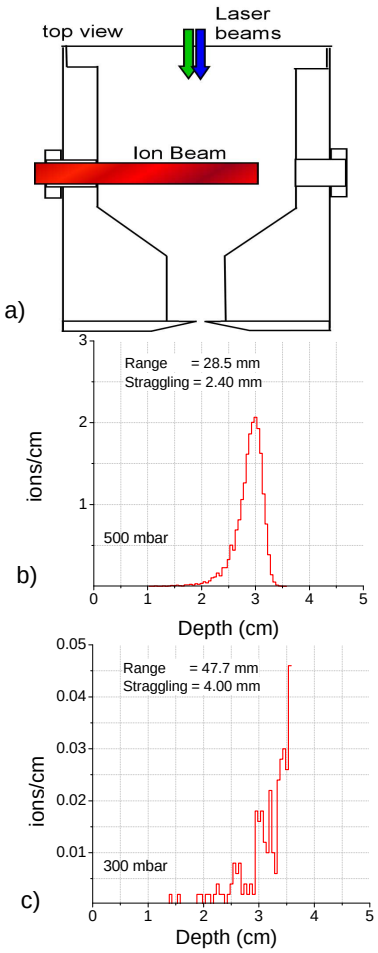

FIG. 5.5: a) The schematic layout of the gas cell. The darkened area represents the path of the cyclotron ion beam implanted in the gas cell. Note that this is a top view of the gas cell from Fig.2.6, thus the electrodes are not seen. b) SRIM calculation of the nickel ion distribution in the gas catcher. A 185 MeV nickel-58 beam from the cyclotron is retarded by two molybdenum foils and is stopped in the center of the gas cell filled by 500 mbar argon, c) the same as b but with argon pressure 300 mbar.

of the gas cell in their ionic state can be mass analyzed. In Fig.5.6 mass scans are presented for the case where a DC beam of $9.4{\cdot}10^{10}$ pps ^{58}Ni is implanted in the large cell filled with argon gas. The energy lost by the primary ^{58}Ni ions in this gas cell is 45 MeV. Scan a) is obtained when no lasers are applied: the spectrum is

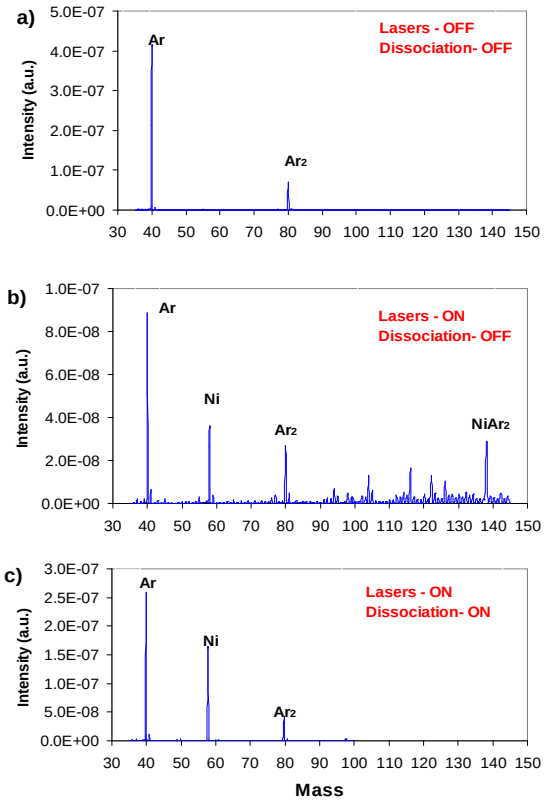

Fig. 5.6: Mass spectrum of ions obtained with the gas cell bombarded with a ^{58}Ni beam current of $9.4{\cdot}10^{10}$ pps (DC): a) lasers are off, $V_{dc} = 0$, b) lasers are on-resonance, no dissociation voltage is applied between the gas cell and the SPIG, $V_{dc} = 0$, c) lasers are on-resonance, dissociation voltage $V_{dc} = 250$ V .

completely dominated by Ar^+ and Ar_2^+ ions. Switching on the lasers on the nickel resonance, many peaks related to nickel ions do pop up (scan b). When applying a dissociation voltage between the gas cell and the SPIG rods (see section 2.3.2) the molecular side bands disappear and the main peaks are coming from Ar^+, Ni^+ and Ar_2^+ ions (scan c).

The evacuation properties of the gas cell

The evacuation properties of the ion source have also been studied with the cyclotron beam in a pulsed mode.

Fig.5.7.a shows time profiles of nickel ions coming out the large gas cell (see Fig.2.3) with lasers on and off and also of argon ions. The cyclotron beam time structure was 50 ms ON and 3000 ms OFF for argon buffer gas. The time "0" corresponds to the beginning of the cyclotron pulse. At $6.25 \cdot 10^9$ pps nickel beam current, the argon ions appear in the exit hole region immediately after the beginning of the cyclotron beam. This effect must be related to an ionization process near the exit hole as ions created in the beam interaction zone need time to travel to the exit hole. Most probably it is related to ionization of argon atoms in the vicinity of the exit hole by energetic photons emitted as a result of the stopping process in the buffer gas. The huge amount of argon ions created in the beam interaction zone are not giving a significant signal in the present setup. They are below the dynamic range of the measuring unit. The nickel atoms come with a time delay to the exit hole region where they are ionized by laser light. The "saw-tooth" structure observed with the lasers on in the nickel signal is related with the laser pulse repetition rate of 20 Hz. The nickel signal reaches its maximum after 500 ms. This time corresponds to the calculated evacuation time from the region where the energetic nickel ions are stopped. Due to diffusion the first atoms are observed in the exit hole region already at a time delay of 150 ms. One of the factors that further defines the shape of the ion signal is the spatial overlapping of the laser beam and the cloud of nickel atoms. At the end of the cyclotron OFF time (3000 ms), the nickel signal is not yet at zero. We can see a further drop in the nickel signal during the beam ON time due to ion-electron recombination caused by the next cyclotron pulse. Note the logarithmic scale in Fig.5.7. The signal with the lasers-off at mass 58 has a similar time behavior but of course no laser-related structure is observed. One can deduce the selectivity of the laser ion source of 100 from the ratio of the mass 58 signal with the lasers on to the signal with the lasers off.

For comparison, the evacuation of nickel atoms stopped in 740 mbar of helium is shown in Fig.5.7.b. In this case precision energy retardation of the nickel beam is applied by using a rotatable degrader. The longitudinal straggling of the ions is comparable with the size of the cell. The cyclotron beam has a time structure of 50 ms ON and 1000 ms OFF. The beam current equals to $6.25 \cdot 10^8$ pps and the lasers run at 100 Hz pulse repetition rate. As expected the maximum of the ion signal in the case with the lasers on corresponds to a time of 170 ms, which is three times shorter than for argon buffer gas. However the fast peak in the signal with the lasers on or off on mass 58 appears during the cyclotron pulse and apparently consists not of ^{58}Ni ions, but of molecular ions created due to ionization by the projectile beam. In contrast to the case of the argon filled gas cell, in helium, the selectivity of the laser ion source can not be accurately deduced, as the mass 58 signal with the lasers off drops down dramatically after 120 ms after the beam pulse. However a lower limit of 2 can be given.

The consequence of stopping ion beams with high intensity in the large cell filled with argon gas is that most of the argon ions created in the beam interaction zone recombine during their journey to the exit hole. The argon ion signal extracted from this cell consists mainly of argon ions created close to the exit hole by energetic photons emitted during the cyclotron beam pulse. No direct comparison with the extraction of helium ions from the cell when filled with helium gas can be done because these ions are not transported through SPIG. Further on, time profiles of the argon ion signal extracted from this cell filled with argon gas will be discussed

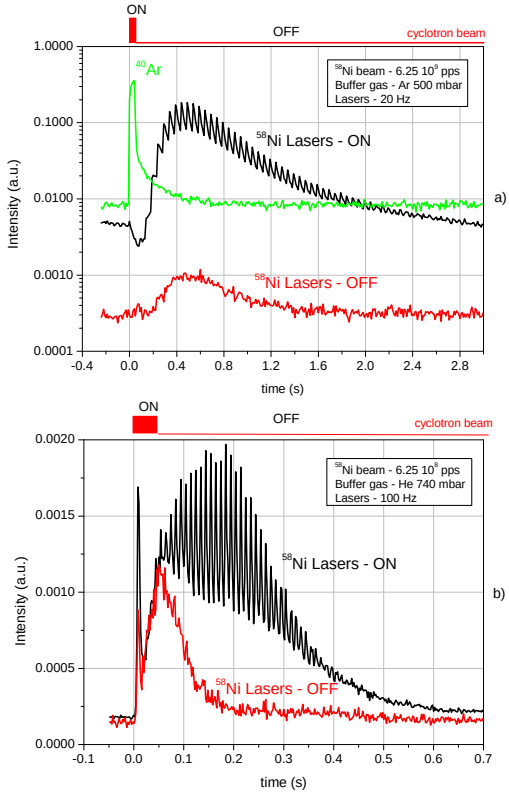

Fig. 5.7: a) The time profiles of nickel ions coming out of the source after pulse injection (50 ms - ON, 3000 ms-OFF) in argon (500 mbar) with lasers on and off and of argon ions at mass 40. Lasers are at 20 Hz pulse repetition rate. The beam current is $6.25 \cdot 10^9$ pps as measured in DC mode, b) The time profiles of the nickel ion signal coming out of the source after pulse injection (50 ms - ON, 1000 ms-OFF) of nickel-58 ions in helium (740 mbar) with lasers on and off. Lasers are at 20 Hz pulse repetition rate. The beam current is $6.25 \cdot 10^8$ pps measured in DC. Remark: No equivalent He ion signal as in the case of Ar buffer gas can be extracted from the cell and be mass separated because the helium ions are not transported through the SPIG due to the too low RF frequency.

as a function of the beam intensity and evidence will be given for Ar ions surviving from the beam interaction zone. The nickel ion signal extracted from this cell filled with argon gas and without laser ionization consists of ^{58}Ni ions stopped in the beam interaction zone and which have survived against recombination before evacuation by the gas flow. When laser ionization is used the maximum nickel ion signal extracted from the large cell filled either with argon or helium gas is recorded with a time delay equal to the evacuation time of the cell by the gas flow from the beam interaction zone. This means that most of the nickel arrive at the exit hole as neutral atoms.

The evacuation properties of the 10 mm channel ion guide have also been studied with the cyclotron beam in a pulsed mode. Due to the reduced dimension of this cell only argon has been used as buffer gas. As discussed in section 3.1.2 this cell filled with 0.5 bar helium gas is capable of stopping ^{58}Ni ions having less than 2 MeV energy. Tuning the energy of the ^{58}Ni ions at this low value requires the use of a number of degrader foils arranged in beam, which leads to an increase of the beam energy spread comparable with the beam energy. Therefore the stopping of primary ^{58}Ni ions in this cell filled with helium gas is not effective.

Typical time profiles of the ^{58}Ni signal with the lasers on and off, extracted from the 10 mm channel ion guide are shown in Fig.5.8.a and Fig.5.8.b, respectively. These time profiles have been measured by using the digital ion counter mounted after the mass separator in the beam focal plane (see section 2.6.2). Note that the intensity of the ion signal is given in "count/channel" with one channel having 3.02 ms width. A mechanical grid has been used in front of the secondary electron multiplier in order to reduce the count rate by a factor 100. The width of the cyclotron beam pulse is 20 ms. For the case with the lasers on, two beam intensities have been used, i.e. $3.6{\cdot}10^8$ pps and $3.2{\cdot}10^{10}$ pps as measured in DC mode, respectively. The maximum ion signal is observed at 240 ms in both cases which corresponds to the theoretical value of the evacuation time from the beam-center position of this gas cell filled with argon, as resulted from the FLUID32 code calculation [FLUID]. For the case with the lasers off, the measurement could not be performed for the lowest beam current ($3.6{\cdot}10^8$ pps) as the count rate was already very low with a beam current of $3.2{\cdot}10^{10}$ pps. From the ratio at mass 58 of the signal with the lasers on to the signal with the lasers off, for the beam intensity of $3.2{\cdot}10^{10}$ pps, one can deduce a selectivity of $\sim$500 for this configuration. One can integrate the time profiles from Fig.5.8.a for the signal on mass 58 with the lasers on. As the beam intensity is reduced from $3.2{\cdot}10^{10}$ pps by a factor of 90, using a mechanical mesh, it is observed that the integral of the signal drops by a factor of 100. This means that the efficiency of the laser ion source for the two cases of primary beam intensity is approximately the same. Table 5.1 gives the ionization rate (Q), the recombination time constant (τ_r), the equilibrium electron-ion pair density during the beam pulse (n_{eq}) and the pair density after 240 ms for the two cases of beam intensity (I_{beam}) used to measure the time profiles from Fig.5.8. For both beam intensities the equilibrium pair density is fastly established during the beam pulse. The interesting issue is that after 240 ms the density of electron-ion pairs near the exit hole of the gas cell is $4.2{\cdot}10^6$ cm^{-3} for both beam intensities (see Table 5.1). Therefore, the fact that the laser ion source efficiency is nearly constant when the beam intensity is changed by a factor 100 can be explained by the constant rate of recombination of the laser produced ions near the exit hole in the same background density of electron-ion pairs. However, as it will be seen later, this is not a general statement and, especially at low beam currents (below 10^6 pps), deviations are seen. As in the case of the large gas cell, the maximum

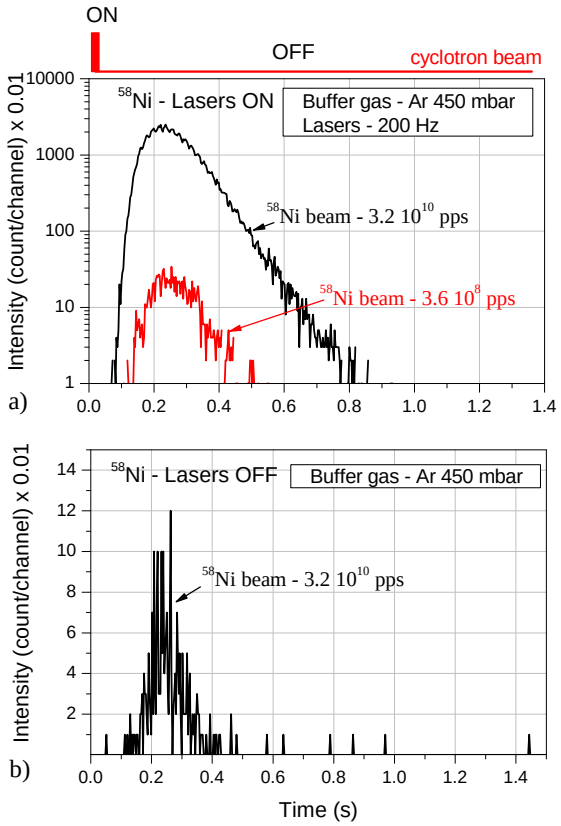

Fig. 5.8: The time profiles of nickel ion signal coming out of the source after pulse injection (20 ms - ON, 3000 ms-OFF) in argon (450 mbar): a) with lasers on. Lasers are at 200 Hz pulse repetition rate. Two values of the beam current have been used: $3.6{\cdot}10^{8}$ pps and $3.2{\cdot}10^{10}$ pps as measured in DC mode, respectively; b) with the lasers off, for a beam intensity of $3.2{\cdot}10^{10}$ pps as measured in DC mode. The intensity is given in "count/channel" and it is reduced by a factor 100; one channel has 3.02 ms width.

TABLE 5.1: The recombination time constant, τ_r (using eq.(3.14)), and the equilibrium density, n_{eq} (using eq.(3.15)), for given intensities of the ^{58}Ni beam (I_{beam}) in argon gas at 450 mbar pressure. The ionization rates Q (electron-ion pairs/cm^{3}s) are given. The recombination coefficients α_{Ar}^{295K} from Table 3.3 has been used. The electron ion pair density after 240 ms (n(240 ms)) is calculated using eq.(3.17).

I_{beam} (pps)	Q (pairs/cm^{3}s)	τ_r (s)	n_{eq} (cm^{-3})	n(240 ms) (cm^{-3})
$3.6{\cdot}10^8$	10^{14}	$95{\cdot}10^{-6}$	10^{10}	$4.2{\cdot}10^6$
$3.2{\cdot}10^{10}$	10^{16}	$10{\cdot}10^{-6}$	10^{11}	$4.2{\cdot}10^6$

nickel ion signal extracted from the 10 mm channel gas cell is recorded with a time delay equal to the cell evacuation time by gas flow from the beam interaction zone regardless of the fact that the lasers are on or off[1].

It is interesting to study the effect of a cyclotron beam pulse with a width comparable or longer than the evacuation time of the gas cell, on the nickel beam extracted from the ion source. The time profiles of the signal on mass 58 extracted from the 10 mm channel ion guide with the lasers on and off are presented in Fig.5.9.a and b, respectively, for a cyclotron beam pulse with 1.5 s width. As for the case of the short beam pulse, two beam currents have been used, namely $3.2{\cdot}10^{10}$ pps and $3.6{\cdot}10^8$ pps as measured in DC mode. The extracted signal on mass 58 with the lasers off (see Fig.5.9.b) during the beam pulse contains the contribution of those ions which survive neutralization after the thermalization process and the contribution of nickel which is non-resonantly re-ionized by the beam or by the energetic photons emitted during the slowing down of the projectile ions. The energetic photons ionize the buffer gas as well, and especially at the exit hole of the gas cell, the presence of electron-buffer gas ion pairs contributes to the recombination of nickel ions. At the end of the beam pulse, the non-resonant ionization by the cyclotron beam (e.g. the flux of photons) immediately stops and the survival chance of nickel ions increases. Inspecting Fig.5.9 one can observe that during the beam pulse the signal on mass 58 extracted from the ion source is reduced compared to the signal after the beam pulse. Exception makes the time profile measured for the lower beam current ($3.6{\cdot}10^8$ pps in DC mode) with the lasers off (see Fig.5.9.b), where no clear enhancement of the signal after the beam pulse is observed. It is important to mention that this latter time profile was measured using the attenuation grid in front of the SEM counter (see section 2.6.2) and that the count rate was little above the threshold, thus it must be interpreted with caution. Switching on the lasers, clearly increases the signal of nickel ions extracted from the ion source (see Fig.5.9.a), and by comparing the signal with the lasers on and off for a beam intensity of $3.2{\cdot}10^{10}$ pps, one can find a laser ion source selectivity of 120 in this configuration. This selectivity is a factor of 4 less than the laser ion source selectivity in the case of short beam pulses (see Fig.5.8), obtained with the same beam current (as measured in DC mode).

[1]No reproducible argon ion signal extracted from this gas cell could be measured due to the presence of a discharge between the exit hole flange and the SPIG rods at that time. No explanation for this phenomenon could yet be found.

Using the time profiles from Fig.5.8 and 5.9 one can deduce the ion source efficiency with the lasers on (ϵ_{ON}) and off (ϵ_{OFF}), respectively, for the two widths of the cyclotron beam pulse. The obtained values using a beam current of $3.2{\cdot}10^{10}$ pps as measured in DC mode are given in Table 5.2 together with the laser ion source efficiency (S_{LIS}) for each case of pulse width. If one defines the "pulsed mode" as the working regime of the laser ion source with beam pulses shorter than the evacuation time of the gas cell (from the beam interaction zone), one can see from Table 5.2 that the selectivity of the laser ion source is enhanced in the pulsed mode compared to the DC mode, i.e. when a cyclotron beam is continuously implanted in the gas cell (or pulse width much longer than the cell evacuation time by gas flow). On other hand, the ion source efficiency with the lasers on is approximately the same in both the pulsed and DC mode, while without lasers the

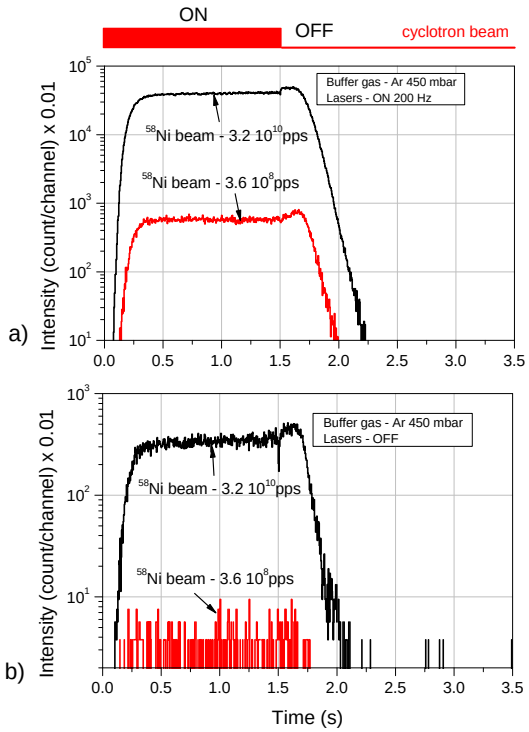

Fig. 5.9: The time profiles of nickel ion signal coming out of the source after a long pulse injection (1.5 s-ON, 3 s-OFF) in argon (450 mbar): a) with lasers on (200 Hz pulse repetition rate) and b) with lasers off. Two values of the beam current were used: $3.2{\cdot}10^{10}$ pps and $3.6{\cdot}10^{8}$ pps as measured in DC mode. The intensity of the measured mass-separated current was reduced by a factor 100. One channel has 4.5 ms width.

TABLE 5.2: The ion source efficiency with the lasers on (ϵ_{ON}) and off (ϵ_{OFF}) and the laser ion source selectivity (S_{LIS}) for a cyclotron beam pulse of 20 ms and 1.5 s width, respectively. A beam intensity of $3.2{\cdot}10^{10}$ pps as measured in DC mode was used. The quoted values are obtained from the time profiles presented in Fig.5.8 and Fig.5.9.

	Beam pulse width	
	20 ms	1.5 s
ϵ_{ON} (%)	2.1	2.9
ϵ_{OFF} (%)	0.004	0.025
S_{LIS}	500	120

ion source efficiency is a factor of 6 higher in DC than in pulsed mode. Therefore, the lower selectivity in DC mode is due to the higher efficiency for extraction of non-resonant[2] nickel ions from the gas cell than in pulsed mode. As will be seen later, this can be explained by the occurrence of a secondary ionization mechanism in the gas cell during the cyclotron beam pulse when high beam currents (as measured in DC mode) are used, due to the energetic photons, which may well contribute to the re-ionization of neutralized nickel.

From the examples presented above it is clear that the presence of the primary cyclotron beam and its intensity have a great impact on the performance of the laser ion source. However, in an on-line experiment involving the production of radioactive isotopes it is difficult to define the priorities, as the aim is to work at the highest yield of that particular isotope, which actually imposes the use of the highest possible projectile beam current. Therefore, it is essential to know what is the survival chance of laser produced ions in the background of electron-ion pairs created by the primary beam. This density of charges is highest in the beam path and it decreases when approaching the exit hole of the gas cell. The time profiles of ions extracted from the gas cell after pulse injection of a nickel beam in argon gas can be studied by ionizing nickel atoms at different time delays after the cyclotron pulse. The results obtained with the large gas cell (see Fig.2.3) are shown in Fig.5.10. The maximum signal is observed at the laser trigger delay time of 500 ms. This value coincides with the maximum of the ion signal in Fig.5.7.a and it shows that the survival of laser produced ions is enhanced in the zone where the density of electron-ion pairs is smallest. Recalling the results presented in Fig.5.7.a one can see that when the nickel ions arrive at the exit hole (the time profile with the lasers off), i.e. $\sim$500 ms, the Ar ion signal is much smaller and thus the density of electron-ion pairs near the exit hole is lower. Nickel atoms resonantly ionized in this region will thus have a higher survival chance against neutralization before extraction from the gas cell.

It is possible to study the time behavior of buffer gas ions as function of the implanted beam intensity. The large gas cell (see Fig.2.3) has been used in that

[2]The term "non-resonant" refers to either nickel ions which have survived neutralization during their journey to the exit hole or re-ionized nickel atoms (i.e. recombined Ni ions) during the cyclotron beam pulse.

respect. The time profiles of the ion signal on mass 40 extracted after a cyclotron beam pulse injection (10 ms width) in argon gas at 500 mbar pressure are shown in Fig.5.11. At very low beam intensity (330 pps as measured in DC mode) the maximum ion signal is observed at time delays comparable with the evacuation time of the gas cell from the beam interaction zone. Increasing the beam intensity results in the shift of the maximum ion signal towards short delays with respect to the cyclotron pulse. This means that the beam impact also creates electron-ion pairs outside the beam interaction zone and that the recombination of buffer gas ions becomes more and more important in the beam interaction zone as the current is increased. However, at the highest beam current ($2.8{\cdot}10^8$ pps as measured in DC mode) a prominent peak appears in the ion signal without delay with respect to the cyclotron beam pulse. This signal lasts as long as the beam is on and it shows that during the beam pulse, at sufficiently high intensities, secondary ionization process such as due to energetic photons becomes important near the exit hole. Here the evacuation is so fast that part of these ions survives neutralization. After some delay, ions coming deeper from the gas cell appear and the maximum ion signal is observed with 80 ms delay after the beam pulse stops. However, at very high beam intensities this picture changes completely, as shown in Fig.5.7.a. There the cyclotron beam pulse lasts for 50 ms and the beam intensity is $6.25{\cdot}10^9$ pps. One can see from Fig.5.7.a that the the time profile of the ion signal on mass 40 is

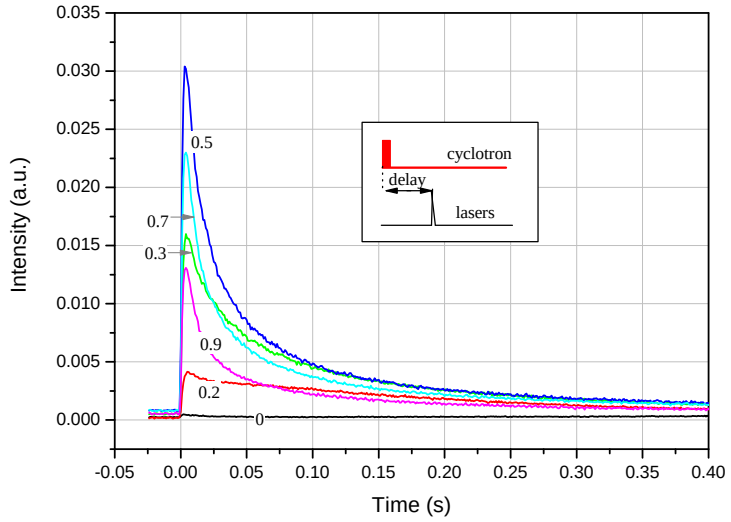

Fig. 5.10: The time profiles of nickel ion signal coming out of the source after cyclotron pulse injection (50 ms - ON, 3000 ms-OFF) in argon (500 mbar) with one laser pulse fired at different delays (in seconds) with respect to the cyclotron pulse start (trigger set on the laser pulse). The beam current is $2.5{\cdot}10^{10}$ pps as measured in DC mode.

completely dominated by those ions created in the vicinity of the exit hole during the beam pulse and that the contribution of the ions coming deeper from the gas cell is insignificant within the dynamic range of the detection unit.

The efficiency and selectivity of the laser ion source

The most important parameters of the laser ion source are the efficiency and selectivity. The efficiency is defined as the ratio of the number of mass separated ions extracted from the ion source to the number of ions on the same mass entering the stopping volume of the gas cell. The selectivity of the laser ion source is defined as the number of ions of a specific element in the mass-separated beam when the lasers are tuned on resonance to the number of ions of that element in the mass-separated beam when the lasers are off. Losses of ions occur during their transport through the SPIG (34% losses) and the mass separator (20% losses). In some circumstances the total current coming out of the gas cell can also be important; this current mainly consists of buffer gas ions and ionized impurities.

The mass-analyzed ion current has been investigated in a wide range of pri-

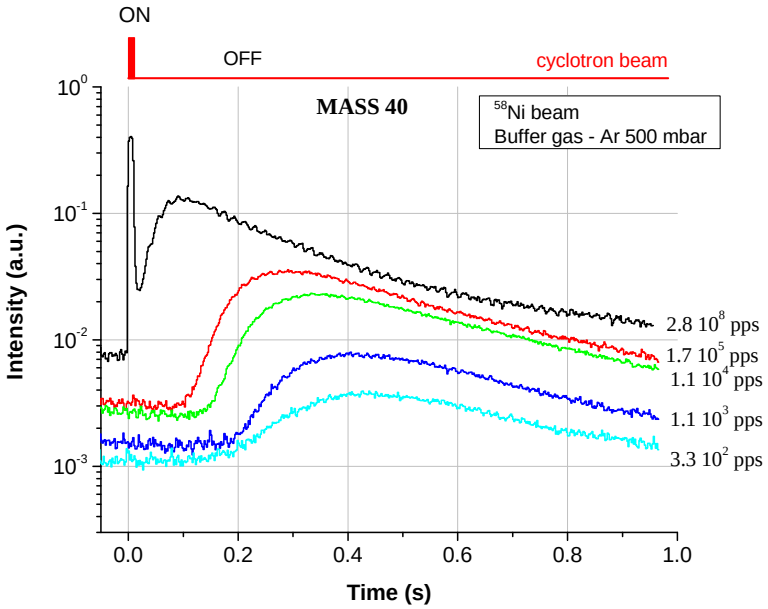

FIG. 5.11: The time profiles of ion signal on mass 40 coming out of the source after cyclotron pulse injection (10 ms - ON, 1490 ms-OFF) in argon (500 mbar). The ^{58}Ni beam current ranged from 330 pps up to $2.8{\cdot}10^8$ pps as measured in DC mode. The different offset of the time profiles at moment "0" is due to the different intensity scales used on the measuring oscilloscope.

mary beam current. Fig.5.12 gives the efficiency of the gas cell as function of the primary beam intensity[3]. The mass-separated ions can be photo-ionized ^{58}Ni ions

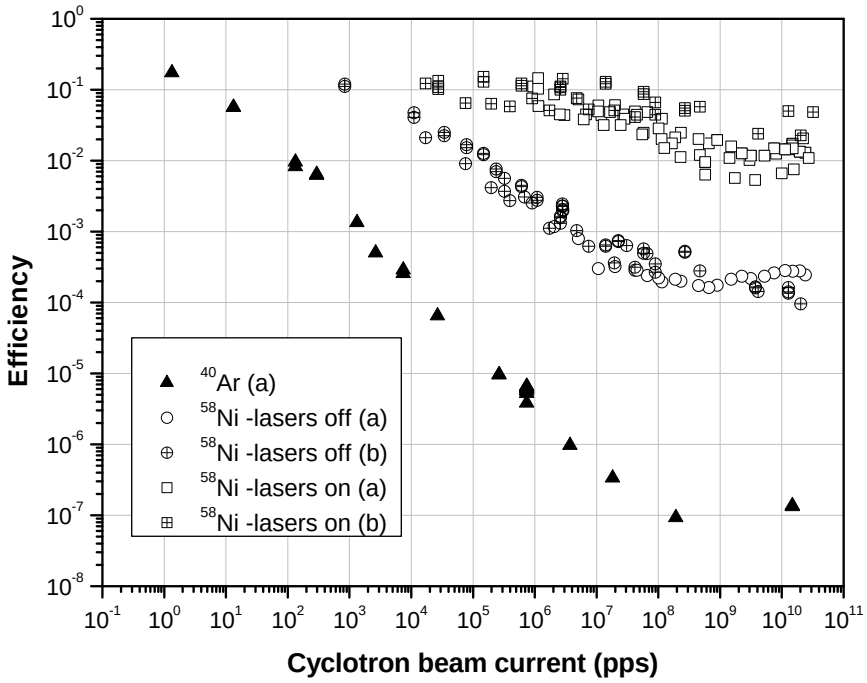

Fig. 5.12: The efficiency of the laser ion source for extraction of ^{58}Ni ions with the lasers-on (squares) and the lasers-off (circles), respectively, as function of the primary beam intensity. The efficiency for extraction of Ar ions (triangles) produced by the beam impact is also shown as function of the beam current. The different symbols represent the data obtained with the large gas cell (a) and with the 10 mm channel ion guide (b).

(laser pulse repetition rate of 200 Hz), argon ions from the beam impact and ^{58}Ni ions which survived the thermalization and evacuation processes. The efficiency for the case of ^{40}Ar ions is defined as the ratio of the number of mass-separated ions and the number of argon ions created in the gas cell by the primary beam, taking $W = 26$ eV as the mean energy for creation of an electron-ion pair (see section 3.5).

[3]The laser ion source efficiencies plotted in Fig.5.12 have no error bars as the obtained values are multi-parameter dependent. An estimate of the reproductibility of the ion source efficiency can be deduced from the scattering of the data points.

The experimental data were collected during 192 beam-hours with different configurations using the large gas cell (see Fig.2.3) and the 10 mm channel gas cell (see Fig.2.6) presented in section 2.3.1. The beam intensity was controlled by varying the settings of the cyclotron and when at the lower intensity side unstable conditions were met by introducing mechanical pepper-pots. The cyclotron beam was on the ms scale a DC beam and its intensity was monitored in the high intensity domain with a Faraday cup and in the low intensity domain with a plastic scintillator (see section 2.6.1). The mass-separator intensity was measured in the high intensity domain with a Faraday cup and in the low intensity domain with a secondary electron multiplier (see section 2.6.2). Special care was taken to intercalibrate the different gauges. Measuring beam-currents with a Faraday cup is performed with an accuracy within 2%, while measuring low beam-currents with the plastic scintillator (see section 2.6.1) could be performed with the same accuracy for beam currents above 500 pps. However, due to the charge-state distribution of the measured beam, as well as due to the fact that different measurements of the cyclotron current with the Faraday cups and with the plastic scintillator were performed with some time delay, a maximum value of 20% of the uncertainty of the primary beam current is realistic. This uncertainty is mainly due to the fluctuations of the primary beam current between measurements and due to the overall stability of the whole setup.

When the initial nickel beam intensity is as low as 1 pps more than 10% of the created argon ions (one nickel ion stopped in argon creates $3.85 \cdot 10^4$ ion-electron pairs/MeV) are extracted and mass separated. For this very low beam intensity the gas cell is completely evacuated during the time between two projectile ions. This efficiency steeply decreases when the beam intensity increases and finally levels off at 10^{-5} %. Measuring the efficiency for the mass-separated nickel ions to very low intensities is more difficult than for argon ions as the charge-creating multiplication factor is not present. At primary nickel intensities around 10^4 pps and below, an efficiency around 10% is observed. This number is not sensitive to the fact if the lasers are on (squares) or off (circles). Increasing the intensity also decreases the efficiency of collecting the nickel ions with the lasers off (those nickel ions which survive in the 1^+ ionic state after thermalization in the buffer gas and during transport in the gas cell). The efficiency levels off at 0.02%. The signal of nickel re-ionized by laser light does show a less dramatic behavior as a function of the beam intensity although the efficiency also drops to reach a 1% level. The difference in behavior between nickel ions without lasers and laser-produced ions results also in a change in selectivity from 1 around 10^4 pps over 100 around 10^7 pps to 50 at the highest intensities. The fact that around 10^4 pps no enhancement is observed with lasers on means that the number of neutral nickel atoms in their atomic ground state available for laser ionization is small compared to the number of surviving nickel ions. As the efficiency for the Ni ions is maximum 12% (at low intensities, independent if the lasers are on or off) and taking into account transport efficiency through SPIG and separator (56%) means that 75% of the nickel stopped in the gas cell cannot be traced back. Diffusion losses inside the gas cell play a significant role as was shown in off-line studies of laser ionization of radioactive ^{57}Co atoms, where it was found found that at least 40% of atoms evaporated from the filament were deposited on the inner cell surface [Kud01]. At intensities around 10^6 pps, the efficiency for laser-produced Ni ions is also around 12% but the fact that 30% of the nickel atoms are in a metastable state and thus not available for laser ionization (see Fig.1.6 in section 1.4.2) [Kud01]) means that diffusion losses of laser ions are less severe. This can be understood as the laser ions are produced closer to the exit hole. The large difference in efficiency between argon and nickel ions without lasers

is striking. This may be due to the difference in ion-electron density in the ion track region, where most of the argon ions are created, and the stopping region where the nickel ends up. As can be seen in Fig.3.12 from section 3.5, the ion-electron density is 10 times lower in the place where the nickel ion stops. Furthermore the energy of the nickel beam was chosen such that ions are stopped in the middle of the cell where the gas flow is faster than in the regions closer to the wall. It is also possible, as discussed in section 3.7, that the recombination mechanisms for the buffer gas ions and nickel ions are different, with different recombination constant rates, which can differ by orders of magnitude.

Laser-produced nickel ions can not only recombine with electrons created by the primary beam but also with electrons created in the resonant laser ionization. This loss process becomes important when the density of the photo-ions (in argon) is higher than $\sim 10^8$ cm^{-3} (see ref. [Kud01] for more details). This corresponds to a nickel beam intensity entering the gas cell of $\sim 4 \cdot 10^9$ pps assuming that all the electron-buffer gas ion pairs have recombined. Recombination of laser created nickel ions with the photo-electrons can partially explain the lower efficiency for extraction of nickel ions from the gas cell, when the lasers are on, at primary beam intensities larger than 10^9 pps (see Fig.5.12). However, losses of laser produced ions are observed for beam currents around 10^7 pps and higher meaning that for these beam intensities not all the created electron-buffer gas ion pairs have recombined before arriving in the exit hole region. The reason why the efficiency remains constant for as well Ni (lasers on and off) as Ar ions (although only one measurement) at beam intensities above 10^8 pps is not yet understood.

Ion source efficiencies for the extraction of nickel (lasers off and on) and argon ions up to 12% were observed. Due to the different electron-ion pair density along the stopped nickel ion track and different recombination paths of argon and nickel ions the maximum ion source efficiency for extraction of Ar ions is observed for a beam current which is three to four orders of magnitude lower than the beam current for which the extraction of Ni ions from the ion source takes place with the same efficiency. The ion source efficiency for extraction of Ar ions steeply decreases inversely proportional to the cyclotron beam intensity until it reaches a value of 10^{-5}%. The laser ionization of Ni becomes effective for cyclotron beam currents stopped in the gas cell higher than 10^4 pps. For beam intensities around this value the nickel ion signal extracted from the ion source consists entirely of surviving nickel ions stopped in the gas cell, and it is the same regardless to the fact that the lasers are on or off, meaning that there are no nickel atoms available for laser ionization. Below this beam current value it is difficult to measure the ion source efficiency for the extraction of nickel ions. The ion source efficiency for the extraction of nickel ions without laser ionization decreases inversely proportional to the square-root of the beam intensity until it reaches a value of about $2{\cdot}10^{-2}$%. The ion source efficiency for the extraction of laser produced nickel ions remains around 10% for cyclotron beam intensities ranging from 10^3 up to 10^7 pps and it decreases down by a factor of 10 at beam intensities around 10^{10} pps. The efficiency of the (laser) ion source is intensity and element dependent.

5.1.3 The effect of electrical fields in the gas cell

From the previous section (see section 5.1.2) one can conclude that the main process which limits the performance of a gas cell used as an ion catcher is the recombination of the ions of interest with the electrons created by the primary beam during the slowing down. When the intensity of the cyclotron beam exceeds 10^9 pps, the

recombination of laser produced ions with the photo-electrons also becomes important. It is clear that the presence of the electrons is undesirable and DC/RF electrical fields can be applied in the gas cell in order to stop the recombination by removing the electrons. Electric fields could also be used to drive the ions towards the exit hole of the gas catcher (DC field) and to keep them on trajectories away from the walls of the cell (RF field) [Wad03]. However, the selectivity of the laser ion source is based on the fast neutralization of the reaction products and therefore electrical fields in the gas cell should be temporarily or locally applied.

As already discussed in the Chapter 4, two configurations have been used at LISOL in order to probe the effect of DC/RF electrical fields in a gas cell. First is the large gas cell with two parallel plates inserted in the cell volume (see Fig.5.13.a), and secondly, the 10 mm channel gas cell (see Fig.5.13.b). The gas cell is operating as a classical ionization chamber except that the gas is continuously flowing out of the cell through the exit hole. A cyclotron beam is implanted in the gas cell, and the ionization current could be measured on the biased/grounded plate as shown in Fig.5.13 for both used configurations. On other hand, the extracted ion current from the gas cell when electric fields are applied can be mass separated and measured.

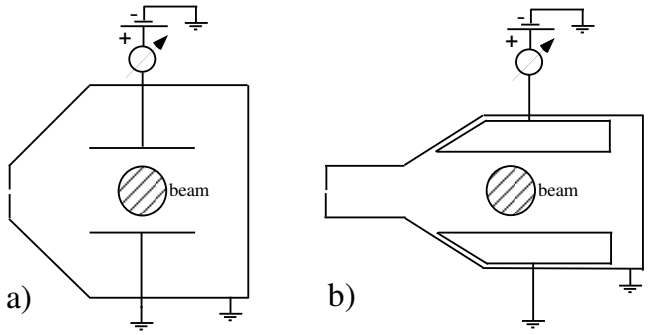

FIG. 5.13: The schematic view of the configuration of a) the large gas cell and b) the 10 mm channel gas cell, respectively, used to study the effect of DC/RF electrical fields in the gas cell. The ionization current can be measured with an Ampere-meter either connected to the biased plate (as shown on figures) or the grounded one. The body of the cell was grounded. The hashed area represents a cross section view of the cyclotron beam interaction zone.

The studies concerning the effect of applied electrical fields in a gas cell for stopping and transporting ions can be divided into two major categories:

1. Measurements of the collector current (DC cyclotron beam, continuous DC electrical field), i.e. ionization chamber mode;
    - Collector current-voltage ($I - V$) characteristics for a given cyclotron beam intensity;
    - Collector current as a function of the cyclotron beam intensity and a fixed DC field strength (both with Ar and He buffer gas).

2. Measurements of the mass separated beam current and/or time behavior.
   - Application of a continuous DC field:
     - measurement of the mass separated beam current using a DC cyclotron beam;
     - measurement of the time profile of the mass separated beam using a single pulse of cyclotron beam.
   - Application of a single pulse DC field using a single pulse of cyclotron beam:
     - measurements of the time profiles of the mass separated ^{40}Ar and ^{58}Ni (lasers off/on) ion signal as a function of the field strength, cyclotron beam intensity and time delays between cyclotron pulse, field pulse and lasers pulse.

This section is structured according to the above categories.

The gas cell as an ionization chamber

a. The large gas cell

The first check is to ensure that the applied voltage on the electrodes produces an electric field strong enough to collect all the charges created by the primary beam (saturation of current I as a function of the biasing voltage V). $I-V$ characteristics must be measured at different intensities of the cyclotron current. The resulted $I-V$ characteristics for the case of a 45 MeV ^{58}Ni beam implanted in the large cell filled with argon gas at 500 mbar are shown in Fig.5.14.

From Fig.5.14 one can observe that for low beam currents, i.e. below $1.9{\cdot}10^7$ pps, the maximum applied voltage of -250 V is enough to ensure the saturation of the I-V characteristic. For high beam currents, i.e. above $1.9{\cdot}10^7$ pps, the I-V characteristics are clearly not saturated and higher applied voltages are required in order to collect all the created charges in the active volume of the ionization chamber.

The collector current has been measured for a fixed voltage of +/-235 V applied on one of the electrodes and by changing the intensity of the primary beam implanted in the large cell filled with argon gas at 500 mbar pressure. The obtained results are shown in Fig.5.15. The corresponding ionization rates Q are given on the upper axis of the graph. The formalism for a parallel plate ionization chamber (see section 4.5) has been used to calculate the theoretical collector current (shown as dashed line on the graph). Table 5.3 summarizes the experimental collector efficiencies for both applied voltages -(+)235 V ($f^{exp}_{IC-(+)}$) as well as the theoretical collector efficiency (f^{theor}_{IC}) and width of the field free zone (s^{theor}) as for a plane parallel ionization chamber with a spacing of the electrodes $d_0 = 2$ cm and 500 mbar argon as filling gas. The agreement between the theory and the experimental data obtained with a biasing voltage of V_0=+235 V is reasonable. At low intensities of the incoming ion beam the drift field is strong enough to collect all the charges. For a cyclotron beam current of about 10^5 pps ($Q = 1.67 \cdot 10^{10}$ cm^{-3}s^{-1}) the field at the anode has been cancelled, i.e. the space charge limit has been reached. If the intensity of the cyclotron beam is further increased a field free region starts to develop at the anode as result of the increased counteracting field produced by the space charge. As one can see from Table 5.3 the calculated width of the field free zone increases from 8.2 mm up to 18.8 mm when the beam current is increased from 10^6 pps up to 10^{10} pps. However, this theory can not explain the experimental

data obtained with a biasing voltage of -235 V. This is partially understood as a geometrical effect of the grounded walls of the chamber. In the case of negative voltage applied on one of the electrodes, the other electrode and the grounded walls of the cell play the role of the anode electrode, therefore the description of the field free zone in a simple parallel plate geometry becomes inaccurate.

b. The 10 mm channel gas cell

This effect has been further studied using the 10 mm channel gas cell. The electrical field in this gas cell resembles more the electrical field in a cylindrical ionization chamber than in a plane parallel geometry (see section 4.5 for more details). A fixed voltage +/-216 V was applied on one of the electrodes on which the collector current was measured. The experimental results are shown in Fig.5.16 together with the calculated pair production rate (full line) and the theoretical results of the collector current (dashed line) as in a cylindrical ionization chamber (shown in Fig.4.7.b of section 4.5) when +216 V are applied on the inner electrode. The results from Fig.5.16 together with the theoretical values of the ion collector efficiency and width of the field free zone in a cylindrical ionization chamber equivalent to the gas cell configuration, are summarized in Table 5.4. It is important to

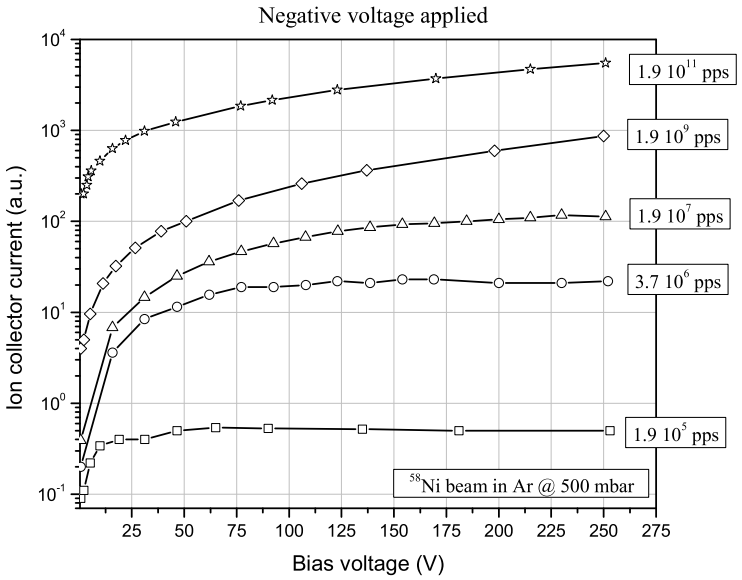

FIG. 5.14: The current-voltage (I-V) characteristics measured with the large gas cell filled with 500 mbar of argon used as ionization chamber. The values of the primary beam (45 MeV ^{58}Ni) currents were $1.9{\cdot}10^5$ pps, $3.7{\cdot}10^6$ pps, $1.9{\cdot}10^7$ pps, $1.9{\cdot}10^9$ pps and $1.9{\cdot}10^{11}$ pps, respectively. The spacing of the electrodes is 2 cm. The collector current is measured on the grounded electrode and the other electrode is biased with a negative voltage.

mention here that in a cylindrical ionization chamber the saturation curves depend on voltage polarity [Nov96], and the space charge limit for a given voltage is higher (in terms of ionization rate Q) when the outer electrode is made cathode having a greater area available for collection of slowly drifting positive ions [Sha64]. This is observed in Table 5.4 where for a given beam intensity the collector efficiency is higher when the inner electrode (i.e. measuring electrode) is made anode compared to the reverse case. Nevertheless this still can not explain the large discrepancies between the experimental and theoretical collector efficiencies when V_0=-216 V. The agreement between the calculated and the experimental values of the ion collector efficiency when a positive voltage is applied on the measuring electrode (+216V) is reasonable. The theoretical description of the field free zone in this

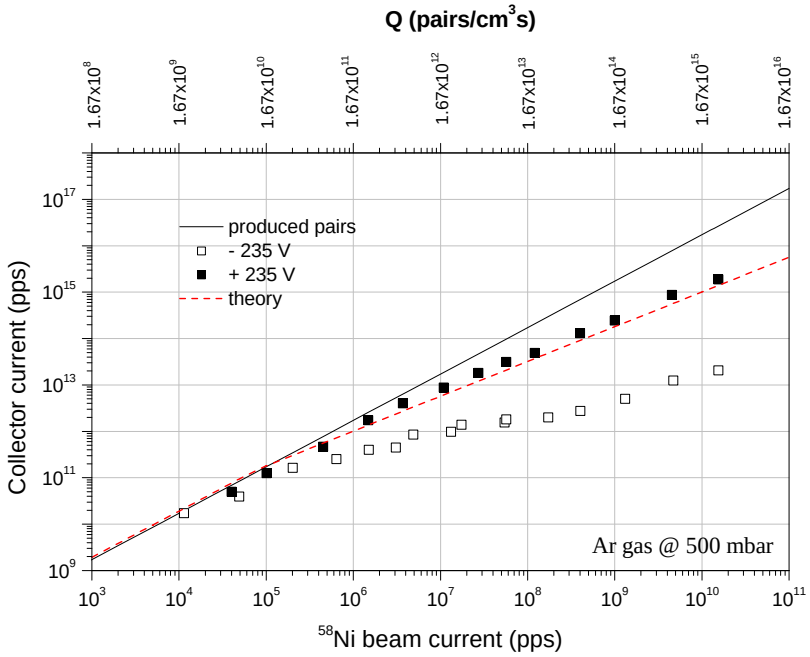

Fig. 5.15: The collector current in the large cell filled with argon gas at 500 mbar pressure as function of the primary beam intensity. The full squares are the data obtained with a +235 V biasing voltage and the open squares represent the results obtained with -235 V applied on one electrode. The full line corresponds to the total number of charge pairs produced per second and the dashed line is the result of the calculation for a plane parallel ionization chamber with 2 cm spacing of the electrodes (eq.(4.25) was used). Note the double log-scale.

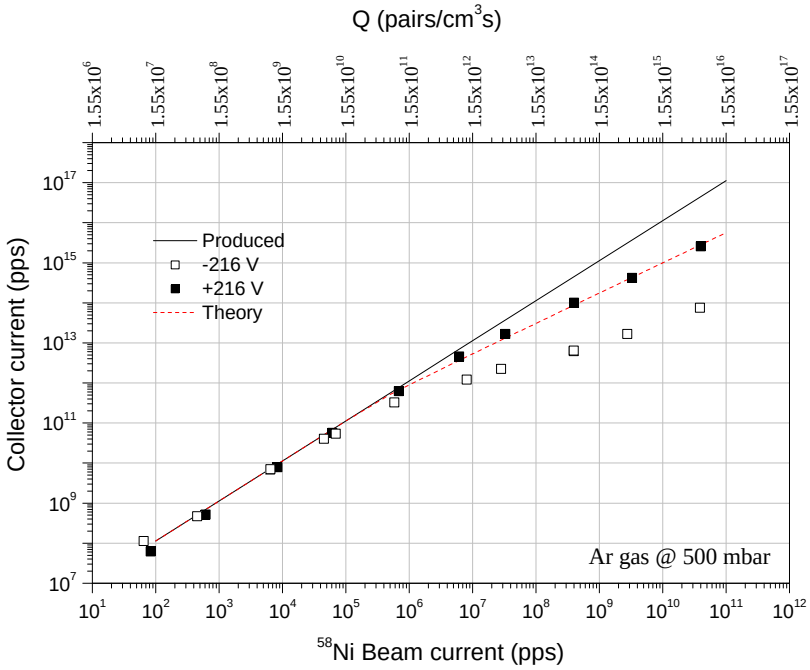

FIG. 5.16: The collector current in the 10 mm channel ion guide filled with argon gas at 500 mbar pressure as function of the primary beam intensity. The full squares are the data obtained with a +216 V biasing voltage and the open squares represent the results obtained with -216 V applied on one electrode. The full line corresponds to the total number of charge pairs produced per second and the dashed line is the result of the calculation for a cylindrical ionization chamber with 1.8 cm spacing of the electrodes and 2 cm the radius of the inner electrode (eq.(4.26) was used). Note the double log-scale.

case is accurate, given the exact knowledge of the anode electrode geometry. The measured ion collector efficiencies above unity must be interpreted as a mismatch between the calculated and actual value of the ionization rate Q.

One can attempt to generalize the obtained results for different experimental conditions with a given collector geometry. In this respect, the universal parameter ξ was introduced [Boa52, Boa63, Pal99]:

$$\xi = \frac{d^2}{V_0}\sqrt{\frac{Qe}{\epsilon_0 \mu}}. \tag{5.1}$$

The universal parameter ξ is convenient to plot collector efficiencies on the same graph, when measurements are performed in different experimental conditions, i.e. ionization rates Q and/or applied voltages V_0. The space charge limit corresponds to a value of the parameter ξ equal to 2. The same experimental data as in Fig.5.16 are plotted in Fig.5.17 in terms of collector efficiency as function of the universal parameter ξ. The deviation of the experimental collector efficiencies compared to the theoretical ones, for intermediate ξ parameter from 2 to 100 suggests that the effect of the space charge has been overestimated in our approach. The collector efficiency has been calculated using the approximation of an infinitely long cylindrical capacitor. In reality, the cylindrical capacitor has a finite length and, since there is no axial electric field applied between its end-caps, ions and electrons may escape from the active volume of the collector. The mutual Coulomb repulsion of ions within the space charge (see section 4.6) acts isotropically and it may be

Table 5.3: The experimental ion collector efficiency† with V_0=-235 V (f_{IC-}^{exp}) and V_0=+235 V (f_{IC+}^{exp}) applied between the two parallel plates ($d_0 = 2$ cm) in the large cell filled with 500 mbar argon gas, and the corresponding theoretical values of the collector efficiency (f_{IC}^{theor}) and width of the field free zone (s^{theor}). Note that in an ideal plane parallel geometry the polarity of the applied voltage does not affect the charge collection efficiency.

	Experimental		Theoretical	
	V_0=-235 V	V_0=+235 V	V_0=+/-235 V	
I_{beam} (pps)	f_{IC-}^{exp} (%)	f_{IC+}^{exp} (%)	f_{IC}^{theor} (%)	s^{theor} (mm)
10^4	93.70	74.10	100.00	0.0
10^5	47.10	72.00	100.00	0.0
10^6	18.40	67.10	58.70	8.2
10^7	3.80	47.40	33.20	13.3
10^8	1.10	25.00	18.70	16.2
10^9	0.24	14.20	10.50	17.9
10^{10}	0.09	8.00	5.80	18.8

† The experimental collector efficiency at each beam intensity was calculated using a straight line interpolation to the two nearest data points.

responsible for loss of ions trough the end-cap surfaces. Thus, as a consequence of the modified boundary conditions the space charge density may be lower than the result of eq.(4.21), which accounts for the mutual repulsion of positive ions only in the radial direction.

For completeness purposes, the 10 mm gas cell has been used as ionization chamber when filled with helium gas at 500 mbar pressure. The ^{58}Ni ions have lost in average 17 MeV in the gas cell and they were implanted in the exit window of the chamber (Mo - 5 μm). This value fluctuates with $\pm$2 MeV and it was obtained by measuring the collector current at very low cyclotron current (10^3 - 10^4 pps) when the space charge effect is small and no field free zones are formed (thus the collection efficiency was 100%). The energy loss straggling in helium has been discussed in the section 3.1.2. The obtained collector currents at positive and negative biasing voltage as function of the cyclotron beam intensity are plotted in Fig.5.18 together with the total production rate of ions (line) and the calculated collector current (dashed line) in a cylindrical ionization chamber with the dimensions given in Fig.4.7.b when the inner electrode is biased at +216 V. Due to the higher mobility of ions in helium gas (see Table 4.1) the space charge limit occurs in helium at higher ionization rates Q than in argon. The results from Fig.5.18 together with

TABLE 5.4: The experimental ion collector efficiency[‡] with V_0=-216 V (f^{exp}_{IC-}) and V_0=+216 V (f^{exp}_{IC+}) applied between the two parallel plates (d_0 = 1.8 cm) in the 10 mm channel cell filled with 500 mbar argon gas, and the corresponding theoretical values of the collector efficiency ($f^{theor}_{IC-(+)}$) and width of the field free zone ($s^{theor}_{-(+)}$) as for an equivalent cylindrical ionization chamber (see Fig.4.7.b). Note that in a cylindrical ionization chamber for different polarities of the voltage applied on the inner electrode the collector efficiency is not the same. For a +(-) polarity the field free zone develops at the inner(outer) electrode.

	Experimental		Theoretical			
	V_0	V_0	V_0	V_0	V_0	V_0
	-216V	+216V	-216V	+216V	-216V	+216V
I_{beam}	f^{exp}_{IC-}	f^{exp}_{IC+}	f^{theor}_{IC-}	f^{theor}_{IC+}	s^{theor}_{-}	s^{theor}_{+}
(pps)	(%)	(%)	(%)	(%)	(mm)	(mm)
10^2	160.8	93.5	100.0	100.0	0.0	0.0
10^3	113.6	97.6	100.0	100.0	0.0	0.0
10^4	103.3	100.4	100.0	100.0	0.0	0.0
10^5	62.7	92.0	100.0	100.0	0.0	0.0
10^6	37.7	83.4	55.9	79.1	6.6	4.8
10^7	13.1	59.0	29.3	47.1	11.4	10.8
10^8	3.3	26.7	15.8	27.3	14.2	14.0
10^9	0.8	14.8	8.6	15.6	15.8	15.8
10^{10}	0.6	13.7	4.8	8.8	16.7	16.7

[‡] The experimental collector efficiency at each beam intensity was calculated using a straight line interpolation to the two nearest data points.

the theoretical values of the ion collector efficiency and width of the field free zone in a cylindrical ionization chamber filled with 500 mbar helium, equivalent to the 10 mm channel gas cell configuration, are summarized in Table 5.5, for both negative and positive polarity of the applied voltage on the inner electrode (-/+216 V).

As in the case of argon gas, the above discussed geometrical effect due to the increased surface of the anode electrode when a biasing voltage of -216 V is used shows up in helium as well. For a biasing voltage of +216 V the agreement between the theoretical prediction and the experimental values of the ion collector efficiency is reasonable (see Table 5.5).

It is interesting to discuss here the use of a large cell (0.5-1 m long, Ø 0.2-0.5 m) filled with helium gas (0.2-1 bar pressure) in order to stop, thermalize and transport ions from a fragment separator[4], as discussed within the frame of the RIA [Sav02, Sav03, Wei04] and EURISOL [Eur03] projects. In the pilot projects completed so far, prototype cells have been built and tested. They make use of DC electric fields in the range of 10-25 V/cm in order to transport the ions towards a nozzle (optionally RF field nozzle) and further to the exit hole. Due to the DC dragging field, the time that ions do spend in the cell is drastically reduced (less than 10 ms) compared to the evacuation time of the chamber by the flow itself

[4]Beams with a large spatial and energy divergence are injected in such a large gas cell in order to avoid high ionizing rate Q.

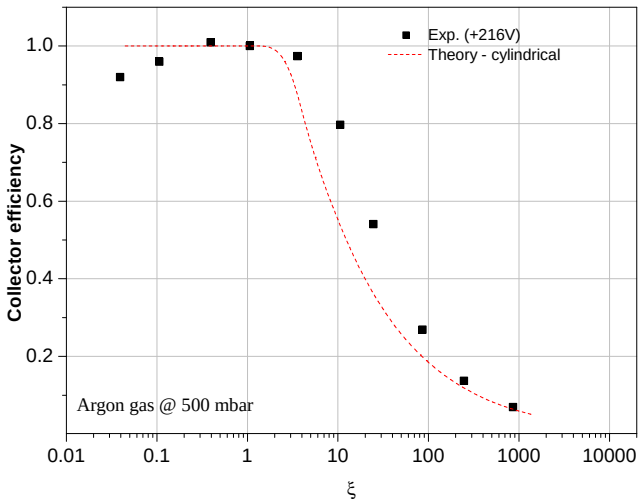

Fig. 5.17: The collector efficiency (symbols) in the 10 mm channel ion guide filled with argon gas at 500 mbar pressure as function of the universal parameter ξ given by eq.(5.1). The voltage applied between the electrodes is +216 V. The dashed line represents the theoretical efficiency as given by eq.(4.26) for a cylindrical ionization chamber with the dimensions shown in Fig.4.7.b.

(usually tens of seconds). If one considers a 50 cm long gas cell filled with 1 bar of helium gas and a 25 V/cm DC electric field applied along the chamber, according to the eq.(5.1), the parameter ξ is equal to 2 (space charge limit) when the ionizing rate is $Q = 5.6 \cdot 10^6$ cm^{-3}s^{-1}. Such a chamber is capable of stopping 6.38 MeV/amu ^{58}Ni ions which would create $9 \cdot 10^6$ electron-ion pairs/ion. Assuming a ^{58}Ni beam with a spot size of 10 cm diameter results that an intensity of 2450 pps of the ^{58}Ni beam is sufficient for the space charge limited regime to occur. This is a very low beam current, therefore such a system would never work efficiently to stop, store and transport ions. However, looking at Table 4.5 in the section 4.5 one can observe that for a 50 cm long cell filled with helium gas and an applied field of 25 V/cm the space charge density reaches its steady state within hundreds of milliseconds

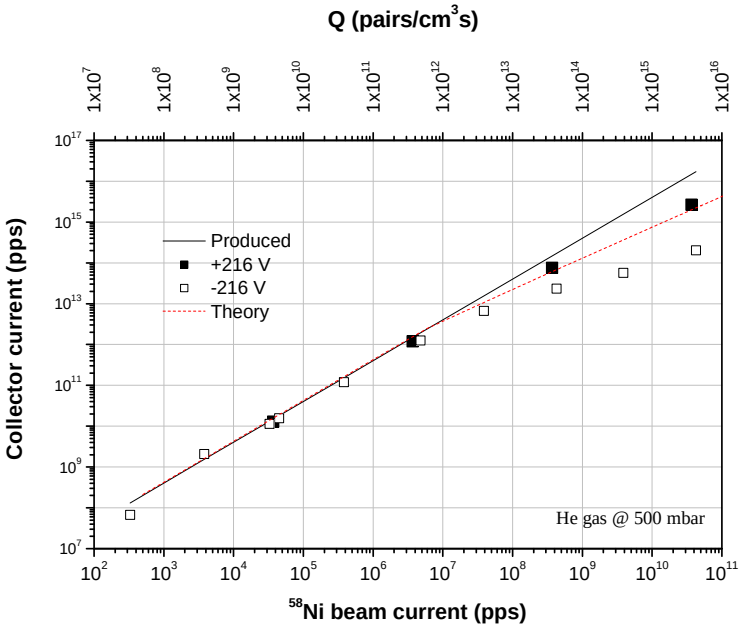

FIG. 5.18: The collector current in the 10 mm channel ion guide filled with helium gas at 500 mbar pressure as function of the primary beam intensity. The full squares are the data obtained with a +216 V biasing voltage and the open squares represent the results obtained with -216 V applied on one electrode. The full line corresponds to the total number of charge pairs produced per second and the dashed line is the result of the calculation for a cylindrical ionization chamber with 1.8 cm spacing of the electrodes and 2 cm the radius of the inner electrode (eq.(4.26) was used). The average energy lost by the ^{58}Ni ions in the cell is 17 MeV. Note the double log-scale.

independently on the ionization rate. Hence, due to the 10 ms evacuation time of the cell by the drift of the heavy ions the steady state of the space charge density is never reached and the counteracting field produced by the space charge is much smaller than the result predicted by the eq.(4.16). A complete description of the space charge in such a large gas cell must include the time evolution as well (see eq.(4.11)). The limitation of a drift gas cell comes from the recombination-free working regime, as the created buffer gas ions and the ions of interest have to be transported and confined towards the exit hole. Considering a 6.38 MeV/amu ^{58}Ni beam with an intensity of $2.5{\cdot}10^3$ pps and a 10 cm spot size diameter stopped in 1 bar of helium, one finds that at the end of the nickel track (the last centimeter of the track) the total amount of created ions is $3{\cdot}10^7$ ions/s. Confining these ions in a sphere with 1 mm radius requires electrical fields as high as 430 V/cm in order to compensate for the mutual repulsion of the ions in the space charge cloud. This is technically feasible but challenging and one should point out that the exit hole diameter is usually in the sub-millimeter domain, thus even higher confining electrical fields are required in order to focus the ions towards the exit hole.

In a small gas cell as those used at LISOL laser ion source, relatively high electric fields can easily be applied. The cyclotron beam entering the gas cell is well focused in a spot having a diameter of 6 mm, thus the ionization rate Q can be very high at relatively low beam currents. The space charge limit (i.e. zero net field at the anode) in 500 mbar argon and 117.5 V/cm electric field applied between the two electrodes in the large gas cell is achieved for an ionization rate of about $1.67{\cdot}10^{10}$ electron-ion pairs/cm^{3}s corresponding to a ^{58}Ni beam with an intensity of $\cdot 10^5$ pps entering the gas cell. The space charge limit in 500 mbar argon(helium) and 120 V/cm electric field applied between the two electrodes in the 10 mm channel gas cell

Table 5.5: The experimental ion collector efficiency[§] with V_0=-216 V (f^{exp}_{IC-}) and V_0=+216 V (f^{exp}_{IC+}) applied between the two parallel plates ($d_0 = 1.8$ cm) in the 10 mm channel cell filled with 500 mbar helium gas, and the corresponding theoretical values of the collector efficiency ($f^{theor}_{IC-(+)}$) and width of the field free zone ($s^{theor}_{-(+)}$) as for an equivalent cylindrical ionization chamber (see Fig.4.7.b).

	Experimental		Theoretical			
	V_0	V_0	V_0	V_0	V_0	V_0
	-216V	+216V	-216V	+216V	-216V	+216V
I_{beam}	f^{exp}_{IC-}	f^{exp}_{IC+}	f^{theor}_{IC-}	f^{theor}_{IC+}	s^{theor}_{-}	s^{theor}_{+}
(pps)	(%)	(%)	(%)	(%)	(mm)	(mm)
10^5	81.7	83.5	100.0	100.0	0.0	0.0
10^6	69.5	81.2	100.0	100.0	0.0	0.0
10^7	52.0	62.0	58.0	88.1	6.3	2.9
10^8	23.2	52.0	31.5	53.2	11.0	9.8
10^9	7.2	30.0	17.5	30.8	13.9	13.5
10^{10}	2.0	19.0	9.3	17.6	15.7	15.5

[§] The experimental collector efficiency at each beam intensity was calculated using a straight line interpolation to the two nearest data points.

is achieved for an ionization rate of about $5{\cdot}10^{10}(5{\cdot}10^{11})$ electron-ion pairs/cm^{3}s corresponding to a ^{58}Ni beam with an intensity of $5{\cdot}10^5(6{\cdot}10^6)$ pps entering the gas cell. Beyond the space charge limit the collection of charges in the electrodes gap can be explained by the formation of field free zones in the anode vicinity, using the correct values of the applied electric field (e.g. analogy with the field in a regular geometry of the electrodes). In the field free region the electron-ion pairs are freely recombining, thus the charges created in this zone do not give contribution to the collector current.

The effect of DC electrical fields on the ion signal extracted from the laser ion source

The extraction of ions from the gas cell when electric fields are applied between the two plates can be affected by the competition between the evacuation by the gas flow and the drift of the ions towards the cathode electrode.

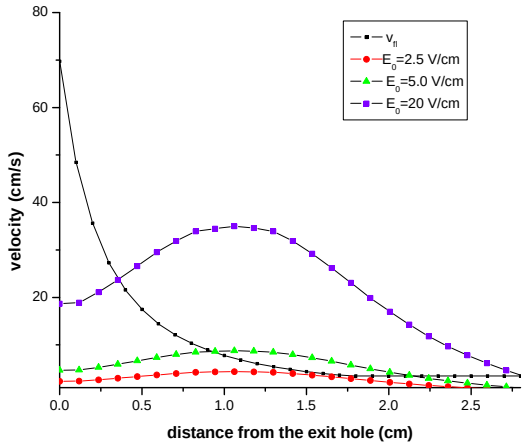

FIG. 5.19: The calculated flow velocity in the large cell filled with 500 mbar argon (line+small symbol) and the ion drift velocity along the extraction axis of the cell (line+big symbol) for different electric fields E_0 applied between the plates. Poisson Superfish [POIpr] was used to calculate the electric field along the extraction axis. No space charge effect is considered.

The velocity of an ion in the cell has two major components, one due to the flow (v_{fl}) and one due to the drift in the electric field ($v_d = \mu_+ \cdot E$ with E being the electric field strength). Other processes such as Coulomb repulsion between the ions and diffusion can add more components to the resultant velocity of the ion. Nevertheless, the transport of ions proceeds through the gas flow in the regions of the cell where the flow velocity is larger than the drift velocity. It is important to recall here that it has been shown in the section 4.5 (see Fig.4.4.b) that in the case of the large cell the electric field penetrates at the exit hole region which may influence the evacuation of ions. Fig.5.19 shows the calculated flow velocity and the

drift velocity of ions along the extraction axis of the gas cell for different electric fields applied between the plates. The flow velocity has been calculated using the conductance of the exit hole as defined in section 1.3.1[5]. The drift velocity along the extraction axis was calculated using the values of the electric field computed with the Poisson Superfish code [POIpr]. The transversal electric field (i.e. across the gap of the electrodes) can be calculated using eq.(4.16). As most of the ions are created/implanted at 1 cm distance from each electrode (in the middle of the gap of the electrodes) and at a distance of about 2.8 cm from the exit hole, one has to compare the time scale for collection of the ions on the cathode with the time scale for their evacuation by the gas flow. The evacuation time of the large cell by gas flow when filled with 500 mbar argon gas was found to be around 500 ms (see Fig.5.7.a), which is equal to the time that an ion needs to drift 1 cm in a 0.58 V/cm electric field. Nevertheless, in on-line experiments, when a reasonable beam current is implanted into the gas cell, higher electric fields are required in order to efficiently collect the charges. This will shorten the time that ions need to drift towards the cathode and thus their collection on the cathode will prevail against evacuation by the gas flow. As can be seen in Fig.5.19, increasing the field applied between the plates in the cell leads to an increase of the drift velocity of ions in a direction parallel to the extraction axis. When the electric field between the plates is 20 V/cm, the flow velocity is higher than the drift velocity along the extraction axis of the cell in a region close to the exit hole having a width of 5 mm. Ions from this region will be evacuated by the flow, while in other zones of the cell the motion of ions is due to the drift in electric field.

Continuous DC field

The effect of DC electric field in the gas cell was studied by measuring the intensity of the separated beam on mass 40 and mass 58 with the lasers on extracted from the ion source at different applied voltages on the electrode. The results are shown in Fig.5.20. A low cyclotron beam intensity, $I_{beam} = 2.9{\cdot}10^3$ pps, was chosen for the case of the ^{40}Ar signal measurement. The mass 40 separated beam current is measured by increasing the electric field from 0.1 V/cm up to 60 V/cm. Measuring the ^{58}Ni signal at low beam currents implanted in the cell is more difficult. Therefore, a cyclotron beam of $I_{beam} = 5.76{\cdot}10^8$ pps was chosen in order to measure the influence of a DC field ($0.1 \div \sim$100 V/cm) on the laser produced ^{58}Ni beam current extracted from the ion source. Table 5.6 gives the calculated width (w) of the collection zone (i.e. the difference $d_0 - s$ between the electrodes gap width, d_0, and the width of the field free zone s - see section 4.5) and the ion collector efficiency (f_{IC}) as for a plane parallel ionization chamber, and the (laser) ion source efficiency (ϵ_{IS}) for extraction of a) ^{40}Ar and b) laser produced ^{58}Ni ions from the ion source as resulting from the experimental data presented in Fig.5.20.

It is observed from Fig.5.20 and Table 5.6.a that for the case of a low intensity cyclotron beam ($I_{beam} = 2.9{\cdot}10^3$ pps) increasing the electric field strength results in a more effective collection of ions and thus a lower efficiency for extraction of ^{40}Ar ions from the gas cell. When the electric field is lower than 2 V/cm the efficiency for extraction of ^{40}Ar ions from the gas cell is the same as in the case when no electric field is applied in the cell (see Fig.5.12). This is due to the fact that the ions are collected in a narrow region close to the cathode where their creation is actually

[5]However, the actual flow velocity in the region close to the exit hole can be around 30% of the sound velocity [Bru01].

much lower than in the beam interaction zone. Beyond field values of 2 V/cm not only the collection of ions is performed over a wider range of the electrodes gap but the field penetrating at the exit hole becomes also larger. At the maximum field of 100 V/cm applied between the plates, the electric field at the exit hole is about 27 V/cm (see Fig.4.4.b) thus the drift velocity of ions is higher than the flow velocity in this zone (see Fig.5.19). Nevertheless ^{40}Ar ions created very close to the exit hole are extracted from the gas cell and the ion source efficiency is $5{\cdot}10^{-4}$%. The signal of laser produced ^{58}Ni has a smooth dependence on the applied electric field between the electrodes (see Fig.5.20). The laser ion source efficiency for extraction of laser produced ^{58}Ni ions when electric fields lower than 1 V/cm are applied in the cell is approximately the same as without application of electric fields (see Fig.5.12). As can be seen in Table 5.6.b the ion collector efficiency for a cyclotron beam of $5.76{\cdot}10^{8}$ pps and maximum applied electric field (100 V/cm) is only 7% (ions are collected in a region of 1.3 mm width close to the cathode). The collector efficiency is very low and most of the gap of the electrodes is thus field free. Nickel implanted ions will therefore neutralize during their journey to the exit hole where subsequent laser ionization takes place. Nevertheless, when the applied electric field is 100 V/cm the laser ion source efficiency is 25 times lower than for the lowest applied electric field (0.1 V/cm). This is due to the fact that as the electric field

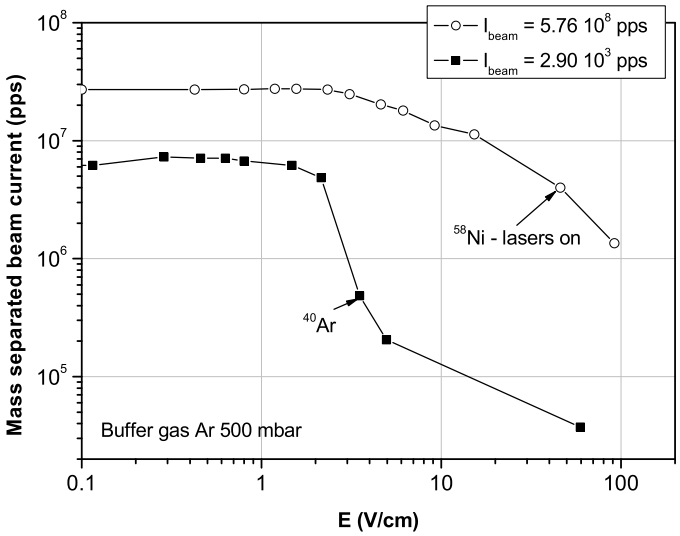

FIG. 5.20: The intensity of the beam on mass 40 (full squares) and on mass 58 with the lasers on (open circles) extracted from the laser ion source as function of the amplitude of the DC electric field applied between the electrodes. The large cell (see Fig.5.13.a) filled with argon at 500 mbar pressure was used. Note that the cyclotron beam currents were different for the two measurements.

applied between the plates is increased so does the field penetrating at the exit hole. It has been shown before (see Fig.5.10 and the associated text) that most of the laser produced nickel ions exiting the gas cell come from a region close to the exit hole. If the electric field there is high, the drift velocity becomes larger than the flow velocity and ions are driven onto the cell walls instead of following the flow stream-lines towards the exit hole.

The collection of Ar ions in the gas cell at low ionization rates using relatively low electric fields (< 2 V/cm) can reduce the number of electron ion pairs in the cell without inducing major losses of laser produced ions. It is essential to know in the case of a short cyclotron beam pulse how the argon ions are collected during the beam pulse and after. Therefore, the evacuation properties of the Ar ions from the gas cell have been studied at the LISOL mass separator using pulsed cyclotron beams and continuous DC electrical fields. The time profile of the Ar ion signal extracted from the ion source is recorded. A typical time profile of the signal on mass 40 extracted from the large gas cell filled with argon gas at 500 mbar when a short ^{58}Ni cyclotron beam pulse (10 ms width) of low intensity ($1.2{\cdot}10^5$ pps) enters the ion source, and no electrical field in the cell is used, looks like in Fig.5.21 (the curve labelled "OFF"). When a continuous DC electrical field is applied between the electrodes, the maximum ion signal on mass 40 shifts towards short times. The calculated width of the ion collection zone (w) and the ion collector efficiency (f_{IC}) as for a DC beam current $I_{beam} = 1.2{\cdot}10^5$ pps for a plane parallel geometry (d_0 = 2 cm) when electrical fields with the strengths as in Fig.5.21 are applied across the electrodes gap are given in Table 5.7, together with the corresponding ratios $\frac{A-A_{OFF}}{A_{OFF}}$, where A_{OFF} and A are the areas of the time profiles from Fig.5.21 without electrical field and with an applied electrical field with the given amplitude, respectively. It is important to mention here that using eq.(4.15) it is possible

Table 5.6: The calculated width (w) of the collection zone and ion collector efficiency (f_{IC}) as for a plane parallel ionization chamber, and the (laser) ion source efficiency (ϵ_{IS}) for extraction of a) ^{40}Ar and b) laser produced ^{58}Ni ions from the ion source as resulting from the measurements presented in Fig.5.20. Note that for each case a different beam current I_{beam} was implanted in the gas cell.

a) $I_{beam} = 2.9{\cdot}10^3$ pps, ^{40}Ar

E_0 (V/cm)	w (cm)	f_{IC} (%)	ϵ_{IS} (%)
0.1	0.09	4.5	0.15
1.0	0.28	14.2	0.15
10.0	0.9	45.0	0.0037
100.0	2.0	100.0	0.0005

b) $I_{beam} = 5.76{\cdot}10^8$ pps, ^{58}Ni

E_0 (V/cm)	w (cm)	f_{IC} (%)	ϵ_{IS} (%)
0.1	0.0042	0.2	4.7
1.0	0.014	0.7	4.7
10.0	0.043	2.1	2.2
100.0	0.135	7.0	0.2

to deduce that for a parallel plate ionization chamber having the spacing of the electrodes of 2 cm, the saturation density of the space charge is reached within 10 ms when electric fields of 60 V/cm are applied across the gap. For lower fields the space charge saturation is practically not reached and the density of the space charge can be calculated using eq.(4.13).

For an applied electric field $E_0 = 0.12$ V/cm, the maximum ion signal is observed at 180 ms which corresponds to the evacuation time from a region 1.5 cm away from the exit hole. The collection of the primary electrons is effective in that region of the gas cell, while during their journey to the exit hole the ions drift a negligible distance in this low electric field. In the beam interaction zone the electron-ion pair density is $1.5{\cdot}10^8$ cm^{-3} (using eq.(3.15) and $Q = 2.1 \cdot 10^{10}$ cm^{-3}s^{-1}) provided that the applied field penetrates only within a narrow region of the gap. The ion collector efficiency for a DC beam with the same intensity and a DC field of 0.12 V/cm is only 1.9% as one can see in Table 5.7. If the field is increased further to $E_0 = 2.15$ V/cm, the maximum ion signal is recorded at 85 ms which corresponds to the evacuation time of the gas cell from a region 1 cm from the exit hole. There the creation of charges is due to the energetic photons emitted during the cyclotron

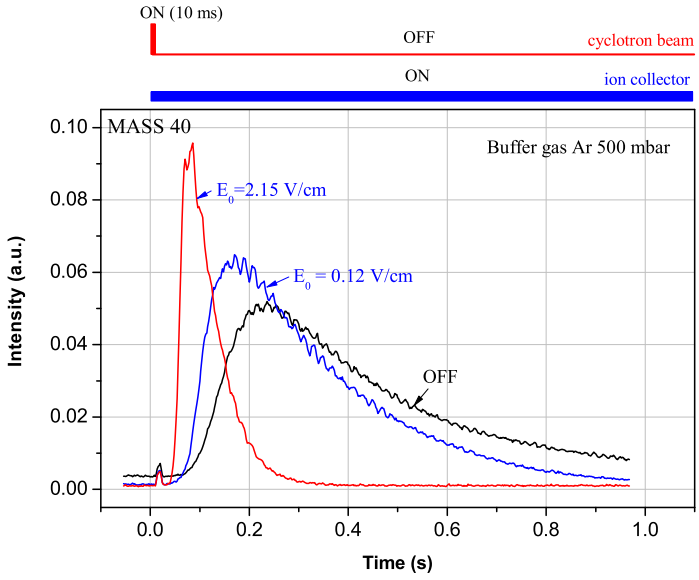

FIG. 5.21: A pulsed beam of ^{58}Ni (10 ms width) enters the laser ion source. The intensity of the beam is $1.2{\cdot}10^5$ pps as measured in DC mode. The large cell filled with argon gas at 500 mbar was used. The time behavior of the extracted ions on mass 40 is recorded without electric field (the curve labelled "OFF") and with a continuous DC field applied between the electrodes with different amplitudes (as indicated on the graph).

beam impact. The ion collector efficiency using a DC beam current with the same intensity and an applied DC field of 2.15 V/cm is 8.2%, therefore the field free zone spans over 1.84 cm of the gap. The width of the field free zone starts to decrease when the beam pulse is stopped, such that after 200 ms the electron-ion pair density has decreased down to $5{\cdot}10^6$ cm^{-3} and all the remaining electrons can be collected with a 2.15 V/cm electric field. During 200 ms the cloud of charges (created electrons and ions and implanted ions) moved 7 mm in the electrodes gap along the extraction axis of the cell due to the gas flow. The cloud continues to move longitudinally[6] with $v_{fl} = 2$ cm/s towards the exit hole, while the transversal drift velocity[7] $v_d = 7.3$ cm/s is almost 4 times higher, thus most of the ions are collected onto the cathode before reaching the exit hole region. Inspecting Table 5.7 one can see that increasing the ion collection efficiency in the beam interaction zone by a factor 4 leads to a decrease of the ^{40}Ar ion signal by a factor $\sim$2 (comparing the quantities $1 - \frac{A-A_{OFF}}{A_{OFF}}$). This means that ions which are created close to the exit hole have still higher chance to be evacuated before being collected onto the cathode (consisting here of one plate and the rest of the cell body).

The use of continuous DC field in the gas cell in order to collect the electrons and ions created by the stopping of a DC cyclotron beam is limited by the space charge effects. For a low beam current (i.e $2.9{\cdot}10^3$ pps) a strong field can ensure a charge collection efficiency equal to unity, thus the buffer gas ions and the ions of interest are collected before their evacuation from the gas cell. The ion source efficiency for extraction of Ar ions can be reduced by few orders of magnitude in this manner. However, the collection of the Ni ions before their neutralization and subsequent laser re-ionization is undesirable. For high beam currents (i.e. $5.76{\cdot}10^8$ pps) the charge collection efficiency is very low even when the applied field is as high as 100 V/cm. Most of the Ar ions as well as Ni ions in the beam interaction zone recombine before their evacuation from the cell. Penetration of the field in the exit hole region can lead to an increase of the amount of Ar ions evacuated from this zone of the gas cell. This means that once that the electrons are collected from this region, the survival chance of the Ar ions is increased and those ions which are faster evacuated by the flow than drifted to the cathode can be extracted from the

[6] or along the extraction axis

[7] transversal to the electrodes, across the gap

Table 5.7: The calculated width of the ion collection zone (w) and the ion collector efficiency (f_{IC}) as for a DC beam current $I_{beam} = 1.2{\cdot}10^5$ pps for a plane parallel geometry ($d_0 = 2$ cm) when electrical fields with the strengths as in Fig.5.21 are applied across the electrodes gap, and the corresponding ratios $\frac{A-A_{OFF}}{A_{OFF}}$, where A_{OFF} and A are the areas of the time profiles from Fig.5.21 without electrical field curve labelled "off") and with an applied electrical field with the given amplitude, respectively.

E_0 (V/cm)	w (cm)	f_{IC} (%)	$\frac{A_{OFF}-A}{A_{OFF}}$ (%)
0.12	0.0381	1.9	-15.3
2.15	0.165	8.2	-59.5

ion source and mass separated. However, the neutral nickel atoms are resonantly ionized during their transport towards the exit hole by the gas flow using high repetition rate laser pulses. As these ions approach the exit hole region the electric field they experience becomes stronger because the space charge in that region has a much lower density. Consequently, part of the laser produced ions reach a point when they are faster drifted towards the cathode than flown to the exit hole. As result, the loss of laser produced ions increases with the applied electric field. In order to keep the advantage of electron collection close to the exit hole and minimize the loss of laser produced ions due to the faster drift to the cathode, the collection of charges could be performed during a short pulse of electric field after the cyclotron beam pulse.

Pulsed electric field

It is essential to search for a working regime of the laser ion source where the use of DC electrical fields is feasible in the sense of increasing the laser ion source efficiency and selectivity. It was shown above that the electrons and the buffer gas ions created by the primary beam can be collected using DC electrical fields. However, once that the electrons and buffer gas ions have been collected the action of the electric field must stop in order to allow laser produced ions to be evacuated from the gas cell. One can imagine a pulsed mode scheme with a short pulse of a cyclotron beam being implanted in the gas cell, a "waiting" period for the electron-ion pair density to decay through recombination processes and neutralization of 99% of ions of interest (see Fig.3.13 in section 3.7) followed by a pulse of electrical field to remove effectively the remaining electrons and ions. Laser ionization is to be more effective after the DC field pulse, assuming all the electrons created by the primary beam have been collected, thus the recombination of the photo-ions with the primary electrons is no longer possible. However, this method has to be adjusted for every particular case of a cyclotron beam type and intensity, buffer gas, element to be laser ionized, cell geometry and intensity of the electric field.

A first step in adjusting the above procedure is to ensure an effective collection of the electrons and buffer gas ions without inducing significant losses of primarily stopped and/or laser produced Ni ions. The evacuation of Ar ions is essentially determined by the recombination with the electrons created by the primary particle beam. The presence of these electrons limits the amount of the Ni ions surviving recombination as well. When electrical fields are used in the gas cell, an increased signal of ^{40}Ar ions extracted from a region of the ion source compared to the case when no electric field is present will be "translated" as an effective collection of the primary electrons in that zone, while the motion of ions remains flow dominated. Considering an applied field of 30 V/cm in 500 mbar argon gas one can easily calculate that during a 1 ms pulse of DC field the ion will drift only 1 mm while the electrons are collected at the anode in their totality. Therefore, for an electric field lower than 30 V/cm applied in a pulse of 1 ms width the ions are practically unperturbed and the "ion collector efficiency" (f_{IC}) essentially applies to the collection of electrons.

The evacuation properties of buffer gas ions from the ion source have been studied using a cyclotron beam pulse of 1 ms width implanted in the large gas cell filled with argon at 500 mbar pressure. The ^{58}Ni beam intensity was decreased down to $2{\cdot}10^2$ pps as measured in DC mode in order to minimize the space charge effects. A pulse of electric field (1 ms width) is applied with a delay of 3 ms with respect to the start of the cyclotron pulse. The time profile of the ion signal on mass

40 extracted from the gas cell is measured and the results are plotted in Fig.5.22 for different amplitudes of the electric field pulse (E_0).

When no DC field pulse (curve labelled "off") is applied the maximum ion signal is recorded at 450 ms which corresponds to the evacuation of the cell by gas flow from the beam interaction zone. The ^{58}Ni beam creates electron-ion pairs with a rate $Q = 3.5 \cdot 10^7$ cm^{-3}s^{-1} and the density of charges in the beam interaction zone at the end of the cyclotron pulse is $3.5 \cdot 10^4$ cm^{-3}. When the pulse of electric field is applied, only 0.01% of electron-ion pairs have recombined. If the amplitude of the DC field pulse is 3 V/cm, the collector efficiency for electrons should be 90%. It is important to estimate the losses of ions due to drift. The drift velocity of ions in an electric field of 3 V/cm is 10 cm/s in argon at 500 mbar pressure meaning that during 1 ms those ions which are closer than 0.1 mm to the cathode will be collected. However, this distance is comparable with the mean displacement of the ions due to the diffusion (see section 3.9), thus the loss of ions due to their collection is negligible.

Table 5.8 summarizes the results plotted in Fig.5.22, in terms of $\frac{A-A_{OFF}}{A_{OFF}}$, where

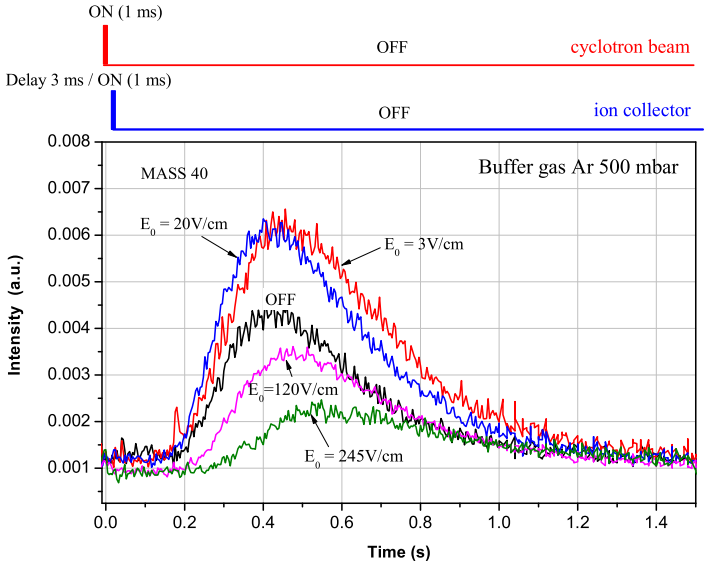

Fig. 5.22: A pulsed beam of ^{58}Ni (1 ms width) enters the laser ions source. The intensity of the beam is $2 \cdot 10^2$ pps as measured in DC mode. The large cell filled with argon gas at 500 mbar was used. The time behavior of the extracted ions on mass 40 is recorded without electric field (the curve labelled "OFF") and with a pulse (1 ms width) of an electric field applied between the electrodes with different amplitudes E_0 (as indicated on the graph) and with a time delay of 3 ms with respect to the start of the cyclotron beam pulse.

A_{OFF} and A are the areas of the time profiles from Fig.5.22 without the pulse of DC field and with a DC field pulse with the amplitude E_0, respectively. The calculated width of the zone where the charges are collected and collector efficiency as for a DC beam of $2{\cdot}10^2$ pps and a DC electric field with the amplitude E_0 are also given in Table 5.8. The ion signal when a field pulse with the amplitude of 3 V/cm and 1 ms width is applied increases with 36% compared to the signal without DC field pulse. The result for a 20 V/cm field pulse is roughly similar to the 3 V/cm pulse. The fact that the ion signal is not reduced using DC field pulses (1 ms width) with these amplitudes is consistent with the fact that the motion of ions is flow dominated and it is practically not perturbed by the electric field as the drift distance is negligible. Increasing the amplitude of the applied electric field up to 120 V/cm results in a drastic reduction of the ^{40}Ar ion signal intensity. For a field amplitude $E_0 = 245$ V/cm the ion signal is 34% less than in the case when no DC field pulse is applied. For this amplitude of the DC field the ions will drift a distance of 8.3 mm towards the cathode during the field pulse, thus a large fraction of the Ar ions, and implicitly Ni ions, will be collected during this period.

Two alternative procedures for the application of the field pulse can be identified here:

(i) the removal of electrons only from the beam interaction zone by the application of a low DC field pulse (< 20 V/cm) after the beam pulse;

(ii) the removal of both electrons and (partially) ions from the beam interaction zone by the application of a high DC field pulse (> 100 V/cm).

Using the procedure of type (i) can lead to an increase of the amount of Ar ions extracted from this region and implicitly of primarily stopped Ni ions which survive recombination. Thus the ion source efficiency for the extraction of "non-resonant" nickel ions is enhanced. The procedure of type (ii) ensures an increase of the laser ion source selectivity by reducing the amount of "non-resonant" Ni ions extracted from the ion source. However, the collection of Ni ions before their neutralization must be carefully employed as the principle of the laser ion source is based on the neutralization of a major part of the ions of interest and their subsequent laser re-ionization close to the exit hole of the gas cell. Therefore, the method of type

TABLE 5.8: The calculated width of the ion collection zone (w) and the ion collector efficiency (f_{IC}) as for a DC beam current $I_{beam} = 2.0{\cdot}10^2$ pps for a plane parallel geometry ($d_0 = 2$ cm) when electrical fields with the strengths as in Fig.5.22 are applied across the electrodes gap, and the corresponding ratios $\frac{A-A_{OFF}}{A_{OFF}}$, where A_{OFF} and A are the areas of the time profiles from Fig.5.22 without electrical field (curve labelled "off") and with an applied electrical field with the given amplitude, respectively.

E (V/cm)	w (cm)	f_{IC} (%)	$\frac{A-A_{OFF}}{A_{OFF}}$ (%)
3	1.8	90	+36
20	2.0	100	+23
120	2.0	100	-14
245	2.0	100	-34

(ii) must be adjusted so as to allow the neutralization of Ni ions in the time interval between the cyclotron beam pulse and the field pulse.

Using the procedure of type (i) it is essential to adjust the time delay between the cyclotron beam pulse and the field pulse in order to maximize the amount of ions extracted from the beam interaction zone of the gas cell. This has been measured using the gas cell configuration and cyclotron beam settings as in the previous example (i.e. 1 ms beam pulse, $2{\cdot}10^2$ pps as in DC mode). For this low beam intensity it is difficult to measure the mass separated ^{58}Ni current, thus the time profile of the ion signal on mass 40 extracted from the ion source was recorded and the results are shown in Fig.5.23. The electric field pulse with an amplitude of 20 V/cm and width of 1 ms is applied with different time delays with respect to the start of the cyclotron pulse. This field amplitude ensures an electron collection efficiency equal to unity. When no field pulse is applied the

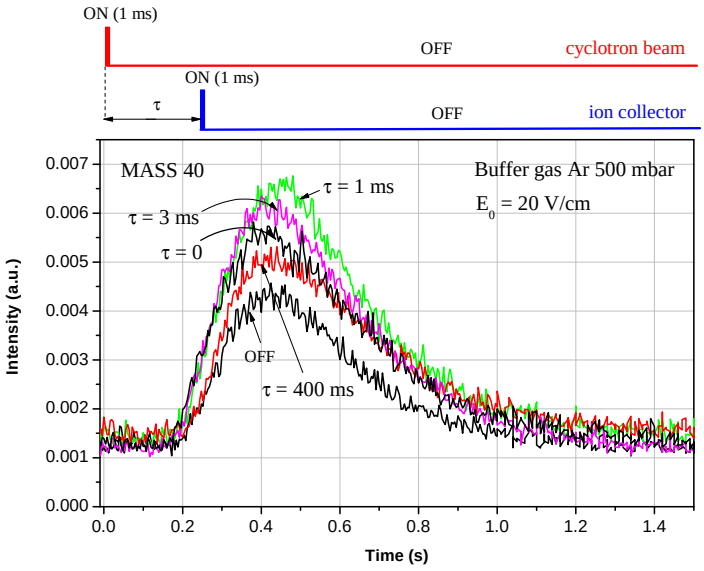

Fig. 5.23: A pulsed beam of ^{58}Ni (1 ms width) enters the laser ions source. The intensity of the beam is $2{\cdot}10^2$ pps as measured in DC mode. The large cell filled with argon gas at 500 mbar was used. The time behavior of the extracted ions on mass 40 is recorded without electric field (the curve labelled "OFF") and with a pulse (1 ms width) of an electric field applied between the electrodes (E_0 = 20 V/cm) with different time delays with respect to the start of the cyclotron beam pulse (as indicated on the graph).

calculated electron-ion pair density in the beam interaction zone is $3.5{\cdot}10^4$ cm^{-3}. This density remains constant for a long period of time as 28 s are required to be halved by recombination processes. However, in reality the energy, spatial and

time distribution of the cyclotron beam prevents the ionization rate Q from being constant. The ^{40}Ar ion signal increases when the field pulse is applied during the beam pulse, τ=0 (see Fig.5.23). This clearly shows that even at very low beam intensity the electron-ion recombination processes are present. The maximum ion signal is obtained when the field pulse is applied immediately after the cyclotron beam pulse, τ=1 ms. If the time delay τ is further increased the electron-ion recombination reduces the amount of electrons which can be collected by the field pulse, and consequently the ^{40}Ar ion signal extracted from the ion source decreases. However, even at long time delays (i.e. τ=400 ms) the extracted ion signal can be improved by collecting the remaining electrons.

Application of a field pulse immediately after the cyclotron beam pulse is suitable for low beam intensities. In the case of high beam currents (i.e. high ionization rates) the charge density immediately after the beam pulse is high, the applied electric field does not penetrate across the electrodes gap and field free zones are formed. Consequently, most of the electron-ion pairs in the beam interaction zone recombine without experiencing electric field forces. An approach to overcome space charge effects and effectively collect the remaining electrons and ions is to increase the time delay between the high intensity beam pulse and the field pulse. This delay must be shorter than the evacuation time from the beam interaction zone of the gas cell. This has been studied using a 50 ms ^{58}Ni beam pulse with the intensity of $1.4{\cdot}10^{10}$ pps as measured in DC mode stopped in the large cell filled with 500 mbar argon. The time profile of the mass separated ^{58}Ni beam extracted from the ion source without laser ionization is recorded. The result obtained in the absence of an electric field pulse is plotted in Fig.5.24 as the curve labelled "OFF". The maximum ion signal is observed at 500 ms, i.e. the evacuation time of the cell from the cyclotron beam position where the nickel ions are stopped. The ionization rate is $Q = 2.5 \cdot 10^{15}$ cm^{-3}s^{-1} and the electron-ion density immediately after the cyclotron beam pulse is 10^{10} cm^{-3}. This density drops down to $2.8{\cdot}10^{6}$ cm^{-3} after 350 ms (400 ms with respect to start of the beam pulse) during the transport to the exit hole by the gas flow. Collecting all the remaining electrons at this moment results in the formation of a positive ion cloud which induces an electric field of only $\sim$ 1.25 V/cm, thus the Coulomb repulsion among ions is negligible. If the applied field is high, depending on the duration of the field pulse, the remaining ions can also be collected. The time profiles of the ion signal on mass 58 measured with electric field pulses (245 V/cm) with different widths and a time delay of 400 ms with respect to the start of the beam pulse are plotted in Fig.5.24. Table 5.9 summarizes the results from Fig.5.24 in terms of $\frac{A-A_{OFF}}{A_{OFF}}$ for each field pulse width, where A_{OFF} and A are the areas of the time profiles from Fig.5.24 for $t > 0.4$ s, without electrical field (curve labelled "off") and with an electrical field pulse with the given width (as indicated), respectively.

Inspecting Fig.5.24 and Table 5.9 one can observe that the ^{58}Ni ion signal with a pulse of electric field is always less than without the field pulse due to the high drift velocity of the ions during the field pulse. As the width of the electric field pulse is increased from 1 ms to 10 ms, the distance that ions drift in argon at 500 mbar increases from 8.3 mm up to 8.3 cm. When a 245 V/cm field pulse with the width of 10 ms is applied in the gas cell the nickel ion signal completely disappears after the field pulse. Neutral nickel atoms can thus be subsequently laser ionized close to the exit hole in an environment free of electron-ion pairs created by the primary beam or other surviving ions. Recalling the results presented in Fig.5.12

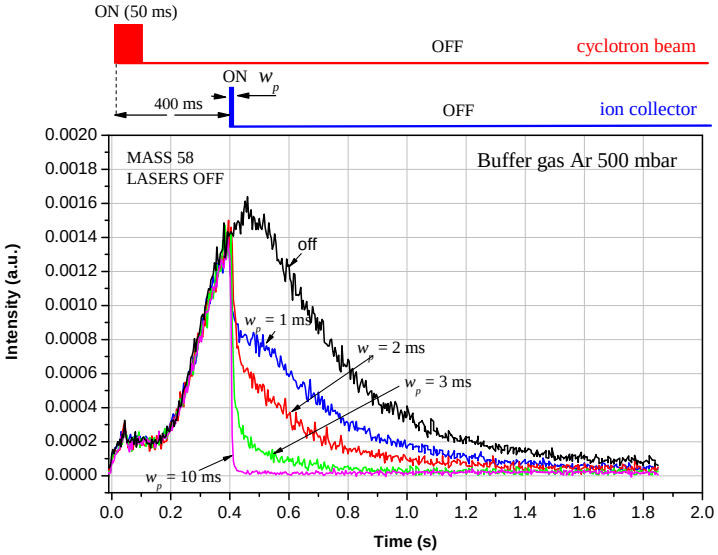

Fig. 5.24: A pulsed beam of ^{58}Ni (50 ms width) enters the laser ions source. The intensity of the beam is $1.4{\cdot}10^{10}$ pps as measured in DC mode. The large cell filled with argon gas at 500 mbar was used. The time behavior of the extracted ions on mass 58 with the lasers off is recorded without electric field (the curve labelled "OFF") and with a pulse of a DC field ($E_0 = 245$ V/cm) with different widths (as indicated on the graph) applied between the electrodes with a delay of 400 ms with respect to the start of the cyclotron beam pulse.

Table 5.9: The width of the electric field pulse (w_p) and the corresponding ratios $\frac{A-A_{OFF}}{A_{OFF}}$, where A_{OFF} and A are the areas of the time profiles from Fig.5.24 for $t > 0.4$ s, without electrical field (curve labelled "off") and with an electrical field pulse, respectively, with the given width applied 350 ms after the cyclotron beam pulse (50 ms width, $1.4{\cdot}10^{10}$ pps as measured in DC mode).

w_p (ms)	$\frac{A-A_{OFF}}{A_{OFF}}$ (%)
1	-48.7
2	-68.3
3	-90.2
10	-98.7

one can see that the laser ion source selectivity for a beam current[8] of $1.4{\cdot}10^{10} \cdot \frac{0.05}{2.05}$ = $3.4{\cdot}10^{8}$ pps is ∼100. This selectivity can be increased by orders of magnitude if the "off-resonant" nickel ion signal extracted from the ion source is reduced by applying a high field pulse before the laser ionization. It is important to increase the selectivity of the laser ion source as the "non-resonant" ion signal extracted from the ion source may consist of molecular-ion and/or other ionic species having the same A/q ratio as ^{58}Ni and which can not be dissociated. It will be shown in the section 5.2 that this is particularly important when radioactive ions are to be extracted from the ion source, mass separated and their γ-decays measured at a detection station. The contribution of "non-resonant" ions implanted at the detection station can significantly increase the background in the γ-spectrum.

The second step in adjusting the method mentioned in the beginning of this section is to apply laser ionization after the electric field pulse. The extraction of laser produced ^{58}Ni ions from the large gas cell filled with 500 mbar argon was studied using the following procedure: an electrical field pulse of 5 ms width and 10 V/cm amplitude is applied with different time delays with respect to the ^{58}Ni cyclotron beam pulse (50 ms width) and a subsequent laser pulse is fired only once, 100 ms after the start of the cyclotron pulse. The results obtained with a cyclotron beam current of $2.9{\cdot}10^{10}$ pps as measured in DC mode are plotted in Fig.5.25. The time profile labelled "OFF" from Fig.5.25 corresponds to the ion signal for the case when no electric field pulse was applied. The effect of the laser pulse is immediately observed at the moment when it is fired (100 ms). The nickel ions are produced in the lasers beam path along the extraction axis of the gas cell (perpendicular on the cyclotron beam direction) and the maximum signal is observed at 180 ms which corresponds to the evacuation of the cell by the gas flow from a zone 1.5 cm distance from the exit hole. The cyclotron beam pulse creates electron-ion pairs with a rate $Q = 5.1 \cdot 10^{15}$ cm^{-3}s^{-1} and the density at the end of the cyclotron pulse is $7.2{\cdot}10^{10}$ cm^{-3} in the beam interaction zone. When the lasers are fired (50 ms later), the density is decreased to $2.0{\cdot}10^{7}$ cm^{-3}. Collection of charges in this density of electron-ion pairs is effective only if electrical fields stronger than 9 V/cm are used. Therefore an electric field pulse with an amplitude of 10 V/cm was used.

Table 5.10 gives the calculated electron-ion pair density after a time delay τ, ant the corresponding width of the ion collection zone (w) and ion collector efficiency (f_{IC}) for a plane parallel geometry (d_0 = 2 cm) when a 10 V/cm field pulse is applied across the electrodes gap at time delay τ as well as the corresponding ratios $\frac{A-A_{OFF}}{A_{OFF}}$, where A_{OFF} and A are the areas of the time profiles from Fig.5.25 without electrical field (curve labelled "off") and with a field pulse, respectively. The electron-ion pair density 10 ms after the end of the beam pulse[9] pulse is 4 times higher than after 40 ms. Electric fields of 45 V/cm are needed in order to efficiently collect all the electrons. However, the ion signal is enhanced with 17% compared to the ion signal without electric field. When the time delay τ is 90 ms, this increase accounts for 62% of the ion signal without electrical field. Applying the electric field pulse after the laser pulse (τ = 150 ms) leads also to an increase of the extracted ^{58}Ni ion signal. This means that the recombination of laser produced ions with the remaining electrons in the gas cell or eventually with the photo-electrons can also be reduced by applying a field pulse after laser ionization.

Once that the optimum time delay sequence between the cyclotron beam pulse,

[8] The quantity $\frac{0.05}{2.05}$ represents the duty-cycle of the cyclotron beam pulsing.

[9] Note the difference of 50 ms between the cyclotron beam pulse start and end.

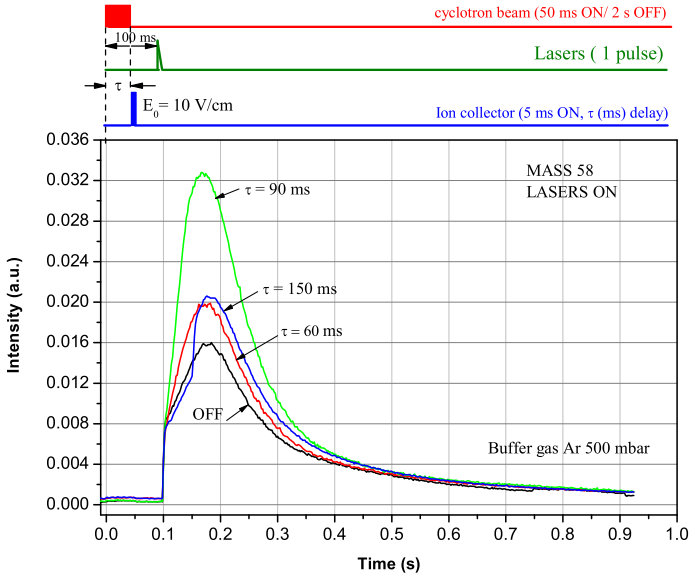

Fig. 5.25: A pulsed beam of ^{58}Ni (50 ms width) enters the laser ions source. The intensity of the beam is 2.9·10^{10} pps as measured in DC mode. The large cell filled with argon gas at 500 mbar was used. A laser pulse is fired 100 ms after the start of the cyclotron beam pulse. The time behavior of the extracted ^{58}Ni ions is recorded without electric field (the curve labelled "OFF") and with a pulse (5 ms width) of a DC field (E_0 = 10 V/cm) applied between the electrodes with different delays with respect to the start of the cyclotron beam pulse (as indicated on the graph).

Table 5.10: The calculated electron-ion pair density after a time delay τ, ant the corresponding width of the ion collection zone (w) and ion collector efficiency (f_{IC}) for a plane parallel geometry (d_0 = 2 cm) when a 10 V/cm field pulse is applied across the electrodes gap with a time delay τ; and the corresponding ratios $\frac{A-A_{OFF}}{A_{OFF}}$, where A_{OFF} and A are the areas of the time profiles from Fig.5.25 without electrical field (curve labelled "off") and with a field pulse, respectively. I_{beam} = 2.9·10^{10} pps.

Delay τ (ms)	$n(\tau)$ (e-ion pairs/cm^{3}s)	w (cm)	f_{IC} (%)	$\frac{A-A_{OFF}}{A_{OFF}}$ (%)
60	1.0·10^8	1.22	62.0	17
90	2.5·10^7	1.9	95.0	62
150	1.0·10^7	2.0	100.0	21

the field pulse and laser pulse was found one can start tuning the amplitude of the electric field. This was studied using a ^{58}Ni beam pulse of 50 ms width, with the intensity of $2.0{\cdot}10^{10}$ pps as measured in DC mode, implanted in the large gas cell filled with argon at 500 mbar pressure. A lasers pulse is fired once with a time delay of 100 ms with respect to the start of the cyclotron pulse. A 5 ms electric field pulse with different amplitudes is applied 10 ms before the lasers pulse. The signal on mass 58 extracted from the gas cell is measured and the obtained results are plotted in Fig.5.26. Without applying electrical field the time profile of the

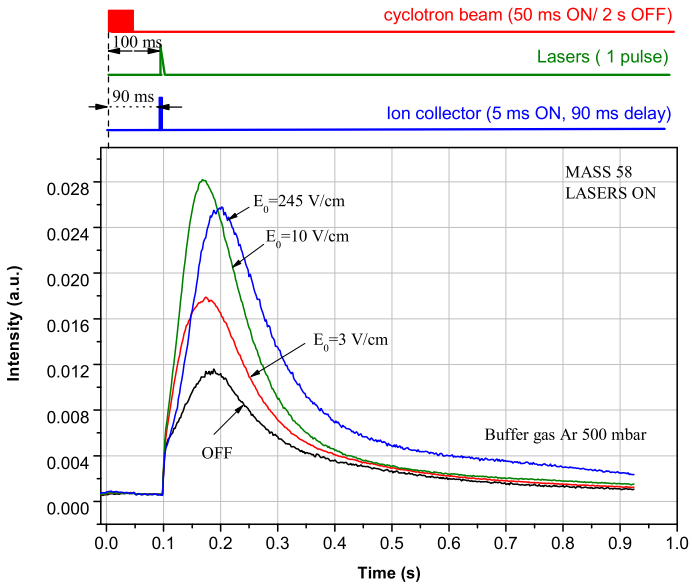

FIG. 5.26: A pulsed beam of ^{58}Ni (50 ms width) enters the laser ions source. The intensity of the beam is $2.0{\cdot}10^{10}$ pps as measured in DC mode. The large cell filled with argon gas at 500 mbar was used. A lasers pulse is fired 100 ms after the start of the cyclotron beam pulse. The time behavior of the extracted ^{58}Ni ions is recorded without electric field (the curve labelled "OFF") and with a pulse (5 ms width) of electric field applied with a delay of 90 ms with respect to the start of the cyclotron beam pulse and with different amplitudes E_0 (as indicated on the graph).

^{58}Ni ion signal extracted from the ion source (the curve labelled "OFF") is similar to the one plotted in Fig.5.25 and it was already discussed. Table 5.11 gives the calculated width of the ion collection zone (w) and ion collector efficiency (f_{IC}) for a plane parallel geometry ($d_0 = 2$ cm) when a field pulse is applied across the electrodes gap with a 40 ms time delay with respect to the end of the beam pulse as well as the corresponding ratios $\frac{A-A_{OFF}}{A_{OFF}}$, where A_{OFF} and A are the areas of the time profiles from Fig.5.26 without electrical field (curve labelled "off") and

with a field pulse, respectively. An electrical field pulse with an amplitude of 3 V/cm is strong enough to collect 64% of remaining electrons leading to an increase of 34% of the ion signal compared to the signal without electric field. An increase of the electric field pulse amplitude up to 10 V/cm makes the electron collection 72% and the corresponding increase of the ion signal is about 75% of the signal without electric field. The increase of the ion signal with a field pulse of 245 V/cm accounts for more than 100% of the ion signal without electric field. The ion drift velocity in the case of an electric field of 245 V/cm applied in argon gas at 500 mbar is 830 cm/s which means that during the pulse of 245 V/cm electric field practically all the electrons, nickel and argon ions present in the cell are collected on the electrodes. Therefore, the result obtained for this amplitude of the field pulse can be explained by an increase of the surviving chance of the laser produced ions against recombination in a cell free of electron-ion pairs.

Before concluding this section it is worth to mention that another technique to collect the electrons in the gas cell is to apply a Radio-Frequency (RF) electric field with frequencies in the kHz domain. Despite the large data set collected in on-line experiments performed at the LISOL laser ion source, due to the incomplete understanding of the processes undergoing in the gas cell using RF fields, the results obtained with 2-5 kHz RF fields are presented and discussed in the Appendix A.

Field pulses applied in the gas cell prior to laser ionization can provide an environment free of charges which would thus increase the survival chance of laser produced ions against recombination. High intensity beams stopped in the gas cell require either longer time delays between the cyclotron beam pulse and the field pulse or the use of higher field strengths in order to overcome the space charge limitations. However, increasing the time delay between the beam pulse and the field pulse leads to an increase of the time delay between the cyclotron pulse and the laser pulse and, consequently, a reduction of the duty-cycle of the laser ion source. Nevertheless, the time delay between the beam pulse and the field pulse must allow the majority of the ions of interest to recombine. Once that the remaining electrons and ions are collected by the field pulse, laser ionization can be applied. In order to reduce or stop the recombination of laser produced ions with photo-electrons one could apply a continuous weak DC field in the gas cell after the laser pulse so as to remove the photo-electrons and maintain the flow dominated motion of ions. All the tunable parameters of the electric field pulse (width, time delay, amplitude)

Table 5.11: The calculated width of the ion collection zone (w) and ion collector efficiency (f_{IC}) for a plane parallel geometry (d_0 = 2 cm) when a field pulse is applied across the electrodes gap with a 40 ms time delay with respect to the end of the beam pulse; and the corresponding ratios $\frac{A-A_{OFF}}{A_{OFF}}$, where A_{OFF} and A are the areas of the time profiles from Fig.5.26 without electrical field (curve labelled "off") and with a field pulse, respectively. $I_{beam} = 2.0{\cdot}10^{10}$ pps.

E_0 (V/cm)	w (cm)	f_{IC} (%)	$\frac{A-A_{OFF}}{A_{OFF}}$ (%)
3	1.28	64	34
10	1.4	72	75
245	2.0	100	107

must be adjusted according to the width and intensity of the primary beam pulse.

5.2 Experiments with heavy-ion induced fusion reactions

One of the applications of a gas cell for production of radioactive isotope beams at LISOL is the production of neutron deficient ruthenium and rhodium isotopes using the fusion reaction ^{58}Ni(^{36,40}Ar,xnyp). These isotopes are not available at other on-line isotope separator facilities due to their refractory nature. Two different configurations of the gas cell have been used such that the 99% enriched ^{58}Ni target (3.7 μm thick foil) mounted inside the gas cell is either at normal incidence or tilted at 45° with respect to the cyclotron beam direction. In the first configuration, the 10 mm channel gas cell was used (see Fig.2.6) and the target is mounted next to the entrance window (Mo - 4.1 μm foil) perpendicular on the cyclotron beam direction. Stopping of nuclear reaction products recoiling out of the target can take place in a 37 mm thick layer of 500 mbar argon gas. In the second configuration, the "classical" heavy-ion fusion guide was used (see Fig.2.4), with the target mounted on an insert at 45° with respect to the cyclotron beam direction. Between the gas cell entrance window (Mo - 4.3 μm foil) and the target there is a 10 mm layer of argon gas at the same pressure as in the whole cell. The reaction product recoiling out of the target can be stopped in a layer of argon gas of about 22 mm thickness. The advantages in this configuration are an increased effective thickness of the target and a shorter evacuation time of the recoiling products by the gas flow. The disadvantage of this cell is that a compromise on the buffer gas pressure should be made such that the stopping of the recoiling products is at maximum, while the energy of the projectile beam can not be finely tuned for the maximum yield due to the gas layer between the target and the entrance window of the cell[10].

The residence of Ru/Rh isotopes inside the gas cell is relatively short compared to their decay half-life and resonant two-step laser ionization is applied to enhance the extraction of a particular isotope. Following selection on the basis of their A/q ratio, nuclei are implanted onto a movable tape at the centre of the detection setup (see section 2.6.3). A detailed description of the detection and acquisition setup is found in reference [Dea04T]. The efficiency of the laser ion source for production of Ru/Rh isotopes represents the ratio of the number of implanted nuclei on the tape per time unit, to the number of nuclei recoiling out of the target per time unit.

5.2.1 The yields of Ru and Rh isotopes from the target

The energy of the projectile beam was optimized for the maximum production of the particular Rh, Ru isotopes using the HIVAP [Rei81] and LISE [LIS02, LISpr] codes. Although the predicted energy for maximal cross section coincides for the two calculations, large variations of the theoretical cross section of Ru and Rh isotopes are observed. As a consequence, the calculated production yields of Ru and Rh isotopes cannot be used to deduce laser ion source efficiencies. Therefore, an off-line method to measure the number of Ru/Rh atoms recoiling out of the target has been used. A support, holding a target (enriched ^{58}Ni - 3.7 μm thickness) and a stopper foil (tantalum - 5 μm thickness) behind the target is positioned in the

[10]The ^{40}Ar projectiles lose an energy $\Delta E \simeq 15$ MeV in the buffer gas layer between the entrance window of the gas cell and the target foil.

beam path in the vacuum chamber of the laser ion source, outside the gas cell (see Fig.5.27). The target is irradiated for 100 seconds with a precisely known beam

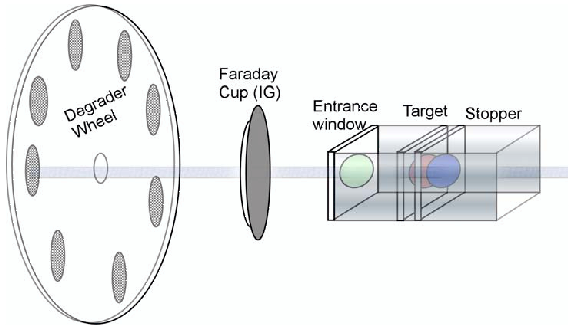

Fig. 5.27: The experimental setup used to measure the yields from the target. After the projectile beam current is measured, the Faraday cup is removed from the beam path. The target and entrance window foils are identical to the ones mounted in the gas cell.

current and energy. The reaction products are collected on a stopper foil, and after a delay of about 3 minutes, the stopper and the target foils are placed each separately in front of a germanium detector, which recorded the gamma decays of the implanted nuclei[11]. The efficiency of the Ge detectors was calibrated using an intensity calibrated ^{60}Co gamma source. During the measurements of the gamma decays from the stopper and the target foils the dead-time of the acquisition system was monitored by placing a standard intensity calibrated gamma source (^{137}Cs, ^{22}Na) at a fixed distance from each of the Ge detector. Consecutive measurements of 50 s each were performed in order to identify the isotopes of interest through their specific gamma lines and half-lives.

Fig.5.28 and Fig.5.29 show the gamma spectra measured in singles[12] from the target and stopper foils, respectively, during 16 sessions of 50 s each. The ^{40}Ar projectile beam current was 25.6 pnA and the beam energy was 142 MeV. Due to the delay between the irradiation and the start of the decay measurements, only a limited number of Rh and Ru as well as Tc isotopes, relatively long-lived, could be identified in the stopper foils (given in Table 5.12).

As mentioned before, the spectra from Fig.5.28 and Fig.5.29 were recorded in 16 sessions of 50 s each. A particular isotope was identified not only through its gamma-lines but also the half-life. In that respect, the half life is determined from the fit of the count rate as function of the time. It is worth to note that a particular isotope was not always identified in both target and stopper foils. The number of counts in the 941.5 keV gamma-line of ^{95}Rh from the stopper foil during each 50 s session is plotted in Fig.5.30 as function of the time. The 142 MeV ^{40}Ar projectile beam (intensity of 25.6 pnA) irradiated the target for 100 s (moment "0" on the

[11]The 3 minutes delay is due to the fact that the front-end box must be vented and afterwards the foils are manually moved to the detection setup.

[12]The singles spectra are those spectra measured without any conditions on event timing or energy.

graph represents the start of the irradiation). The decay fit to the time behavior of the 941.5 keV γ line from Fig.5.30 provides the value of the experimental decay constant $\lambda_{exp}^{941.5keV} = 0.00213(0.0003)$. This value is in good agreement with the theoretical decay constant $\lambda_{theor}^{941.5keV} = 0.0023$, thus the ^{95}Rh isotope is undoubtedly identified.

The production rate P (in atom per second[13]) of a particular isotope from the target can be deduced from the count rate of one of its specific gamma lines from the stopper foil provided the photo-peak efficiency (η_γ) of the Ge detector and the

[13]Usually we express the yield in particle micro-Coulomb (pμC) of beam dose. 1 pμC represents the dose given by a projectile beam current of 1 particle micro-Ampere (pμA) during 1 second. Thus the yield $Y = P/I_{beam}$(pμA).

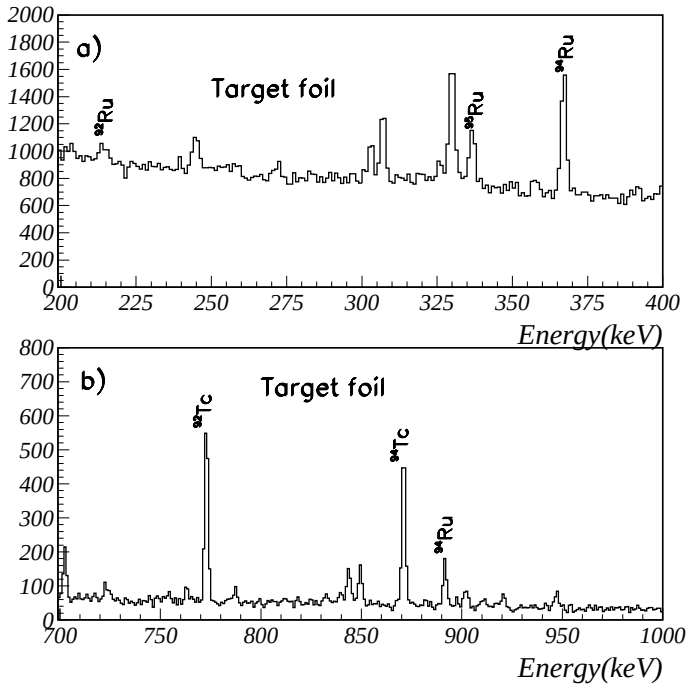

FIG. 5.28: The measured partial gamma-spectrum (total counts in singles) from the target foil: a) 200-400 keV photon energies and b) 700-1000 keV photon energies. The radioactive isotopes are produced by a 142 MeV ^{40}Ar projectile beam with the intensity of 25.6 pnA. The enriched ^{58}Ni target (3.7 μm thickness) was perpendicular on the beam direction. The spectra are collected during 800 s.

γ-intensity (b_γ) are known:

$$P(\text{atom/p}\mu\text{C}) = \frac{c_i A(t_{si})}{b_\gamma \eta_\gamma}, \tag{5.2}$$

where c_i is a correction to account for those nuclei which decay during the implantation period, i.e. during the 100 s of irradiation of the target, and $A(t_{si})$ is the γ line count-rate at the end of the implantation time (t_{si}). The quantity $A(t_{si})$ is determined from the extrapolation to t_{si} of the decay fit of the number of counts in a γ line (see Fig.5.30 for the example of the ^{95}Rh isotope).

A value of $\eta_\gamma = 1.4\%$ for each Ge detector was measured using the 1332 keV γ-line from a ^{60}Co gamma-source placed at the same distance as the target/stopper foil, i.e. 24 mm (in some circumstances this distance was substantially increased

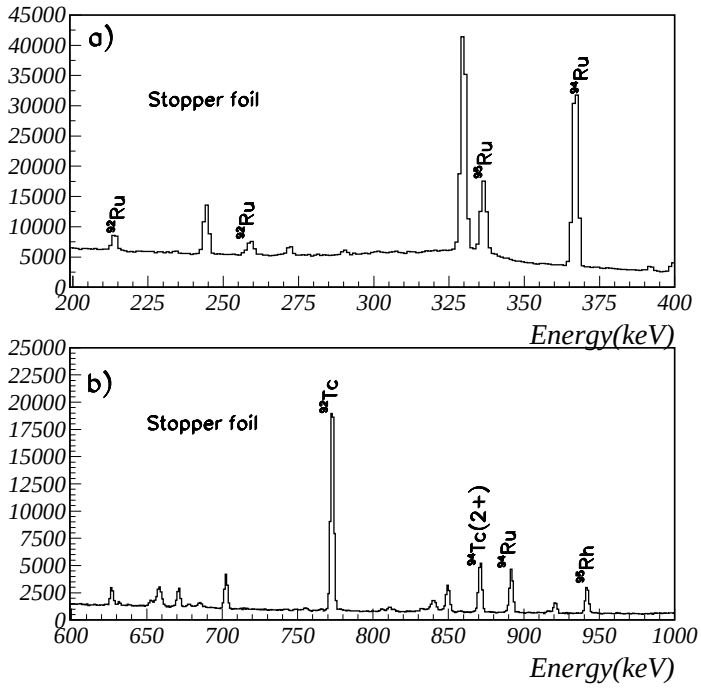

Fig. 5.29: The measured partial gamma-spectrum (total counts in singles) from the stopper foil: a) 200-400 keV photon energies and b) 600-1000 keV photon energies. The radioactive isotopes are produced by a 142 MeV ^{40}Ar projectile beam with the intensity of 25.6 pnA in an enriched ^{58}Ni target (3.7 μm thickness) perpendicular on the beam direction. The spectra are collected during 800 s.

TABLE 5.12: The half-lives, gamma-decay energies and branching ratios (number of γ-rays in particular γ-line per 100 decay) of the neutron deficient Rh, Ru and Tc isotopes, respectively.

Isotope	$T_{1/2}$ (min)	γ energy (keV)	b_γ (%)	Reference
^{95}Rh	5.02	941.5	72	[Wei75]
^{95}Ru	98.58	336.4	70.8	[Pin68]
^{94}Ru	51.8	366.9	75	[Bos68]
		891.7	25	[Bos68]
^{94}Tc (2+)	51.8	871.1	94.2	[Med50]
^{92}Ru	3.65	134.6	66	[Lan76]
		213.8	96	[Lan76]
		259.3	92	[Lan76]
^{92}Tc	4.23	147.8	71	[Lie64]
		773.0	100	[Lie64]

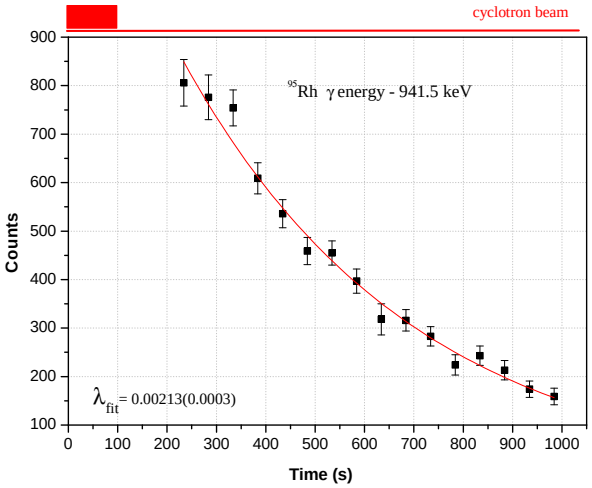

FIG. 5.30: The measured number of counts in the 941.5 keV gamma-line of the ^{95}Rh isotope implanted in the stopper foil as function of the time. Each data-point represents the number of counts acquired during one 50 s session. The rhodium nuclei are produced by a 142 MeV ^{40}Ar projectile beam (intensity 25.6 pnA) in an enriched ^{58}Ni target (3.7 μm thickness) during 100 s of irradiation. The line represents the decay fit to the time behavior of the 941.5 keV γ line.

Table 5.13: The experimental yields of ^{92}Tc, ^{92,94,95}Ru and ^{95}Rh isotopes from a 3.7 μm thick enriched ^{58}Ni target irradiated with a ^{40}Ar projectile beam with energies between 111 and 171 MeV. Eq.(5.2) was used. Note that this is the projectile beam energy in front of the target. No errors of the quoted values are given due to the multi-step analysis procedure. These errors may level up to 30% only from the integration of the photo-peaks in the gamma-spectra.

Beam Energy (MeV)	^{92}Tc (at/pμC)	^{92}Ru (at/pμC)	^{94}Ru (at/pμC)	^{95}Ru (at/pμC)	^{95}Rh (at/pμC)
111	$6.5{\cdot}10^5$	$5.9{\cdot}10^4$	$2.9{\cdot}10^6$	$3.1{\cdot}10^6$	$4.1{\cdot}10^5$
124	$2.4{\cdot}10^6$	$2.2{\cdot}10^5$	$8.3{\cdot}10^6$	$9.1{\cdot}10^6$	$9.7{\cdot}10^5$
127	$3.3{\cdot}10^6$	$2.7{\cdot}10^5$	$1.8{\cdot}10^7$	$2.1{\cdot}10^7$	$1.2{\cdot}10^6$
142	$8.1{\cdot}10^6$	$5.2{\cdot}10^5$	$2.6{\cdot}10^7$	$2.8{\cdot}10^7$	$1.8{\cdot}10^6$
148	$9.8{\cdot}10^6$	$5.4{\cdot}10^5$	$2.6{\cdot}10^7$	$3.6{\cdot}10^7$	$1.4{\cdot}10^6$
158	$1.3{\cdot}10^7$	$6.0{\cdot}10^5$	$2.9{\cdot}10^7$	$4.1{\cdot}10^7$	$9.1{\cdot}10^5$
171	$1.4{\cdot}10^7$	$3.8{\cdot}10^5$	$1.2{\cdot}10^7$	$3.4{\cdot}10^7$	$3.3{\cdot}10^5$

in order to compensate for the dead-time of the acquisition system due to the high count-rates). The experimental yields of ^{92}Tc, ^{92,94,95}Ru and ^{95}Rh isotopes from a 3.7 μm thick enriched ^{58}Ni target irradiated with a ^{40}Ar projectile beam with energies[14] between 111 and 171 MeV are tabulated in Table 5.13. The Ru isotopic yields have been corrected for the feeding through the decay of the Rh-parent isotopes, directly produced in the reaction. Such a correction for Rh was not necessary as no γ-lines of parent Pd isotopes have been identified in the recorded spectra. Due to the multi-step analysis procedure, no errors of the quoted values of the yields in Table 5.13 are given. These errors may level up to 30% only from the integration of the photo-peaks in the gamma-spectra.

5.2.2 Stopping and thermalization of Ru and Rh recoils in the gas cell

In the case of the heavy ion fusion reactions performed at LISOL, in contrast to the experiments with a ^{58}Ni beam implanted in the gas cell, the projectile beam traverses the gas cell. The reaction products recoiling out of the target emerge in the gas cell in a forward cone with an opening of about 10°, typical for Ru/Rh/Tc isotopes produced in ^{58}Ni(^{40}Ar, $xnyp$) reactions at beam energies below 4.5 MeV/amu [LISpr]. At this projectile beam energy, the reaction products initially at 0.75 MeV/amu are slowed down in the target and they lose energy according to the thickness of the target material they have to pass. It is important to know for each particular nuclear reaction what is the capability of the gas cell to stop the reaction products leaving the target. The energy distribution of the reaction products leaving the target can be calculated using the LISE code [LISpr]. Two examples for the case of ^{95}Rh isotopes produced in a perpendicular (see Fig.5.31.a) and a

[14] This is the projectile beam energy in front of the target. The projectile loses in average 50 MeV of its initial energy in the target.

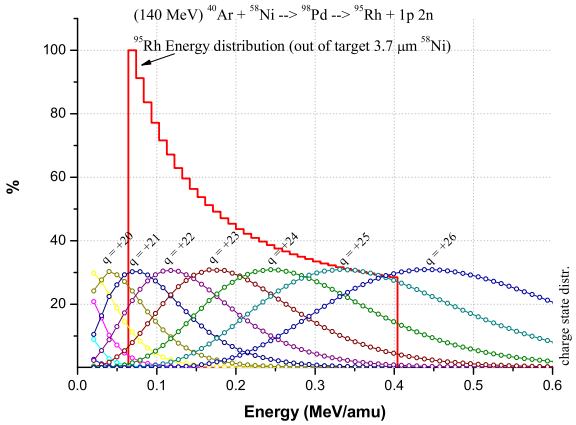

a)

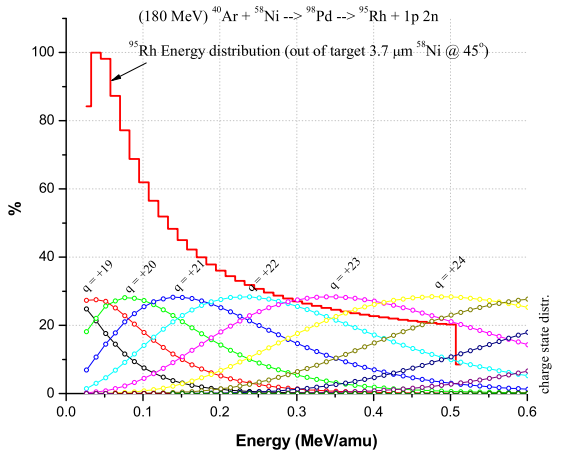

b)

FIG. 5.31: The calculated energy and charge-state distributions [LISpr] of ^{95}Rh radioactive ions recoiling out of a) a 3.7 μm ^{58}Ni target perpendicular on the beam direction and b) a 45° tilted ^{58}Ni target (3.7 μm thickness). The ^{40}Ar projectile beam energy in front of the target is a) 140 MeV and b) 180 MeV.

45° tilted (see Fig.5.31.b) ^{58}Ni target (3.7 μm thick) by a ^{40}Ar beam with energy of 140 MeV and 180 MeV, respectively, are given below. For the 45° tilted target the required projectile beam energy is larger as such to match the maximum cross section for production as well as the maximum transmission through the target of the Rh isotopes. The charge-state distributions of the ^{95}Rh ions leaving the target are also depicted in Fig.5.31.a and b. As one can see the rhodium ions have a

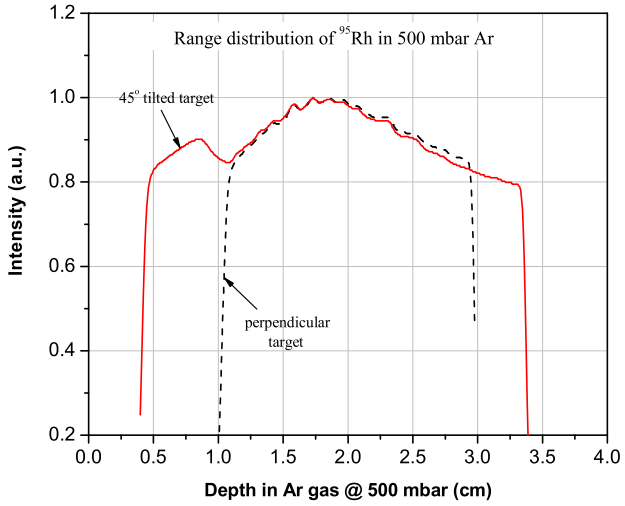

Fig. 5.32: The range distribution of ^{95}Rh ions with the energy distribution from Fig.5.31.a (dashed line) and Fig.5.31.b (full line), respectively, in 500 mbar argon gas.

charge distribution ranging from +19 up to +26. This is particularly important as the stopping power of the ions in the gas is proportional to the effective charge of the ions (see section 3.2). In contrast to the experiments with a stable ^{58}Ni ions implanted in the gas cell, where the charge state distribution of the ions entering the cell is narrow, the charge state distribution of the radioactive rhodium ions produced in the fusion reaction and recoiling out of the target is much broader. This will contribute to a broadening of the range distribution of the stopped rhodium ions in the gas cell. However, given the energy and charge state distributions of the rhodium ions recoiling out of the target, the stopping and neutralization of these ions of interest takes place all along the projectile beam path in the gas cell. This is in contrast with the case of the ^{58}Ni ions implanted in the cell filled with argon gas, where the spatial distribution of the stopped nickel ions is well localized at the end of the beam track, in a place where the electron-ion pair density is 10 times lower than in the beam path (see section 3.5). The ^{40}Ar beam deposits around 50 MeV energy in the buffer gas, which corresponds to a normalized ionization rate $Q/\text{ion} \simeq 2 \cdot 10^6$ electron-ion pairs/cm^{3}s.

The energy distributions from Fig.5.31.a and b have been used to calculate the range distribution of the ^{95}Rh ions stopped in Ar gas at 500 mbar pressure, using the ATIMA computer code [ATIpr] implemented in the LISE program [LISpr]. The results are shown in Fig.5.32. One can observe from Fig.5.32 that in the case of a normal incidence of the projectile beam on the ^{58}Ni target, the ^{95}Rh radioactive ions recoiling out of the target can be easily stopped in the 10 mm channel gas cell as its dimension along the cyclotron beam path is 37 mm (see Fig.2.6). In the case of the 45° tilted target (see Fig.2.4) the stopping distance in the gas cell is only 22 mm and 37% of the Rh nuclei are implanted in the cell walls.

The linear energy loss dissipated in form of ionization in the path of a ^{40}Ar beam in argon gas at 500 mbar pressure is shown in Fig.5.33 [SRIpr], where also the range distribution of the ^{95}Rh ions from Fig.5.32.a is plotted. The energy of the ^{40}Ar beam in front of the target was taken 150 MeV. Comparing this figure with Fig.3.11, where the case of stopping a ^{58}Ni beam in the gas cell is depicted, one can observe that the ^{95}Rh ions are stopped along the beam path and that the electron-ion pair density does not change significantly along the beam path, in contrast to the case of stopping a nickel beam in the gas cell. Thus, the laser ion

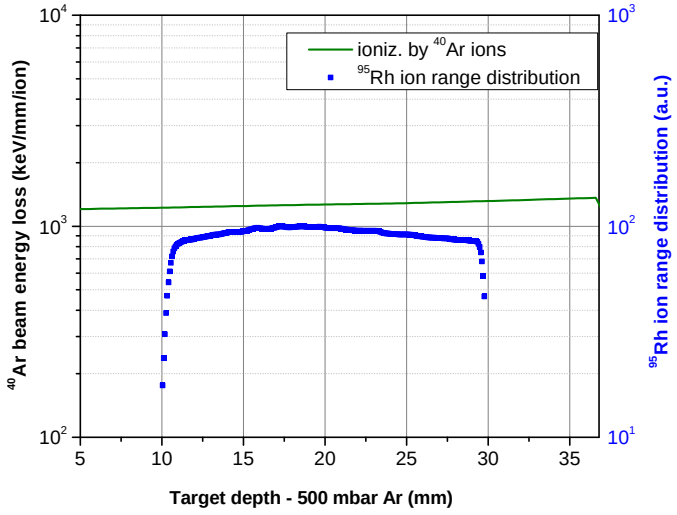

FIG. 5.33: The linear energy loss, dissipated in form of ionization, in the path of a ^{40}Ar ion beam passing through the gas cell filled with 500 mbar Ar [SRIpr]. The range distribution of the stopped ^{95}Rh ions (■) from Fig.5.32.a is plotted, where the target is mounted at normal incidence to the projectile beam direction. The energy of the ^{40}Ar beam in front of the target is 150 MeV. Note the double labelling of the vertical axis.

source efficiency for the production of neutron-deficient isotopes (shown in the next

section, Fig.5.36) as a function of the argon beam intensity can not be directly compared with the efficiency for the extraction of ^{58}Ni ions (see Fig.5.12) as a function of the nickel beam intensity stopped in the gas cell.

Not mentioned yet is the transmission efficiency of the isotopes of interest through the target. The transmission efficiency of produced ^{95}Rh nuclei through the

Table 5.14: The experimental transmission efficiencies of ^{95}Rh nuclei in a 45° tilted target (^{58}Ni - 3.7 μm thickness) produced by a ^{40}Ar projectile beam with the given energies in front of the target.

^{40}Ar Beam Energy (MeV)	109	119	133	148	163
^{95}Rh transmission efficiency (%)	9	10	44	60	98

target has been measured using a 45° tilted ^{58}Ni foil with respect to the cyclotron beam direction. The obtained values are given in Table 5.14. The transmission efficiency of ^{95}Rh decreases from 98% down to 9% when the projectile beam energy is degraded from 163 MeV down to 109 MeV. The maximum production from the laser ion source will thus come from the interplay between the production cross-section in the target, recoil energy of the nuclei of interest and their stopping in the gas cell.

5.2.3 The efficiency and selectivity of the heavy-ion fusion guide

As discussed above, a fraction of the reaction products leaving the target is stopped and thermalized as +1 ions or neutrals in the gas cell. Resonant laser ionization is applied in the gas cell in order to enhance the extraction of a particular species from the ion source. A macrocycle time structure of the cyclotron beam is used (50 ms ON - 50 ms OFF) such as to permit the laser produced ions to be evacuated and to minimize their loss through recombination with electrons produced at projectile beam impact. The SPIG (extraction from the gas cell), mass separator and data acquisition system are opened in antiphase with the cyclotron beam. However, it is important to note that in what is following only preliminary tests[15] of the laser ion source for production of Ru/Rh isotopes are discussed, when the cyclotron beam was continuously (DC) impinging on the target. A summary and discussion of the spectroscopic results obtained for the neutron deficient Ru/Rh isotopes produced at LISOL can be found in reference [Dea04T].

Typical (partial) γ-spectra recorded in singles at the tape station, when the mass separator is tuned to select ions with the ratio $A/q = 94$ extracted from the gas cell are shown in Fig.5.34 with the lasers switched off (a) and the lasers on (b) tuned to resonantly ionize Ru. One can observe that without laser ionization the ^{94}Ru/Rh isotopes are present in the extracted beam from the ion source. Application of resonant laser ionization of Ru element clearly increases the count-rate in

[15]These tests were performed prior to the "production" experiments (or "physics experiments"), when for the sake of statistics purposes the maximum production of a particular isotope is desired even at low performance of the laser ion source. A micro- and macro-cycle for the projectile beam is always used in these experiments.

the specific γ-lines of Ru isotopes implanted at the detection station. The ratio of the number of detected radioactive ions with laser ionization to the number of those ions detected without laser ionization in the same given experimental conditions represents the selectivity of the laser ion source. From Fig.5.34 a laser ion source selectivity of $\sim$11 is deduced for the extraction of ^{94}Ru isotope from the gas cell (from the 366.9 keV γ-line).

The performance of the laser ion source for extraction of Ru/Rh isotopes has been extensively studied on-line in connection with the off-line measurements of the isotopic yields from the target aiming at characterization and determination of the efficiency and the selectivity of our experimental setup. The experimental isotopic yields of ^{95}Rh obtained on-line from the laser ion source and off-line from the target (measured in the stopper foils), are presented in Fig.5.35.a for the configuration with a normal ^{58}Ni target foil on the projectile beam direction, and in Fig.5.35.b

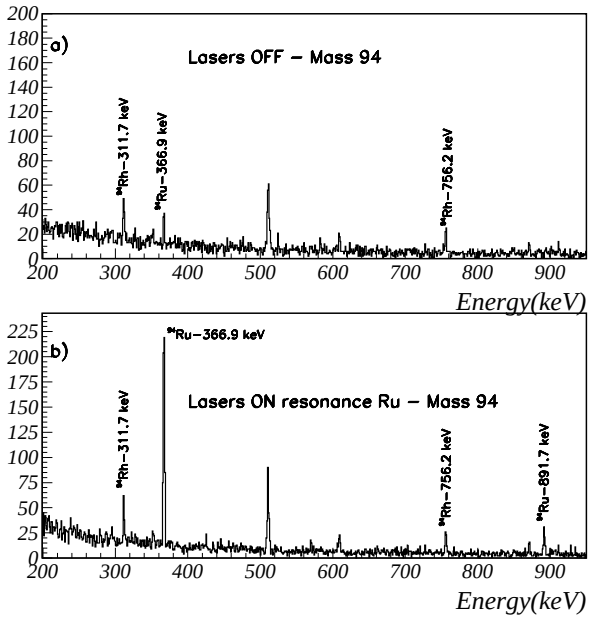

FIG. 5.34: The singles γ-spectra of radioactive ions with the ratio A/q=94 extracted from the ion source a) with the lasers off and b) the lasers on, tuned to ionize Ru, respectively, and implanted onto the tape at the detection station. The 10 mm channel gas cell was used (normal projectile beam incidence on the 3.7 μm ^{58}Ni target). The ^{40}Ar projectile beam energy in front of the target was 148 MeV and its intensity 13.5 pnA. The buffer argon gas pressure in the cell was 400 mbar. The acquisition time was 300 s.

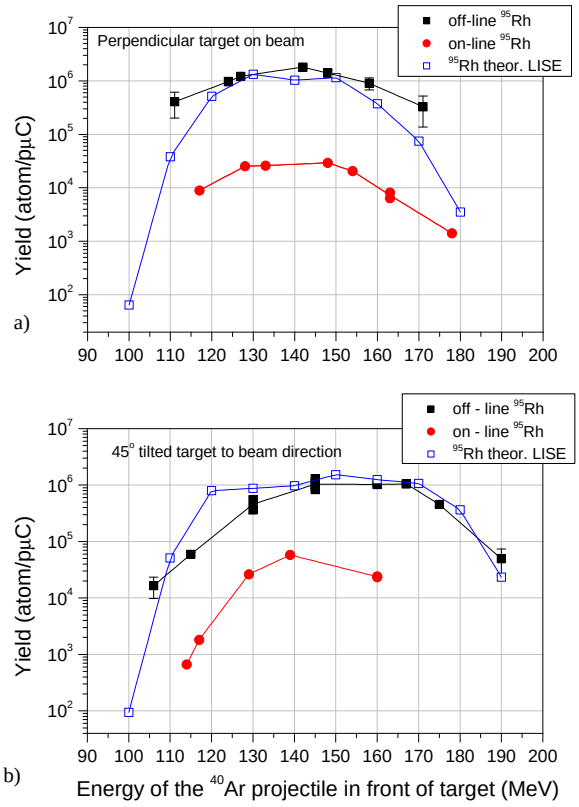

Fig. 5.35: The experimental on-line (full circles) and off-line (full squares) yields of ^{95}Rh isotope, and the theoretical yields calculated using cross sections predicted by the LISE code (open squares) [LISpr], respectively, as function of the beam energy in front of the a) normal target foil, b) 45° tilted with respect to the beam direction. The on-line data points have been obtained with a) the 10 mm channel gas cell and b) the "classical" heavy ion fusion guide.

for the configuration with a 45° tilted target with respect to the beam direction, respectively, as function of the ^{40}Ar beam energy in front of the target. The effective target thickness induces an energy loss of the ^{40}Ar projectile of about 50 MeV. The yields of the laser ion source was measured in both configurations with a 20 pnA ($1.25{\cdot}10^{11}$ pps) ^{40}Ar beam current impinging on the target. The ratio of the on-line yields to the off-line yields, at the same projectile energy, gives the efficiency of the laser ion source for the production of this particular isotope. The experimental off-line yields of the ^{95}Rh isotope were found to be in a better agreement with the yields predicted by the the LISE code, than those predicted by HIVAP. The calculated yields for both configurations as resulting from LISE are also shown (open squares) in Fig.5.35.

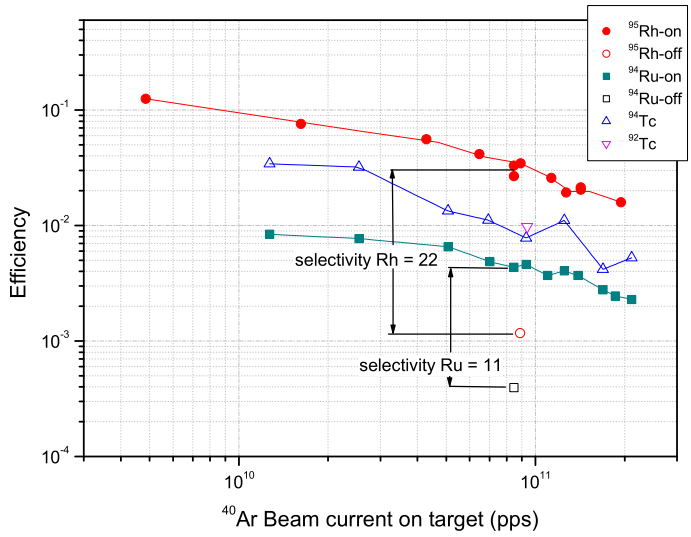

FIG. 5.36: The dependence of the laser ion source efficiency on the primary ^{40}Ar beam intensity, for production of ^{95}Rh with lasers on (full circles), without lasers (open circle), ^{94}Ru with lasers on (full squares), without lasers (open square), ^{94}Tc (open up-triangles) and ^{92}Tc (open down-triangle) isotopes. The heavy ion induced fusion reaction was ^{58}Ni(^{40}Ar,$xnyp$).

The laser ion source efficiency for the production of Rh and Ru isotopes has been measured as function of the primary beam intensity at the optimum beam energy. The dynamic range of the beam currents is not as wide as in experiments with stable ^{58}Ni beam and it was limited by the count rate of specific Rh/Ru gamma-lines in the low-current domain, and by the risk of damaging the target foil at high beam currents. The experimental efficiencies of the laser ion source for the production of neutron-deficient ^{95}Rh and ^{94}Ru isotopes are shown in Fig.5.36 as

function of the primary ^{40}Ar beam intensity impinging on the ^{58}Ni target. It is striking that the laser ion source efficiency for the production of ^{95}Rh isotope is in average one order of magnitude higher than for the production of ^{94}Ru isotope. One possible explanation of this difference in efficiency might be related to a different chemical reactivity of Ru with the buffer gas impurities, compared to the Rh, which may lead to more severe losses of Ru isotopes in molecular bonds. Secondly it was observed that in the case of Ru, the second step in the laser ionization could not fully been saturated.

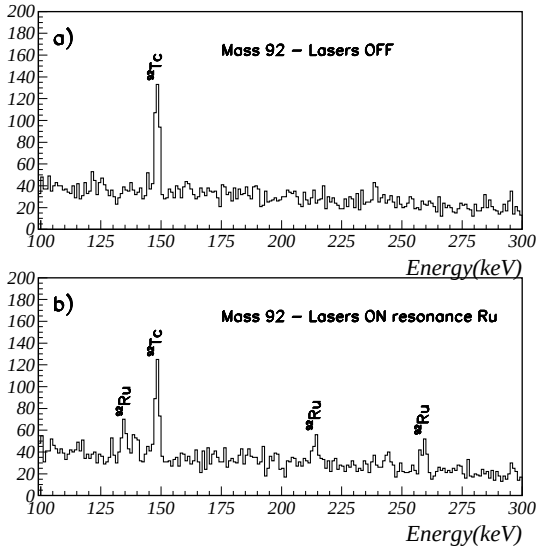

Fig. 5.37: The singles (partial) γ-spectra of radioactive ions with the ratio A/q=92 extracted from the ion source a) with the lasers off and b) the lasers on, tuned to ionize Ru, respectively, and implanted onto the tape at the detection station. The 10 mm channel gas cell was used (normal projectile beam incidence on the 3.7 μm ^{58}Ni target). The ^{40}Ar projectile beam energy in front of the target was 163 MeV and its intensity 13.5 pnA. The buffer argon gas pressure in the cell was 400 mbar. The acquisition time was 300 s.

However, as in the experiments with the stable ^{58}Ni beam, the laser ion source efficiency for the production of neutron-deficient isotopes in heavy ion fusion reactions is also beam intensity dependent. For the production of ^{95}Rh isotope this efficiency rises from 1.5% at $2{\cdot}10^{11}$ pps primary beam current, up to 12% at $4.8{\cdot}10^{9}$ pps incoming beam intensity. It is more difficult to measure the selectivity of the laser ion source for the production of radioactive reaction products in a wide dynamic range of the primary beam intensities, as the main limitation comes from the reaction cross section. Therefore the laser ion source selectivity for the production

of ^{95}Rh isotope has been measured for a fixed beam intensity of 9 $\cdot 10^{10}$ pps (1.5 pnA) and its value has been found to be around 22, as shown in Fig.5.36. The laser ion source efficiency for the production of ^{94}Ru isotope has its highest value of 0.8% at 1.3 $\cdot 10^{10}$ pps beam intensity, and it levels down to 0.2% at 2.1$\cdot 10^{11}$ pps beam current impinging on the target. The laser ion source selectivity for the production of the ^{94}Ru isotope, as mentioned above, amounts to 11 for a primary beam intensity of 8.5 $\cdot 10^{10}$ pps.

A remarkable feature observed during experiments with heavy ion induced fusion reactions aiming at production of neutron deficient Ru and Rh was the high yield of Tc isotopes from the ion source. The Tc isotopes implanted onto the tape have a two fold source: decay of the parent implanted Ru isotopes which were laser ionized prior to their extraction from the gas cell, or survival in the buffer gas in ionic state of Tc nuclei directly produced in reaction. An illustrative example is given in Fig.5.37. The partial γ-spectra of the radioactive ions with A/q=92 extracted from the cell without laser ionization (see Fig.5.37.a) and with laser ionization of Ru (see Fig.5.37) and implanted onto the tape at the detection system are shown. Without laser ionization the 147.8 keV ^{92}Tc γ-line peak is popping out and no specific γ lines of ^{92}Ru are observed. With the lasers on tuned to ionize Ru the specific γ-lines of ^{92}Ru appear in the spectra, while the decay of ^{92}Tc remains the same as in the case without lasers. Thus the origin of ^{92}Tc isotopes implanted at the detection station is not lasers related as the feeding from the parent Ru isotopes is negligible.

The ion source efficiency for the production of ^{94}Tc without laser ionization has its maximum value of 3% at 1.3 $\cdot 10^{10}$ pps beam intensity and it levels down to 0.5% at 2 $\cdot 10^{11}$ pps beam current impinging on the target.

The obtained results do show that the efficiency and selectivity of the laser ion source is as well element dependent (chemistry) as projectile beam intensity dependent. It is worth to mention at the end of this section that the production of neutron-rich Co and Ni isotopes in 30 MeV proton induced fission of ^{238}U was extensively studied. The obtained results and a short discussion are provided in the Appendix B. As in the case of the heavy ion induced fusion reactions, the laser ion source efficiency for production of neutron-rich isotopes is element- and beam intensity dependent.

Chapter 6

Conclusions and outlook

At the Leuven Isotope Separator On-Line (LISOL) resonant laser ionization of the reaction products stopped and stored in a buffer noble-gas (helium or argon) cell has been used for years. Thin-foil targets are placed in the buffer gas cell and are bombarded by a primary beam delivered by the CYCLONE 110 cyclotron. The reaction products recoiling out of the target enter the buffer gas and, depending on their initial kinetic energy, a substantial fraction is stopped in the buffer gas. The primary beam is traversing the gas cell and is stopped downstream in a beam dump. In the background of the electron-ion pairs produced by the slowing down of the primary beam, the majority of reaction products stopped in the buffer gas neutralize and are transported by the gas flow towards the exit hole of the cell. Before the atoms leave the gas cell, the isotopes of interest are ionized with resonant laser ionization.

In order to enlarge the possibilities of a gas cell for the production of intense radioactive ion beams it is of crucial importance to characterize the different stages a radioactive ion undergoes from its production to its decay. The usual delays in the gas cell at LISOL are from few tens of milliseconds up to several hundreds of milliseconds, depending on the geometrical configuration and the buffer gas type. The history of the radioactive ion starts at the nuclear reaction with a recoil into the gas cell, followed by the slowing process down to thermal energies. From then on a major role is played by the different interactions of the radioactive nucleus, in its atomic or ionic form, with the buffer gas atoms, with impurities, with electrons and eventually with electric fields. The most important parameters of the laser ion source are its efficiency and selectivity. The precise determination of these two parameters and their principal dependencies in on-line conditions is essential.

The on-line studies presented in this thesis can be divided in three categories:

(I) conversion of a high-energy (185 MeV) ^{58}Ni beam into a mass separated low-energy one (40 keV) involving stopping and resonant laser ionization in a gas cell;

(II) production of neutron-deficient Ru and Rh isotopes in the heavy ion induced fusion-evaporation reaction ^{58}Ni(^{40}Ar,xnyp);

(III) production of neutron-rich Ni and Rh isotopes in proton induced fission of ^{238}U reactions.

In the first case (I) the ions of interest are stopped in the middle of a gas cell, at the end of the beam path where the electron-ion pair density can be few orders of magnitude lower than at the entrance of the gas cell. The parameters of the ion beam implanted in the gas cell, such as intensity, time structure, charge state and energy can accurately be controlled, thus one can determine with precision the (laser) ion source efficiency and selectivity. In contrast, in the second (II) type of studies the particles of interest (the radioactive nuclei) are essentially stopped in the region where the accelerator beam also passes. Finally, in the third (III) type of studies the radioactive nuclei are stopped in a region which is separated from the primary beam path by a shielding cylinder.

The consequence of the use of a gas cell for production of radioactive beams with a laser ion source is that during the primary projectile beam passage through the buffer gas (beam-on period) a high-density of electron-ion pairs is created, and subsequent neutralization of most of the created pairs and ions of interest takes place. Laser ionization of the species of interest can be applied in a zone where ion-electron pair density is low enough and the laser-produced ions have a high survival chance against recombination.

The evacuation properties of the LISOL gas cell have been extensively studied in on-line experiments of type (I). The release of both buffer gas ions created by the Ni beam and of the Ni ions was studied without and with laser ionization, respectively. The ion source efficiency for extraction of Ar ions steeply decreases inversely proportional to the cyclotron beam intensity until it reaches a value of 10^{-5}%. The ion source efficiency for the extraction of nickel ions without laser ionization decreases inversely proportional to the square-root of the beam intensity until it reaches a value of about $2{\cdot}10^{-2}$%. Laser ionization of Ni becomes effective for cyclotron beam currents stopped in the gas cell higher than 10^4 pps. For beam intensities around this value the nickel ion signal extracted from the ion source consists entirely of surviving nickel ions stopped in the gas cell, and it is the same regardless to the fact that the lasers are on or off, meaning that there are no nickel atoms available for laser ionization. The ion source efficiency for the extraction of laser produced nickel ions remains around 10% for cyclotron beam intensities ranging from 10^3 up to 10^7 pps and it decreases down to 1% at beam intensities around 10^{10} pps. The difference in behavior between nickel ions without laser ionization and laser-produced ions also results in a change of the laser ion source selectivity from 1 around 10^4 pps over 100 around 10^7 pps to 50 at the highest intensities. Ion source efficiencies up to 12% were measured for the extraction of argon and nickel ions (without and with laser ionization), respectively.

DC electrical fields can be applied in a gas cell for stopping, storing and transporting radioactive ions in order to drift the ions towards the exit hole of the gas chamber and/or remove the electrons created during the slowing down of the primary beam. At the LISOL laser ion source the effect of electrical fields in a gas cell was studied by applying electrical fields across the cell perpendicular on the extraction axis in experiments of type (I). In a small gas cell as those used at the LISOL laser ion source, relatively high electric fields can easily be applied. The cyclotron beam entering the gas cell is well focused in a spot having a diameter of 6 mm, thus the ionization rate Q can be very high at relatively low beam currents. Using the correct configuration of the electric field in the gas cell it is possible to calculate the ionization rate (Q_{SCL}) for which the space charge limit (i.e. zero net field at the anode) is encountered, by applying the theoretical formalism developed to describe the charge collection in classical ionization chambers. The space charge limit in 500 mbar argon(helium) and 120 V/cm electric field applied between the

two electrodes in the 10 mm channel gas cell is achieved for an ionization rate of about $5{\cdot}10^{10}(5{\cdot}10^{11})$ electron-ion pairs/cm^{3}s corresponding to a ^{58}Ni beam with an intensity of $5{\cdot}10^5(6{\cdot}10^6)$ pps entering the gas cell. The measured values of the Q_{SCL} are in good agreement with the calculated ones, for both cases of helium and argon as buffer gas.

Another technique to collect the electrons only in the gas cell is to apply a Radio-Frequency (RF) electric field with frequencies in the kHz domain. Despite the large data set collected in on-line experiments performed at the LISOL laser ion source, due to the incomplete understanding of the processes undergoing in the gas cell using RF fields, the results obtained with 2-5 kHz RF fields are presented and discussed in the Appendix A.

In the case of the heavy ion fusion reactions performed at LISOL (i.e. experiments of type (II)), in contrast to the experiments with a ^{58}Ni beam implanted in the gas cell, the projectile beam traverses the gas cell. The reaction products recoiling out of the target emerge in the gas cell in a forward cone with an opening of about 10°, typical for Ru/Rh/Tc isotopes produced in ^{58}Ni(^{40}Ar, $xnyp$) reactions at beam energies below 4.5 MeV/amu. The laser ion source efficiency for the production of Rh and Ru isotopes has been measured as function of the primary beam intensity at the optimum beam energy. As in the experiments with the stable ^{58}Ni beam, the laser ion source efficiency for the production of neutron-rich isotopes in heavy ion fusion reactions is also beam intensity dependent. A laser ion source efficiency up to 12% for the production of ^{95}Rh isotope was measured. The laser ion source efficiency for the production of ^{94}Ru isotope has its highest value of 0.8%. A remarkable feature observed during experiments with heavy ion induced fusion reactions was the high "non-resonant" yield of Tc isotopes from the ion source. The ion source efficiency for the production of ^{94}Tc has its maximum value of 3%. The measured selectivities of the laser ion source for the production of Rh and Ru isotopes are 22 and 11, respectively. The obtained results do show that the efficiency and selectivity of the laser ion source is as well element dependent (chemistry) as projectile beam intensity dependent.

The production of neutron-rich Ni and Rh isotopes in 30 MeV proton induced fission of ^{238}U was also extensively studied (category (III)). The analysis of the experimental data is not completed yet and a selection of results and a short discussion are provided in the Appendix B. However, as in the case of the heavy ion induced fusion reactions, the laser ion source efficiency for production of neutron-rich isotopes is element- and beam intensity dependent. Nevertheless, in the case of the fission ion-guide, the use of the shielding cylinder around the targets makes this dependence less stringent. The primary beam interaction zone and the laser ionization region are completely separated. Despite this separation, an important source of ionization in the fission gas cell is the presence of the high radioactivity. This limits the survival chance of the laser produced ions against recombination. The laser ion source efficiency for the production of neutron-rich ^{71}Ni and ^{112}Rh nuclei is 0.2% and 1.2%, respectively. A laser ion source selectivity for the extraction of ^{112}Rh isotopes of 65 was measured.

As an outlook, the results obtained in this work have led to a new operation scheme for the laser ion source (shown in Fig.6.1). This scheme will improve the efficiency and the selectivity and might be considered for the gas catcher systems currently under discussion for fragmentation reactions as well. The target is irradiated with a cyclotron beam pulse 50 ms wide, then during a time period τ_1 the recombination processes neutralize the ions and the electron-ion pair density in the gas cell decreases down to a level when an electrical field pulse ("Field 1") can

efficiently collect all the remaining electrons and ions. The lasers tuned to ionize the species of interest are switched on after this electrical field pulse without time delay. Immediately after the first laser pulse a continuous or pulsed weak electrical field ("Field 2") can be applied to remove the photo-electrons only, while the ions are transported by the gas flow unaffected by the electric field.

Using this working mode the laser ion source efficiency for the extraction of laser-produced ^{58}Ni ions could be increased by a factor 2.2 (see section 5.1.3). In that case a cyclotron beam pulse with the width of 50 ms and the intensity of $2.9{\cdot}10^{10}$ pps (as measured in DC mode) was stopped in the gas cell. A 245 V/cm field pulse was applied during 5 ms with a delay of 50 ms after the cyclotron pulse. This field is strong enough to collect all the remaining electrons and ions and a subsequent laser pulse ionizes the Ni atoms in an environment free of charges. If 50 ms after the laser pulse a 5 ms 10 V/cm field pulse is applied, the photo-electrons can be removed and the laser produced ion signal increases with 20%. The resulting efficiency of the laser ion source for the extraction of the laser produced Ni ions after this whole procedure amounts to ∼10% (assuming a duty-cycle of the cyclotron beam of 50/2050). The laser ion source selectivity can be improved by orders of magnitude as during the field pulse of 245 V/cm ("Field 1") practically all the "non-resonant" nickel ions which survive neutralization are collected on the cathode electrode.

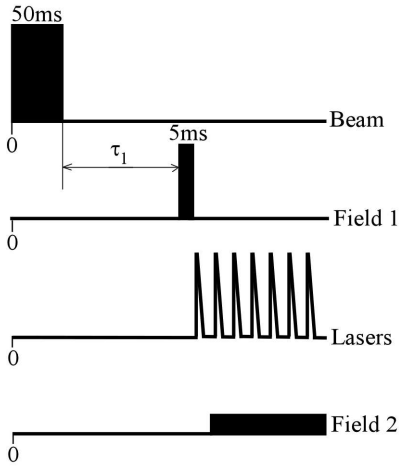

FIG. 6.1: The operation scheme of the laser ion source using pulsed cyclotron beam and pulsed electric field. A cyclotron beam pulse impinges on the target, then during a time period τ_1 the recombination processes neutralize the ions and the electron-ion pair density in the gas cell decreases down to a level when an electrical field pulse ("Field 1") can efficiently collect all the remaining electrons and ions. The lasers tuned to ionize the species of interest are switched on after this field pulse. Immediately after the first laser pulse a continuous or pulsed weak electrical field ("Field 2") can be applied to remove the photo-electrons only.

Application of electric fields in the fission gas cell requires modifications of the present configuration due to the special arrangement of the targets and beam shielding cylinder. However, in the case of the heavy ion induced fusion-evaporation reactions electric fields could be applied in the gas cell. The ^{40}Ar which creates electron-ion pairs with the same rate as a $2.9{\cdot}10^{10}$ pps ^{58}Ni beam, has an intensity of $2.2{\cdot}10^{10}$ pps (this beam passes the gas cell, thus the electron ion pairs are created all along the beam, plus that the ^{40}Ar projectiles lose about 50 MeV of their energy during the slowing down in the buffer gas). The measured laser ion source efficiency for the production of ^{95}Rh at this beam current is 10%. The use of a scheme equivalent to the one presented in Fig.6.1 would boost the laser ion source for the production of neutron-deficient Rh isotopes to 22%. A cyclotron beam pulse with a width of 125 ms and intensity of $2.2{\cdot}10^{10}$ pps (as measured in DC mode) impinges on the target. A 245 V/cm field pulse can be applied during 5 ms with a delay of 50 ms after the cyclotron pulse. This field is strong enough to collect all the remaining electrons and ions and a subsequent laser pulse ionizes the Rh atoms in an environment free of charges. After the laser pulse a 10 V/cm continuous field can be applied to remove the photo-electrons, and the laser-produced Rh ion signal can be improved further with at least 20%. Application of the 245 V/cm field pulse between the cyclotron pulse and the laser pulse would not only increase the survival chance of the laser produced ions but also the laser ion source selectivity. In this way the contaminant ions which would survive recombination and would thus be extracted and mass separated are completely removed on the collector electrodes and their γ-decay in the measured spectrum at the detection station does no longer contribute to the background counts.

Finally, it should be noted that a combination of RF and DC electrical fields applied along the extraction axis of the gas cell can speed up the evacuation of the photo-ions from the laser ion source. In this way the rather small duty-cycle of the above mentioned solutions can be partly overcome. These ideas will be tested with fission products from a spontaneous fission source (^{252}Cf) placed inside the LISOL laser ion source. Experiments with a ^{252}Cf spontaneous fission source mounted inside a newly constructed gas cell are ongoing at the LISOL laser ion source.

Appendix A

The effect of RF fields in the gas cell

A.1 General considerations

Another technique to collect the electrons in a gas cell and prevent the recombination of ions is to apply a Radio-Frequency (RF) electric field with frequencies in the kHz domain. In this way the motion of electrons and ions is decoupled. If one considers an RF electric field $E(x,t) = E_{RF}(x)\cos(2\pi\cdot\nu_{RF}\cdot t)$ applied along an axis (x) over the gap of two parallel electrodes, with $E_{RF}(x)$ the amplitude and ν_{RF} the frequency, the average drag force that an ion experiences due to the gradient RF field is given by [Wad03]:

$$\overline{F}(x) = -\nabla E_{RF}^2(x)\frac{e^2}{4m}\frac{1}{(4\pi^2\nu_{RF}^2 + 1/\tau_v^2)}, \tag{A.1}$$

where $\tau_v = \frac{\mu m}{e}$ is a parameter called the "velocity relaxation time", μ is the ion's mobility and m its mass. The velocity relaxation time is a measure of the damping effect of the gas on the ion motion in the absence of an electric field[1][Moo00]. Eq.(A.1) is simplified in two extreme cases according to the product $4\pi\nu_{RF}^2\tau_v^2$:

[1]When an electric field is applied in an ionized gas, the ions move under the action of the force $F_e = q\cdot E$, with q the charge of the ion and E the intensity of the electric field. The frictional force due to the collisions with the buffer gas atoms acting on the ions is proportional with the velocity v of the ions, and the proportionality constant is the ratio q/μ. If the electric field action suddenly stops, the equation of motion of an ion of mass m moving in the x direction is then:
$\mathrm{m}\ddot{x} = -q/\mu\ \dot{x}$,
which when integrated gives the velocity at a time t:
$v = v_0\exp(-\frac{q}{\mu m}t)$
where v_0 is the initial velocity of the ion. The quantity $\frac{\mu m}{q}$ has the unit of time and is called the "velocity relaxation time".

I. the vacuum limit for $4\pi\nu_{RF}^2\tau_v^2 \gg 1$

$$\overline{F}(x) = -\nabla E_{RF}^2(x)\frac{e^2}{16m\pi^2\nu_{RF}^2}, \tag{A.2}$$

II. the high pressure limit for $4\pi\nu_{RF}^2\tau_v^2 \ll 1$

$$\overline{F}(x) = -\nabla E_{RF}^2(x)\frac{e^2}{4m}\tau_v^2. \tag{A.3}$$

The velocity relaxation time corresponding to ions in argon gas at 500 mbar pressure is only 14.2 ns, therefore in the case of a 5 kHz RF electric field applied in the gas cell under these conditions, the high pressure limit is easily satisfied and the average force that an ion experiences due to the RF field gradient is negligible. The ion motion is thermal while the electrons created by the primary beam impact are efficiently removed by the RF field provided the RF field amplitude is high enough to overcome the space charge limit.

A.2 Effect of RF fields on the extraction of ^{40}Ar ions from the gas cell

The big cell filled with argon gas at 500 mbar pressure has been used to study the effect of an RF electric field on the extracted ion beam from the ion source. In that respect the configuration from Fig.5.13.a has been modified by changing the DC battery with an RF power generator. A ^{58}Ni cyclotron beam was implanted in the gas cell. The current on the collector plates was not monitored. The experimental results of the extracted beam current on mass 40 from the gas cell as function of the RF field amplitude (peak-to-peak) are plotted in Fig.A.1. The cyclotron beam current was $1.5{\cdot}10^5$ pps. Two different frequencies of the RF field were used, 2 and 5 kHz, respectively. According to eq.(A.3) the frequency of the RF electric field does not influence the ion motion and therefore it should not influence the signal of the extracted ion current from the gas cell, as it is observed from the experimental results in Fig.A.1. The ^{58}Ni beam creates electron-ion pairs with a rate $Q = 2.6 \cdot 10^{10}$ cm^{-3}s^{-1} and according to eq.(4.25) the collector efficiency is equal to unity when a DC field $E_0 \geq 120$ V/cm is applied over the 2 cm gap of the electrodes. This means that for all the RF voltage amplitudes from Fig.A.1 the electrons produced by the primary beam are not collected in their totality as the ion collector was working in the space charge limited regime.

The calculated width of the ion collection zone (w) and ion collector efficiency (f_{IC}) for a plane parallel geometry ($d_0 = 2$ cm) when a DC field with the amplitude E_0 is applied across the electrodes gap, the measured ion source efficiency for extraction of ^{40}Ar ions created by a $1.5{\cdot}10^5$ pps ^{58}Ni beam with and without RF field (ϵ_{LIS}), respectively (see Fig.A.1) and the resulting ratios $\frac{\epsilon_{LIS}^{RF}}{\epsilon_{LIS}^{RFoff}}$ are given in Table A.1. As one can see in Table A.1 the ion source efficiency for extraction of the ^{40}Ar ions increases up to $2.8{\cdot}10^{-2}$% for the highest RF field amplitude $E_0 =$ 50 V/cm. This efficiency is ~ 4 times higher than that without RF field.

In the previous example the maximum collection efficiency for electrons was 65%. A 100% collection is desirable, therefore, it is important to study the effect of the cyclotron beam intensity implanted in the cell for a fixed frequency and

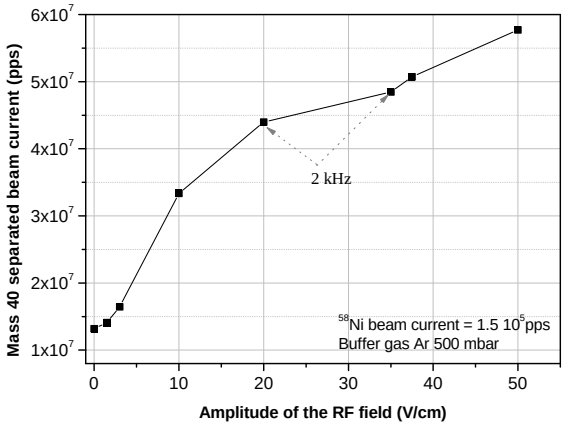

Fig. A.1: The intensity of the current on mass 40 extracted from the big cell filled with Ar at 500 mbar pressure when a ^{58}Ni beam current of $1.5{\cdot}10^5$ pps is implanted in it as function of the RF field amplitude (peak-to-peak). The RF field frequency was 5 kHz, with the exception of the two points indicated on the graph, for which this was 2 kHz.

amplitude of the RF field on the extracted beam current from the ion source. This has been done for an RF electrical field of 5 kHz frequency and 35 V/cm amplitude (peak-to-peak) applied between the two parallel plates in the big gas cell. The extracted beam current on mass 40 from the ion source has been measured

Table A.1: The calculated width of the ion collection zone (w) and ion collector efficiency (f_{IC}) for a plane parallel geometry (d_0 = 2 cm) when a DC field with the amplitude E_0 is applied across the electrodes gap, the measured ion source efficiency for extraction of ^{40}Ar ions created by a $1.5{\cdot}10^5$ pps ^{58}Ni beam with and without RF field (ϵ_{LIS}), respectively (see Fig.A.1) and the resulting ratios $\frac{\epsilon_{LIS}^{RF}}{\epsilon_{LIS}^{RFoff}}$.

E_0 (V/cm)	w (cm)	f_{IC} (%)	ϵ_{LIS} (%)	$\frac{\epsilon_{LIS}^{RF}}{\epsilon_{LIS}^{RFoff}}$
0	-	-	$6.4{\cdot}10^{-3}$	-
3	0.2	11.3	$8.0{\cdot}10^{-3}$	1.2
10	0.6	29.1	$1.6{\cdot}10^{-2}$	2.5
20	0.8	41.2	$2.1{\cdot}10^{-2}$	3.3
35	1.1	54.5	$2.4{\cdot}10^{-2}$	3.7
50	1.3	65.2	$2.8{\cdot}10^{-2}$	4.4

as function of the incoming cyclotron beam current. The results are plotted in Fig.A.2 for the case without and with an RF field applied in the cell, respectively, and summarized in Table A.2 together with some relevant calculated quantities (equilibrium density, n_{eq} (eq.(3.15)), recombination time constant, τ_r (eq.(3.14)), width of the charge collection zone, w, and ion collector efficiency, f_{IC}^{DC}, as for a plane parallel (d_0=2 cm) DC field collector with E_0 = 35 V/cm the amplitude of the field).

At the lowest used beam current ($1.5{\cdot}10^5$ pps) the ion source efficiency for extraction of ^{40}Ar ions increases by a factor 3.7 when an RF electric field with the amplitude of 35 V/cm is applied in the cell compared to the case without field, even though the collection efficiency for electrons as for a DC field with the same amplitude is only 54.5%. It is important to note that the steady state of the space charge density in such a DC field ion collector is reached in about 17 ms, thus a rather long time period. However, in the case of a 5 kHz RF electric field the polarity of the electrodes is inverted every 100 μs, therefore the description of the space charge evolution becomes complicate. In the case of a kHz RF field because the positive ions do not drift towards the cathode electrode, the built-up of the space charge is faster than in the case of a DC electric field. The space charge effects in RF fields have been little studied and our interpretation is more qualitative than quantitative. At the highest used beam intensity ($1.4{\cdot}10^9$ pps) the efficiency for extraction of ^{40}Ar ions from the gas cell remains approximately the same with and without RF field. The collection efficiency for electrons as for a DC field with the same amplitude is only 5.5% and the field free zone spans over

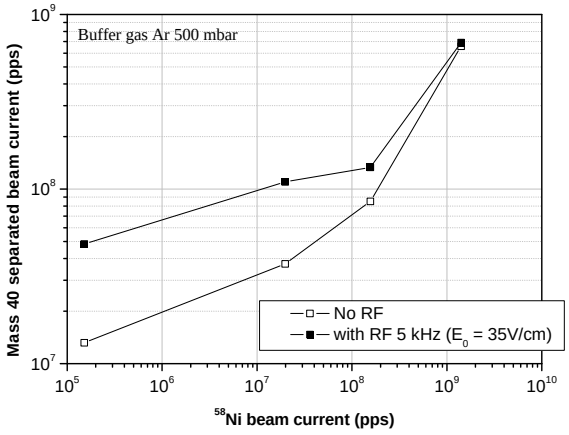

FIG. A.2: The intensity of the current on mass 40 extracted from the big cell filled with Ar at 500 mbar pressure when a ^{58}Ni beam is implanted in it as function of the cyclotron beam current, without (open squares) and with an applied RF field (full squares), respectively. The RF field frequency was 5 kHz and the amplitude 35 V/cm (peak-to-peak).

94.5% of the electrodes gap. Therefore, at such high ionization rates the RF field is almost completely shielded and it does not play any role. The evacuation of the ions from the cell is the same as without RF field.

This can also be seen in the time profiles of the ion signal on mass 40 extracted from the gas cell, shown in Fig.A.3. A cyclotron beam pulse (50 ms width) is implanted in the cell and the extracted time spectrum of the ion signal on mass 40 is recorded with and without an RF field applied between the electrodes. The cyclotron beam intensity is $3.7{\cdot}10^9$ pps ($Q = 6.4 \cdot 10^{14}$ cm^{-3}s^{-1}) as measured in DC mode. As already shown (see Fig.5.7.a), when working in a pulsed mode at high intensities of the ^{58}Ni beam implanted in the big cell filled with argon gas at 500 mbar pressure, most of the ^{40}Ar ions extracted from the ion source in the absence of electrical fields come from a region close to the exit hole of the cell. This can also be seen in Fig.A.3, i.e. the time profile labelled "RF OFF". Applying an RF field with an amplitude 27.5 V/cm (peak-to-peak) and frequency of 2 kHz does not significantly change this time profile (the curve labelled "RF ON (2 kHz, E_0=27.5 V)" on Fig.A.3) meaning that the space charge is rapidly established during the implantation of the nickel beam in the cell and that the applied electric field does not penetrate across the electrodes gap to effectively collect the created electrons. Moreover, even in the exit hole region the evacuation of the ^{40}Ar ions produced by energetic photons is not affected by the application of the RF field. There the amplitude of the electric field is 8 V/cm (see Fig.4.4.b). Recalling the calculations presented in Fig.5.19 one can consider that the electric field in a region 0 to 1 cm from the exit hole is analogous to the field in a cylindrical ionization chamber (similar to the one in Fig.4.7.b) having the radius of the inner(outer) electrode of 1cm(2cm) and 11V biasing voltage on the inner electrode. Such an ionization chamber becomes completely field free when the ionization rate is $6.2{\cdot}10^{12}$ electron-ion pairs/cm^{3}s, thus a factor of 100 lower than in the beam interaction zone. Therefore one can intuitively deduce that the value of the ionization rate in the exit hole region due to the energetic photons emitted during the slowing down of the projectile beam is at least equal to the above given value.

In order to ensure an effective collection of the electrons by an RF electric field one has to reduce the intensity of the implanted beam current in the gas

Table A.2: The calculated equilibrium density, n_{eq} (eq.(3.15)), recombination time constant, τ_r (eq.(3.14)), ion source efficiency ϵ_{LIS}^{RFOFF} and ϵ_{LIS}^{RFON} without and with an RF field (see Fig.A.2), respectively, as well as the calculated width of the charge collection zone, w, and ion collector efficiency, f_{IC}^{DC}, as for a plane parallel (d_0=2 cm) DC field collector with E_0 = 35 V/cm the amplitude of the field.

	RF field OFF			RF field ON	DC field	
I_{beam} (pps)	n_{eq} cm^{-3}	τ_r (ms)	ϵ_{LIS}^{RFOFF} (%)	ϵ_{LIS}^{RFON} (%)	w (cm)	f_{IC}^{DC} (%)
$1.5{\cdot}10^5$	$1.6{\cdot}10^8$	6.20	$6.5{\cdot}10^{-3}$	$2.4{\cdot}10^{-2}$	1.1	54.5
$2.0{\cdot}10^7$	$1.8{\cdot}10^9$	0.54	$1.4{\cdot}10^{-4}$	$4.1{\cdot}10^{-4}$	0.3	16.1
$1.6{\cdot}10^8$	$5.2{\cdot}10^9$	0.19	$4.0{\cdot}10^{-5}$	$6.4{\cdot}10^{-5}$	0.2	9.6
$1.4{\cdot}10^9$	$1.6{\cdot}10^{10}$	0.06	$3.5{\cdot}10^{-5}$	$3.7{\cdot}10^{-5}$	0.1	5.5

cell. The time profiles of the ^{40}Ar ion signal extracted from the big cell filled with argon gas at 500 mbar were recorded with and without an RF electric field applied between the electrodes and cyclotron beam pulses (50 ms width) with intensities of $4.7{\cdot}10^3$ pps and $3.7{\cdot}10^4$ pps, respectively, as measured in DC mode. These time profiles are plotted in Fig.A.4. It is interesting to note that for the lowest intensity of the cyclotron beam, i.e. $4.7{\cdot}10^3$ pps ($Q = 8.3 \cdot 10^8$ cm^{-3}s^{-1}) as measured in DC mode, the application of the RF electric field (2 kHz, E_0=27.5 V/cm) does not induce significant changes of the time profile. This result is in contrast with the fact that a DC field with the same amplitude is strong enough to ensure an electron collection efficiency equal to unity (see f_{IC}^{DC} in Table A.3). The ion source efficiency for extraction of ^{40}Ar ions can be deduced from Fig.5.12 when no RF field is applied (see TableA.3). It shows that ∼99% of the argon ions recombine in the gas cell before being extracted. When the RF field is applied all the electrons are collected and at the end of the cyclotron beam pulse the positive ion cloud left behind contains as much as $3.2{\cdot}10^8$ ions. One can estimate the density of positive ions (n_+) at the end of the cyclotron beam pulse and consequently after 400 ms as given by eq.(4.31). This density is $n_+(400\text{ms}) = 4.0{\cdot}10^5$ cm^{-3} (see TableA.3). Comparing this density with the electron-ion pair density after 400 ms ($n(400\text{ms})$), when no electric field is applied, one can observe that the mutual repulsion of ions after removal of the electrons can induce more losses of ions than the recombination

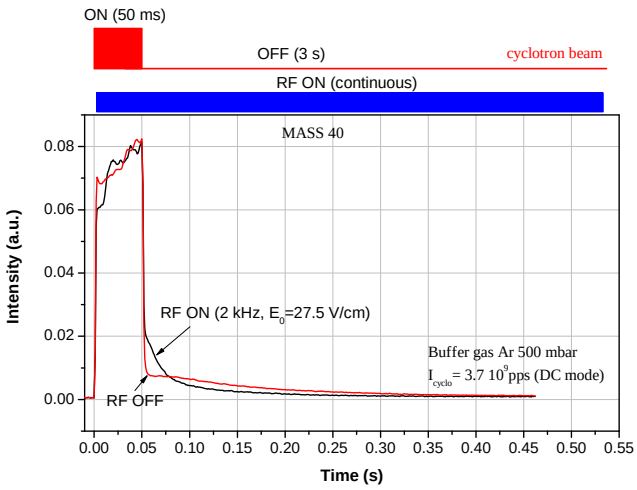

FIG. A.3: The time profiles of the ion signal on mass 40 extracted from the big cell filled with argon gas at 500 mbar when a ^{58}Ni cyclotron beam pulse (50 ms width) is implanted in it and an RF electric field is either applied or not (as indicated on the graph). The cyclotron beam current is $3.7{\cdot}10^9$ pps as measured in DC mode. The RF field frequency is 2 kHz and the amplitude 27.5 V/cm (peak-to-peak). Note that the RF field was applied only in the case of one of the time profiles.

processes.

When a higher beam current is used, $3.7{\cdot}10^4$ pps, the ion signal with RF field is increased by 50% compared to the signal without RF field (see TableA.3). This increase is mainly observed in a region close to the exit hole (100 ms delay) and deep in the cell (delay larger than 500 ms) where the density of electron-ion pairs created by the primary projectiles is smaller than in the cyclotron beam interaction zone (see Fig.A.4). In the beam interaction zone (∼500 ms) no significant increase is seen. There the efficiency for collection of electrons as for a DC field with the same amplitude is 68%. Therefore, the increase of the ion signal with RF field can be explained by two effects: the efficient collection of electrons outside the beam interaction zone and thus enhanced survival chance of the ions against recombination in this zone; and the pushing of ions from the beam interaction zone by the Coulomb mutual repulsion after removal of the electrons.

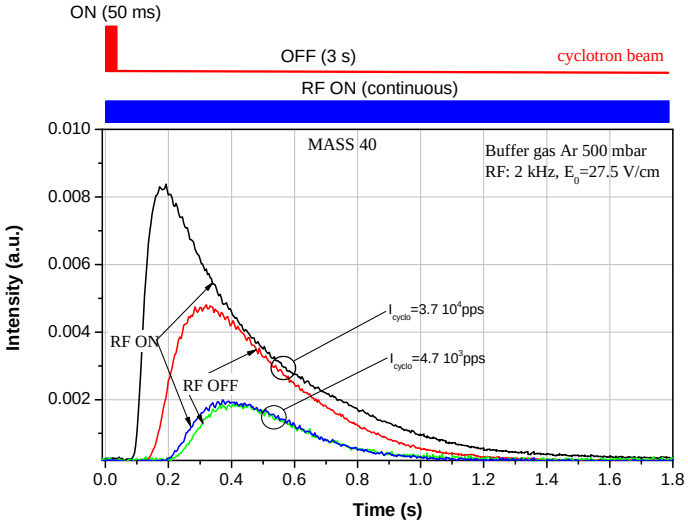

Fig. A.4: The time profiles of the ion signal on mass 40 extracted from the big cell filled with argon gas at 500 mbar when a low intensity ^{58}Ni cyclotron beam pulse (50 ms width) is implanted in it and an RF electric field is either applied or not (as indicated on the graph). Two cyclotron beam intensities were used: $4.7{\cdot}10^3$ pps and $3.7{\cdot}10^4$ pps as measured in DC mode, respectively. The RF field frequency is 2 kHz and the amplitude 27.5 V/cm (peak-to-peak). Note that the RF field was applied only when indicated on the graph.

A.3 Effect of RF fields on the extraction of ^{58}Ni ions from the gas cell

The time profiles of the laser produced ^{58}Ni ion signal extracted from the big gas cell have been studied using RF electric fields applied in the cell. The results are presented in Fig.A.5 for two intensities (as measured in DC mode) of the implanted ^{58}Ni beam in the gas cell filled with 500 mbar Ar: a) $2{\cdot}10^8$ pps and b) $8.4{\cdot}10^6$ pps, respectively. The lasers run at 200 Hz pulse repetition rate. The RF electric field, when applied, has an amplitude of 27.5 V/cm (peak-to-peak) and 2 kHz frequency. The laser ion source efficiency (ϵ_{LIS}^{RFOFF}) as deduced from Fig.5.12 for extraction of laser produced ^{58}Ni ions without electric field, the collector efficiency as for a DC field with the same amplitude (E_0=27.5 V/cm) and the measured ratio $\frac{A_{RFOFF}-A_{RFON}}{A_{RFOFF}}$, where A_{RFOFF} and A_{RFON} are the areas of the time profiles without and with RF field from Fig.A.5, respectively, are given in Table A.4 for both used beam intensities.

A first observation from Fig.A.5 and Table A.4 is that the nickel-58 signal extracted from the gas cell is always less with a continuous RF electric field than without. This is valid for both intensities of the ^{58}Ni beam used in measurements. The maximum ion signal is observed with time delay of about 500 ms, i.e. the evacuation time by gas flow from the beam interaction zone. On another hand, the use of an RF electric field in the gas when DC beams with intensity in the range 10^5 - $5{\cdot}10^8$ pps are used leads to an increase of the ^{40}Ar ion signal extracted from the ion source compared to the ion signal without RF electric field (see Fig.A.2). This increase becomes less important as the cyclotron beam is raised. Inspecting Table A.4 one can see that the reduction of the ^{58}Ni signal using RF field, $\frac{A_{RFOFF}-A_{RFON}}{A_{RFOFF}}$, decreases when the cyclotron beam intensity is raised. The re-

TABLE A.3: The calculated equilibrium density of electron ion pairs after the cyclotron beam pulse, n_{eq} (eq.(3.15)), and after 400 ms, (n(400ms)) (eq.(3.17)), ion source efficiency ϵ_{LIS}^{RFOFF} without RF field (see Fig.5.12), as well as the calculated ion collector efficiency, f_{IC}^{DC}, as for a plane parallel (d_0=2 cm) DC field collector with E_0 = 27.5 V/cm the amplitude of the field and the density of the positive ions 400 ms after the beam pulse, n_+(400ms) (eq.(4.31)), considering the immediate collection of the electrons. The ratio $\frac{A_{RFON}}{A_{RFOFF}}$ represents the ratio of the areas of the time profiles from Fig.A.4 with and without RF field, respectively, for a given beam intensity. Note that the ion source efficiency ϵ_{LIS}^{RFOFF} is calculated for the beam intensity $I_{beam} \cdot \frac{50}{3050}$ and the ion collector efficiency for a DC beam with the quoted value of the intensity.

		RF field OFF		DC field	RF field ON	
I_{beam} (pps)	n_{eq} cm^{-3}	n(400ms) cm^{-3}	ϵ_{LIS}^{RFOFF} (%)	f_{IC}^{DC} (%)	n_+(400ms) cm^{-3}	$\frac{A_{RFON}}{A_{RFOFF}}$
$4.7{\cdot}10^3$	$8.3{\cdot}10^8$	$2.5{\cdot}10^6$	1.39	100.0	$4.0{\cdot}10^5$	1.1
$3.4{\cdot}10^4$	$6.5{\cdot}10^9$	$2.5{\cdot}10^6$	0.27	68.3	$4.1{\cdot}10^5$	1.5

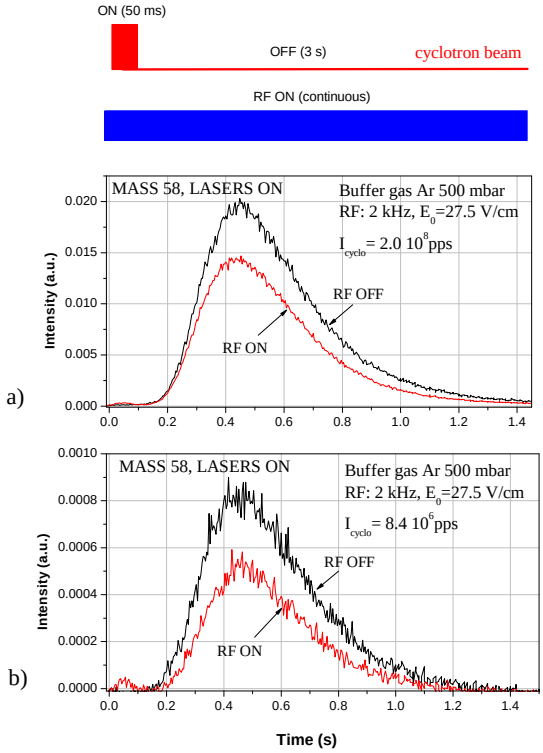

Fig. A.5: The time profiles of the laser produced nickel-58 ion signal extracted from the big cell filled with argon gas at 500 mbar when a cyclotron ^{58}Ni beam pulse (50 ms width) is implanted in it and an RF electric field is either applied or not (as indicated on the graphs). Two cyclotron beam intensities were used: a) $2.0{\cdot}10^8$ pps and b) $8.4{\cdot}10^6$ pps as measured in DC mode, respectively. The lasers are running at 200 Hz pulse repetition rate. Note that the RF field was applied only when indicated on the graph ("RF ON"). The RF field frequency is 2 kHz and the amplitude 27.5 V/cm (peak-to-peak).

duction of the laser produced ^{58}Ni ion signal when an RF field is used may have two sources: the Coulomb repulsion of primarily implanted nickel ions which survive recombination and the Coulomb repulsion of the laser produced nickel ions, respectively, in a high density positive charge cloud left in the gas cell by the removal of the electrons. However, increasing the intensity of the projectile beam implanted into the gas cell results in a reduction of the electron collection efficiency and thus an increase of the width of the field free zone. As the electron collection efficiency becomes lower so does the effect of the Coulomb repulsion of the ions in the gas cell. The ion source efficiency for extraction of laser produced ^{58}Ni ions, when a 50

ms cyclotron beam pulse with the intensity $8.4 \cdot 10^6$ pps (measured in DC mode) is implanted in the gas cell, drops from 6% down to 4.3% when an RF field is used. The corresponding drop of the laser ion source efficiency when $I_{beam} = 2 \cdot 10^8$ pps (DC mode) is from 10% down to 5.6%.

The use of RF electrical fields in the gas cell results in a reduction of the ^{58}Ni ion signal extracted from the laser ion source. This reduction accounts for both losses of initially implanted nickel ions which survive recombination and laser produced nickel ions due to the Coulomb repulsion in the positive charge cloud left in the cell by the removal of a fraction of the electrons. Measuring the ^{58}Ni signal extracted from the ion source with and without laser ionization, and by using or not an RF field, respectively, can help us determine what fraction of implanted(laser produced) Ni ions is lost as result of the electron collection (i.e. increase of the effect of mutual repulsion of ions). The 10 mm channel cell filled with 450 mbar argon gas was used (see Fig.5.13.b). The time behavior of the ^{58}Ni ion signal extracted from the cell when a ^{58}Ni cyclotron beam pulse (1 s width) with the intensity of $6.5 \cdot 10^8$ pps (measured in DC mode) is implanted in it, was recorded with the lasers switched off (see Fig.A.6.a) and the lasers on (see Fig.A.6.b), with and without application of an RF electrical field (10 kHz, 55.5 V/cm)[2], respectively (as indicated on the figures). The time behavior of the ^{58}Ni signal extracted from this cell in the case of long cyclotron beam pulses and without applied electric fields was already discussed (see Fig.5.9). Inspecting Fig.A.6 it becomes clear that the use of RF electrical fields in the gas cell results in losses of both primary nickel ions implanted in the cell which survive neutralization processes as well as of laser produced ^{58}Ni ions. The laser ion source efficiency (ϵ_{LIS}^{RFOFF}) as deduced from Fig.5.12 for extraction of ^{58}Ni ions, with and without laser ionization, without using electric field and the measured ratio $\frac{A_{RFOFF}-A_{RFON}}{A_{RFOFF}}$, where A_{RFOFF} and A_{RFON} are the areas of the time profiles without and with RF field from Fig.A.6, respectively, are given in Table A.5. The electron collector efficiency as for a plane

[2]It has been shown that the electric field in this cell is not like in a plane parallel geometry but similar to the field in a cylindrical ionization chamber. Nevertheless, here we use the approximation for a parallel plate geometry, hence the average value of the electric field is 55.5 V/cm.

TABLE A.4: The laser ion source efficiency (ϵ_{LIS}^{RFOFF}) as deduced from Fig.5.12 for extraction of laser produced ^{58}Ni ions without electric field, the collector efficiency as for a DC field with the same amplitude (E_0=27.5 V/cm) and the measured ratio $\frac{A_{RFOFF}-A_{RFON}}{A_{RFOFF}}$, where A_{RFOFF} and A_{RFON} are the areas of the time profiles without and with RF field from Fig.A.5, respectively. Note that the laser ion source efficiency is calculated for a beam intensity $I_{beam} \cdot \frac{50}{3050}$ and the ion collector efficiency for a DC beam with the quoted value of the intensity.

I_{beam} (pps)	ϵ_{LIS}^{RFOFF} (%)	f_{IC}^{DC} (%)	$\frac{A_{RFOFF}-A_{RFON}}{A_{RFOFF}}$ (%)
$2.0 \cdot 10^8$	∼6	7.9	28.5
$8.4 \cdot 10^6$	∼10	17.6	44.0

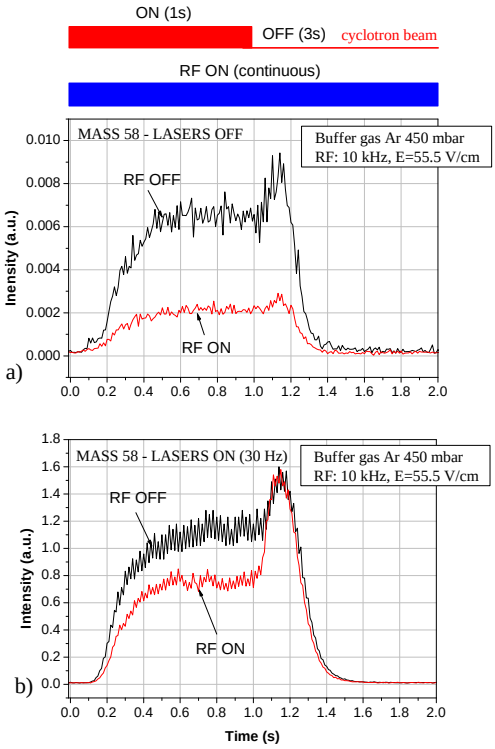

Fig. A.6: The time profiles of the nickel-58 ion signal a) with the lasers off and b) with the lasers on, respectively, extracted from the 10 mm channel cell filled with argon gas at 450 mbar when a cyclotron ^{58}Ni beam pulse (1 s width) is implanted in it and an RF electric field is either applied or not (as indicated on the graphs). The cyclotron beam intensity was $6.5{\cdot}10^{8}$ pps as measured in DC mode. For graph b) the lasers pulse repetition rate is 30 Hz. Note that the RF field was applied only when indicated on the graph ("RF ON"). The RF field frequency is 10 kHz and the amplitude 55.5 V/cm (peak-to-peak).

parallel geometry when a DC electric field of 55.5 V/cm is applied across the 1.8 cm gap between the electrodes and a DC cyclotron beam with the intensity of $6.5{\cdot}10^{8}$ pps is implanted in the gas cell is only 10%. Extrapolating this result for the case of an RF electric field applied in the cell one could say that the collection of 10% of the total number of created electrons results in the loss of 64.5% of the implanted nickel ions which have survived recombination and 26.6% of the laser produced nickel ions, respectively, due to the mutual repulsion of the ions in the positive charge cloud. Further on, using the ion source efficiencies from Table A.5, it is possible to estimate that a number of $8.8{\cdot}10^{4}$ nickel ions from a total of $3.3{\cdot}10^{5}$

which would have been extracted from the ion source without using RF field, are lost due to the mutual repulsion after their implantation in the gas cell and removal of 10% of the electrons. Ions which do not survive recombination neutralize and are subsequently laser ionized. When no RF field is used in the cell, a number of $1.4{\cdot}10^7$ nickel ions (from a total of $6.5{\cdot}10^8$ ions implanted in the cell) can be extracted using laser ionization. Using RF field results in the loss of $3.7{\cdot}10^6$ of them. It is interesting to mention that the laser ion source selectivity in the case without RF field is 170 and that it increases up to 370 when the RF field is switched on. However, the increase of the selectivity does not mean an improvement of the laser ion source performance, as the efficiency for extraction of ^{58}Ni ions from the cell is less with the RF field on than without electric field.

An interesting issue observed in Fig.A.6.b is the fact that at the end of the cyclotron beam pulse the ^{58}Ni ion signal with RF field rapidly becomes identical to the signal without RF field. One explanation could be that during the cyclotron beam the energetic photons ionize the buffer gas at the entrance of the channel where the RF field is capable of collecting the electrons, and thus a positive charge cloud is formed there repelling the laser produced nickel ions. Once the creation of charges at the entrance of the channel has stopped, the charge cloud disappears and the laser produced ions can be evacuated from the cell. The ion signal with RF field grows to the same value as without RF field within 60 ms, i.e the evacuation time of the channel region.

RF electric fields can be applied in the gas cell aiming to collect the electrons created during the primary beam impact. The electron collection efficiency is limited by the space charge effects at high ionization rates. An increase of the signal of ^{40}Ar ions extracted from the gas cell is observed when an RF field is used and the intensity of the primary beam is low enough to permit electron collection. This increase is mainly due to ^{40}Ar ions created in zones close to the exit hole and deep in the cell. There the electron-ion pairs are created by the ionization due to energetic photons emitted during the stopping of the primary projectiles and their density is much lower than in the beam interaction zone. Collection of the electrons close to the exit hole may explain the poor evacuation of ^{58}Ni ions when RF fields are used. A positive charge cloud is formed there, repelling the nickel ions which thus can not be evacuated from the gas cell. Both losses of primarily implanted nickel ions which have survived neutralization and of laser produced ^{58}Ni ions are observed. The laser ion source selectivity with RF field is higher than without electric field

TABLE A.5: The laser ion source efficiency (ϵ_{LIS}^{RFOFF}) as deduced from Fig.5.12 for extraction of ^{58}Ni ions, with and without laser ionization, without using electric field and the measured ratio $\frac{A_{RFOFF}-A_{RFON}}{A_{RFOFF}}$, where A_{RFOFF} and A_{RFON} are the areas of the time profiles without and with RF field from Fig.A.6, respectively. Note that the laser ion source efficiency is calculated for a beam intensity $6.5 \cdot 10^8 \cdot \frac{1}{4}$ pps.

Lasers	ϵ_{LIS}^{RFOFF} (%)	$\frac{A_{RFOFF}-A_{RFON}}{A_{RFOFF}}$ (%)
ON	2.1	26.6
OFF	0.02	64.5

as result of the more severe reduction of non-resonant (without lasers) nickel ions. However, using RF fields leads to a reduction of the laser ion source efficiency for extraction of ^{58}Ni ions (with or without lasers).

Appendix B

Experiments with proton induced fission of ^{238}U reactions

Neutron-rich radioactive isotopes are produced on-line at the LISOL laser ion source using the fission reaction of ^{238}U induced by a 30 MeV proton projectile beam. Two ^{238}U targets 10mg/cm^2 each are placed inside the gas cell at 20° angle with respect to the projectile beam direction. Argon gas at 500 mbar pressure is used to stop the fission fragments recoiling out of the target.

It is worthwhile to mention that in the case of a fission reaction the ionization produced in the gas cell is equally due to the passage of the cyclotron beam through the gas cell as to the stopping of the fission fragments recoiling out of the target. The cyclotron beam creates $\sim 10^{16}$ electron-ion pairs per μC. Additionally, $1.2{\cdot}10^7$ fission fragments per μC of projectile beam are created according to a total fission cross-section of 1.3 barn for 30 MeV protons on ^{238}U [Bab71]. The average energy imparted to the fission fragments is given by the Viola's law [Fra99]:

$$E_F^* \approx \frac{A_T - A_F}{A_T} \cdot E^* \tag{B.1}$$

where E^* is the total energy released to fission fragments

$$E^* = 0.1189 \frac{Z_T^2}{A_T^{1/3}} + 7.3\text{MeV} \tag{B.2}$$

with T and F subscripts for the target and the fragment, respectively. Assuming an average mass $A_F \simeq 100$ for the fission fragments and an average nuclear charge $Z_F \simeq 45$ one can calculate the ionization produced by the fission fragments only. This amounts to $1{\cdot}10^8$ electron-ion pairs per fragment, resulting in $1.2{\cdot}10^{15}$ electron-ion pairs per μC of projectile beam. However, the fission fragments deposit their energy all over in the gas cell, while the primary proton beam creates electron ion pairs only in its path. Moreover, radioactivity also contributes to the electron-ion pair density in the cell. Therefore, it is difficult to estimate the density of electron-

ion pairs in the gas cell in the case of proton induced fission reactions. To reduce the high pair density, the beam interaction zone is shielded from the rest of the gas cell volume by a cylinder surrounding the targets. The cylinder having a diameter of 16 mm holds a 3 μm thick Al foil. It consists of 18 slits 1.1 mm wide each. The geometrical transmission of the fission fragments through the cylinder is 64% (the chance of fission fragments recoiling out of the target inside the cylinder to pass through a slit in the volume of the gas cell).

B.1 Neutron-rich isotopes produced in ^{238}U(p,f) reactions

There is considerable amount of work performed in the field of proton induced fission (see [Fra99]) and the literature is very rich. At LISOL the interest is concentrated in the study of β-decay of neutron rich Co ($A = 70 - 71$) and Ni ($A = 72 - 76$) nuclei [Fra98, Fra01, Kru02]. From the Ni isotopic chain, the most produced one in the 30 MeV proton induced fission of ^{238}U reaction is the ^{70}Ni isotope [Kru02]. However, the spectroscopic information about the γ transitions belonging to this nucleus is poor. Therefore, the ^{71}Ni isotope ($T_{1/2}^{exp} = 2.56(3)$ s [Fra98]) has been used to tune the laser ion source for the production of neutron rich nickel isotopes. The γ transition at 534.4 keV ($I_\gamma = 58\%$) has been used to monitor the yield of ^{71}Ni [Fra98].

In order to deduce the laser ion source efficiency for the production of neutron-rich nickel isotopes one has to know the independent cross-section for the production of those nuclei in proton induced fission of ^{238}U reaction. Fig.B.1 shows the cross-sections for production of Co and Ni neutron-rich isotopes as function of the fragment mass, taken from reference [Kru02]. The experimental cross-sections (symbols) are based on the isotopic yields of neutron rich Co and Ni produced at LISOL in 30 MeV proton-induced fission of ^{238}U [Kru02, Tho04]. The theoretical cross-section (lines) are obtained using the PROFI computer code [Mue00]. The cross-section for production of ^{71}Ni isotope in 30 MeV proton induced fission of ^{238}U amounts to 0.14(3) mb.

During the on-line experiments a Rh isotope ($A = 112$) is used to tune and optimize the laser ion source for production of neutron-rich isotopes. This is due to the fact that the ^{112}Rh isotope is produced with a much higher cross-section and the lasers can be easily tuned to ionize it. An ample discussion concerning the ^{112}Rh isotopes produced at LISOL can be found in reference [Wei02]. Both ground- and isomeric-state decays of ^{112}Rh have been observed in the γ-spectra. Experimental and theoretical cross-sections for production of neutron-rich Rh isotopes in 19.8 MeV proton induced fission of ^{238}U reaction can be found in reference [Jau94]. The projectile energy in that work is slightly lower than the proton energy used at LISOL to produce neutron-rich nuclei, however, as the fission cross-section is already in saturation at proton energies $\sim$ 15 MeV [Bab71], the extrapolation of the independent isotopic cross-sections at 30 MeV proton energy is realistic. Fig.B.2 shows the cross-sections for production of Tc, Ru and Rh neutron-rich isotopes as function of the fragment mass. The experimental cross-sections are based on the independent isotopic yields given in reference [Jau94]. The calculated values have been taken from the same paper [Jau94] where the theoretical model is explained.

B.2 Yield of ^{112}Rh and ^{71}Ni from the laser ion source

Typical γ-spectra obtained for mass separated ions with $A/q = 112$ are presented in Fig.B.3 with the lasers off (a) and on (b) tuned to ionize Rh. The Ge detector is energy and intensity calibrated using standard ^{152}Eu and ^{60}Co γ sources. The 560 keV transition of the ^{112m}Rh isomer has been used to deduce the yield of Rh on mass 112 due to the fact that the ground-state of ^{112}Rh can be also fed through the β-decay of the parent ^{112}Ru nucleus. The half-life of the ^{112m}Rh isomer is $T_{1/2} =$ 6.8 s [Lhe99]. In the spectrum with the lasers off (Fig.B.3.a) many line transitions belonging to ^{112}Rh^{g,m} are observed as well as γ-lines belonging to the parent ^{112}Ru and the contaminant ^{96}Y. As shown in ref.[Wei02] the ^{96}Y contaminant is implanted on the tape at the detection station in the form of molecular ion ^{96}Y^{16}O which is not dissociated by the voltage applied between the gas cell exit and SPIG rods (see section 2.3.3). Switching on the lasers to resonantly ionize Rh clearly increases the count-rate in the specific γ-lines of ^{112}Rh. From the spectra from Fig.B.3 one can see that the acquired number of counts in 100 s is reasonable therefore the tuning of the parameters of the laser ion source can be done fast and reliably. The maximum yield of ^{112}Rh from the laser ion source was obtained with a proton beam current of $2.8{\cdot}10^{11}$ pps, namely $1.8{\cdot}10^{4}$ atom/μC (or 806 atom/s).

Once the laser ion source is optimized for the maximum production of the ^{112}Rh

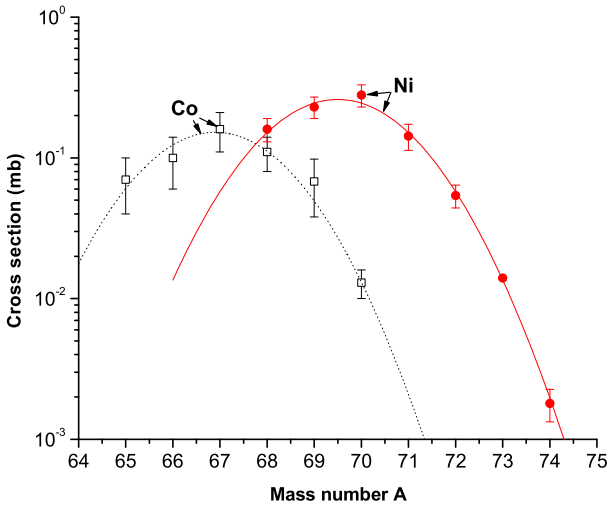

Fig. B.1: Experimental and theoretical cross-sections for production of neutron-rich Co and Ni isotopes in the 30 MeV proton-induced fission of ^{238}U [Kru02].

isotope, the mass separator is tuned to select ions with the ratio $A/q = 71$. Typical obtained γ-spectra for mass separated ions with $A/q = 71$ are presented in Fig.B.4 with the lasers off (a) and on (b) tuned to ionize Ni. The β-gated spectra are studied this time in order to ensure the correct identification of the isotopes provided their low production cross-section, thus low count-rates in the specific γ-lines. The β detection efficiency was measured to be 29% [Tho04]. In the γ spectrum with the lasers off (Fig.B.4.a) one can not observe transitions belonging to the ^{71}Ni isotope. The daughter isotope ^{71}Cu can be observed (489.7 keV) but it is not obvious that these are not ^{71}Cu ions directly produced in the reaction , which have survived neutralization in the gas cell (according to reference [Kru02] the cross-sections for production of ^{71}Ni and ^{71}Cu, respectively, are comparable). An interesting feature observed in Fig.B.4.a is the presence of the specific γ-lines of ^{142}Ba isotope and its daughter ^{142}La. The half-lives of these isotopes are much longer than that of the ^{71}Ni: $T_{1/2}$ (^{142}Ba) = 10.6 min [Geh81] and $T_{1/2}$ (^{142}La) = 91.1 min [Mac89]. Moreover, both ^{142}Ba and ^{142}La can be implanted onto the tape at the detection station only if they were extracted from the gas cell as +2 ions. The ^{142}Ba and ^{142}La γ-lines are present with the same intensity in the γ-spectrum recorded with the lasers on tuned to ionize Ni (see Fig.B.4.b) showing the non-resonant nature of production of these isotopes from the ion source.

In the γ spectrum recorded with the lasers on (Fig.B.4.b) tuned to ionize nickel, the specific γ-transitions of ^{71}Ni appear. Given the short half-life of the ^{71}Ni isotope, the γ-lines of the daughter ^{71}Cu actually dominate the spectrum. The maximum

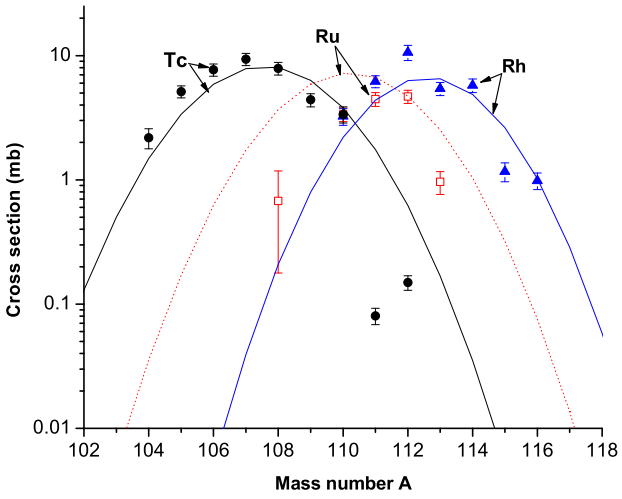

FIG. B.2: Experimental and theoretical cross-sections for production of neutron-rich Tc, Ru and Rh isotopes in the 19.8 MeV proton-induced fission of ^{238}U [Jau94].

yield of the ^{71}Ni isotope from the laser ion source was obtained with a $5.7{\cdot}10^{12}$ pps proton beam current, namely 35(5) atom/μC (or 32(4) atom/s).

B.3 The efficiency and selectivity of the fission ion guide

The efficiency of the laser ion source for production of neutron-rich isotopes in 30 MeV proton induced fission of ^{238}U is calculated as the ratio of the measured yield (for a particular isotope) to the predicted yield in the target according to the measured/theoretical cross-section from literature. The selectivity of the laser ion source is defined as in the case of heavy ion fusion reactions by the ratio of the yield of a particular isotope with the lasers on to the yield obtained without lasers. The laser ion source efficiency for production of the ^{112}Rh isotope has been studied as function of the primary proton beam intensity. Due to the low production cross-section of the nickel isotopes this was not possible for the ^{71}Ni isotope. However,

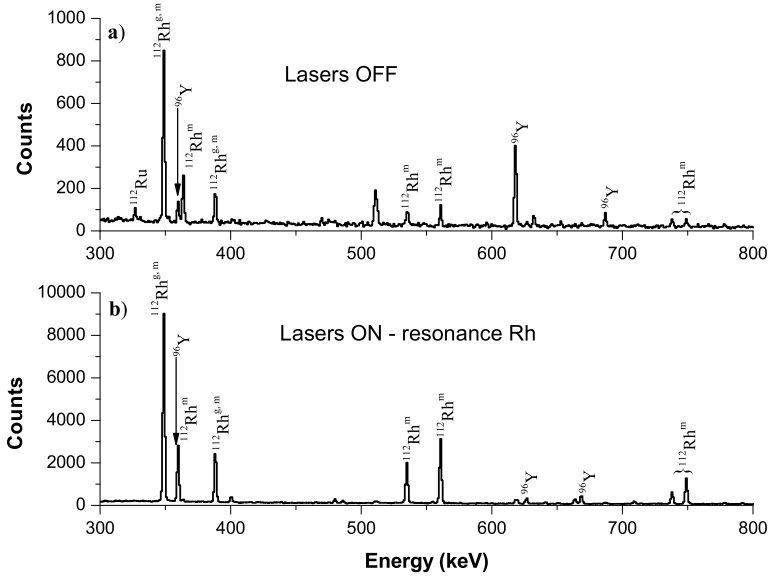

Fig. B.3: The obtained γ-spectra (in singles) for mass value 112 with a) the lasers off, and b) with the lasers on tuned to ionize Rh. The proton beam current impinging on the ^{238}U targets is $5.7{\cdot}10^{12}$ pps. The γ-transitions of ^{112}Ru, ^{112}Rh^{g,m} radioactive ions are indicated on the graphs as well as the γ-lines from the non-resonant ^{96}Y^{16}O molecular ion (see text). The acquisition time was 100 s.

the dynamic range of the proton beam is restricted to $2.8{\cdot}10^{11}$ - $1.1{\cdot}10^{13}$ pps. The experimental results are shown in Fig.B.5 (full circles). The laser ion source efficiency for production of ^{112}Rh with the lasers on has a smooth dependence on the cyclotron beam intensity in the dynamic range used for the measurements. This efficiency is at its maximum 0.31% for a beam current of $2.8{\cdot}10^{11}$ pps. At the maximum cyclotron beam current ($1.1{\cdot}10^{13}$ pps) the laser ion source efficiency drops down to 0.14%. Comparing the γ-spectra from Fig.B.3 and Fig.B.4 one can observe that the selectivity of the laser ion source could be deduced only for the ^{112}Rh isotope, while this was not possible for the case of the ^{71}Ni as in the γ spectrum taken with the lasers off there is no evidence for its specific γ-transitions. The experimental ion source efficiency for the production of ^{112}Rh with the lasers off are included in Fig.B.5 (open circles). A laser ion source selectivity of ~ 65 can be deduced from Fig.B.5 for the case of the ^{112}Rh isotope. The few experimental data points obtained for the laser ion source efficiency for the production of the ^{71}Ni isotope with the lasers on are also shown on Fig.B.5.

The laser ion source efficiency for the production of ^{71}Ni (lasers on), although

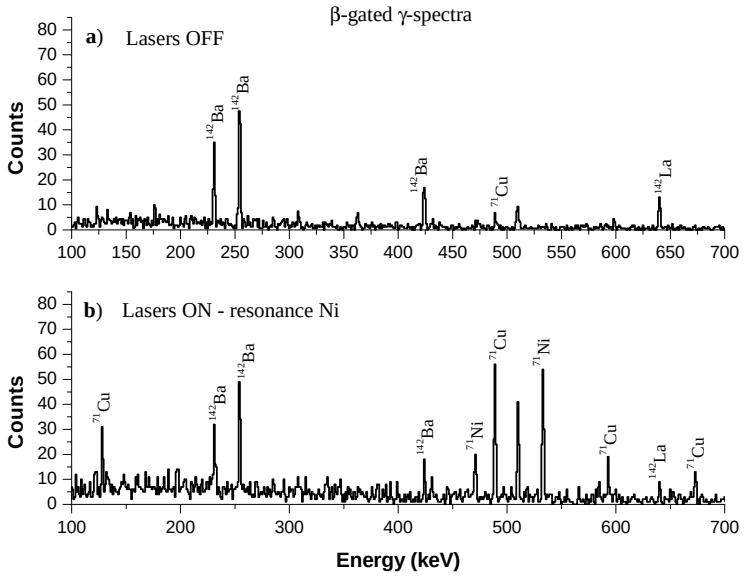

FIG. B.4: The obtained γ-spectra (β-gated) for mass value 71 with a) the lasers off, and b) with the lasers on tuned to ionize Ni. The proton beam current impinging on the ^{238}U targets is $5.7{\cdot}10^{12}$ pps. The γ-transitions of ^{71}Cu and ^{71}Ni are indicated on the graphs as well as the γ-lines from the non-resonant ^{124}Ba and ^{124}La (see text). The acquisition time was 1800 s.

only two measurements, is a factor of ∼6 less than that for the production of ^{112}Rh (lasers on) for the same projectile beam current. This difference may well arise from the theoretical cross sections used to deduce the yield in the target. However, further considerations concerning the transmission through the elements of the ion source and the stopping efficiency in the gas cell are necessary due to the special arrangement of the target-gas catcher system in the case of the fission cell. According to Viola's law (see eq.(B.1)) the difference between the kinetic energy imparted to ^{112}Rh and ^{71}Ni fragments, respectively, is 30 MeV. As the fission fragments are isotropically emitted inside the ^{238}U target the difference of the energy and the nuclear charge (Z) they have may result in a different transmission through the target as well as through the other elements inside the gas cell. Not of less importance is the stopping efficiency of the fission fragments in the gas cell volume. The SRIM computer code [SRIpr] has been used to simulate fission fragments emitted isotropically in a ^{238}U target (10 mg/cm^2 thickness). The result reveals that 42% of the initially produced ^{112}Rh nuclei are stopped inside the target, while the corresponding fraction of ^{71}Ni is 26% of the initially produced nuclei. Additional correction factors for the loss of fission fragments must account for the transmission through the buffer gas inside the shielding cylinder, transmission through the cylinder and the 3 μm Al foil as well as for the stopping efficiency

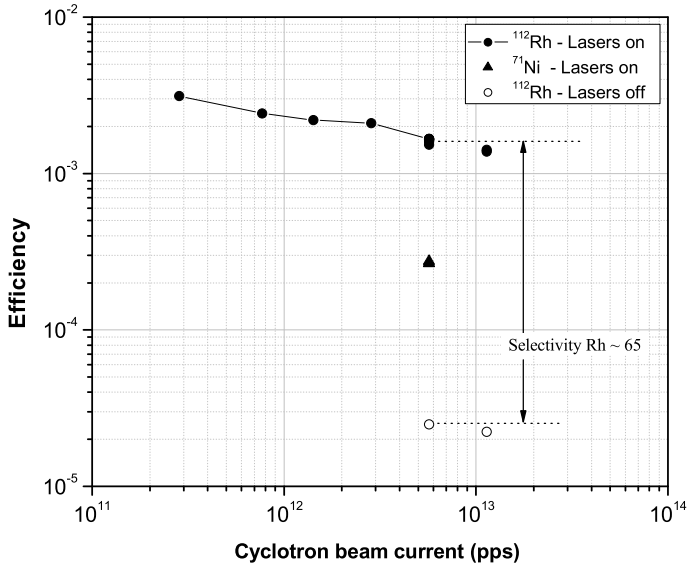

Fig. B.5: The dependence of the laser ion source efficiency on the primary proton beam intensity, for production of ^{112}Rh with lasers on (full circles), without lasers (open circles), as well as for ^{71}Ni with lasers on (full triangles).

inside the effective volume of the gas cell. These correction factors are summarized in Table B.1.

TABLE B.1: The calculated correction factors for the transmission and stopping of the ^{71}Ni and ^{112}Rh nuclei produced in the proton induced fission of ^{238}U: ϵ_t - the transmission efficiency through the target (fraction of total produced in the target 10 mg/cm^2 thick), ϵ_{cyl}^{geom} - geometrical transmission through the cylinder, ϵ_{cyl}^{Ar+Al} - the transmission efficiency through the gas (500 mbar Ar) inside the cylinder and through the 3 μm Al foil surrounding the cylinder (fraction of nuclei recoiled out of the target), ϵ_{stop} - the stopping efficiency of the nuclei inside the effective volume of the gas cell (fraction of nuclei transmitted through the cylinder).

	ϵ_t (%)	ϵ_{cyl}^{geom} (%)	ϵ_{cyl}^{Ar+Al} (%)	ϵ_{stop} (%)
^{71}Ni	74	64	64	46
^{112}Rh	58	64	39	85

If one considers that the total number of a particular isotope species produced in the target is N_t, using the correction factors from Table B.1, one deduces that a fraction $(1 - \epsilon_t \epsilon_{cyl}^{geom} \epsilon_{cyl}^{Ar+Al} \epsilon_{stop}) N_t$ is actually lost either inside the target, the gas in the cylinder, the shielding cylinder or on the cell walls, neglecting other loss mechanisms. Thus only 14%(13%) of the ^{71}Ni(^{112}Rh) nuclei produced in the target are stopped in the gas and can be flown in the laser ionization zone. With the above corrections it is possible to define the laser ion source efficiency as the ratio of the number of nuclei extracted from the gas cell and measured at the detection system to the number of nuclei stopped inside the gas cell outside the shielding cylinder. Using the values for the correction factors from Table B.1 one finds that the laser ion source efficiency for the extraction of ^{71}Ni and ^{112}Rh nuclei stopped in the gas cell is 0.2% and 1.2%, respectively, for a cyclotron beam intensity of $5.7 \cdot 10^{12}$ pps. Thus the laser ion source efficiency for the production of ^{71}Ni is a factor of 6 less than for the production of ^{112}Rh. This factor is not understood yet.

As in the case of the heavy ion induced fusion reactions, the laser ion source efficiency is element- and beam intensity dependent. However, in the case of the fission ion-guide, the use of the shielding cylinder around the targets makes this dependence less stringent. The primary beam interaction zone and the laser ionization region are completely separated. Despite this separation, an important source of ionization in the fission gas cell is the presence of the high radioactivity. This limits the survival chance of the laser produced ions against recombination. The fact that the γ-decays of ^{142}Ba and ^{142}La have been observed in the recorded γ-spectra on mass 71 shows that ions in a +2 state can be extracted from the gas cell. Further investigations should clarify whether this is the result of charge exchange processes or efficient thermalization of ions in the +2 state (see also section 3.8).

Samenvatting

1. Inleiding en motivatie

De atoomkern is één van de fundamentele bouwstenen van materie in de natuur. De kernkaart telt ongeveer 3000 verschillende bekende kernen maar de huidige modellen voorspellen dat er nog minstens 4000 andere kernen te ontdekken zijn. De grenzen van dit landschap op de kernkaart (Fig.1.1), worden afgebakend door de proton (B_p=0) en neutron (B_n=0) druppellijnen, buiten deze grenzen zijn de kernkrachten niet sterk genoeg meer om de kern bij elkaar te houden en vervalt deze onmiddellijk door het uitstoten van protonen en neutronen. Een derde grens, afgezien van de proton en neutron druppellijnen, wordt bepaald door de maximale lading en massa die een atoomkern en een atoom kan bereiken. Het aantal elementen dat geproduceerd kan worden in een kernreactie wordt beperkt door de toenemende waarschijnlijkheid van fissie, α- en protonemissie bij toenemende nucleaire lading.

Aangezien radioactieve kernen niet in de natuur voorkomen moeten ze eerst geproduceerd worden in een kernreactie, bijvoorbeeld in zware ionen genduceerde fragmentatie of in neutrongenduceerde fissie. Daarom is de voortdurende ontwikkeling van technieken om Radioactieve Ionen Bundels (RIB) te produceren nodig om moeilijk bereikbare gebieden op de kernkaart te kunnen bestuderen, in het bijzonder kernen op de grens van deeltjes stabiliteit. Wetenschappelijk onderzoek dat gebruik maakt van radioactieve ionenbundels speelt een voortrekkersrol in de kernfysica en richt zich tot fundamentele vragen in verband met de kernstructuur , nucleaire astrofysica en de fysica van fundamentele interacties.

Een nieuwe generatie RIB faciliteiten tracht twee gekende technieken, de invlucht techniek en de ISOL techniek (Isotopen Separatie On-Line) te combineren om de meest exotische, kortlevende isotopen te produceren. Door de voordelen van beide technieken te combineren kan men de lange vertragingstijden die eigen zijn aan de ISOL techniek vermijden. De reactieproducten worden gestopt in een cel gevuld met edelgas en de ionen worden met de hulp van elektrische velden uit de gascel geleid. Een radiofrequente (RF) koeler zorgt voor de extractie van de ionen uit het gas en injecteert ze in een versneller. De Leuven Isotopen Separator On-Line (LISOL) gebruikt een gascel gevuld met helium of argon om de reactieproducten te stoppen van zware ionen genduceerde fusiereacties [Sav02, VDu03, Huy04] of lichte ionen genduceerde fissie van uranium [Fra98, Fra99, Fra01]. Vervolgens worden de isotopen van een welbepaald element geoniseerd door resonante laserionisatie, versneld, naar massa gescheiden en gemplanteerd op een verplaatsbare tape. Het beta- en gamma-verval kan dan worden gedetecteerd.

Om de mogelijkheden van het gebruik van een gascel voor de productie van in-

tense radioactieve bundels uit te breiden is het karakteriseren van de verschillenden processen die zich hierbij afspelen van groot belang. Typische vertragingstijden in de LISOL gascel variren van enkel tientallen milliseconden tot meerdere honderdtallen milliseconden, afhankelijk van de geometrische configuratie. De geschiedenis van een radioactief ion start met de terugstoot van een kern uit de trefschijf na een kernreactie en de thermalisatie ervan in de gascel. Vanaf dit moment treden er verschillende interacties op tussen de radioactieve kern (in atomaire vorm of als ion), met buffergas atomen, onzuiverheden in het gas, elektronen en elektrische velden. Vooraleer de parameters van de gascel geoptimaliseerd worden, is van het van belang om de primaire bundel zodanig af te regelen dat de werkzame doorsnede maximaal is voor de gewenste kern. Samen met de keuze van de dikte van de trefschijf zorgt dit voor een optimale productie en transmissie. De eigenschappen van de bundel die uit de gascel wordt verkregen worden vooral bepaald door de eigenschappen van de gas jet die ontstaat bij de uitlaatopening van de cel. Differentieel pompen zorgt hier voor de juiste omstandigheden om de ionen met een RF ionengeleider te scheiden van het gas, te versnellen en te injecteren in een elektromagnetische massaseparator.

2. Experimentele methode

De LISOL separator bevindt zich in het Centre de Recherches du Cyclotron in Louvain-La-Neuve, België. Een schematisch overzicht van de opstelling is weergegeven in Fig.2.1. De primaire bundel van het cyclotron staat loodrecht op de richting van de extractie-as van de gascel. Het cyclotron is verbonden met de front-end van de separator via een hoogvacum bundellijn met daarin een scheidingsfolie van 4 tot 5 μm dun molybdeen. Het laserlokaal bevindt zich boven de front-end , van hieruit worden de laserbundels met prisma's tot in de gascel geleid. De ionen die de gascel verlaten worden door de RF ionengeleider uit de gasjet geleid en vervolgens versneld met een hoogspanning van 40 kV. Een Einzel lens focusseert de bundel vooraleer die de separatiemagneet binnenkomt. De separator kan bundels bezorgen in drie bundellijnen : BTL-left, BTL-center en BTL-right.

Aangezien de ruimtelijke spreiding van de reactieproducten van fissie- en fusiereacties verschillend is, hebben we verschillende configuraties van trefschijf en gascel nodig. Meerdere configuraties werden uitgetest met stabiele en met radioactieve ionen. Stabiele bundels kunnen we ofwel off-line produceren door een filament in de gascel resistief op te warmen en de gevaporeerde atomen resonant te ioniseren, ofwel on-line door de ionen van de primaire bundel in de gascel te stoppen en opnieuw te ioniseren door resonante laser ionisatie. In totaal hebben we vier verschillende gascellen gebouwd:

1. De grote gascel - de evacuatie tijd vanaf de zone waar de interactie met de bundel plaatsvindt bedraagt ongeveer 500 ms wanneer argon gebruikt wordt als buffergas (Fig.2.3);

2. De fissie gascel - een versie van de grote gascel waarin een cilindrisch inzetstuk met een diameter van 16 mm rond de bundel-interactie zone geplaatst is en die twee uranium trefschijven bevat van elk 10 mg/cm^2, onder een hoek van 20 graden geplaatst ten opzichte van de primaire bundel (Fig.2.5);

3. De fusie cel (een versie van de grote gascel met een inzetstuk dat een trefschijf bevat dat onder een hoek van 45° gemonteerd is (Fig.2.4). De evacuatietijd vanaf de bundel-interactiezone bedraagt hier ongeveer 80 ms wanneer argon gebruikt wordt als buffergas);

4. Een cel met een kanaal van 10 mm - met ook 2 massieve electrodes die gebruikt kunnen worden om de invloed van elektrische velden binnenin de gascel te bestuderen. De evacuatietijd met argon gas bedraagt ongeveer 240 ms (Fig.2.6).

Het gebruik van dye lasers waarbij men de golflengte kan variëren laat toe om de energie van de laserfotonen af te stemmen op de elektron transities van het gewenste element. De Lisol laser ionenbron gebruikt twee-staps ionisatieschema's, waarbij het valentie-electron eerst wordt aangeslagen tot een hogere, maar nog steeds gebonden toestand, en vervolgens tot een toestand boven de ionisatie-limiet. Efficiënte twee-staps ionisatie schema's voor de laserconfiguratie beschreven in 2.4 werden gevonden voor de elementen Ti, Mn, Co, Ni, Cu, Ru en Rh. Tabel 1.2 toont de golflengtes die hierbij gebruikt werden [Kud01].

Bij off-line studies worden er atomen van een radioactief isotoop of van een stabiel element geëvaporeerd van een heet filament binnenin de gascel. Vooraleer deze atomen de gascel verlaten worden ze met laserlicht resonant geoniseerd. Omdat de meeste off-line studies dateren van voor dit thesiswerk, zal er hier slechts een selectie van de off-line resultaten besproken worden. Meer details kan de lezer vinden in [Kud01].

On-line condities verschillen essentieel van de condities bij off-line experimenten. Eerst en vooral is de dichtheid van elektronen en ionen in het gas veel groter. Dit komt zowel door de doorgang van de primaire bundel door het gas, als door het afremmen van de reactieproducten. Een tweede verschil is dat de geproduceerde ionen tijdens het afrem proces hun ladingstoestand veranderen van meervoudig geladen ionen tot dubbel- en enkelvoudig geladen ionen of tot neutrale atomen. Een derde verschil tenslotte is dat de gascel zich nu in een zone met hoge radioactiviteit bevindt. Om deze effecten te bestuderen werd er een serie van on-line experimenten uitgevoerd. De resultaten hiervan zullen in de volgende paragrafen besproken worden. Dit omvat:

- De invloed van de cyclotronbundel op het signaal van lasergeproduceerde ionen, afkomstig van een filament;
- De studie van het afremproces, de thermalisatie, de her-ionisatie door de lasers en de extractie uit de gascel van een stabiele ionenbundel;
- De invloed van de primaire bundel op de productie van radioactieve isotopen in zware ionen genduceerde fusie reacties en lichte ionen genduceerde fissie reacties in een gascel.

3. Resultaten en discussie

3.1 Experimenten met stabiele bundels

3.1.1 De efficiëntie en selectiviteit van de laser ionenbron

Een belangrijke reeks experimenten met stabiele ionen betrof de conversie van een hoog energetische bundel van het CYCLONE cyclotron van Louvain-la-Neuve (zie paragraaf 2.1 naar een laag energetische (40 keV) bundel, door de primaire ionen af te remmen in een buffergas en resonant te her-ioniseren in een gascel. Een

voordeel van dit soort experimenten is dat men de intensiteit van de primaire bundel zeer goed kan controleren. Hiervoor werden speciaal aangepaste bundeldiagnose instrumenten ontwikkeld om een groot dynamisch bereik in bundelintensiteit toe te laten, gaande van bundels van enkele ionen per seconde tot op het deeltjes-micro-Ampère niveau.

De belangrijkste parameters van de laser ionenbron zijn de efficintie en de selectiviteit. De efficintie is gedefinieerd als de verhouding van het aantal massagesepareerde ionen tot het aantal ionen van dezelfde massa die het afrem volume van de gascel binnenkomen. De selectiviteit is de verhouding tussen het aantal ionen in de massagesepareerde bundel dat verkregen wordt wanneer de lasers afgeregeld zijn voor resonante ionisatie, tot het aantal ionen dat in dezelfde condities verkregen wordt zonder de laserbundels. Beide parameters werden opgemeten voor een ^{58}Ni bundel die gestopt wordt in de gascel gevuld met 500 mbar Argon als buffergas en dit voor verschillende intensiteiten van de primaire Ni bundel in een groot dynamisch bereik.

De maximale efficiëntie van de ionenbron voor de extractie van nikkel en argon ionen (zowel met als zonder lasers) die we gemeten hebben was 12% (zie Fig.5.12). De maximale efficintie voor argon ionen wordt bereikt bij een primaire bundelintensiteit die drie grootteordes lager is dan die intensiteit die de maximale efficiëntie oplevert voor nikkel ionen. Dit verschil wordt verklaard door de verschillende dichtheid van elektron-ion paren in de afrem zone en door het verschillende recombinatie pad. De efficiëntie voor Argon ionen zakt zeer snel wanneer de cyclotronbundelintensiteit toeneemt, om daarna te stabiliseren in de buurt van 10^{-5}%. Laser ionisatie van nikkel atomen wordt efficiënt vanaf een intensiteit van de primaire bundel van 10^4 deeltjes per seconde.

Bij deze bundelintensiteit overleven alle afgeremde nikkel ionen als eenwaardig geladen ion het afremproces en neemt de intensiteit van de gextraheerde secundaire bundel niet toe door het gebruik van de lasers, wat erop wijst dat er geen nikkel atomen beschikbaar zijn voor resonante ionisatie. Bij lagere bundelintensiteit wordt het meten van de ionenbronefficiëntie moeilijk. Wanneer er geen lasers gebruikt worden verloopt de ionenbronefficiëntie voor nikkel ionen omgekeerd evenredig met de vierkantswortel van de primaire bundelintensiteit tot op het niveau van $2{\cdot}10^{-2}$%. Bij gebruik van de lasers stijgt dit tot 10% voor bundelintensiteiten tussen 10^3 en 10^7 deeltjes per seconde en daalt met een factor 10 voor bundelintensiteiten in de buurt van 10^{10} deeltjes per seconde. De selectiviteit varieert van 1 (primaire bundel van 10^4 deeltjes per seconde), tot 100 (10^7 deeltjes per seconde) tot 50 bij de meest intense primaire bundels. De efficintie van de laser ionenbron is afhankelijk van de intensiteit en van het element.

3.1.2 Elektrische velden in de gascel

DC en RF velden werden in de gascel toegepast om elektronen in het gas te verwijderen. Hierdoor vermindert het aantal ionen dat recombineert in de gascel. Door de ionen te verwijderen uit het buffergas, net voordat een laser puls de atomen zal ioniseren, kan de selectiviteit verhoogd worden. Om deze processen te bestuderen werden er elektrodes geplaatst in de grote gascel en in de gascel met 10 mm kanaal. Tussen deze elektrodes werden er DC spanningen, korte spanningspulsen of RF signalen aangelegd. Een stabiele nikkel bundel werd gestopt in de gascel terwijl ofwel de stroom op de elektrodes, ofwel de massagesepareerde 58Ni of 40Ar bundels werd opgemeten.

A. De gascel als ionisatiekamer

Als eerste test werd er nagegaan of de aangelegde elektrische velden sterk genoeg zijn om alle ladingen die gecreerd worden door de primaire bundel te collecteren. Hiervoor werden er I-V karakteristieken opgemeten waarbij V de aangelegde spanning op de elektrodes is en I de stroom die door de elektrodes vloeit als gevolg van de collectie van ladingen in de gascel. Wanneer de I-V karakteristiek satureert kunnen we stellen dat alle ladingen gecollecteerd worden. Zulke karakteristieken werden opgemeten voor verschillende bundelintensiteiten. Een voorbeeld hiervan is Fig.5.14 die de I-V karakteristiek toont die opgemeten is voor een ^{58}Ni bundel met een energie van 45 MeV die gestopt werd in de grote gascel, gevuld met 500 mbar argongas. Voor bundelintensiteiten kleiner dan $1.9 \cdot 10^7$ pps is de maximum aangelegde spanning van -250 V voldoende om de I-V karakteristiek te satureren. Voor meer intense bundels is dit niet het geval en moeten er hogere spanningen worden aangelegd om alle ladingen in het actieve volume van de ionisatiekamer te collecteren.

In een kleine gascel, zoals diegene die gebruikt wordt voor de LISOL ionenbron, kunnen relatief hoge elektrische velden tamelijk eenvoudig worden toegepast. De cyclotronbundel die de gascel binnenkomt is goed gefocusseerd in een spot met een diameter van ongeveer 6 mm zodat de ionisatiesnelheid Q zeer hoog kan zijn bij relatief lage bundelintensiteiten. De gecreëerde ladingen worden efficint gecollecteerd door het aangelegde veld op voorwaarde dat het ruimteladingseffect dit veld niet opheft. Het theoretisch formalisme dat gebruikt werd voor ionisatiekamers werd met succes toegepast om de collectie van ladingen in de LISOL gascel te verklaren. De ruimteladingslimiet (waarbij het aangelegde veld volledig opgeheven wordt) bij 500 mbar argon in de grote gascel en een elektrisch veld van 117.5 V/cm wordt bereikt wanneer er per seconde 10^{10} elektron-ion paren per cm^3 worden gevormd. Dit komt overeen met een ^{58}Ni bundel met een intensiteit van 10^5 ionen per seconde. Bij de de gascel met 10 mm kanaal gevuld met 500 mbar argon en met een veld van 120 V/cm ligt de ruimteladingslimiet in de buurt van $5 \cdot 10^{11}$ elektron-ion paren per cm3 en per seconde, wat overeenkomt met een ^{58}Ni bundel van 10^6 ionen per seconde cell (Fig.5.16 en Fig.5.18). Voorbij de ruimteladingslimiet worden er veldvrije zones gevormd in de buurt van de anode. De ladingen die in deze zones worden gevormd kunnen vrij recombineren en geven geen bijdrage in de stroom die op de elektrodes wordt gemeten.

B. Het effect van DC velden op het geëxtraheerde Ni/Ar signaal

Het gebruik van DC velden in het gas om ladingen te collecteren wordt beperkt door het ruimteladingseffect. Voor laag intense bundels kan een sterk veld praktisch alle ladingen collecteren zodat buffergasionen verwijderd kunnen worden voordat ze de gascel verlaten. Op deze manier kan de efficintie van de gascel voor Ar ionen met enkele grootteordes verlaagd worden Fig.5.20. Anderzijds is de collectie van Ni ionen vooraleer ze kunnen neutraliseren om later resonant geïoniseerd te worden niet gewenst. Voor meer intense bundels is de collectie van ladingen erg inefficiënt, zelfs wanneer het elektrisch veld verhoogd wordt tot 100 V/cm. De meeste Ar en Ni ionen in de bundelinteractiezone recombineren vooraleer ze uit de cel geëvacueerd kunnen worden. Penetratie van het elektrisch veld in de uitlaatopening van de gascel kan leiden tot een toename het aantal Ar ionen die uit deze zone geevacueerd worden. Dit komt omdat de elektronen uit deze zonde worden verwijderd door het

aangelegde veld en de overlevingskans van Ar ionen dus toeneemt. Ar ionen die sneller meegevoerd worden door gasflow dan ze door de kathode gecollecteerd kunnen worden, kunnen gextraheerd worden uit de gascel en naar massa gesepareerd worden. Neutrale nikkel atomen worden resonant geoniseerd door de laserpulsen tijdens hun drift naar de uitlaatopening. Wanneer deze ionen de uitlaatopening naderen komen ze in een zone terecht waar het netto elektrisch veld sterker wordt aangezien de ruimtelading in die zone veel kleiner is. Een deel van de lasergeproduceerde ionen zal dus ook gecollecteerd worden. Om enerzijds dit verlies te minimaliseren en anderzijds het voordeel van het collecteren van elektronen in de buurt van de uitlaatopening te behouden, kunnen we het elektrisch veld gepulst aanleggen.

C. Het effect van gepulste velden op het gextraheerde Ni/Ar signaal

Om de selectiviteit en efficientie van de ionenbron te verhogen en om, zoals hierboven uitgelegd, het ruimteladingseffect te verminderen, kan de ionenbron in een gepulste mode gebruikt worden. In deze mode wordt de cyclotronbundel slechts tijdens een korte tijd in de gascel geplanteerd. Hierna volgt er een *wachtperiode* waarin de dichtheid van electron-ion paren afneemt door recombinatie en waarin 99% van de ionen neutraliseren. (zie Fig.3.13 in sectie 3.7). Na deze periode wordt er een spanningspuls gezet op de collectie-elektrodes om de overgebleven ladingen te verwijderen.

Om dit te bestuderen werd er een ^{58}Ni bundel gebruikt met een intensiteit van $2 \cdot 10^{10}$ pps (gemeten in DC mode). Deze bundel werd gedurende 50 ms geimplanteerd in de grote gascel, opnieuw gevuld met 500 mbar argon als buffergas. Na een wachttijd van 40 ms werd er gedurende 5 ms een elektrisch veld aangelegd en 5 ms na het elektrisch veld werd er één enkele laserpuls afgevuurd. Ondertussen werd de geëxtraheerde ^{58}Ni bundel opgemeten. De resultaten van deze metingen zijn weergegeven in Fig.5.26. Een puls van het elektrisch veld met een amplitude van 3 V/cm blijkt sterk genoeg te zijn om 64% van de overgebleven elektronen te collecteren, wat leidt tot een toename met 34% van het signaal van de gextraheerde ionen. Bij een veld van 10 V/cm worden 72% van de elektronen gecollecteerd en neemt het signaal van de ionen met 75%. Bij een veld van 245 V/cm neemt het ionen signaal met meer dan 100% toe. Bij deze veldsterkte bedraagt de driftsnelheid van de ionen in het buffergas 830 cm/s, wat betekend dat praktische alle elektronen en ionen gecollecteerd worden op de elektrodes tijdens de puls. Het toegenomen Ni signaal in dit geval kan verklaard worden door de veel kleinere recombinatiekans in een cel die bijna vrij is van elektronen, waardoor de overlevingskans van de door de lasers geproduceerde Ni ionen toeneemt.

Een andere mogelijkheid om de elektronen in de gascel te collecteren ligt in het gebruik van Radio-Frequentie (RF) velden met frequenties in het kHz gebied. De resultaten van metingen die we hebben uitgevooerd met velden van 2 tot 5 kHz worden besproken in Appendix A.

3.2 Experimenten met zware ionen geinduceerde fusiereacties

Één van de toepassingen van de LISOL gascel is de productie van neutron-arme ruthenium en rhodium isotopen waarbij de volgende fusiereactie gebruikt werd

^{58}Ni(^{36,40}Ar,xnyp). Door hun refractair karakter kunnen deze isotopen niet aan andere on-line isotopenseparators geproduceerd worden.

De energie van de primaire bundel werd geoptimaliseerd om een maximale productie van Rh of Ru isotopen te bereiken. Hiervoor werden de programma's HIVAP [Rei81] en LISE [LIS02, LISpr] gebruikt. Alhoewel de twee programma's dezelfde optimale energie voorspelden, werden er toch grote afwijkingen vastgesteld in de voorspelde werkzame doorsnede. Hierdoor kunnen we de berekende producties van Ru en Rh isotopen niet gebruiken om de efficintie van de laser ionenbron af te leiden. Daarom werd er een off-line methode gebruikt om het aantal Ru en Rh atomen dat uit de trefschijf terugstoot te meten. Tabel 5.13 toont de behaalde producties van ^{92}Tc, ^{92,94,95}Ru en ^{95}Rh, geproduceerd met een 3.7 μm dunne trefschijf van verrijkt ^{58}Ni en een primaire bundel van ^{40}Ar met een energie tussen de 111 MeV en 171 MeV.

De performantie van de laser ionenbron voor Ru en Rh isotopen werd uitgebreid bestudeerd. Hiervoor werden de off-line gemeten producties van een bepaalde isotoop in het target vergeleken met de on-line gemeten producties. De verhouding van deze getallen geeft de efficintie van de ionenbron voor deze bepaalde isotoop.

De efficiëntie van de laser ionenbron voor de productie van Rh en Ru werd ook gemeten in functie van de intensiteit van de primaire bundel bij optimale energie. De intensiteit kon echter niet zo ruim gevarieerd worden als bij de experimenten met stabiele ^{58}Ni bundel, we werden begrensd door enerzijds, bij lage bundelintensiteit de telsnelheid voor de Rh en Ru gammalijnen en anderzijds het risico om de trefschijf te beschadigen door te hoge bundelintensiteiten. Figuur 5.36 toont de experimenteel bepaalde efficintie van de ionenbron voor neutronarme ^{95}Rh en ^{94}Ru isotopen in functie van de primaire bundelintensiteit. Het valt op dat de efficintie voor 95Rh gemiddeld een grootteorde hoger is dan de efficientie voor ^{94}Ru. Dit verschil zou te maken kunnen hebben met een verschillende chemische reactiviteit van Ru met buffergasonzuiverheden wat kan leiden tot het verlies van Ru ionen in moleculaire bindingen. Bovendien kon voor Ru de tweede stap in het laserionisatie proces niet volledig gesatureerd worden. Zoals bij de experimenten met een stabiel ^{58}Ni bundel, blijkt ook hier de ionenbron efficiëntie afhankelijk te zijn van de intensiteit van de primaire bundel. Voor de productie van ^{95}Rh varieert de efficiëntie van 1.5% bij $2{\cdot}10^{11}$ pps tot 12% bij $4.8{\cdot}\ 10^{9}$ pps. Voor een primaire bundel van 10^{10} pps lag de selectiviteit voor ^{95}Rh in de buurt van 22. De efficiëntie van de bron voor de productie van ^{94}Ru was maximaal 0.8% bij $1.3{\cdot}10^{10}$ pps en zakte tot 0.2% bij 2.1 10^{11} pps. De selectiviteit in dit geval bedroeg ongeveer 11 voor een primaire bundelintensiteit van 8.5 10^{10} pps.

Tijdens de productietesten met Ru en Rh werd er een opvallende hoge efficiëntie waargenomen voor Tc isotopen. Voor ^{94}Tc werd er, zonder laserionisatie, een maximale ionenbronefficiëntie van 3% bereikt bij een bundel van $1.3{\cdot}10^{10}$ pps. Bij $2{\cdot}10^{11}$ pps was de efficiëntie nog 0.5%.

De behaalde resultaten tonen aan dat de efficintie en selectiviteit van de laser ionenbron zowel afhankelijk is van het element (chemische eigenschappen), als van de intensiteit van de primaire bundel. Ook de productie van neutronrijke Co en Ni isotopen in proton genduceerde fissiereacties werd uitgebreid bestudeerd. De resultaten worden samen met een beknopte bespreking voorgesteld in Appendix B. Net zoals bij de fusiereacties blijkt ook hier de efficintie afhankelijk van het element en van de bundelintensiteit.

4. Besluit en toekomstperspectieven

Een gevolg van het gebruik van een gascel voor de productie van radioactieve bundels met behulp van laser ionisatie is dat de doortocht van de primaire bundel doorheen het buffergas een hoge concentratie van elektron-ion paren creert, waardoor de meeste ionen die we willen bestuderen opnieuw neutraliseren. Laserionisatie kan toegepast worden in zones waar de dichtheid van ion-elektron paren voldoende laag is zodat de laser geproduceerde ionen een voldoende kans hebben om als ion het recombinatieproces te overleven.

Het evacuatieproces van de LISOL gascel werd uitgebreid bestudeerd tijdens on-line experimenten met stabiele Ni bundels. De productie van zowel buffergas ionen gecreëerd door de Ni bundel als Ni ionen geoniseerd door de lasers werd bestudeerd. De ionenbronefficintie werd gemeten voor verschillende intensiteiten van de primaire bundel (in een groot dynamisch bereik) en was maximaal 12%. Deze efficintie blijkt afhankelijk te zijn van het element en van de intensiteit van de bundel. Ook de selectiviteit is afhankelijk van de bundelintensiteit.

Elektrische velden werden toegepast in de gascel om de ion-elektron paren die gecreerd worden tijdens het afremmen van de primaire bundel te verwijderen. Met een juiste configuratie van de elektrische velden in de gascel was het mogelijk om de ionisatiesnelheid (Q_{SCL}) waarbij de ruimteladingslimiet bereikt werd te bepalen. Hiervoor werd het theoretisch formalisme gebruikt dat ontwikkeld werd om de ladingscollectie in klassieke ionisatiekamers te beschrijven.

In tegenstelling tot de experimenten met stabiele nikkel bundel doorkruist de primaire bundel de gascel bij experimenten met zware ionen genduceerde fusiereacties. De efficintie van de laser ionenbron voor de productie van Rh en Ru isotopen werd opgemeten als functie van de primaire bundelintensiteit bij optimale bundelenergie. Net zoals bij de metingen met een stabiele ^{58}Ni bundel blijkt ook hier de efficintie afhankelijk te zijn van de bundelenergie. De maximale efficiëntie was 12% voor de productie van ^{95}Rh, 0,8% voor de productie van ^{94}Ru en 3% voor de productie van ^{94}Tc. De gemeten waarde voor de selectiviteit was 22 voor Rh en 11 voor Ru. De behaalde resultaten tonen duidelijk de afhankelijkheid van de efficiëntie en de selectiviteit van zowel het element (scheikundige eigenschappen) als de bundelintensiteit.

De resultaten die behaald werden in dit werk hebben geleid tot een nieuwe configuratie voor de ionenbron die getoond wordt in Fig.6.1. Deze configuratie zal de efficiëntie en de selectiviteit verbeteren en kan ook in overweging genomen worden bij het ontwerp van gascatchers voor fragmentatiereacties, een mogelijkheid die momenteel bestudeerd wordt. Met deze configuratie kan de efficientie voor laser geproduceerde ^{58}Ni ionen met een factor 2.2 toenemen (zie paragraaf 5.1.3). Een combinatie van RF en DC elektrische velden, aangelegd langs de extractie-as van de gascel kan de evacuatie van de foto-ionen uit de gascel versnellen. Op deze manier kan de lage duty-cycle die een gevolg is van de hoger beschreven techniek gedeeltelijk voorkomen worden. Om deze ideeën uit te testen worden er momenteel experimenten uitgevoerd met de LISOL laser ionenbron waarbij de fissieproducten van een ^{252}Cf bron (spontane fissie), geplaatst binnenin de gascel, gebruikt worden.

Bibliografie

[Ahm00] S. N. Ahmed et al. Nucl. Instr. and Meth. in Phys. Res. A449 (2000) p.248.

[AirPr] http://www.airproducts.com

[And77] H. H. Andersen and J. F. Ziegler, *Hydrogen Stopping Powers and Ranges in All Elements* in The Stopping and Ranges of Ions in Matter, Vol.3, Pergamon Press Inc. (1977).

[Arj81] J.Arje and K. Valli, Nucl. Instr. and Meth. 179 (1981) p.533.

[Arm67] P. Armbruster, J. Eidens, E. Roeckl, Ark. Fysik 36 (1967) p.293.

[ATIpr] http://www-aix.gsi.de/ scheid/ATIMA1.html

[Ays01] J. Aysto, Nucl. Phys. A 693 (2001) p.477.

[Bab71] S. Baba et al., Nucl. Phys. A175 (1971) p.177.

[Bac97] H. Backe et al., Nucl. Instr. and Meth. in Phys. Res. B126 (1997) p.406.

[Bap99] B. Bapat, J. Phys. B: At. Mol. Opt. Phys. 32 (1999) p. 1859.

[Bli92] S. Bliman et al., J. Phys. B: At. Mol. Opt. Phys. 25 (1992) p.2065.

[Boa52] J. W. Boag and T. Wilson, Brit. J. Appl. Phys. 3 (1952) p.222.

[Boa63] J. W. Boag, Phys. Med. Biol. 8 (4) (1963) p.461.

[Bos68] G. G. J. Boswell, T. McGee, J. Inorg. nucl. Chem. 30 (1968) p.1139.

[Bra72] B. H. Bransden, *The Theory of the Charge Exchange*, Rep. Prog. Phys. 35 (1972) p.949.

[Bru92] M. J. Brunger et al., J. Phys. B: At. Mol. Opt. Phys. 25 (1992) p.1823.

[Bru01] B. Bruyneel, Private communication.

[Cai96] X. Cai et al., Nucl. Instr. and Meth. in Phys. Res. B119 (1996) p.452.

[Cav03] E. G. Cavalcanti et al., J. Phys. B: At. Mol. Opt. Phys. 36 (2003) p.3087.

[Che74] F. C. Chen, *Introduction to Plasma Physics*, Plenum, New York (1974).

[Coc79] C. L. Cocke, Phys. Rev. A 20, 3 (1979) p.749.

[Coh58] B. L. Cohen, C. B. Fulmer, Nucl. Phys. 6 (1958) p.547.

[Col74] C. Colmenares, Nucl. Instr. and Meth. in Phys. Res. 114 (1974) p.350.

[Coo93] R. Cooper et al., J. Chem. Phys. 98, 1 (1993) p.383.

[Das85] A. Dasgupta and A. K. Bhatia, Phys. Rev. A 32, 6 (1985) p.3335.

[Dea04] S. Dean et al., Eur. Phys. J. A21, 2 (2004) p.243.

[Dea04T] S. Dean, *The Beta Decay of Neutron-Deficient Rhodium and Ruthenium Isotopes*, Ph.D. Thesis K.U.Leuven (2004).

[Dec91] P. Decrock et al., Nucl. Instr. and Meth. in Phys. Res. B58 (1991) p.252.

[Den87] K. Deneffe et al., Nucl. Instr. and Meth. in Phys. Res. B26 (1987) p.399.

[Den97] P. Dendooven, Nucl. Instr. and Meth. in Phys. Rev. B 126 (1997) p.182.

[EMIS02] Many references on these facilities can be found in the Proceedings of the 14th International Conference on Electromagnetic Isotope Separator Techniques Related to their Applications, Victoria, Canada, 6-10 May 2002.

[Eur03] The EURISOL Report, EUROPEAN COMMISSION CONTRACT No. HPRI-CT-1999-50001(2003), `http://www.ganil.fr/eurisol/Final_Report.html`.

[Eva74] P. Rice-Evans, *Spark Streamer Proportional and Drift Chambers*, The Richelieu Press, London (1974).

[Fac04] M. Facina et al., Nucl. Instr. and Meth. in Phys. Res. B226 (2004) p.401.

[FLUID] `http://www.raczynski.com/pn/updfl.htm`

[Fra98] S. Franchoo et al., Phys. Rev. Lett. 81, 5 (1998) p.3100.

[Fra99] S. Franchoo, "Evolution of Nuclear Structure Towards ^{78}Ni investigated by the β Decay of Laser-Ionized $^{68-74}$Ni", Ph.D. Thesis, K.U. Leuven (1999).

[Fra01] S. Franchoo et al., Phys. Rev. C 64 (2001) p.64.

[Gae03] M. Gaelens et al., Nucl. Instr. and Meth. in Phys. Res. B204 (2003) p.48.

[Gar92] J. D. Garrett, Proceedins of the Second International Symposium on Nuclear Astrophysics, Karlsruhe, Germany (1992) p.287.

[Geh81] R. J. Gehrke, Int. J. Appl. Radiat. Isotop. 322 (1981) p.377.

[Gei92] H. Geissel et al., Nucl. Instr. and Meth. in Phys. Res. B70 (1992) p.286.

[Gor00] M. Gorska et al., Proceedings of the International Workshop PINGST 2000, June 6th-10th 2000, Lund, Sweden (2000) p.108.

[Heg82] R. Hegerberg et al., J. Phys. B: At. Mol. Phys. 15 (1982) p.797.

[Hel77] H. Helm, J. Phys. B: At. Mol. Phys. 10 (1977) p.3683.

[Hui04] J. Huikari et al., Nucl. Instr. and Meth. in Phys. Res. B222 (2002) p.632.

[Hur79] G. S. Hurst et al., Rev. Mod. Phys. 51 (1979) p.767.

[Huy02] M. Huyse et al., Nucl. Instr. and Meth. in Phys. Res. B187 (2002) p.535.

[Huy04] M. Huyse, *The Why and How of Radioactive-Beam Research* To be published in 'Euroschool Lectures on Physics of Exotic Beams, Vol. 1', Lect. Notes Phys. 651 (2004), Springer Verlag.

[Jau94] P. P. Jauho et al., Phys. Rev. C49, 4 (1994) p.2036.

[Kan98] T. Kanai et al., Phys. Med. Biol. 43 (1998) p.3549.

[Kel89] C. Kelbch et al., J. Phys. B: At. Mol. Opt. Phys. 22 (1989) p.2171.

[Kir92] R. Kirchner, Nucl. Instr. and Meth. in Phys. Res. B70 (1992) p.186.

[Kir97] R. Kirchner, Nucl. Instr. and Meth. in Phys. Res. B126 (1997) p.135.

[Kof51] O. Kofoed-hansen, K. O. Nielsen, Phys. Rev. 82 (1951) p.96.

[Koy02] G. K. Koyanagi et al., J. Phys. Chem. A 106 (2002) p. 4077.

[Kra94] M. Kramer and G. Kraft, Radiat. Environ. Biophys. 33 (1994) p.91.

[Kri88] E. Krishnakumar and S. K. Srivastava, J. Phys. B: At. Mol. Opt. Phys. 21 (1988) p.1055.

[Kru02] K. Kruglov et al., Eur. Phys. J. A 14 (2002) p.365.

[Kud96] Y. Kudryavtsev et al., Nucl. Instr. and Meth. in Phys. Res. B114 (1996) p.350.

[Kud01] Y. Kudryavtsev et al., Nucl. Instr. and Meth. in Phys. Res. B179 (2001) p.412.

[Kud03] Y. Kudryavtsev et al., Nucl. Phys. and Instr. in Phys. Res. B 204 (2003) p.336.

[Lan76] J. C. de Lange et al., nucl. Phys. A 258 (1976) p.141.

[Leo87] W. R. Leo, *Techniques for nuclear and particle physics experiments*, Springer-Verlag Berlin Heidelberg, Germany (1987).

[Let87] V. S. Letokhov, "Laser Photoionization Spectroscopy, Academic Press, Orlando (1987).

[Lhe99] G.Lhersonneau et al., Phys.Rev. C60 (1999) p.014315.

[Lie64] R. van Lieshout et al., Phys. Lett. 9 (1964) p.164.

[Lin73] W. Lindinger, Phys. Rev. A 7, 1 (1973) p.328.

[LIS02] D. Bazin et al., Nucl. Instr. and Meth. in Phys. Res. A482 (2002) p.307.

[LISpr] http://groups.nscl.msu.edu/lise

[Ma98] X. Ma et al., Nucl. Instr. and Meth. B 146 (1998) p.67.

[Mac89] H. Mach et al., Nucl. Instr. and Meth. in Phys. Res. A280 (1989) p.49.

[Mar87] P. Marseille et al., J. Phys. B: At. Mol. Phys. 20 (1987) p.L423.

[Mas74] H. S. W Massey and H. B. Gilbody, *Recombination and Fast Collisons of Heavy Particles* in Electronic and Ionic Impact Phenomena, Oxford University Press (1974).

[McD64] E. W. McDaniel, Collision Phenomena in Ionized Gases, John Wiley & Sons, Inc., (1964).

[Med50] H. Medicus et al., helv. Phys. Acta 23 (1950) p.299.

[Mit73] M. Mitcher and C. H. Kruger, Jr., *Partially Ionized Gases*, ed. S. C. Brown, John Wiley & Sons, Inc. (1973).

[Moo00] R. B. Moore, *Buffer Gas Cooling of Ion Beams*, Lecture Notes - Web Page http://www.physics.mcgill.ca/ moore/Notes/BeamCooling.pdf.

[Mos94] R. Moshammer et al., Phys. Rev. Lett. 73, 25 (1994) p.3371.

[Mue00] W. Mueller et al., Phys. Rev. C61 (2000) p.54308.

[Mun92] G. Munzenberg, Nucl. Instr. and Meth. in Phys. Res. B 70 (1992) p.265.

[Mus78] S. M. Mustafa and K. Mahesh, Nucl. Instr. and Meth. in Phys. Res. 150 (1978) p.549.

[Nas71] E. Nasser, *Fundamentals of Gaseous Ionization and Plasma Electronics*, ed. S. C. Brown, John Wiley & Sons, Inc. (1971).

[NIST] The values of the second ionization energies are taken from the NIST database (http://physics.nist.gov/PhysRefData/Handbook/Tables/).

[Nov96] D. Novkovic et al., Phys. Med. Biol. 41 (1996) p.725.

[NuP04] NuPECC Report, "NuPECC Long Range Plan 2004: Perspectives for Nuclear Physics Research in Europe in the Coming Decade and Beyond"(2004).

[Ost95] V. N. Ostrovsky, J. Phys. B: At. Mol. Opt. Phys. 28 (1995) p.3901.

[Qam92] Z. N. Qamhieh et al., Nucl. Instr. and Meth. in Phys. Res. B70 (1992) p.131.

[Qam94] Z. N. Qamhieh, "Resonant Laser Photo-Ionization in a Gas Cell and the Development of an Element Selective On-Line Ion Source", Ph.D. Thesis, K.U. Leuven (1994).

[Pal99] S. Palestini et al., Nucl. Instr. and Meth. in Phys. Res. A 421 (1999) p.75.

[Pet02] G. M. Petrov et al., J. Plasma Phys. 68, 5 (2002) p.321.

[Pin68] J. A. Pinston et al., J. Phys. (Paris) 29 (1968) p.257.

[POIpr] POISSON SUPERFISH code, Los Alamos National Laboratory, `http://lacg1.lanl.gov/laacg`.

[Pou99] O. Poujade et al., Nucl. Instr. and Meth. in Phys. Res. A 433 (1999) p.673.

[Rak78] A. B. Rakshit et al., J. Phys. B: At. Mol. Phys. 11, 24 (1978) p.4237.

[Rei81] W. Reisdorf, Z. Phys. A 300 (1981) p.227.

[Rod97] V. D. Rodriguez, Nucl. Instr. and Meth. in Phys. Res. B 132 (1997) p. 250.

[Rot98] H. Rothard et al., Phys. Rev. 57, 5 (1998) p.3660.

[Rud76] M. E. Rudd et al., Atomic Data and Nuclear Data Tables 18 (1976) p.413.

[Rud79] M. E. Rudd et al., Atomic Data and Nuclear Data Tables 23 (1979) p.405.

[Sat97] K. Sato et al., *The Behavior of Ionization Chambers Under the Irradiation of High-Flux X-Ray Beam*, SPRING8 Annual Report (1997) `http://www.spring8.or.jp/ENGLISH/publication/ann_rep/`.

[Sau91] F. Sauli, *Principles of Operation of Multiwire Proportional and Drift Chambers*, in: T. Ferbel (Ed.), Experimental Techniques in High-Energy Nuclear and Particle Physics, World Scientific (1991).

[Sav02] G. Savard et al., Nucl. Phys. A 701 (2002) p.292.

[Sav03] G. Savard, Nucl. Instr. and Meth. in Phys. Res. B 204 (2003) p.771.

[Sch88] G. Schiwietz et al., Phys. Rev. A38, 11 (1988) p.5552.

[Sei03] K. Seiersen et al., Phys. Rev. A 68 (2003) p.22708.

[Sen88] M. Senba, J. Phys. B: At. Mol. Opt. Phys. 21 (1988) p.3093.

[Sha64] J. Sharpe, Nuclear Radiation Detectors, Methuen, London (1964).

[Shi86] K. Shima et al., Atomic Data and Nuclear Data Tables 34 (1986) p.357.

[SHIP] SHIPTRAP homepage `http://www.aix.gsi.de/~shiptrap/index.html`

[Sin99] M. J. Singh et al., PRAMANA J. Phys. 53, 4, Indian Academy of Sciences (1999)p.743.

[Son92] R. J. van Sonsbeek et al., J. Chem. Phys. 97, 3 (1993) p.1800.

[SRIpr] J.F. Ziegler, J.P.Biersack, http://www.srim.org

[Sug96] Y. Sugaya et al., Nucl. Instr. and Meth. in Phys. Res. A368 (1996) p.635.

[Tho04] J. C. Thomas, Private communication.

[Ton89] T. Tonuma et al., Phys. Rev. A 40, 11 (1989) p.6238.

[VBe97] P. Van Den Bergh et al., Nucl. Instr. and Meth. in Phys. Res. B126 (1997) p.194.

[VDu97] P. Van Duppen, Nucl. Instr. and Meth. in Phys. Res. B 126 (1997) p.66.

[VDu03] P. Van Duppen, Nucl. Instr. and Meth. in Phys. Res. B 204 (2003) p.9.

[Vel01] C. Velissaris, *Principles of Ionization Chamber Operation Under Intense Ionization Rates*, internal NuMI report NuMI-NOTE-GEN-717, `http://www-numi.fnal.gov/numinotes/public/pdf/numi0717/numi0717.pdf` (29 January 2001).

[Vel02] C. Velissaris, *A time dependent solution for an ionization chamber space charge density*, internal NuMI report NuMI-NOTE-GEN-814, `http://www-numi.fnal.gov/numinotes/public/pdf/numi0814/numi0814.pdf` (15 January 2002).

[Ver94] L. Vermeeren et al., Phys. Rev. Lett. 73 (1994) p.1935.

[Ver81] J. Verplancke et al., Nucl. Instr. and Meth. 186 (1981) p.99.

[Wad03] M. Wada et al., Nucl. Instr. and Meth. in Phys. Res. B 204 (2003) p.570.

[War75] J. M. Warman and M. P. de Haas, J. Chem. Phys. 63, 5 (1975) p.2094.

[Way73] A. Wayne Johnson, and J. B. Gerardo, Phys. Rev. A 7 (1973) p.1339.

[Wei75] C. Weiffenbach et al., Can. J. Phys. 53 (1975) p.101.

[Wei99] L. Weissman et al., Nucl. Instr. and Meth. in Phys. Res. A 423 (1999) p.328.

[Wei00] H. Weick et al., Nucl. Instr. and Meth. in Phys. Res. B 164-165 (2000) p.168.

[Wei02] L. Weissman et al., Nucl. Instr. and Meth. in Phys. Res. B 483 (2002) p.593.

[Wei04] L. Weissman et al., Nucl. Instr. and Meth. in Phys. Res. B 522 (2004) p.212.

[Whi04] H. J. Whitlow, and H. Timmers, *Charge Exchange and Electron Stripping* in Electrostatic Accelerators - Techniques and Applications, Springer (2004) in press.

[Wol87] H. Wollnik, "Optics of Charged Particles", Academic Pres, Inc., San Diego (1987) p.31.

[Zap02] T. Zäpfel et al., Nucl. Instr. and Meth. in Phys. Res. B 193 (2002) p.651.

[Zie80] J. F. Ziegler, *Handbook of Stopping Cross Sections for Energetic Ions in All Elements*, Vol. 5 of *The Stopping and Ranges of Ions in Matter*, Pergamon Press Inc., (1980).

[Zie85a] J. F. Ziegler, J. P. Biersack, and U. Littmark, *The Stopping and Range of Ions in Solids*, Pergamon Press Inc., (1985).

[Zie85b] J. F. Ziegler and J. P. Biersack, in *treatise on Heavy Ion Science*, edited by D. A. Bromley, Plenum Press, New York (1985), vol.6, p.95.

[Zie96] M. Zielczynski et al., Nucl. Instr. and Meth. in Phys. Res. A 370 (1996) p.563.

[Zie99] J. F. Ziegler, J. Appl. Phys./Rev. Appl. Phys. 85 (1999) p. 1249.

[Zwa03] R. M. Zwaska et al., IEEE Transactions on Nuclear Science 50(4), (2003) p.1129 (arXiv: hep-ex/0212011). v1 5 Dec 2002.

[Xu93] H. J. Xu et al, Nucl. Instr. and Meth. in Phys. Res. A 333 (1993) p.274.